

Doctoral thesis

Doctoral theses at NTNU, 2021:40

Henning Goa Hugdal

A study of proximity-induced and magnon-mediated superconductivity on the surface of topological insulators

NTNU
Norwegian University of Science and Technology
Thesis for the Degree of
Philosophiae Doctor
Faculty of Natural Sciences
Department of Physics



Norwegian University of
Science and Technology

Henning Goa Hugdal

A study of proximity-induced and magnon-mediated superconductivity on the surface of topological insulators

Thesis for the Degree of Philosophiae Doctor

Trondheim, February 2021

Norwegian University of Science and Technology
Faculty of Natural Sciences
Department of Physics



Norwegian University of
Science and Technology

NTNU

Norwegian University of Science and Technology

Thesis for the Degree of Philosophiae Doctor

Faculty of Natural Sciences

Department of Physics

© Henning Goa Hugdal

ISBN 978-82-326-6945-5 (printed ver.)

ISBN 978-82-326-5597-7 (electronic ver.)

ISSN 1503-8181 (printed ver.)

ISSN 2703-8084 (online ver.)

Doctoral theses at NTNU, 2021:40

Printed by NTNU Grafisk senter

ABSTRACT

This thesis presents a study of superconducting phases in different effectively two-dimensional (2D) systems with spin-orbit coupling, with particular emphasis on systems consisting topological insulators (TIs) in proximity to superconductors (S) and magnetic insulators. The research has led to five papers.

The first paper examines the possible superconducting phases in a 2D repulsive Hubbard model with Zeeman splitting and Rashba spin-orbit coupling, showing that the Kohn-Luttinger mechanism is responsible for the effective attractive pairing. The spin-orbit coupling, however, indirectly affects the symmetry of the order parameter, leading to a chiral $p \pm ip$ or p state depending on the orientation of the Zeeman field.

Two papers consider the proximity effect between a superconductor and topological insulator, and the interplay with exchange fields. When a spin valve is placed on top of a TI Josephson junction, we find that vortices can be induced on the surface of the TI depending on the spin valve configuration. We also study the possibility of a strong inverse proximity effect — a significant reduction in the superconducting gap — in an S-TI bilayer, finding that this is unlikely for a conventional s -wave superconductor, but might occur in unconventional superconductors with low Fermi energies.

The final two papers examine superconductivity mediated by magnons on the surface of a TI coupled to a magnetic insulator. When neglecting the frequency dependence of the magnons we find that, depending on the coupling between the magnons, both BCS type and Amperean p -wave pairing is possible. Including the magnon frequency dependence, we also find the possibility of odd-frequency s -wave Amperean pairing.

PREFACE

This thesis is submitted in partial fulfillment of the requirements of the degree of philosophiae doctor at the Norwegian University of Science and Technology (NTNU) in Trondheim, Norway. The research presented in this thesis and the enclosed papers [1–5] was conducted as part of the 4-year graduate program in physics, including one year of teaching duties at the Department of Physics, NTNU, and coursework totaling 30 ECTS credits. The research has been supervised by Prof. Asle Sudbø, with Prof. Jacob Linder as co-supervisor, and funded through the Research Council of Norway Grant Number 250985 “Fundamentals of Low-dissipative Topological Matter”.

ACKNOWLEDGMENTS

First of all I would like to thank my supervisor Asle for giving me the opportunity to do research in the very interesting field of superconductivity, for sharing his immense insight and knowledge of the field, for patiently answering my questions whenever I stuck my head in his office door, and for giving me trust and responsibility, allowing me to grow as a researcher. I would also like to thank my co-supervisor Jacob for interesting collaborations and discussions, insightful comments and suggestions, and words of encouragement.

I would like to thank Morten for many interesting and helpful discussions and collaborations during both our Master and PhD studies. Thank you also to my other collaborators Flavio, Stefan, Sol, and Snorre, and to Even and Eirik for very useful discussions when working on similar research topics. I have also greatly appreciated the company of my fellow office mates Stefan, Fredrik Nicolai, Frode, and Tancredi, who together with the rest of QuSpin have made the last four years very enjoyable!

A big thank you to my parents for all your love and support, and for always giving me the freedom to learn out of curiosity and love of exploration rather than out of requirement.

I want to thank my children Johan and Martha for filling my life with so much joy, and the possibility of rediscovering the world with you. Finally, to my wife Åshild, thank you for your never-ending love, patience and support, and for always believing in me when I struggle to.

PUBLICATIONS

1. H. G. Hugdal and A. Sudbø,
p-wave superconductivity in weakly repulsive 2D Hubbard
model with Zeeman splitting and weak Rashba spin-orbit
coupling,
Physical Review B, **97**, 024515 (2018).
doi:10/fk8k.
2. M. Amundsen, H. G. Hugdal, A. Sudbø and J. Linder,
Vortex spin valve on a topological insulator,
Physical Review B, **98**, 144505 (2018).
doi:10/d2k5.
3. H. G. Hugdal, M. Amundsen, J. Linder and A. Sudbø,
Inverse proximity effect in s-wave and d-wave superconductors
coupled to topological insulators,
Physical Review B, **99**, 094505 (2019).
doi:10/gfwst7.
4. H. G. Hugdal, S. Rex, F. S. Nogueira and A. Sudbø,
Magnon-induced superconductivity in a topological insulator
coupled to ferromagnetic and antiferromagnetic insulators,
Physical Review B, **97**, 195438 (2018).
doi:10/fk8h.
5. H. G. Hugdal and A. Sudbø,
Possible odd-frequency Amperean magnon-mediated super-
conductivity in topological insulator – ferromagnetic insulator
bilayer,
Physical Review B, **102**, 125429 (2020).
doi:10/fk8j.

CONVENTIONS

We use the de Gennes convention of $e = -|e|$ being the charge of the electron [6, p. 436]. Unless otherwise stated, we have set the reduced Planck constant and Boltzmann constant to unity, $\hbar = 1$, $k_B = 1$.

Unit vectors in the three Cartesian coordinate directions are written as \hat{x} , \hat{y} and \hat{z} .

The spatial and imaginary time Fourier transform is

$$f(\tau, \mathbf{r}) = \frac{1}{\beta V} \sum_{\mathbf{k}, \omega_n} e^{i\mathbf{k}\cdot\mathbf{r} - i\omega_n\tau} f(\omega_n, \mathbf{k}),$$

$$f(\omega_n, \mathbf{k}) = \int d\mathbf{r} \int_0^\beta d\tau e^{-i\mathbf{k}\cdot\mathbf{r} + i\omega_n\tau} f(\tau, \mathbf{r}),$$

where V is the volume of the system, and $\beta = (k_B T)^{-1}$ with temperature T .

For 2D wave-vectors we will often use the notation $\mathbf{k} = (k_x, k_y) = |\mathbf{k}|(\cos \phi_{\mathbf{k}}, \sin \phi_{\mathbf{k}})$. 3-vector notation is also frequently used, such as $\mathbf{k} = (\omega_n, \mathbf{k})$ and $\mathbf{q} = (\Omega_n, \mathbf{q})$, where $\omega_n = (2N + 1)\pi/\beta$ and $\Omega_n = 2N\pi/\beta$ with $N \in \mathbb{Z}$ are fermionic and bosonic Matsubara frequencies respectively. We also use the Pauli vector notation $\boldsymbol{\sigma} = (\sigma_x, \sigma_y, \sigma_z)$, with Pauli matrices

$$\sigma_x = \begin{pmatrix} 0 & 1 \\ 1 & 0 \end{pmatrix}, \quad \sigma_y = \begin{pmatrix} 0 & -i \\ i & 0 \end{pmatrix}, \quad \sigma_z = \begin{pmatrix} 1 & 0 \\ 0 & -1 \end{pmatrix}.$$

In equations with matrix structure, the $N \times N$ identity matrix $\hat{1}_N$ is seldom explicitly written, meaning that e.g. $i\omega_n + \mathbf{k} \cdot \boldsymbol{\sigma}$ should be interpreted as $i\omega_n \hat{1}_2 + \mathbf{k} \cdot \boldsymbol{\sigma}$.

CONTENTS

Publications	vii
Conventions	ix
1 INTRODUCTION	1
2 SUPERCONDUCTIVITY	3
2.1 Early history and defining properties	3
2.2 The Ginzburg-Landau theory	4
2.3 Superconductivity from attractive pairing	11
2.4 Phonon-mediated superconductivity	18
2.5 Unconventional superconductivity	25
2.6 Superconductivity in two dimensions	26
3 KOHN-LUTTINGER SUPERCONDUCTIVITY	31
3.1 Superconductivity from weak on-site interaction	31
3.2 Spin-polarized systems	36
3.3 Rashba spin-orbit coupling	37
3.4 Spin-splitting and Rashba SOC	41
4 TOPOLOGICAL INSULATORS	49
4.1 The Hall effects	49
4.2 Model for topological insulators	52
4.3 Surface states	55
4.4 Breaking the time-reversal symmetry	58
5 TOPOLOGICAL SUPERCONDUCTING PROXIMITY EFFECT	61
5.1 Proximity effect on the topological insulator surface	62
5.2 Vortex spin valve	64
5.3 Inverse proximity effect	65
6 MAGNON-MEDIATED SUPERCONDUCTIVITY	73
6.1 Ferromagnetic insulator	74
6.2 Magnon-mediated interaction	76
6.3 The gap equation	79
6.4 Zero frequency limit	81

6.5	Frequency dependent gap solutions	85
7	OUTLOOK	89
	BIBLIOGRAPHY	91
	LIST OF ABBREVIATIONS	113
 <i>Appendix</i>		
A	PATH INTEGRAL FORMALISM	117
	ENCLOSED PAPERS	125

INTRODUCTION

Condensed matter physics is a relatively new field of study [7], but is currently one of the largest research fields in physics, and includes a wide range of topics. In this field systems of a large number of particles are studied using quantum mechanics, statistical mechanics and electromagnetic theory, which leads to entirely new phenomena not possible to envision from studying only a few particles [8]. The field of condensed matter physics and its predecessor, solid state physics, has also taken a great part in many of the technological developments of the last decades which we now benefit from in our daily lives: The development of the transistor has lead to computer processors becoming smaller and faster, and the discovery of the giant magnetoresistance effect [9, 10] lead to compact hard disk drives [11]. Moreover, the discovery of superconductivity and subsequent development of superconducting magnets has applications in medical imaging [12].

Some of the technological advances of the last century are due to discoveries that can be considered serendipitous, and exemplify the fact that it can often be difficult to predict the outcome of research. Perhaps it is thus best to strike a balance between research directly focused on solving the various problems at hand, and strictly curiosity-driven fundamental research of which the outcome is more uncertain. There is at least little doubt that there are many big problems yet to be solved, such as the ever greater need for more powerful and energy efficient computers.

Research toward these goals currently go along many lines, for instance in utilizing the electron spin instead of the charge as an information carrier using magnetic materials — spintronics instead of electronics [13, 14], and combining this with superconductors — superconducting spintronics [15–17]. Progress is also being done in making quantum computers, where the possibility of quantum superpositions of the classical bit states 0 and 1 can allow for much faster computing for certain types of problems [18].

The topic of this thesis lies in this landscape, though the focus on technological applications has taken a back seat. The aim has been to study different superconducting states and mechanisms for superconductivity in effectively two-dimensional systems, such as at the interface between two materials, with the main emphasis being on superconductivity on the surface of topological insulators (TIs).

The following chapters give an introduction to the main topics of the thesis and the results of the enclosed papers. Chapter 2 gives an introduction to the topic of superconductivity, outlining the early history of the field while introducing the main theoretical framework used in the thesis. Chapter 3 discusses the Kohn-Luttinger mechanism for superconductivity in various systems, before turning to the specific system discussed in Paper [1]. We subsequently give an introduction to topological insulators (Chapter 4), the class of materials on which we have focused the most. In the following two chapters we discuss superconductivity on the surface of a TI due to proximity coupling to a superconductor (Chapter 5, Papers [2, 3]), and due to interactions with magnons in a magnetic insulator (Chapter 6, Papers [4, 5]). Chapter 7 gives a brief outlook on possible future work.

In the grand scheme of furthering our knowledge and technological advancement, this thesis represents my tiny, but hopefully not entirely insignificant, contribution.

2

SUPERCONDUCTIVITY

The overarching topic of this thesis is superconductivity, which will be introduced and discussed in some detail in this chapter. We start with a brief historical account of the discovery of superconductors, and their defining properties. We then go into some detail of one of the early phenomenological theories of superconductivity — the Ginzburg-Landau (GL) theory. This leads us into a discussion of the celebrated microscopic Bardeen-Cooper-Schrieffer (BCS) theory of superconductivity, where we will also introduce the general theoretical framework used throughout most of the thesis. After a brief account of unconventional superconductivity, we will finally address changes to the superconducting state due to the reduced dimensionality in the effective 2D systems discussed in the thesis.

2.1 EARLY HISTORY AND DEFINING PROPERTIES

In 1911¹ Kamerlingh Onnes [20] discovered something remarkable when cooling mercury using liquid helium: Below a certain temperature the DC resistance suddenly dropped to zero. The material had become superconducting. Two decades later, another feature of the superconducting state was discovered, namely the expulsion of magnetic fields from the interior of superconductors upon cooling

¹Only a very brief historical account of the main early developments of superconductivity is given here and the following sections. For a more thorough overview see e.g. the books by Tinkham [6], and Fossheim and Sudbø [19].

down the material — the Meissner effect [21]. These two properties, perfect conductivity ($\sigma = \infty$) and perfect diamagnetism (magnetic susceptibility $\chi = -1$) below a critical temperature T_c and critical field H_c , established that a superconductor is a new thermodynamic state defined by the thermodynamic variables temperature T and applied field H [6, 19].

It was later discovered that there are in fact two types of superconductors: In type I superconductors the transition from the superconducting state with total expulsion of magnetic field (the Meissner phase) to the normal state occurs abruptly at the critical field $H = H_c$. In type II superconductors, however, there is no sudden change from the Meissner phase to the normal phase when increasing the field strength. Instead there is an intermediate mixed state where some magnetic flux penetrates the superconductor, occurring for H above the first critical field H_{c1} . The amount of flux increases with increasing H , reaching full penetration and thus the normal state at the second critical field H_{c2} [19]. The phase diagrams of type I and II superconductors, and the magnetic field response is illustrated in Fig. 2.1.

2.2 THE GINZBURG-LANDAU THEORY

On the theoretical side, the first phenomenological theory of superconductivity was proposed by London and London [22] in 1935, describing the main electromagnetic phenomena of superconductivity [6]. Two decades later Ginzburg and Landau [23] incorporated the London theory into a new theory based on Landau's theory for phase transitions.

The GL theory is based on a free energy expansion in terms of a complex order parameter ψ [6, 19, 24],

$$F = F_N + a(T)|\psi|^2 + \frac{b}{2}|\psi|^4 + \frac{1}{2m_*}|(-i\hbar\nabla - e_*\mathbf{A})\psi|^2 + \frac{1}{2\mu_0}\mathbf{B}^2, \quad (2.1)$$

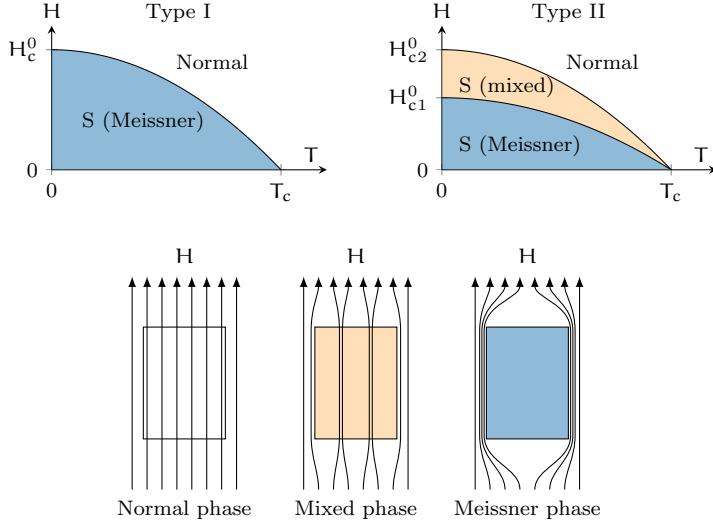


Figure 2.1: (top) Sketch of $T-H$ phase diagram for type I (left) and type II (right) superconductors, showing the transitions between the normal phase, and superconducting (S) mixed and Meissner phases. H_c^0 , H_{c1}^0 and H_{c2}^0 denote the critical fields at zero temperature. (bottom) Sketch of response to an applied magnetic field for the normal phase, mixed phase, and Meissner phase (left to right). Based on figures in Ref. [19].

where F_n is the free energy in the normal phase, \mathbf{A} is the vector potential, $\mathbf{B} = \nabla \times \mathbf{A}$ is the magnetic induction, and m_* and e_* is an effective mass and charge. $a = a_1(T - T_c)/T_c$ and $b > 0$ are phenomenological coefficients. The free energy is relevant for the superconducting electrons, with number density n_s assumed proportional to $|\psi|^2$ [6, 19].

We now minimize the free energy with respect to variations in ψ and ψ^* using the Euler-Lagrange equations

$$\frac{\partial F}{\partial \psi^{(*)}} - \nabla \cdot \frac{\partial F}{\partial (\nabla \psi^{(*)})} = 0, \quad (2.2)$$

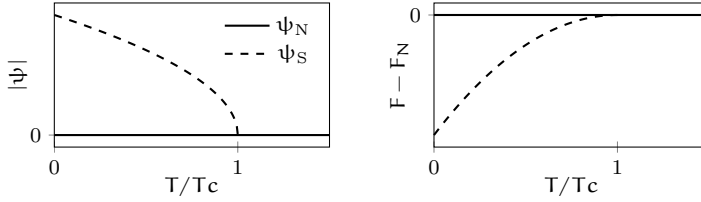


Figure 2.2: (left) Sketch of the solutions ψ_N and ψ_S , and the corresponding free energy (right) as a function of temperature.

resulting in the first GL equation

$$\alpha(T)\psi + b|\psi|^2\psi + \frac{1}{2m_*}(-i\hbar\nabla - e_*\mathbf{A})^2\psi = 0. \quad (2.3)$$

The second GL equation is obtained by varying \mathbf{A} , resulting in

$$\frac{e_*}{2m_*}[\psi^*(-i\hbar\nabla - e_*\mathbf{A})\psi + \text{c.c.}] = \frac{1}{\mu_0}[\nabla(\nabla \cdot \mathbf{A}) - \nabla^2\mathbf{A}] = \mathbf{J}, \quad (2.4)$$

where c.c. denotes the complex conjugate. Here we have identified \mathbf{J} as the supercurrent density by using Maxwell's equation $\nabla \times \mathbf{B} = \mu_0\mathbf{J}$ [6, 19].

Assuming no fields and a homogeneous system, the first GL equation has solutions

$$\psi_N = 0, \text{ and } |\psi_S| = \sqrt{-\frac{\alpha_1}{b} \frac{T - T_c}{T_c}}, \quad (2.5)$$

where the latter is valid only for $T < T_c$, see Fig. 2.2. Inserting these solutions into the free energy Eq. (2.1), we see from Fig. 2.2 that above T_c we only have the trivial solution ψ_N , corresponding to the normal state. Below T_c however, ψ_S minimizes the free energy compared to the normal state free energy, and we thus have superconductivity, where the density of superconducting electrons n_s increases with decreasing temperature.

The solution Eq. (2.5) only specifies the magnitude of $\psi = |\psi|e^{i\varphi}$, not the phase. There are therefore infinitely many degenerate solutions corresponding to different values of φ , of which the system

spontaneously “chooses” one global value when the temperature drops below T_c . When including spatial variations of ψ , this freedom in choosing φ ensures that the free energy is gauge invariant, which is necessary for physical observables such as the supercurrent to be gauge invariant, see Eq. (2.4) [19]. The magnetic induction \mathbf{B} is invariant under the local transformation $\mathbf{A} \rightarrow \mathbf{A}' = \mathbf{A} - \nabla\theta$, where $\theta(\mathbf{r})$ is a real function. For the free energy to be invariant we must simultaneously transform the phase according to $\varphi \rightarrow \varphi' = \varphi - e_*\theta/\hbar$.²

FLUX QUANTIZATION From the gauge transformation of the superconducting wavefunction ψ one can already deduce one of the remarkable facts about superconductors, namely that the flux Φ through a normal region embedded in a superconductor, such as a vortex in the mixed superconducting phase described above, is quantized in terms of a flux quantum Φ_0 . In order for the order parameter to be single-valued at any point, a line integral in a closed circle has to satisfy

$$\oint d\mathbf{l} \cdot \nabla\varphi = 2\pi N, \quad (2.6)$$

where $N \in \mathbb{Z}$. This must hold also for a gauge transformed phase φ' . Using the gauge freedom to choose $\mathbf{A}' = 0$ in a superconducting region with $\mathbf{B} = 0$, we get $\mathbf{A} = \nabla\theta$. Integrating around a closed loop enclosing a normal region with $\mathbf{B} \neq 0$, we therefore get

$$\oint d\mathbf{l} \cdot \nabla\varphi' = \oint d\mathbf{l} \cdot \nabla\varphi - \frac{e_*}{\hbar} \oint d\mathbf{l} \cdot \mathbf{A} = 2\pi N. \quad (2.7)$$

²It is often stated that the superconducting state spontaneously breaks the $U(1)$ gauge symmetry of the system. It is important to point out that a local gauge symmetry cannot be spontaneously broken [25]. The local gauge $U(1)$ symmetry in this case is not a physical symmetry (such as e.g. the $O(3)$ symmetry of an isotropic ferromagnet), but rather a redundancy in our mathematical description [26, 27]. The system does however break the global $U(1)$ phase rotation symmetry [26], meaning superconductors can have different phases, as is evident in e.g. Josephson junctions.

Using Stokes' theorem, this results in

$$\int_{\Lambda} d\mathbf{S} \cdot \mathbf{B} = \Phi = \frac{2\pi\hbar}{e_*} N \equiv \Phi_0 N, \quad (2.8)$$

where we have defined the flux quantum $\Phi_0 = 2\pi\hbar/|e_*|$.

PERFECT CONDUCTIVITY Using the London approximation of $|\psi|$ constant in space [19], the second GL equation simplifies to

$$\mathbf{J} = -\frac{e_*^2 |\psi|^2}{m_*} \left[\mathbf{A} - \frac{\hbar}{e_*} \nabla \varphi \right]. \quad (2.9)$$

We see that the vector potential \mathbf{A} in a static magnetic field, as well as phase gradients, lead to supercurrents [19]. Moreover, taking the time-derivative of the above equation, assuming $\nabla \varphi = 0$, we get $\mathbf{E} \sim \partial_t \mathbf{J}$. This implies perfect conductivity since an electric field accelerates a supercurrent, instead of just maintaining it [6], and a stationary current is possible even when $\mathbf{E} = 0$ [22].

MEISSNER EFFECT Rewriting Eq. (2.9) in terms of the field $\tilde{\mathbf{A}} = \mathbf{A} - \hbar \nabla \varphi / e_*$, we get

$$\nabla \times \mathbf{B} = \mu_0 \mathbf{J} = -\frac{\mu_0 e_*^2}{m_*} |\psi|^2 \tilde{\mathbf{A}}. \quad (2.10)$$

Taking the curl of this equation results in

$$\mathbf{B} = \frac{m_*}{\mu_0 e_*^2 |\psi|^2} \nabla^2 \mathbf{B}, \quad (2.11)$$

where we have used $\nabla \times (\nabla \times \mathbf{B}) = -\nabla^2 \mathbf{B}$ since $\nabla \cdot \mathbf{B} = 0$ [28]. This means that a uniform non-zero magnetic field is not possible inside a superconductor. In one dimension, assuming a constant field B_{ex} outside the superconductor ($x < 0$), we get the following solution inside the superconductor ($x > 0$) [19, 27],

$$B(x) = B_{\text{ex}} e^{-\frac{x}{\lambda_L}}, \quad (2.12)$$

where we have defined the London penetration depth

$$\lambda_L = \sqrt{\frac{m_*}{\mu_0 e_*^2 |\psi|^2}}. \quad (2.13)$$

Hence, in the superconducting phase an external field is screened from the interior of the superconductor by supercurrents on the surface of the superconductor, with penetration depth λ_L [6, 12, 19]. For decreasing temperatures the density of superconducting electrons increases, leading to a more efficient screening of the magnetic field. In reality the effective penetration depth λ can deviate significantly from λ_L [6, 19] due to non-local effects [6, 19, 29].

TYPE I AND II SUPERCONDUCTORS In addition to the above phenomena, which was also described by the London theory,³ the GL equations also allowed for the study of superconductors in strong fields, and with variations in ψ [6]. In the latter case, assuming zero field and variation in only one dimension, the first GL equation Eq. (2.3) gives [24]

$$a(T)\psi + b|\psi|^2\psi - \frac{\hbar^2}{2m_*} \partial_x^2 \psi = 0. \quad (2.14)$$

Defining $\tilde{\psi} = \psi/\psi_S$, we can rewrite the above as

$$-\tilde{\psi} + |\tilde{\psi}|^2\tilde{\psi} - \xi(T)^2 \partial_x^2 \tilde{\psi} = 0, \quad (2.15)$$

where we have defined the GL coherence length [6, 19, 24]

$$\xi(T) = \frac{\hbar}{\sqrt{|2m_* a(T)|}}, \quad (2.16)$$

as the characteristic length scale over which ψ varies.

We thus have two length scales associated with the superconductor: the penetration depth λ and the correlation length ξ , see Fig. 2.3.

³For both the Meissner effect and perfect conductivity paragraphs, we essentially use some form of the London equations derived from the GL equations.

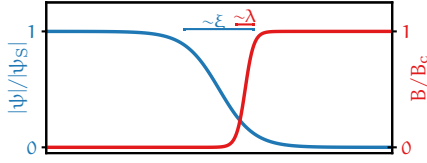


Figure 2.3: Variation of ψ and magnetic field B at the interface between superconducting and normal regions, illustrating the length scales λ and ξ . Based on similar figures in Refs. [6, 19, 24].

Since both diverge approximately as $(T - T_c)^{-1/2}$ as $T \rightarrow T_c$, the dimensionless quantity

$$\kappa = \frac{\lambda}{\xi}, \quad (2.17)$$

the Ginzburg-Landau parameter, is approximately constant close to T_c [6]. Abrikosov [30, 31] showed that the size of κ determines if a superconductor is of type I or II. A simplified argument goes as follows [6, 19, 24]: At the interface between a normal and a superconducting region with an applied field H_c parallel to the surface, there is a decrease in the free energy compared to the bulk normal state associated with the screening of the magnetic field over a length scale λ . However, there is also an increase in energy compared to the bulk superconducting state due to the lost condensation energy over a length scale ξ , see Fig. 2.3. The surface energy — the change in free energy due to the interface — is therefore approximately proportional to the difference between these length scales, $\Delta F_{\text{surf}} \sim (\xi - \lambda)$ [6, 19, 24]. Hence, if $\kappa < 1^4$ the surface energy is positive and the system tries to minimize the interface area. This is a type I superconductor. On the other hand, $\kappa > 1$ results in a negative surface energy, and the system tries to maximize the interface area. However, as we have seen above, the minimum flux allowed is the flux quantum Φ_0 . Type II superconductors therefore have quantized flux lines of flux Φ_0 in the mixed phase [19, 24].

⁴The exact separation point between type I and II superconductors is $\kappa = 1/\sqrt{2}$. [6, 19, 24, 31]

2.3 SUPERCONDUCTIVITY FROM ATTRACTIVE PAIRING

When the GL theory was proposed in 1950, though it correctly described the key features of superconductors, it was purely phenomenological, and not derived from a microscopic theory. There were several hints to what ingredients such a theory should contain. For instance experiments had shown that there was an energy gap $2\Delta \sim k_B T_c$ separating the ground state and lowest excited state [6]. Moreover, when measuring the critical temperature for different isotopes the transition temperature was found to increase with decreasing nuclear mass [32, 33], indicating that the microscopic mechanism was related to interactions between the electrons and the lattice vibrations — the phonons — of the material [34].

Finally, in 1957 Bardeen, Cooper and Schrieffer [35] published their theory of superconductivity, describing how effective interactions between electrons due to phonons lead to the formation of bound pairs of electrons — Cooper pairs [36]. Their theory predicted an energy gap of $2\Delta = 3.5k_B T_c$ at zero temperature, in good agreement with experiments [6, 35]. Later, Gor'kov [37, 38] showed that the GL theory could be derived from the microscopic BCS theory for temperatures close to the critical temperature, with the GL wavefunction ψ being proportional to the gap parameter Δ [6, 24].

Before discussing the BCS theory in more detail, we will take a detour to introduce a more general formulation of a superconducting theory [39] where we do not consider any particular pairing mechanism. This theory will then be specialized to the BCS theory with phonon-mediated attraction, and later applied to the other various cases studied in the thesis. Our starting point is the quantum partition function⁵

$$\mathcal{Z} = \int \mathcal{D}\psi^\dagger \mathcal{D}\psi e^{-S[\psi^\dagger, \psi]} \quad (2.18)$$

⁵For an introduction to the path integral formalism see e.g. Altland and Simons [40], Lancaster and Blundell [41] or Negele and Orland [42], or Appendix A for a short summary.

where we have defined the action

$$\begin{aligned}
S = S_0 + S_{\text{int}} &= \frac{1}{\beta V} \sum_{\mathbf{k}} \sum_{\sigma, \sigma'} (-i\omega_n \delta_{\sigma\sigma'} + h_{\mathbf{k}, \sigma\sigma'}) \psi_{\mathbf{k}, \sigma}^\dagger \psi_{\mathbf{k}, \sigma'} \\
&+ \frac{1}{2(\beta V)^3} \sum_{\mathbf{k}, \mathbf{k}', \mathbf{q}} \sum_{\substack{\sigma_1, \sigma_2, \\ \sigma_3, \sigma_4}} V_{\mathbf{k}\mathbf{k}'}^{\sigma_1 \sigma_2 \sigma_3 \sigma_4}(\mathbf{q}) \\
&\times \psi_{\mathbf{k}+\mathbf{q}, \sigma_1}^\dagger \psi_{-\mathbf{k}+\mathbf{q}, \sigma_2}^\dagger \psi_{-\mathbf{k}'+\mathbf{q}, \sigma_3} \psi_{\mathbf{k}'+\mathbf{q}, \sigma_4}. \tag{2.19}
\end{aligned}$$

Here $\psi_{\mathbf{k}, \sigma}$ denotes Grassmann fields for the electrons [40] with 4-momentum $\mathbf{k} = (\omega_n, \mathbf{k})$, where $\omega_n = (2n + 1)\pi/\beta$, $n \in \mathbb{Z}$ is a Fermionic Matsubara frequency, $\beta = 1/k_B T$, and \mathbf{k} is the wavevector. σ denotes the (pseudo-)spin state of the field. $h_{\mathbf{k}, \sigma\sigma'}$ is the single particle Hamiltonian, and $V_{\mathbf{k}\mathbf{k}'}^{\sigma_1 \sigma_2 \sigma_3 \sigma_4}(\mathbf{q})$ is a two-particle interaction potential depending on 4-momenta \mathbf{k} and \mathbf{k}' , spin states σ_i , and the 4-momentum $\mathbf{q} = (\Omega_n, \mathbf{q})$ which defines the center-of-mass momentum $2\mathbf{q}$. Here, $\Omega_n = 2\pi n/\beta$ is a bosonic Matsubara frequency.

2.3.1 Hubbard-Stratonovich transformation

The above action is difficult to handle in its current form because of the 4-field interaction. One method of handling this is by introducing a new bosonic field through a Hubbard-Stratonovich (HS) decoupling [40]. For notational simplicity we will write the interaction as

$$\frac{1}{2(\beta V)^3} \sum_{\substack{\alpha_1, \alpha_2, \\ \alpha_3, \alpha_4}} V_{\alpha_1 \alpha_2 \alpha_3 \alpha_4} \psi_{\alpha_1}^\dagger \psi_{\alpha_2}^\dagger \psi_{\alpha_3} \psi_{\alpha_4}, \tag{2.20}$$

where $\alpha_i = (\mathbf{k}_i, \sigma_i)$, meaning that we have now implicitly added $\delta(\mathbf{k}_1 + \mathbf{k}_2 - \mathbf{k}_3 - \mathbf{k}_4)$ to the potential to ensure that frequency and momentum is conserved. In principle α_i can be any set of quantum numbers, and the result of the HS transformation is therefore quite

general. The starting point of the HS transformation is the identity [40, 42]

$$1 = \int \mathcal{D}\varphi^\dagger \mathcal{D}\varphi \exp \left\{ \beta V \sum_{\substack{\alpha, \alpha' \\ \beta, \beta'}} \varphi_{\alpha\alpha'}^\dagger V_{\alpha\alpha'\beta\beta'}^{-1} \varphi_{\beta\beta'} \right\}, \quad (2.21)$$

where $V_{\alpha_1\alpha_2\alpha_3\alpha_4}^{-1}$ denotes the matrix elements of the inverse of V , and $\varphi_{\alpha\alpha'}$ are bosonic fields. Writing the interaction as [39, 40]

$$V_{\alpha_1\alpha_2\alpha_3\alpha_4} = \langle \alpha_1\alpha_2 | \hat{V} | \alpha_3\alpha_4 \rangle, \quad (2.22a)$$

$$V_{\alpha_1\alpha_2\alpha_3\alpha_4}^{-1} = \langle \alpha_1\alpha_2 | \hat{V}^{-1} | \alpha_3\alpha_4 \rangle, \quad (2.22b)$$

we find

$$\begin{aligned} \sum_{\beta\beta'} V_{\alpha_1\alpha_2\beta\beta'}^{-1} V_{\beta'\beta\alpha_3\alpha_4} &= \sum_{\beta\beta'} \langle \alpha_1\alpha_2 | \hat{V}^{-1} | \beta\beta' \rangle \langle \beta'\beta | \hat{V} | \alpha_3\alpha_4 \rangle \\ &= \delta_{\alpha_1\alpha_4} \delta_{\alpha_2\alpha_3} - \delta_{\alpha_1\alpha_3} \delta_{\alpha_2\alpha_4}, \end{aligned} \quad (2.23)$$

where we have used the completeness relation $\sum_{\beta} |\beta\rangle \langle \beta| = 1$ [24, 40, 43] and $\hat{V}^{-1} \hat{V} = 1$. The two delta-function terms reflect the fact that the interaction $V_{\alpha_1\alpha_2\alpha_3\alpha_4}$ is odd under interchange of α_1 and α_2 , or α_3 and α_4 due to the anticommutation of the fermionic fields ψ . The consequences of this will be discussed more below.

We next rescale the bosonic fields,

$$\varphi_{\alpha\alpha'}^\dagger \rightarrow \varphi_{\alpha\alpha'}^\dagger + \frac{1}{2(\beta V)^2} \sum_{\gamma\gamma'} \psi_\gamma^\dagger \psi_{\gamma'}^\dagger V_{\gamma\gamma'\alpha'\alpha}, \quad (2.24a)$$

$$\varphi_{\beta\beta'} \rightarrow \varphi_{\beta\beta'} + \frac{1}{2(\beta V)^2} \sum_{\gamma\gamma'} V_{\beta'\beta\gamma\gamma'} \psi_\gamma \psi_{\gamma'}, \quad (2.24b)$$

which when inserted into Eq. (2.21) results in the relation [42]

$$\begin{aligned} e^{-\frac{1}{2(\beta V)^3} \sum_{\alpha_1\alpha_2\alpha_3\alpha_4} V_{\alpha_1\alpha_2\alpha_3\alpha_4} \psi_{\alpha_1}^\dagger \psi_{\alpha_2}^\dagger \psi_{\alpha_3} \psi_{\alpha_4}} \\ = \int \mathcal{D}\varphi^\dagger \mathcal{D}\varphi e^{\beta V \sum_{\alpha\alpha'\beta\beta'} \varphi_{\alpha\alpha'}^\dagger V_{\alpha\alpha'\beta\beta'}^{-1} \varphi_{\beta\beta'}} \\ \times e^{-\frac{1}{\beta V} \sum_{\alpha\beta} [\varphi_{\alpha\beta}^\dagger \psi_\alpha \psi_\beta + \psi_\alpha^\dagger \psi_\beta^\dagger \varphi_{\alpha\beta}]}. \end{aligned} \quad (2.25)$$

Hence, we are able to exchange the interaction with four fermionic fields at the cost of introducing bosonic fields. These fields describe the Cooper pairs. Applying this to the theory in Eq. (2.19), we get the partition function

$$\mathcal{Z} = \int \mathcal{D}\varphi^\dagger \mathcal{D}\varphi e^{-S_{\varphi,0}[\varphi^\dagger, \varphi]} \int \mathcal{D}\psi^\dagger \mathcal{D}\psi e^{-S_0[\psi^\dagger, \psi] - S_{\text{HS}}[\psi^\dagger, \psi, \varphi^\dagger, \varphi]}, \quad (2.26)$$

with S_0 defined in Eq. (2.19), and

$$S_{\varphi,0} = -\beta V \sum_{\mathbf{k}, \mathbf{k}', \mathbf{q}} \sum_{\substack{\sigma_1, \sigma_2 \\ \sigma_3, \sigma_4}} \varphi_{\mathbf{q}, \sigma_1 \sigma_2}^\dagger(\mathbf{k}) [V^{-1}]_{\mathbf{k} \mathbf{k}'}^{\sigma_1 \sigma_2 \sigma_3 \sigma_4}(\mathbf{q}) \varphi_{\mathbf{q}, \sigma_3 \sigma_4}(\mathbf{k}'), \quad (2.27)$$

$$S_{\text{HS}} = \frac{1}{\beta V} \sum_{\mathbf{q}, \mathbf{k}} \sum_{\sigma \sigma'} [\varphi_{\mathbf{q}, \sigma \sigma'}^\dagger(\mathbf{k}) \psi_{-\mathbf{k}+\mathbf{q}, \sigma} \psi_{\mathbf{k}+\mathbf{q}, \sigma'} + \psi_{\mathbf{k}+\mathbf{q}, \sigma}^\dagger \psi_{-\mathbf{k}+\mathbf{q}, \sigma'}^\dagger \varphi_{\mathbf{q}, \sigma \sigma'}(\mathbf{k})]. \quad (2.28)$$

2.3.2 Symmetries of the Cooper pair field

Since the fields ψ anticommute, the bosonic fields φ have to satisfy certain symmetry properties. From action S_{HS} we get

$$\begin{aligned} & \sum_{\mathbf{k}} \sum_{\sigma \sigma'} [\varphi_{\mathbf{q}, \sigma \sigma'}^\dagger(\mathbf{k}) \psi_{-\mathbf{k}+\mathbf{q}, \sigma} \psi_{\mathbf{k}+\mathbf{q}, \sigma'} + \text{h.c.}] \\ &= \sum_{\mathbf{k}} \sum_{\sigma \sigma'} [-\varphi_{\mathbf{q}, \sigma' \sigma}^\dagger(-\mathbf{k}) \psi_{-\mathbf{k}+\mathbf{q}, \sigma} \psi_{\mathbf{k}+\mathbf{q}, \sigma'} + \text{h.c.}], \end{aligned} \quad (2.29)$$

where h.c. denotes the Hermitian conjugate. Here we have anticommutated the fermionic fields, used the sum to let $\mathbf{k} \rightarrow -\mathbf{k}$, and renamed the spin indexes $\sigma \leftrightarrow \sigma'$. Hence, we must have

$$\varphi_{\mathbf{q}, \sigma \sigma'}^\dagger(\mathbf{k}) = -\varphi_{\mathbf{q}, \sigma' \sigma}^\dagger(-\mathbf{k}), \quad (2.30)$$

and the same for the field $\varphi_{\mathbf{q}, \sigma \sigma'}(\mathbf{k})$. The three operations made when going from the left to the right-hand side in the above equation is essentially a (pseudo-)spin permutation (\mathcal{S}), a relative spatial

Table 2.1: The allowed symmetries of $\varphi_{\mathbf{q},\sigma\sigma'}(\mathbf{k})$ under the operations \mathcal{S} , \mathcal{P} and \mathcal{T} leading to an overall negative sign under the combined operation $\mathcal{S}\mathcal{P}\mathcal{T}$, where $+(-)1$ means that the bosonic field is even (odd) under the operation.

\mathcal{S}	\mathcal{P}	\mathcal{T}	$\mathcal{S}\mathcal{P}\mathcal{T}$
-1	+1	+1	-1
+1	-1	+1	-1
+1	+1	-1	-1
-1	-1	-1	-1

coordinate permutation (\mathcal{P}), leading to $\mathbf{k} \rightarrow -\mathbf{k}$, and a relative time coordinate permutation (\mathcal{T}), $i\omega_n \rightarrow -i\omega_n$ [44–49]. Since the combined operation of these three permutations leads to a negative sign, we get the condition [44]

$$\mathcal{S}\mathcal{P}\mathcal{T} = -1 \quad (2.31)$$

for the bosonic fields φ and φ^\dagger . The different allowed combinations of symmetries under the three operations are summarized in Table 2.1 [44, 50].

2.3.3 The mean field gap equations

We next rewrite the fermionic terms S_0 and S_{HS} in a form which allows us to integrate out the fermionic fields. Before doing so, however, we will make a couple of assumptions. First, we assume only two (pseudo-)spin states labeled $\sigma = \uparrow, \downarrow$. Moreover, we restrict the analysis to Cooper pairs with one common center-of-mass momentum \mathbf{Q} , and zero center-of-mass frequency, writing

$$\varphi_{\phi,\sigma\sigma'}(\mathbf{k}) = \frac{1}{2} \delta_{\Omega_n,0} \delta_{\mathbf{q},\mathbf{Q}} \Delta_{\mathbf{Q},\sigma\sigma'}(\mathbf{k}). \quad (2.32)$$

Since the center-of-mass momentum \mathbf{Q} can be finite, this includes the possibility of Fulde-Ferrel-Larkin-Ovchinnikov (FFLO) [51, 52] states.

We now define the Nambu spinor

$$\Psi_Q(\mathbf{k}) = \left(\psi_{\mathbf{k},\uparrow} \quad \psi_{\mathbf{k},\downarrow} \quad \psi_{-\mathbf{k}+2\mathbf{Q},\uparrow}^\dagger \quad \psi_{-\mathbf{k}+2\mathbf{Q},\downarrow}^\dagger \right)^T, \quad (2.33)$$

and the matrices⁶

$$\Delta_Q(\mathbf{k}) = \begin{pmatrix} \Delta_{Q,\uparrow\uparrow}(\mathbf{k}) & \Delta_{Q,\uparrow\downarrow}(\mathbf{k}) \\ \Delta_{Q,\downarrow\uparrow}(\mathbf{k}) & \Delta_{Q,\downarrow\downarrow}(\mathbf{k}) \end{pmatrix}, \quad (2.34a)$$

$$\bar{\Delta}_Q(\mathbf{k}) = \begin{pmatrix} \Delta_{Q,\uparrow\uparrow}^\dagger(\mathbf{k}) & \Delta_{Q,\uparrow\downarrow}^\dagger(\mathbf{k}) \\ \Delta_{Q,\downarrow\uparrow}^\dagger(\mathbf{k}) & \Delta_{Q,\downarrow\downarrow}^\dagger(\mathbf{k}) \end{pmatrix}, \quad (2.34b)$$

where $Q = (0, \mathbf{Q})$. This allows us to write the action $S_\Psi = S_0 + S_{\text{HS}}$ as

$$S_\Psi = -\frac{1}{2\beta V} \sum_{\mathbf{k}} \Psi_Q^\dagger(\mathbf{k} + \mathbf{Q}) \mathcal{G}_Q^{-1}(\mathbf{k}) \Psi_Q(\mathbf{k} + \mathbf{Q}), \quad (2.35)$$

where we have defined the inverse Green's function

$$\mathcal{G}_Q^{-1}(\mathbf{k}) = \begin{pmatrix} G_0^{-1}(\mathbf{k} + \mathbf{Q}) & -\Delta_Q(\mathbf{k}) \\ -\bar{\Delta}_Q(\mathbf{k}) & -[G_0^{-1}(-\mathbf{k} + \mathbf{Q})]^T \end{pmatrix}, \quad (2.36)$$

and the inverse non-interacting single-particle Green's function

$$G_0^{-1}(\mathbf{k}) = \begin{pmatrix} i\omega_n - h_{\mathbf{k},\uparrow\uparrow} & -h_{\mathbf{k},\uparrow\downarrow} \\ -h_{\mathbf{k},\downarrow\uparrow} & i\omega_n - h_{\mathbf{k},\downarrow\downarrow} \end{pmatrix}. \quad (2.37)$$

Integrating out the fermionic fields, we get the effective action for the Cooper pair fields [53, 54]

$$S_\varphi = S_{\varphi,0} - \frac{1}{2} \text{Tr} \ln(-\mathcal{G}_Q^{-1}), \quad (2.38)$$

where Tr denotes a trace over all degrees of freedom, including the matrix trace tr . The self-consistency equation — the gap equation —

⁶We use the notation $\bar{\Delta}_Q(\mathbf{k})$ instead of $\Delta_Q^\dagger(\mathbf{k})$, since $[\Delta_Q(\mathbf{k})]^\dagger \neq \bar{\Delta}_Q(\mathbf{k})$.

for the bosonic fields $\Delta_{Q,\sigma\sigma'}$ is found by doing a stationary phase approximation, i.e. by requiring [40]

$$\frac{\partial S_\varphi}{\partial \Delta_{Q,\sigma\sigma'}(\mathbf{p})} = 0, \quad (2.39)$$

resulting in

$$\begin{aligned} & \sum_{\mathbf{k}} \sum_{\sigma_1, \sigma_2} \Delta_{Q,\sigma_1\sigma_2}^\dagger(\mathbf{k}) [V^{-1}]_{\mathbf{k},\mathbf{p}}^{\sigma_1, \sigma_2, \sigma, \sigma'}(Q) \\ &= -\frac{2}{\beta V} \text{tr} \left[\mathcal{G}_Q(\mathbf{p}) \frac{\partial \mathcal{G}_Q^{-1}(\mathbf{p})}{\partial \Delta_{Q,\sigma\sigma'}(\mathbf{p})} \right], \end{aligned} \quad (2.40)$$

where $\mathcal{G}_Q(\mathbf{p})$ is the inverse of $\mathcal{G}_Q^{-1}(\mathbf{p})$. Multiplying both sides with $V_{\mathbf{p}\mathbf{p}'}^{\sigma'\sigma\sigma_3\sigma_4}$ and summing over \mathbf{p} , σ and σ' , we get

$$\Delta_{Q,\sigma_4\sigma_3}^\dagger(\mathbf{p}') = -\frac{1}{\beta V} \sum_{\substack{\mathbf{p}' \\ \sigma_1, \sigma_2}} V_{\mathbf{p}\mathbf{p}'}^{\sigma_1\sigma_2\sigma_3\sigma_4} \text{tr} \left[\mathcal{G}_Q(\mathbf{p}) \frac{\partial \mathcal{G}_Q^{-1}(\mathbf{p})}{\partial \Delta_{Q,\sigma_2\sigma_1}(\mathbf{p})} \right], \quad (2.41a)$$

where we have used $\Delta_{Q,\sigma_3\sigma_4}^\dagger(-\mathbf{p}) = -\Delta_{Q,\sigma_4\sigma_3}^\dagger(\mathbf{p})$, see Eq. (2.30). Using instead the requirement $\delta S_\varphi / \delta \Delta_{Q,\sigma\sigma'}^\dagger = 0$, we get

$$\Delta_{Q,\sigma_2\sigma_1}(\mathbf{p}') = -\frac{1}{\beta V} \sum_{\substack{\mathbf{p}' \\ \sigma_3, \sigma_4}} V_{\mathbf{p}'\mathbf{p}}^{\sigma_1\sigma_2\sigma_3\sigma_4} \text{tr} \left[\mathcal{G}_Q(\mathbf{p}) \frac{\partial \mathcal{G}_Q^{-1}(\mathbf{p})}{\partial \Delta_{Q,\sigma_4\sigma_3}^\dagger(\mathbf{p})} \right]. \quad (2.41b)$$

These are the self-consistency equations, or gap equations. If solutions exist this indicates that the Cooper pair wavefunction is finite, and the system is superconducting below the critical temperature. We now apply this theoretical framework to the theory of phonon-mediated superconductivity.

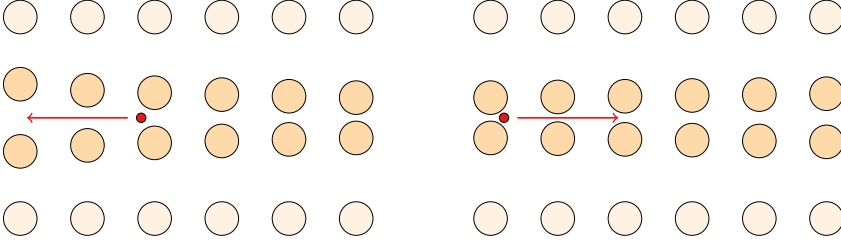


Figure 2.4: (left) An electron moving through a lattice of ions, causing an increase in positive charge density in its wake. Since the ions are much heavier than the electrons, there can be a significant distortion in the lattice quite some time after the electron has passed through. Hence, at a later time, another electron can be attracted to the area with increased charge density (right). The effect is strongest for electrons moving in opposite directions. Drawn based on similar figures in Refs. [19, 55].

2.4 PHONON-MEDIATED SUPERCONDUCTIVITY

In the BCS theory a phonon-mediated effective electron-electron interaction is responsible for overcoming the repulsive Coulomb interaction, and causing the superconducting instability [6, 19, 35]. The physical picture is of an electron attracting the ion cores, thus causing the ion cores to form an area with higher positive charge density. At a later time, another electron is attracted to this area of increased charge density [6], see Fig. 2.4 for an illustration. In reality the interaction is a complicated function of wavenumber and frequency, but one often uses a simplified effective theory [6, 19, 24, 31, 40, 43]

$$\begin{aligned}
 S = & \frac{1}{\beta V} \sum_{\mathbf{k}, \sigma} (-i\omega_n + \epsilon_{\mathbf{k}} - \mu) \psi_{\mathbf{k}, \sigma}^\dagger \psi_{\mathbf{k}, \sigma} \\
 & + \frac{1}{2(\beta V)^3} \sum_{\mathbf{k}, \mathbf{k}', \mathbf{q}} \sum_{\sigma, \sigma'} v_{\mathbf{k}\mathbf{k}'}^{\text{eff}}(\mathbf{q}) \psi_{\mathbf{k}+\mathbf{q}, \sigma}^\dagger \psi_{\mathbf{k}'-\mathbf{q}, \sigma'}^\dagger \psi_{\mathbf{k}', \sigma'} \psi_{\mathbf{k}, \sigma},
 \end{aligned} \tag{2.42}$$

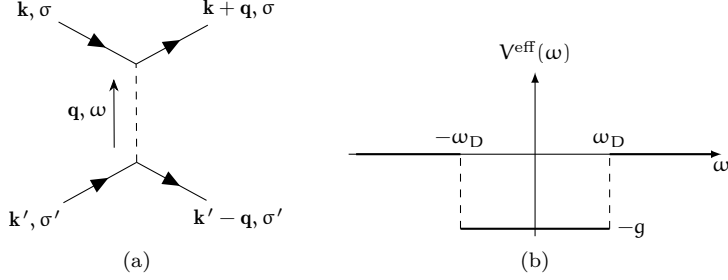


Figure 2.5: (a) Illustration of phonon-mediated electron-electron coupling: Electrons with momentum and spin \mathbf{k}, σ and \mathbf{k}', σ' respectively interact via a phonon transferring momentum \mathbf{q} and energy ω , resulting in two electrons with momentum and spin $\mathbf{k} + \mathbf{q}, \sigma$ and $\mathbf{k}' - \mathbf{q}, \sigma'$. (b) The effective potential is approximated by a constant $-V$ for energy transfers $|\omega| < \omega_D$.

where $\epsilon_{\mathbf{k}} = \mathbf{k}^2/2m$, where m is the electron mass, and μ is the chemical potential. The interaction term is illustrated by the Feynman diagram in Fig. 2.5a), with a potential assumed to take the form [6]

$$V_{\mathbf{k}\mathbf{k}'}^{\text{eff}}(\mathbf{q}) = \begin{cases} -g \text{ for } |\omega| < \omega_D \text{ with } \omega = \xi_{\mathbf{k}}, \xi_{\mathbf{k}+\mathbf{q}}, \xi_{\mathbf{k}'}, \xi_{\mathbf{k}'-\mathbf{q}}, \\ 0 \text{ otherwise,} \end{cases} \quad (2.43)$$

see Fig. 2.5b). Here $\xi_{\mathbf{k}} = \epsilon_{\mathbf{k}} - \mu$, and ω_D is the Debye cut-off frequency, which is assumed to be much smaller than the Fermi energy ϵ_F of the system. Hence, all the interacting electrons should have energies close to ϵ_F , which is easiest to ensure if $\mathbf{k}' = -\mathbf{k}$ with \mathbf{k} close to the Fermi surface, since then $\mathbf{k}' - \mathbf{q}$ and $\mathbf{k} + \mathbf{q}$ both lie on the Fermi surface with an appropriate choice of \mathbf{q} [19]. Moreover, it is expected that choosing opposite spins $\sigma' = -\sigma$ will lead to a stronger

interaction since this allows for a smaller separation between the electrons [6, 19]. Hence, we arrive at the simplified interaction term

$$S_{\text{int}} = -\frac{g}{(\beta V)^3} \sum'_{\mathbf{k}, \mathbf{k}'} \psi_{\mathbf{k}\uparrow}^\dagger \psi_{-\mathbf{k}\downarrow}^\dagger \psi_{-\mathbf{k}'\downarrow} \psi_{\mathbf{k}'\uparrow}, \quad (2.44)$$

where the primed sum indicates that we keep only momenta such that $|\xi_{\mathbf{k}}|, |\xi_{\mathbf{k}'}| < \omega_{\text{D}}$ is satisfied.

Comparing the action in Eqs. (2.42) and (2.44) to the general theory in Eq. (2.19), we see that the matrices in Eqs. (2.34) and (2.37) simplify to

$$\Delta(\mathbf{k}) = \begin{pmatrix} 0 & \Delta_{\uparrow\downarrow}(\mathbf{k}) \\ \Delta_{\downarrow\uparrow}(\mathbf{k}) & 0 \end{pmatrix}, \quad (2.45a)$$

$$\bar{\Delta}(\mathbf{k}) = \begin{pmatrix} 0 & \Delta_{\uparrow\downarrow}^\dagger(\mathbf{k}) \\ \Delta_{\downarrow\uparrow}^\dagger(\mathbf{k}) & 0 \end{pmatrix}, \quad (2.45b)$$

$$G_0^{-1}(\mathbf{k}) = \begin{pmatrix} i\omega_{\mathbf{n}} + \mu - \epsilon_{\mathbf{k}} & 0 \\ 0 & i\omega_{\mathbf{n}} + \mu - \epsilon_{\mathbf{k}} \end{pmatrix}, \quad (2.45c)$$

where we drop the subscript Q since $\mathbf{Q} = 0$. Inserting this into the full inverse Green's function Eq. (2.36) and calculating the inverse we get

$$\mathcal{G}(\mathbf{k}) = - \begin{pmatrix} \frac{i\omega_{\mathbf{n}} + \xi_{\mathbf{k}}}{\omega_{\mathbf{n}}^2 + E_{\mathbf{k},\uparrow\downarrow}^2} & 0 & 0 & \frac{\Delta_{\uparrow\downarrow}(\mathbf{k})}{\omega_{\mathbf{n}}^2 + E_{\mathbf{k},\uparrow\downarrow}^2} \\ 0 & \frac{i\omega_{\mathbf{n}} + \xi_{\mathbf{k}}}{\omega_{\mathbf{n}}^2 + E_{\mathbf{k},\uparrow\downarrow}^2} & \frac{\Delta_{\downarrow\uparrow}(\mathbf{k})}{\omega_{\mathbf{n}}^2 + E_{\mathbf{k},\uparrow\downarrow}^2} & 0 \\ 0 & \frac{\Delta_{\uparrow\downarrow}^\dagger(\mathbf{k})}{\omega_{\mathbf{n}}^2 + E_{\mathbf{k},\uparrow\downarrow}^2} & \frac{i\omega_{\mathbf{n}} - \xi_{\mathbf{k}}}{\omega_{\mathbf{n}}^2 + E_{\mathbf{k},\uparrow\downarrow}^2} & 0 \\ \frac{\Delta_{\downarrow\uparrow}^\dagger(\mathbf{k})}{\omega_{\mathbf{n}}^2 + E_{\mathbf{k},\uparrow\downarrow}^2} & 0 & 0 & \frac{i\omega_{\mathbf{n}} - \xi_{\mathbf{k}}}{\omega_{\mathbf{n}}^2 + E_{\mathbf{k},\uparrow\downarrow}^2} \end{pmatrix}, \quad (2.46)$$

where we have defined

$$E_{\mathbf{k},\uparrow\downarrow} = \sqrt{\xi_{\mathbf{k}}^2 + \Delta_{\uparrow\downarrow}(\mathbf{k})\Delta_{\downarrow\uparrow}^\dagger(\mathbf{k})}, \quad (2.47a)$$

$$E_{\mathbf{k},\downarrow\uparrow} = \sqrt{\xi_{\mathbf{k}}^2 + \Delta_{\downarrow\uparrow}(\mathbf{k})\Delta_{\uparrow\downarrow}^\dagger(\mathbf{k})}, \quad (2.47b)$$

and used $\epsilon_{\mathbf{k}} = \epsilon_{-\mathbf{k}}$. We also have $\frac{\delta g^{-1}(\mathbf{k})}{\delta \Delta_{\uparrow\downarrow}(\mathbf{k})} = -E_{14}$ and $\frac{\delta g^{-1}(\mathbf{k})}{\delta \Delta_{\downarrow\uparrow}(\mathbf{k})} = -E_{23}$, where E_{ij} is a 4×4 matrix with value 1 at index (i, j) and zero otherwise. Hence, from Eq. (2.41a) we get the two gap equations

$$\Delta_{\uparrow\downarrow}^{\dagger}(\mathbf{k}') = \frac{g}{2\beta V} \sum_{\mathbf{k}}' \left[\frac{\Delta_{\downarrow\uparrow}^{\dagger}(\mathbf{k})}{(i\omega_n)^2 - E_{\mathbf{k},\downarrow\uparrow}^2} - \frac{\Delta_{\uparrow\downarrow}^{\dagger}(\mathbf{k})}{(i\omega_n)^2 - E_{\mathbf{k},\uparrow\downarrow}^2} \right], \quad (2.48a)$$

$$\Delta_{\downarrow\uparrow}^{\dagger}(\mathbf{k}') = \frac{g}{2\beta V} \sum_{\mathbf{k}}' \left[\frac{\Delta_{\uparrow\downarrow}^{\dagger}(\mathbf{k})}{(i\omega_n)^2 - E_{\mathbf{k},\uparrow\downarrow}^2} - \frac{\Delta_{\downarrow\uparrow}^{\dagger}(\mathbf{k})}{(i\omega_n)^2 - E_{\mathbf{k},\downarrow\uparrow}^2} \right]. \quad (2.48b)$$

From the above equations we notice two important features. First, there is no explicit dependence on ω_n' on the right-hand side, which means it is natural to assume that $\Delta_{\sigma\sigma'}^{\dagger}(\mathbf{k}) \rightarrow \Delta_{\sigma\sigma'}^{\dagger}(\mathbf{k})$, making it even in frequency ($\mathcal{T} = +1$). Moreover, from the two equations we also find that $\Delta_{\uparrow\downarrow}^{\dagger}(\mathbf{k}) = -\Delta_{\downarrow\uparrow}^{\dagger}(\mathbf{k})$, i.e. we have spin singlets ($\mathcal{S} = -1$). From the symmetry rule in Eq. (2.31) we therefore must have $\mathcal{P} = +1$, i.e. an even parity state $\Delta_{\sigma\bar{\sigma}}(\mathbf{k}) = \Delta_{\sigma\bar{\sigma}}(-\mathbf{k})$, which is consistent with the above equations. In fact, the right-hand side of the above equations do not depend on \mathbf{k}' either, making $\Delta_{\sigma\bar{\sigma}}^{\dagger}(\mathbf{k})$ constant in \mathbf{k} , meaning we have an s -wave solution. Using Eq. (2.41b) we get similar results for $\Delta_{\sigma\sigma'}(\mathbf{k})$.

2.4.1 Solving the gap equation

We now simplify the notation by writing $\Delta_{\uparrow\downarrow}(\mathbf{k}) = \Delta$ and $\Delta_{\downarrow\uparrow}^{\dagger}(\mathbf{k}) = \Delta^{\dagger}$, leading to $E_{\mathbf{k},\uparrow\downarrow} = E_{\mathbf{k},\downarrow\uparrow} \rightarrow E_{\mathbf{k}} = \sqrt{\xi_{\mathbf{k}}^2 + |\Delta|^2}$.⁷ This leads to the simplified gap equation

$$\Delta = -\frac{g}{\beta V} \sum_{\omega_n} \sum_{\mathbf{k}}' \frac{\Delta}{(i\omega_n)^2 - E_{\mathbf{k}}^2}. \quad (2.49)$$

⁷This choice ensures real quasiparticle energies $E_{\mathbf{k}}$.

We perform the fermionic Matsubara sum using the trick [40, p. 171]

$$\frac{1}{\beta} \sum_{\omega_n} h(i\omega_n) = \sum_i \text{Res } h(z) n_F(z) \Big|_{z=z_i}, \quad (2.50)$$

where z_i are the singularities of $h(z)$, and $n_F(\epsilon) = (e^{\beta\epsilon} + 1)^{-1}$ is the Fermi-Dirac distribution function. In the present case we have singularities at $\pm E_{\mathbf{k}}$, leading to

$$1 = -\frac{g}{V} \sum_{\mathbf{k}}' \left[\frac{n_F(E_{\mathbf{k}})}{2E_{\mathbf{k}}} - \frac{n_F(-E_{\mathbf{k}})}{2E_{\mathbf{k}}} \right] = \frac{g}{V} \sum_{\mathbf{k}}' \frac{1}{2E_{\mathbf{k}}} \tanh \frac{\beta E_{\mathbf{k}}}{2}, \quad (2.51)$$

where we have canceled the common constant Δ from both sides of the gap equation, and the gap now enters only in $E_{\mathbf{k}}$. Since $E_{\mathbf{k}} > 0$, the sum is always positive, and it is therefore necessary to have $g > 0$ in order for the gap equation to have a solution in this case.

We solve the gap equation analytically in two limiting cases: at zero temperature, and at the critical temperature. At zero temperature $\tanh \beta E_{\mathbf{k}}/2 = 1$. Changing from a \mathbf{k} summation to an energy integral using the definition of the normal state density of states [40],

$$D(\xi) = \frac{1}{V} \sum_{\mathbf{k}} \delta(\xi_{\mathbf{k}} - \xi), \quad (2.52)$$

we get

$$1 \approx gD(0) \int_0^{\omega_D} d\xi \frac{1}{\sqrt{\xi^2 + |\Delta|^2}} \approx gD(0) \ln \frac{2\omega_D}{|\Delta|}, \quad (2.53)$$

where we have used the assumption $\omega_D \ll \mu$ to let $D(\xi) \rightarrow D(0)$, the normal density of states at the Fermi level, and assumed $|\Delta| \ll \omega_D$. Defining the dimensionless coupling constant $\lambda = gD(0)$, we find the zero temperature gap

$$\Delta_0 = 2\omega_D e^{-\frac{1}{\lambda}}. \quad (2.54)$$

This solution is valid in the weak coupling limit, $\lambda \ll 1$. As was the case for the GL solution found in Section 2.2, the gap equation only determines the magnitude of Δ , not the phase.

At temperatures just below the critical temperature, $T = T_c^-$, the gap is equal to zero. Hence, we get

$$\begin{aligned} 1 &= \lambda \int_0^{\omega_D} d\xi \frac{1}{\xi} \tanh \frac{\beta\xi}{2} \\ &= \lambda \left[\ln \xi \tanh \frac{\beta\xi}{2} \Big|_0^{\omega_D} - \int_0^{\omega_D} d\xi \frac{\beta}{2} \frac{\ln \xi}{\cosh^2 \frac{\beta\xi}{2}} \right], \end{aligned} \quad (2.55)$$

where we have performed a partial integration [19]. Assuming that $k_B T_c \sim \Delta_0 \ll \omega_D$, the first term equals $\ln \omega_D$, and in the latter we can let $\omega_D \rightarrow \infty$, resulting in⁸

$$1 = \lambda \left[\ln \omega_D + \ln \frac{4e^\gamma}{\pi} - \ln \frac{2}{\beta} \right] = \lambda \ln \frac{2e^\gamma \beta \omega_D}{\pi}, \quad (2.56)$$

where $\gamma \approx 0.5772$ is the Euler-Mascheroni constant [19, 24]. Rewriting this in terms of T_c we get

$$k_B T_c = \frac{2e^\gamma \omega_D}{\pi} e^{-\frac{1}{\lambda}} \approx 1.13 \omega_D e^{-\frac{1}{\lambda}}. \quad (2.57)$$

Combining the results for Δ_0 and T_c we find the ratio

$$\frac{2\Delta_0}{k_B T_c} = \frac{2\pi}{e^\gamma} \approx 3.52. \quad (2.58)$$

This universal ratio was found to be in good agreement with the superconductors known at the time the BCS theory was published [6, 35]. Solving Eq. (2.51) numerically, we find the temperature dependence of the gap Δ as shown in Fig. 2.6a).

⁸We here use the formula [24, p. 581]

$$\int_0^\infty dx \frac{\ln x}{\cosh^2 x} = -\ln \frac{4e^\gamma}{\pi}.$$

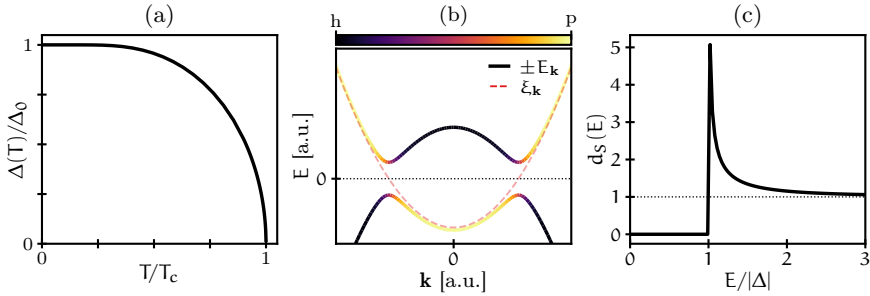


Figure 2.6: (a) Numerical results for the gap Δ as a function of temperature, normalized to the analytical values Δ_0 and T_c . (b) Plot of quasi-particle dispersion $\pm E_k$ as a function of k_x with $k_y = 0$, where the line color indicates whether the quasiparticle is particle-like (p) or hole-like (h). The normal state dispersion ξ_k is also shown for comparison. (c) Plot of the normalized superconducting quasiparticle density of states $d_s(E)$.

2.4.2 Quasiparticles

So far Δ has frequently been called the “gap”. To see the reason for this nomenclature, we take a brief look at the quasiparticles of the system. The eigenvalues of the Green’s function matrix are $[i\omega \pm E_k]^{-1}$, and hence the quasiparticles of the system have eigenenergies $\pm E_k$, shown in Fig. 2.6b). Calculating the superconducting density of states using $D_S(E)dE = D(\xi)d\xi$ [6] while assuming E lies close to the Fermi energy, we find

$$d_s(E) \equiv \frac{D_S(E)}{D(0)} = \begin{cases} \frac{|E|}{\sqrt{E^2 - |\Delta|^2}} & \text{for } |E| > |\Delta|, \\ 0 & \text{for } E < |\Delta|, \end{cases} \quad (2.59)$$

shown in Fig. 2.6c). From both the eigenenergies and the density of states, it is clear that a finite Δ leads to a gap 2Δ between the quasiparticle bands. The quasiparticles are a mix of electrons and holes, as indicated in Fig. 2.6b), with the electron and hole weights given by the residues of the diagonal entries of the Green’s function matrix Eq. (2.46).

In essence, the BCS theory tells us that due to a phonon-mediated electron-electron interaction, electrons form bound pairs, thus decreasing the system's energy. These pairs are described by a macroscopic wavefunction with a common phase, leading to a superfluid flow of electrons. Breaking up a pair into separate quasiparticles requires a finite energy Δ due to the gap in the quasiparticle dispersion, resulting in the superconducting state surviving up to temperatures comparable with the energy gap.

2.5 UNCONVENTIONAL SUPERCONDUCTIVITY

The results of the BCS theory agreed well with experiments for the superconductors known at the time it was published, earning Bardeen, Cooper and Schrieffer the 1972 Nobel Prize in Physics. Common for these superconductors was the fact that the Fermi energy was much larger than the energy set by the critical temperature, $k_B T_c$, or equivalently $T_c \ll T_F$, the Fermi temperature. For instance the critical temperature for Niobium (Nb) is 9.5 K [56], while the Fermi temperature is 6×10^4 K [57]. However, in the late 1970s, superconductivity was discovered in heavy-fermion materials [58, 59], where the critical temperature, though low compared to superconductors known at the time, is closer to the Fermi temperature. Later, in 1986 the high- T_c cuprates [60] were discovered, with rapid developments leading to materials with critical temperatures exceeding 100 K [6], far exceeding those of the conventional superconductors. These findings could not all be explained using the phonon-mediated interaction of the original BCS theory, hence leading to a theoretical search for other microscopic mechanisms which could explain the classes of superconductors known as unconventional superconductors [59]. More than three decades after the discovery of the high- T_c cuprates, the exact microscopic origin of the superconductivity and the otherwise complex phase diagram is still under debate. Since the main focus of this thesis is not the unconventional superconductors specifically, it will not be discussed in further detail. However, there will be

some similarities with spin fluctuation-based theories for cuprate superconductors (e.g. Refs. [61–63]) and the magnon-mediated superconductivity discussed in Chapter 6. Moreover, one unconventional mechanism, the Kohn-Luttinger mechanism [64], will be discussed in the next chapter.

2.6 SUPERCONDUCTIVITY IN TWO DIMENSIONS

As the title of this thesis indicates, the focus will be on superconducting states in systems which are effectively 2D, i.e. the motion of the electrons is restricted in the third dimension. However, from the outset this seems to pose a problem: The Mermin-Wagner theorem states that a continuous symmetry cannot be spontaneously broken at a finite temperature in a system with short-range interactions in one or two dimensions [19, 40, 41, 65, 66]. Recall that the superconducting state breaks the continuous global phase rotation symmetry, and should therefore be subject to the Mermin-Wagner theorem in 2D systems. Two questions arise: Is any type of order possible in two dimensions, and when, if at all, are the effectively 2D systems to be treated as two-dimensional, thus being subject to the Mermin-Wagner theorem?

First of all, Berezinskii [67, 68], and Kosterlitz and Thouless [69, 70] (BKT) showed that a new type of order is possible in two-dimensional systems, so-called topological order, in contrast to long-range order. As an example of such order, consider the XY model, namely a 2D system of spins constrained to lie in the plane, where the direction of a spin at lattice site i can be parametrized by the angle θ_i . If the coupling between the spins is ferromagnetic, any difference between the angle of two neighboring lattice sites, $|\theta_i - \theta_j| > 0$, leads to an increase in energy. At zero temperature the energy E of a single vortex (see Fig. 2.7) diverges logarithmically with the system size N , and is thus unstable [40, 41, 66] and cannot be excited by thermal fluctuations [71]. However, the entropy S due to the possible locations of one vortex is also a logarithmic function of N , and at

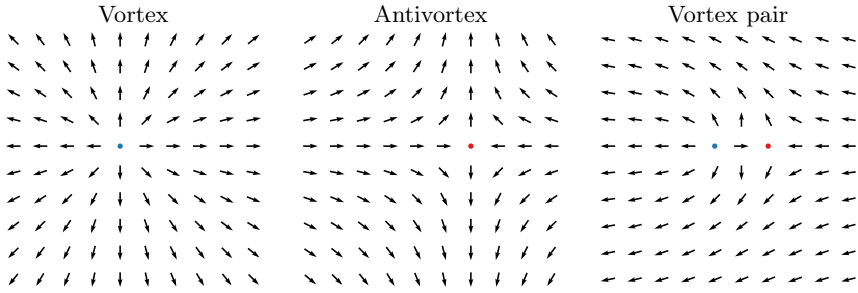


Figure 2.7: Orientation of spins in the vicinity of a vortex, antivortex, and vortex-antivortex pair (left to right). In the latter case the spins can be continuously deformed to a uniform state away from the vortex pair. Based on similar figures in Refs. [19, 41].

some temperature T_{BTK} the free energy $F = E - TS$ will be minimized by the entropy term rather than the energy term, leading to the formation of free vortices.

The energy associated with a vortex-antivortex pair, however, depends logarithmically on the vortex separation [6, 71], and is therefore finite. This difference from a single vortex can be understood from the fact that the spins can be continuously rotated to form a uniform state some distance away from the vortex pair, see Fig. 2.7. Since the energy associated with a bound vortex pair is much smaller compared to that of a single vortex, vortex-antivortex pairs can be thermally excited even at low temperatures. T_{BKT} marks the topological phase transition between a low temperature phase with only bound vortex-antivortex pairs, with quasi-long range order [66], and a high temperature phase where the pairs unbind into free vortices [6, 41].

To answer the question whether the results sketched above have any consequences for thin superconductors, we have to consider the differences between vortices in the XY model described above and vortices in a superconductor: While the spins in the XY model always have the same length, the magnetic field and current density around a vortex in a superconductor decays over a length scale

λ , the penetration depth. For superconducting vortices the energy associated with a vortex-antivortex pair therefore decays differently as a function of separation r depending on if $r \gg \lambda$ or $r \ll \lambda$ [6]. In thin superconductors of thickness d the characteristic length scale is the effective 2D screening length $\lambda_{\perp} = \lambda^2/d$ [72], and the vortex pair energy goes as $\ln r$ for $r \ll \lambda_{\perp}$ and r^{-1} for $r \gg \lambda_{\perp}$ [70, 72, 73], being attractive in the first regime but repulsive in the second. This lead Kosterlitz and Thouless [70] to argue that a BKT type transition could not occur in superconductors.

However, Beasley, Mooij and Orlando [74] later pointed out that since the effective 2D screening length increases with decreasing thickness, λ_{\perp} can be made large enough to justify using the separation energy $\sim \ln r$ more or less over the entire material, just as in the XY model above. They therefore argued that thin superconductors could also undergo a BKT type transition, relating the BKT transition temperature to the BCS mean field critical temperature in terms of the sheet resistance R ,

$$\frac{T_{\text{BKT}}}{T_{\text{BCS}}} \approx \left(1 + 0.173 \frac{R}{R_c}\right)^{-1} \quad \text{for } R \ll R_c, \quad (2.60)$$

where $R_c = \hbar/e^2 \approx 4108 \Omega/\square$ [74]. Hence, T_{BKT} decreases compared to T_{BCS} for increasing sheet resistance [75]. For superconductors with thickness such that the lateral dimension is comparable to the effective 2D screening length, we therefore have a superconducting phase with bound vortex-antivortex pairs for temperatures below T_{BKT} . For $T_{\text{BKT}} < T < T_{\text{BCS}}$ vortex pairs are broken up, leading to a finite resistance due to the lack of phase coherence across the superconductor. As the temperature, and thus the number of vortices is increased, the resistance increases until the normal state with zero superconducting gap is reached at T_{BCS} [76].

From this discussion it clear that superconductivity can arise even in effectively 2D systems, and using mean field theory to calculate the critical temperature will give an indication of whether a superconducting state exists. Depending on the effective thickness of the system, there might also exist a lower temperature corresponding to

the BKT transition. In the work contained in this thesis, however, we have not considered the BKT transition temperature, but rather only used mean field theory to calculate either the critical temperature or the zero temperature gap. Assuming that the above analysis is justified also for superconductivity in topological insulators, T_{BKT} should not be very much reduced compared to T_{BCS} as long as the TI is thick enough for the charge transport to be dominated by the surface states [77, 78].

3

KOHN-LUTTINGER SUPERCONDUCTIVITY

In 1965 Kohn and Luttinger [64] proposed a new mechanism for Cooper pairing. They showed that weak repulsive interactions could lead to an effective attractive interaction. All that is needed is that one momentum channel is attractive [79, 80]. Physically this can arise when an interaction is screened by the Fermi sea, leading to long-range oscillations [81], such as Friedel oscillations in the case of the screened Coulomb interaction [64, 79]. We will begin this chapter with an example illustrating how such a situation can arise, and then build on this example to reach the system studied in Paper [1].

3.1 SUPERCONDUCTIVITY FROM WEAK ON-SITE INTERACTION

We start from a simple model of an electron gas with a δ -function electron-electron coupling with strength U ,¹

$$\begin{aligned} H &= H_0 + H_{\text{int}} \\ &= \frac{1}{V} \sum_{\mathbf{k}\sigma} (\epsilon_{\mathbf{k}} - \mu) c_{\mathbf{k}\sigma}^\dagger c_{\mathbf{k}\sigma} + \frac{U}{V^3} \sum_{\mathbf{k}_1, \mathbf{k}_2, \mathbf{k}_3} c_{\mathbf{k}_1\uparrow}^\dagger c_{\mathbf{k}_2\downarrow}^\dagger c_{\mathbf{k}_3\downarrow} c_{\mathbf{k}_4\uparrow}, \end{aligned} \quad (3.1)$$

where $\mathbf{k}_4 = \mathbf{k}_1 + \mathbf{k}_2 - \mathbf{k}_3$ in order to conserve momentum. In the previous chapter, we saw that this can lead to superconductivity

¹Because of the way we have defined the Fourier transform, the anticommutation relations for the operators are $\{c_{\mathbf{k}\sigma}, c_{\mathbf{k}'\sigma'}^\dagger\} = V\delta_{\mathbf{k},\mathbf{k}'}\delta_{\sigma\sigma'}$ and $\{c_{\mathbf{k}\sigma}, c_{\mathbf{k}'\sigma'}\} = \{c_{\mathbf{k}\sigma}^\dagger, c_{\mathbf{k}'\sigma'}^\dagger\} = 0$.

when $U < 0$. However, we will now assume that U is positive, meaning that the interaction is repulsive.

Assuming that the interaction energy is small compared to the Fermi energy allows us to treat the interaction term perturbatively using a Schrieffer-Wolff transformation [82–84]. We define a transformed Hamiltonian

$$\begin{aligned} H' &\equiv e^{-S} H e^S \\ &= H_0 + H_{\text{int}} + [H_0 + H_{\text{int}}, S] + \frac{1}{2} [[H_0 + H_{\text{int}}, S], S] + \dots, \end{aligned} \quad (3.2)$$

where S is anti-unitary and $[A, B]$ denotes the commutator. By choosing S such that $[H_0, S] = -H_{\text{int}}$, we obtain a low-energy effective Hamiltonian for the system. One choice of S which has the wanted properties is [1, 85]

$$S = \frac{U}{V^3} \sum_{\mathbf{k}_1, \mathbf{k}_2, \mathbf{k}_3} \frac{c_{\mathbf{k}_1 \uparrow}^\dagger c_{\mathbf{k}_2 \downarrow}^\dagger c_{\mathbf{k}_3 \downarrow} c_{\mathbf{k}_4 \uparrow}}{\epsilon_{\mathbf{k}_4} + \epsilon_{\mathbf{k}_3} - \epsilon_{\mathbf{k}_2} - \epsilon_{\mathbf{k}_1}}, \quad (3.3)$$

which can be verified using the commutator relation

$$\begin{aligned} &\left[c_{\mathbf{k} \sigma'}^\dagger c_{\mathbf{k} \sigma'} c_{\mathbf{k}_1 \uparrow}^\dagger c_{\mathbf{k}_2 \downarrow}^\dagger c_{\mathbf{k}_3 \downarrow} c_{\mathbf{k}_4 \uparrow} \right] \\ &= V \left[\delta_{\mathbf{k}' \mathbf{k}_1} \delta_{\sigma' \uparrow} c_{\mathbf{k} \sigma}^\dagger c_{\mathbf{k}_2 \downarrow}^\dagger + \delta_{\mathbf{k}' \mathbf{k}_2} \delta_{\sigma' \downarrow} c_{\mathbf{k}_1 \uparrow}^\dagger c_{\mathbf{k} \sigma}^\dagger \right] c_{\mathbf{k}_3 \downarrow} c_{\mathbf{k}_4 \uparrow} \\ &\quad - V c_{\mathbf{k}_1 \uparrow}^\dagger c_{\mathbf{k}_2 \downarrow}^\dagger \left[\delta_{\mathbf{k} \mathbf{k}_3} \delta_{\sigma \downarrow} c_{\mathbf{k}' \sigma'} c_{\mathbf{k}_4 \uparrow} + \delta_{\mathbf{k} \mathbf{k}_4} \delta_{\sigma \uparrow} c_{\mathbf{k}_3 \downarrow} c_{\mathbf{k}' \sigma'} \right]. \end{aligned} \quad (3.4)$$

With this choice of S we get to $\mathcal{O}(U^2)$,

$$H' = H_0 + \frac{1}{2} [H_{\text{int}}, S] \equiv H_0 + H'_{\text{int}}. \quad (3.5)$$

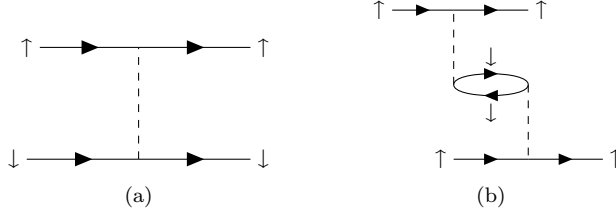


Figure 3.1: (a) Diagram for interaction term H_{int} . (b) Diagram of second order effective interaction between spin up electrons mediated by spin down electrons. Based on similar figures in Refs. [85, 86].

To calculate H'_{int} we use the identity $[AB, C] = A[B, C] + [A, C]B$ and the relation in Eq. (3.4), resulting in

$$\begin{aligned}
 H'_{\text{int}} = & \frac{U^2}{2V^5} \sum_{\mathbf{k}_1, \mathbf{k}_2, \mathbf{k}_3} \sum_{\mathbf{p}_1, \mathbf{p}_2, \mathbf{p}_3} \frac{1}{\epsilon_{\mathbf{p}_4} + \epsilon_{\mathbf{p}_3} - \epsilon_{\mathbf{p}_2} - \epsilon_{\mathbf{p}_1}} \left\{ \right. \\
 & - c_{\mathbf{k}_1 \uparrow}^\dagger c_{\mathbf{p}_1 \uparrow}^\dagger c_{\mathbf{k}_4 \uparrow} c_{\mathbf{p}_4 \uparrow} \left[\delta_{\mathbf{k}_3 \mathbf{p}_2} c_{\mathbf{k}_2 \downarrow}^\dagger c_{\mathbf{p}_3 \downarrow} - \delta_{\mathbf{k}_2 \mathbf{p}_3} c_{\mathbf{p}_2 \downarrow}^\dagger c_{\mathbf{k}_3 \downarrow} \right] \\
 & - c_{\mathbf{p}_2 \downarrow}^\dagger c_{\mathbf{k}_2 \downarrow}^\dagger c_{\mathbf{p}_3 \downarrow} c_{\mathbf{k}_3 \downarrow} \left[\delta_{\mathbf{k}_4 \mathbf{p}_1} c_{\mathbf{k}_1 \uparrow}^\dagger c_{\mathbf{p}_4 \uparrow} - \delta_{\mathbf{k}_1 \mathbf{p}_4} c_{\mathbf{p}_1 \uparrow}^\dagger c_{\mathbf{k}_4 \uparrow} \right] \\
 & + V \delta_{\mathbf{k}_3 \mathbf{p}_2} \delta_{\mathbf{k}_4 \mathbf{p}_1} c_{\mathbf{k}_1 \uparrow}^\dagger c_{\mathbf{k}_2 \downarrow}^\dagger c_{\mathbf{p}_3 \downarrow} c_{\mathbf{p}_4 \uparrow} \\
 & \left. - V \delta_{\mathbf{k}_1 \mathbf{p}_4} \delta_{\mathbf{p}_3 \mathbf{k}_2} c_{\mathbf{p}_1 \uparrow}^\dagger c_{\mathbf{p}_2 \downarrow}^\dagger c_{\mathbf{k}_3 \downarrow} c_{\mathbf{k}_4 \uparrow} \right\}. \quad (3.6)
 \end{aligned}$$

Hence, there are two different classes of terms: six-operator terms such as $c_{\uparrow}^\dagger c_{\uparrow}^\dagger c_{\uparrow} c_{\downarrow} c_{\downarrow}^\dagger c_{\downarrow}$, see Fig. 3.1, and four-operator terms $c_{\uparrow}^\dagger c_{\downarrow}^\dagger c_{\downarrow} c_{\uparrow}$. In the first class of terms we use the approximation $c_{\mathbf{k}\sigma}^\dagger c_{\mathbf{k}'\sigma} \rightarrow V \delta_{\mathbf{k}\mathbf{k}'} n_{\text{F}}(\epsilon_{\mathbf{k}} - \mu)$, where $n_{\text{F}}(\epsilon)$ is the Fermi-Dirac distribution function. Since the Fermi surface is circular, we also assume that the center-of-mass momentum is zero as in the regular BCS case discussed in the previous chapter. Combining these assumptions results in the effective interaction Hamiltonian

$$\begin{aligned}
H'_{\text{int}} = & \frac{U^2}{2V^4} \sum_{\mathbf{k}, \mathbf{k}', \mathbf{p}} \left\{ \right. \\
& \sum_{\sigma} \frac{n_F(\epsilon_{\mathbf{k}' - \mathbf{k} + \mathbf{p}} - \mu) - n_F(\epsilon_{\mathbf{p}} - \mu)}{\epsilon_{\mathbf{k}'} + \epsilon_{\mathbf{k}' - \mathbf{k} + \mathbf{p}} - \epsilon_{\mathbf{p}} - \epsilon_{\mathbf{k}}} c_{\mathbf{k}\sigma}^{\dagger} c_{-\mathbf{k}\sigma}^{\dagger} c_{-\mathbf{k}'\sigma} c_{\mathbf{k}'\sigma} \\
& \left. + \frac{1}{2} \left[\frac{1}{\epsilon_{\mathbf{k}' - \epsilon_{\mathbf{p}}} - \epsilon_{\mathbf{k}}} - \frac{1}{\epsilon_{\mathbf{k}} - \epsilon_{\mathbf{p}}} \right] c_{\mathbf{k}\uparrow}^{\dagger} c_{-\mathbf{k}\downarrow}^{\dagger} c_{-\mathbf{k}'\downarrow} c_{\mathbf{k}'\uparrow} \right\}. \quad (3.7)
\end{aligned}$$

Since only particles close to the Fermi energy are free to interact at low temperatures, we can use the approximation $\epsilon_{\mathbf{k}} \approx \epsilon_{\mathbf{k}'}$. This means that the second term in the above equation can be neglected, leaving us with

$$H'_{\text{int}} = \frac{U^2}{2V^3} \sum_{\mathbf{k}, \mathbf{k}'} \sum_{\sigma} \chi(\mathbf{k}' - \mathbf{k}) c_{\mathbf{k}\sigma}^{\dagger} c_{-\mathbf{k}\sigma}^{\dagger} c_{-\mathbf{k}'\sigma} c_{\mathbf{k}'\sigma}, \quad (3.8)$$

where we have defined the particle-hole susceptibility [79, 85, 86]

$$\chi(\mathbf{q}) = \frac{1}{V} \sum_{\mathbf{p}} \frac{n_F(\epsilon_{\mathbf{p} + \mathbf{q}} - \mu) - n_F(\epsilon_{\mathbf{p}} - \mu)}{\epsilon_{\mathbf{p} + \mathbf{q}} - \epsilon_{\mathbf{p}}}. \quad (3.9)$$

In a rotationally invariant three-dimensional (3D) system we have [79]

$$\chi(\mathbf{q}) \approx -\frac{mk_F}{2\pi^2} \left[1 - \frac{1}{2} \left(\frac{|\mathbf{q}|}{2k_F} \right)^2 + \dots \right], \quad (3.10)$$

where $k_F = \sqrt{2m\mu}$ for a quadratic dispersion $\epsilon_{\mathbf{k}} = \mathbf{k}^2/2m$. Here only the two lowest order momentum channels, the s-wave and p-wave channels have been kept. Inserted into the expression for H'_{int} the terms even in \mathbf{k}' and \mathbf{k}' sum to zero, consistent with a spin-triplet interaction, resulting in

$$H'_{\text{int}} = -\frac{U^2}{2V^3} \frac{m}{8\pi^2 k_F} \sum_{\mathbf{k}, \mathbf{k}'} \sum_{\sigma} \mathbf{k}' \cdot \mathbf{k} c_{\mathbf{k}\sigma}^{\dagger} c_{-\mathbf{k}\sigma}^{\dagger} c_{-\mathbf{k}'\sigma} c_{\mathbf{k}'\sigma} \quad (3.11)$$

Using the result in Eq. (2.41) from the preceding chapter for a general interaction matrix, and performing the Matsubara summation, we get the gap equation

$$\Delta_{\sigma\sigma}(\mathbf{k}') = \frac{U^2 m}{8\pi^2 k_F V} \sum_{\mathbf{k}} \frac{\mathbf{k} \cdot \mathbf{k}' \Delta_{\sigma\sigma}(\mathbf{k})}{2E_{\sigma}(\mathbf{k})} \tanh \frac{\beta E_{\sigma}(\mathbf{k})}{2}, \quad (3.12)$$

where $E_{\sigma}(\mathbf{k}) = \sqrt{(\epsilon_{\mathbf{k}} - \mu)^2 + |\Delta_{\sigma\sigma}(\mathbf{k})|^2}$. Assuming p-wave solutions of the form $\Delta_{\sigma\sigma}(\mathbf{k}) = \Delta_{\sigma\sigma} \cos \theta_{\mathbf{k}}$ [79], where $\theta_{\mathbf{k}}$ is the angle of \mathbf{k} relative to the z axis, and that the main contribution to the sum comes from momenta close to the Fermi surface, we get the following self-consistency equation for T_c :

$$1 = \frac{g}{V} \sum_{\mathbf{k}} \frac{\cos^2 \theta_{\mathbf{k}}}{2\xi_{\mathbf{k}}} \tanh \frac{\beta \xi_{\mathbf{k}}}{2}, \quad (3.13)$$

where we have defined $g = U^2 m k_F / 8\pi^2$, the effective coupling strength. Compared to the BCS gap equation (2.51) the only differences are that the sum has not been constrained to a finite cut-off, and that there is an extra factor of $\cos^2 \theta_{\mathbf{k}}$ which leads to a factor 2/3 when performing the angular integral. Hence, a finite T_c solution exists, below which the system becomes a p-wave spin triplet superconductor, with equal spin ($\uparrow\uparrow$ and $\downarrow\downarrow$) Cooper pairs.

When considering a 2D rotationally invariant system, the susceptibility becomes [79, 85–87]

$$\chi(\mathbf{q}) = -\frac{m}{2\pi} \left[1 - \frac{\text{Re} \sqrt{\mathbf{q}^2 - (2k_F)^2}}{|\mathbf{q}|} \right]. \quad (3.14)$$

For $\mathbf{q} = \mathbf{k}' - \mathbf{k}$ with $|\mathbf{k}'| = |\mathbf{k}| = k_F$, we always have $|\mathbf{q}| \leq 2k_F$, which means that the susceptibility is a constant. Since a momentum-dependent interaction is necessary when considering spin-triplet pairing with no frequency dependence (see Table 2.1), there exists no superconducting state at $\mathcal{O}(U^2)$ [79, 88]. However, going to third order in a perturbation expansion one again finds a p-wave superconducting instability at $T = 0$ [87].

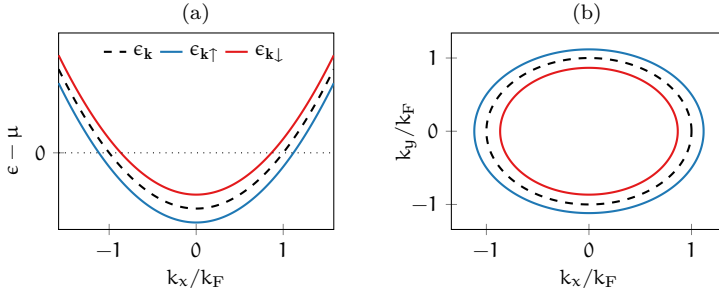


Figure 3.2: (a) Plot of spin energy bands $\epsilon_{\mathbf{k}\sigma} - \mu$ as a function of k_x with $k_y = 0$, and (b) the Fermi surfaces determined by $\epsilon_{\mathbf{k}\sigma} - \mu = 0$. We see that the Fermi momentum $k_{F\sigma}$ increases (decreases) for $\sigma = \uparrow$ (\downarrow) compared to the Fermi momentum k_F at zero field.

3.2 SPIN-POLARIZED SYSTEMS

One way of getting superconductivity to second order in a perturbation expansion in two dimensions is to spin-polarize the system [86, 88]. Adding a Zeeman coupling to an exchange field \mathbf{h} results in the additional term

$$H_B = -\frac{1}{V} \sum_{\mathbf{k}} \sum_{\sigma, \sigma'} \mathbf{h} \cdot \boldsymbol{\sigma}_{\sigma\sigma'} c_{\mathbf{k}\sigma}^\dagger c_{\mathbf{k}\sigma'}. \quad (3.15)$$

This term leads to a splitting of the bands, as seen from the eigenenergies

$$\epsilon_{\mathbf{k}\sigma} = \epsilon_{\mathbf{k}} - \sigma h, \quad (3.16)$$

where \mathbf{h} is aligned along the spin-up direction, and $\sigma = +(-)1$ for spin-up (spin-down) electrons, see Fig. 3.2. Due to the spin splitting of the bands, the Fermi momentum is also different for the two bands, $k_{F\sigma} = \sqrt{2m(\mu + \sigma h)}$ for a quadratic dispersion.

The effective interaction now has a spin-dependence,

$$H'_{\text{int}} = \frac{u^2}{2V^3} \sum_{\mathbf{k}, \mathbf{k}'} \chi_{\bar{\sigma}}(\mathbf{k}' - \mathbf{k}) c_{\mathbf{k}\sigma}^\dagger c_{-\mathbf{k}\sigma}^\dagger c_{-\mathbf{k}'\sigma} c_{\mathbf{k}'\sigma}, \quad (3.17)$$

where $\bar{\sigma} = \downarrow$ (\uparrow) for $\sigma = \uparrow$ (\downarrow), and the susceptibility depends on the spin index [85, 86],

$$\chi_{\sigma}(\mathbf{q}) = -\frac{m}{2\pi} \left[1 - \frac{\text{Re} \sqrt{\mathbf{q}^2 - (2k_{F\sigma})^2}}{|\mathbf{q}|} \right]. \quad (3.18)$$

Since $k_{F\uparrow} > k_{F\downarrow}$, $\mathbf{k}' - \mathbf{k}$ can exceed $2k_{F\downarrow}$ for pairing on the spin-up majority band, and the susceptibility thus has a momentum dependence. Therefore, we expect that we can have pairing on the spin-up majority band, but not on the spin-down minority band, as long as $0 < k_{F\downarrow} < k_{F\uparrow}$ [86].

3.3 RASHBA SPIN-ORBIT COUPLING

When an electron is moving with momentum \mathbf{p} in an electric field \mathbf{E} , we know from the relativistic formulation of electrodynamics that this translates to a magnetic field $\mathbf{B} \sim \mathbf{p} \times \mathbf{E} = -\mathbf{p} \times \nabla\phi$ in the electron's rest frame, where ϕ is the electric potential [28, 89]. Inserted into the Zeeman term Eq. (3.15), this leads to a spin-orbit coupling (SOC) term

$$H_{\text{SOC}} \sim \nabla\phi \cdot [\mathbf{p} \times \boldsymbol{\sigma}], \quad (3.19)$$

that is, the energy of a particle becomes dependent on the relative direction of the spin and momentum. This can also be shown from the non-relativistic limit of the Dirac equation [90]. Due to internal crystal fields, e.g. semiconductors have spin-orbit interactions which increase with the atomic number [91, 92], as will be relevant in the discussion of topological insulators in the next chapter.

In systems with broken structural inversion symmetry the spin of the particles is coupled to the momentum through a Rashba spin-orbit coupling term [89, 93]

$$H_{\text{R}} = \frac{\alpha_{\text{R}}}{V} \sum_{\mathbf{k}} \sum_{\sigma\sigma'} [\mathbf{k} \times \boldsymbol{\sigma}_{\sigma\sigma'}]_z c_{\mathbf{k}\sigma}^{\dagger} c_{\mathbf{k}\sigma'}, \quad (3.20)$$

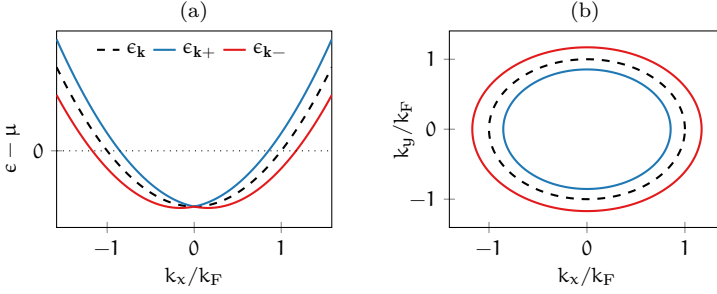


Figure 3.3: (a) Plot of helicity energy bands $\epsilon_{\mathbf{k}\alpha} - \mu$ as a function of k_x with $k_y = 0$, and (b) the Fermi surface determined by $\epsilon_{\mathbf{k}\alpha} - \mu = 0$. Similar to the case of Zeeman split bands, we see that the Fermi momentum $k_{F\alpha}$ increases (decreases) for $\alpha = - (+)$ compared to the Fermi momentum k_F for zero SOC strength α_R .

where α_R is the strength of the coupling, and we have assumed that the inversion symmetry is broken in the z direction. This situation can arise e.g. at the interface between two materials or when an electric field is present in the z direction.

Since Rashba SOC is expected to occur in many effectively 2D systems, we examine if the change in band structure due to the Rashba SOC itself is enough to lead to a superconducting instability from weakly repulsive spin-space interactions. In the next section, we will introduce spin-orbit coupling in a spin-polarized system.

With the inclusion of spin-orbit coupling (SOC), the eigenenergies of the non-interacting system become

$$\epsilon_{\mathbf{k}\pm} = \epsilon_{\mathbf{k}} - \mu \pm \alpha_R |\mathbf{k}|, \quad (3.21)$$

where the Hamiltonian is diagonalized by the operators

$$a_{\mathbf{k}+} = [ie^{i\phi_{\mathbf{k}}} c_{\mathbf{k}\uparrow} + c_{\mathbf{k}\downarrow}] / \sqrt{2}, \quad (3.22a)$$

$$a_{\mathbf{k}-} = -[c_{\mathbf{k}\uparrow} + ie^{-i\phi_{\mathbf{k}}} c_{\mathbf{k}\downarrow}] / \sqrt{2}. \quad (3.22b)$$

where \pm denotes the helicity index. The eigenenergies and Fermi surfaces, $k_{F\pm} = \sqrt{2m\mu + \alpha_R^2 m^2} \mp \alpha_R m$, are illustrated in Fig. 3.3.

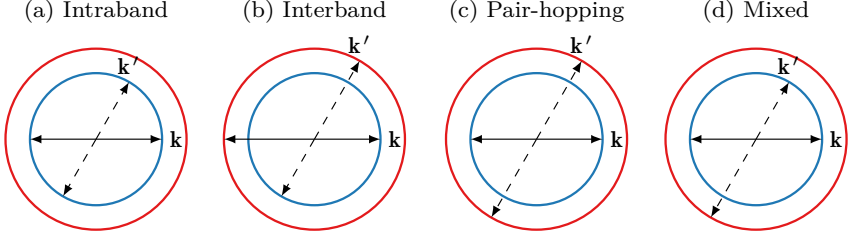


Figure 3.4: The figures illustrate the classes of interaction terms occurring when transforming the interaction term in Eq. (3.1) to the helicity basis: (a) Intraband, (b) interband, (c) pair-hopping, and (d) mixed interaction terms. The incoming momenta are $-\mathbf{k}'$ and \mathbf{k}' (dashed lines) and outgoing momenta \mathbf{k} and $-\mathbf{k}$ (solid lines).

Transforming the interaction term in Eq. (3.1) we generate 16 different interaction terms, which come in four categories: Intraband terms $c_{\alpha}^{\dagger}c_{\alpha}^{\dagger}c_{\alpha}c_{\alpha}$, interband terms $c_{\alpha}^{\dagger}c_{\bar{\alpha}}^{\dagger}c_{\bar{\alpha}}c_{\alpha}$, pair hopping terms $c_{\alpha}^{\dagger}c_{\alpha}^{\dagger}c_{\bar{\alpha}}c_{\bar{\alpha}}$, and mixed terms such as $c_{\alpha}^{\dagger}c_{\bar{\alpha}}^{\dagger}c_{\alpha}c_{\bar{\alpha}}$, where $\alpha = \pm$ and $\bar{\alpha} = \mp$. The different terms are illustrated in Fig. 3.4. In order for an electron to contribute significantly to the dynamics of the system, its energy has to lie within a few $k_{\text{B}}T$ from the Fermi energy [56]. Assuming that the spin splitting is significantly larger than $k_{\text{B}}T$, the interband and mixed processes will only conserve momentum for very specific choices of incoming and outgoing momenta. For the intraband and pair-hopping processes, however, we can simply choose incoming momenta $-\mathbf{k}'$ and \mathbf{k}' , and outgoing momenta \mathbf{k} and $-\mathbf{k}$ close to the Fermi level, thus ensuring momentum conservation. Hence, the phase space of the interband and mixed processes is much smaller compared to the intraband and pair-hopping processes, and the former processes will be suppressed compared to the latter. Keeping only the dominant terms, we get

$$H_{\text{int}}^{\text{R}} = \frac{U}{4V^3} \sum_{\mathbf{k}, \mathbf{k}'} \sum_{\alpha, \beta} \alpha\beta e^{-i\alpha\phi_{\mathbf{k}} + i\beta\phi_{\mathbf{k}'}} a_{\mathbf{k}\alpha}^{\dagger} a_{-\mathbf{k}\alpha}^{\dagger} a_{-\mathbf{k}'\beta} a_{\mathbf{k}'\beta}, \quad (3.23)$$

where α, β take the values ± 1 .

Using the above simplified interaction term and the result Eq. (2.41) from the preceding chapter, we get the two coupled gap equations

$$\Delta_{++}(\mathbf{k}') = -\frac{Ue^{-i\phi_{\mathbf{k}'}}}{4V} \sum_{\mathbf{k}} \left[\frac{\Delta_{++}(\mathbf{k})e^{i\phi_{\mathbf{k}}}}{E_+(\mathbf{k})} \tanh \frac{\beta E_+(\mathbf{k})}{2} - \frac{\Delta_{--}(\mathbf{k})e^{-i\phi_{\mathbf{k}}}}{E_-(\mathbf{k})} \tanh \frac{\beta E_-(\mathbf{k})}{2} \right], \quad (3.24a)$$

$$\Delta_{--}(\mathbf{k}') = -\frac{Ue^{i\phi_{\mathbf{k}'}}}{4V} \sum_{\mathbf{k}} \left[\frac{\Delta_{--}(\mathbf{k})e^{-i\phi_{\mathbf{k}}}}{E_-(\mathbf{k})} \tanh \frac{\beta E_-(\mathbf{k})}{2} - \frac{\Delta_{++}(\mathbf{k})e^{i\phi_{\mathbf{k}}}}{E_+(\mathbf{k})} \tanh \frac{\beta E_+(\mathbf{k})}{2} \right], \quad (3.24b)$$

where $E_{\pm} = \sqrt{(\epsilon_{\mathbf{k}\pm} - \mu)^2 + |\Delta_{\pm\pm}(\mathbf{k})|^2}$. From the above gap equation it is clear that we can write $\Delta_{++}(\mathbf{k}) = \Delta_{++}e^{-i\phi_{\mathbf{k}}}$, and $\Delta_{--}(\mathbf{k}) = \Delta_{--}e^{i\phi_{\mathbf{k}}}$. We also see that for $U > 0$ the intraband interaction is repulsive, while the coupling between different Δ_{++} and Δ_{--} is attractive. Switching to energy integrals with cut-off ω_c in the above equations and using a quadratic dispersion, we get for $T = T_c^-$

$$[1 + K_+] \Delta_{++} = K_- \Delta_{--}, \quad (3.25a)$$

$$[1 + K_-] \Delta_{--} = K_+ \Delta_{++}, \quad (3.25b)$$

with

$$K_{\pm} = \frac{Um}{4\pi} \left(1 \mp \frac{\alpha_R m}{\sqrt{\alpha_R^2 m^2 + 2m\mu}} \right) \ln \frac{2e^{\gamma} \omega_c}{\pi k_B T}, \quad (3.26)$$

where we have assumed $k_B T \ll \omega_c$, see the discussion leading to Eq. (2.56). Combining the two above equations, we get the requirement $1 + K_+ + K_- = 0$, resulting in the critical temperature

$$k_B T_c = 1.13 \omega_c e^{\frac{2\pi}{Um}}. \quad (3.27)$$

Hence, we have no solutions when $U > 0$, since the expression for the critical temperature violates the assumption $k_B T_c \ll \omega_c$ used in the

calculations. For negative U , however, we would have a chiral p-wave superconducting state on both bands, with momentum dependence $k_x \pm ik_y$, where the helical nature of the Cooper pairs is caused by the SOC.

It is possible to construct an effective low-energy theory with attractive interactions also in this case, showing that superconductivity can arise on the majority band [94, 95]. We will however not pursue this further, but instead reintroduce the spin-polarization due to an exchange field, and examine the changes to the momentum dependence of the induced superconducting gap.

3.4 SPIN-SPLITTING AND RASHBA SOC

We thus study a 2D system with weak repulsive interactions, Zeeman splitting and Rashba spin-orbit coupling. This situation is relevant e.g. for the interface between LaAlO_3 and SrTiO_3 , at which one can have a 2D superconducting state, a magnetic state, and a combination of the two [96–103]. SOC is also present in such systems due to the broken inversion symmetry, the strength of which can be tuned by an applied electric field or gate voltage [104, 105].

The effects of Zeeman splitting and spin-orbit coupling on superconductivity in two-dimensional systems has been studied in various cases before [79, 86, 94, 95, 106–109], but we here specialize to the case where the SOC is weak compared to the exchange energy, $\alpha_R/\hbar \ll 1$. This was studied in the case of a quadratic dispersion and a general direction of the magnetic field in Ref. [85], showing that the introduction of the SOC leads to a superconducting gap on the majority band with momentum dependence $\cos \delta \cos \phi_{\mathbf{k}} + i \sin \phi_{\mathbf{k}}$, where δ is the inclination angle of the magnetic field, see Fig. 3.5. However, the critical temperature did not depend on the SOC strength, and the main effect of the SOC was thus to change the momentum dependence of the gap.

In Paper [1] we performed an analysis similar to that in Ref. [85] using the Hubbard model (see e.g. Refs. [40] and [110]) instead of a

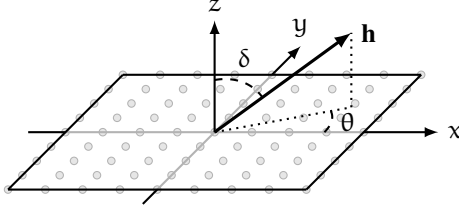


Figure 3.5: Sketch of the geometry considered: A 2D lattice lies in the xy plane, the inversion symmetry is broken along the z direction leading to a Rashba spin-orbit coupling term, and the exchange field \mathbf{h} can be oriented in any direction, determined by the angles δ and θ . Based on similar figure in Ref. [85].

model with quadratic dispersion. The total model is $H = H_t + H_B + H_R + H_{\text{int}} = H_0 + H_{\text{int}}$, where

$$H_t = \frac{1}{V} \sum_{\mathbf{k}, \sigma} (\epsilon_{\mathbf{k}} - \mu) c_{\mathbf{k}\sigma}^\dagger c_{\mathbf{k}\sigma}, \quad (3.28)$$

is the tight-binding model describing hopping between neighboring lattice sites. Here $\epsilon_{\mathbf{k}} = -2t(\cos k_x + \cos k_y)$, where t is the nearest neighbor hopping parameter. The Rashba term for a square lattice is

$$H_R = \frac{\alpha_R}{V} \sum_{\mathbf{k}} \sum_{\sigma\sigma'} (\sigma_{\sigma\sigma'}^y \sin k_x - \sigma_{\sigma\sigma'}^x \sin k_y) c_{\mathbf{k}\sigma}^\dagger c_{\mathbf{k}\sigma'}, \quad (3.29)$$

while the remaining terms are unchanged. The magnetic field vector \mathbf{h} is parametrized using $\mathbf{h} = h(\cos \theta \sin \delta, \sin \theta \sin \delta, \cos \delta)$, see the sketch of the system geometry shown in Fig. 3.5.

Diagonalizing the non-interacting Hamiltonian H_0 , we find the two bands

$$\epsilon_{\mathbf{k}\lambda} = \epsilon_{\mathbf{k}} - \zeta_\lambda [h^2 - 2h\alpha_R(\sin k_x \sin \theta - \sin k_y \cos \theta) \sin \delta + \alpha_R^2(\sin^2 k_x + \sin^2 k_y)]^{\frac{1}{2}}, \quad (3.30)$$

where the band index $\lambda = 1, 2$, and $\zeta_{1(2)} = +(-)1$. When the magnetic field has an in-plane component ($\delta \neq 0$), the Fermi surfaces of

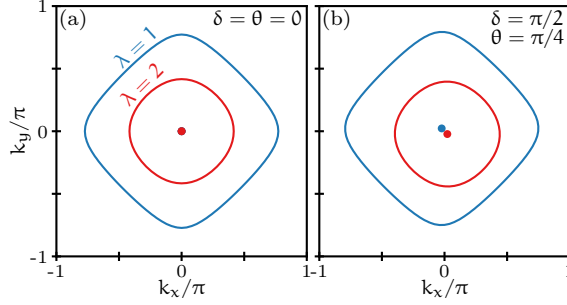


Figure 3.6: Plot of the Fermi surfaces of ϵ_λ for (a) $\delta = \theta = 0$, and (b) $\delta = \pi/2$, $\theta = \pi/4$. The parameter values used are $\hbar = t$, $\alpha_R = 0.2t$ and $\mu = -1.5t$.

the two bands are no longer symmetric about $\mathbf{k} = 0$, as illustrated in Fig. 3.6. The energy eigenstates are no longer spin states, but a mix between spin-up and spin-down electrons depending on the angle of the exchange field. We follow Ref. [85] and treat the SOC as a perturbation compared to the exchange field, $\alpha_R \ll \hbar$, which means that the bands are spin-bands only to lowest order in α_R/\hbar .

Transforming the interaction term H_{int} to the eigenbasis generates the same types of terms discussed in the previous section, see Fig. 3.4. However, since we now treat the SOC perturbatively, they are not all of the same order in α_R/\hbar . The interband terms are of $\mathcal{O}(1)$, the mixed terms are of $\mathcal{O}(\alpha_R/\hbar)$ and higher, and the intraband and pair-hopping terms of $\mathcal{O}(\alpha_R^2/\hbar^2)$.

Performing a Schrieffer-Wolff transformation to get rid of the interband terms naturally generates higher-order term in the interaction strength U . However, assuming that $U/t \ll \alpha_R/\hbar$, we keep only the terms to $\mathcal{O}(U^2/t^2)$ and $\mathcal{O}(U\alpha_R^2/\hbar^2)$. Specializing to zero center-of-mass momentum, we get the effective interaction Hamiltonian

$$H'_{\text{int}} = \frac{1}{2\sqrt{3}} \sum_{\mathbf{k}, \mathbf{k}'} \sum_{\lambda, \mu} V_{\mathbf{k}\mathbf{k}'}^{\lambda\mu} a_{\mathbf{k}\lambda}^\dagger a_{-\mathbf{k}\lambda}^\dagger a_{-\mathbf{k}'\mu} a_{\mathbf{k}\mu}, \quad (3.31)$$

where we have defined

$$V_{\mathbf{k}\mathbf{k}'}^{\lambda\mu} = U^2 \delta_{\mu\lambda} \chi_\lambda(\mathbf{k}' - \mathbf{k}) + \frac{U\alpha_R^2}{2\hbar^2} \Gamma_\lambda(\mathbf{k}) \Gamma_\mu^\dagger(\mathbf{k}'), \quad (3.32)$$

and

$$\Gamma_\lambda(\mathbf{k}) = \zeta_\lambda \left[\sin k_x \cos \theta + \sin k_y \sin \theta + i\zeta_\lambda (\sin k_x \sin \theta - \sin k_y \cos \theta) \cos \delta \right]. \quad (3.33)$$

Comparing the above interaction Hamiltonian with Eq. (3.17), we see that the first term in $V_{\mathbf{k}\mathbf{k}'}^{\lambda\mu}$ is the Kohn-Luttinger term. The second term is similar to that in Eq. (3.23), and is due to the Rashba spin-orbit coupling. The former term only has an intraband coupling, while the latter also has pair-hopping terms. Superconductivity due to the latter term should therefore lead to superconductivity on both bands simultaneously.

The susceptibility $\chi_\lambda(\mathbf{q})$ in the Kohn-Luttinger term is as defined in Eq. (3.9), with $\epsilon_{\mathbf{k}} \rightarrow \epsilon_{\mathbf{k}\lambda}$. In the continuum limit the susceptibility, given by the expression in Eq. (3.18), is independent of the chemical potential. However, when using a lattice model such as the tight-binding model, the shape of the Fermi surface depends on the chemical potential, see Fig. 3.7(a). We therefore also expect the susceptibility to depend on how many electrons are present in the system. Calculating the susceptibility numerically, and expanding it in terms of square lattice harmonics we find that for certain filling fractions it is enough to consider two terms in the expansion,

$$\chi_\lambda(\mathbf{k} - \mathbf{k}') = \chi_\lambda^1 [g_{x+iy}(\mathbf{k})g_{x-iy}(\mathbf{k}') + g_{x-iy}(\mathbf{k})g_{x+iy}(\mathbf{k}')] + \chi_\lambda^2 [g_x(\mathbf{k})g_x(\mathbf{k}') + g_y(\mathbf{k})g_y(\mathbf{k}')], \quad (3.34)$$

where we have defined the orthonormal functions

$$2\pi g_{x\pm iy}(\mathbf{k}) = \sin k_x \pm i \sin k_y, \quad (3.35a)$$

$$2\pi g_x(\mathbf{k}) = 2 \sin k_x \cos k_y, \quad (3.35b)$$

$$2\pi g_y(\mathbf{k}) = 2 \cos k_x \sin k_y. \quad (3.35c)$$

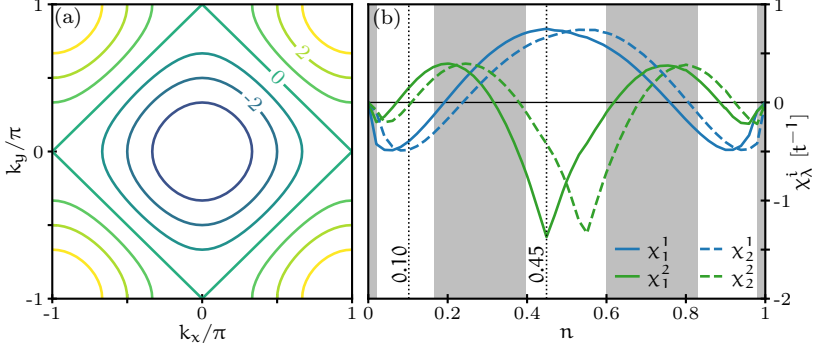


Figure 3.7: (a) Plot of the Fermi surfaces of the tight-binding dispersion for μ/t evenly spaced from -3 to 3 . (b) Plot of the expansion coefficients χ_λ^i in Eq. (3.34) as a function of filling fraction n for field strength $h = 0.2t$ at zero temperature. Keeping only the first two terms in the expansion is sufficient in the white regions, while the gray regions indicate that other terms contribute significantly to the susceptibility.

The expansion in terms of only the two terms in Eq. (3.34) is valid in the white areas of Fig. 3.7(b), which shows a plot of the coefficients of the two terms included in the expansion as a function of filling fraction n . Here $n = 0$ corresponds to an empty system, while $n = 1$ is a full system with two electrons per lattice site.

Calculating the gap equation from the interaction Eq. (3.31), we arrive at

$$\Delta_\mu(\mathbf{k}') = -\frac{1}{2V} \sum_{\mathbf{k}, \lambda} \frac{V_{\mathbf{k}'\mathbf{k}}^{\mu\lambda} \Delta_\lambda(\mathbf{k})}{E_\lambda(\mathbf{k})} \tanh \frac{\beta E_\lambda(\mathbf{k})}{2}. \quad (3.36)$$

By examining the momentum channels in $V_{\mathbf{k}\mathbf{k}'}^{\lambda\mu}$, we find that we can also expand the gap function in terms of square lattice harmonics

$$\begin{aligned} \Delta_\lambda(\mathbf{k}) = & \Delta_\lambda^{x+iy} g_{x+iy}(\mathbf{k}) + \Delta_\lambda^{x-iy} g_{x-iy}(\mathbf{k}) \\ & + \Delta_\lambda^x g_x(\mathbf{k}) + \Delta_\lambda^y g_y(\mathbf{k}), \end{aligned} \quad (3.37)$$

for filling fractions where the expansion in Eq. (3.34) is valid. Close to the critical temperature, the gap equation can therefore be written as

$$\vec{\Delta} = \mathcal{M}(T_c)\vec{\Delta}, \quad (3.38)$$

where $\vec{\Delta} = (\Delta_1^{x+iy} \quad \Delta_1^{x-iy} \quad \dots \quad \Delta_2^y)^T$, and $\mathcal{M}(T)$ is the matrix coupling the different gap coefficients at temperature T . In order for a nontrivial solution to exist, there must exist a temperature T at which $\mathcal{M}(T)$ has eigenvalue 1, corresponding to $\det[\mathcal{M}(T_c) - 1] = 0$. This determines the critical temperature. The eigenvectors of $\mathcal{M}(T_c)$ with eigenvalue 1 gives information about the relative strength between the gap coefficients Δ_λ^i , and thus the dominant momentum channels of the gap.

Solving gap equation numerically for two filling fractions $n = 0.1$ and $n = 0.45$, we find that the $\lambda = 1$ band is superconducting in the $g_{x \pm iy}$ channels in the first case, while in the latter case the $\lambda = 2$ band is superconducting in the g_x and g_y channels, see Fig. 3.8. Hence, it is possible to change which band is superconducting by changing the filling fraction of the system.

Changing the orientation of the magnetic field changes the momentum dependence of the superconducting gap, as can be seen in Fig. 3.8. For a pure out-of-plane field we have $\Delta_\lambda(\mathbf{k}) \sim k_x + \zeta_\lambda i k_y$ in the limit of small $|\mathbf{k}|$, while a pure in-plane field in the x direction gives $\Delta_\lambda(\mathbf{k}) \sim k_y$. This, together with the fact that only one band becomes superconducting at T_c indicates that only the Kohn-Luttinger term is responsible for the attractive pairing, since the Rashba-term would lead to superconductivity on both bands simultaneously with chirality opposite of what was found here. In fact, since the intraband part of the Rashba term is repulsive, the resulting momentum dependence of the gap is such that the effects of the Rashba-term is minimized, thus leading to T_c being independent of α_R . The main effect of the Rashba spin-orbit coupling is therefore the introduction of a chiral p-wave order parameter, compared to the regular p-wave gap for zero SOC. Moreover, though we did not include the shift in the dispersion in the analysis to leading order,

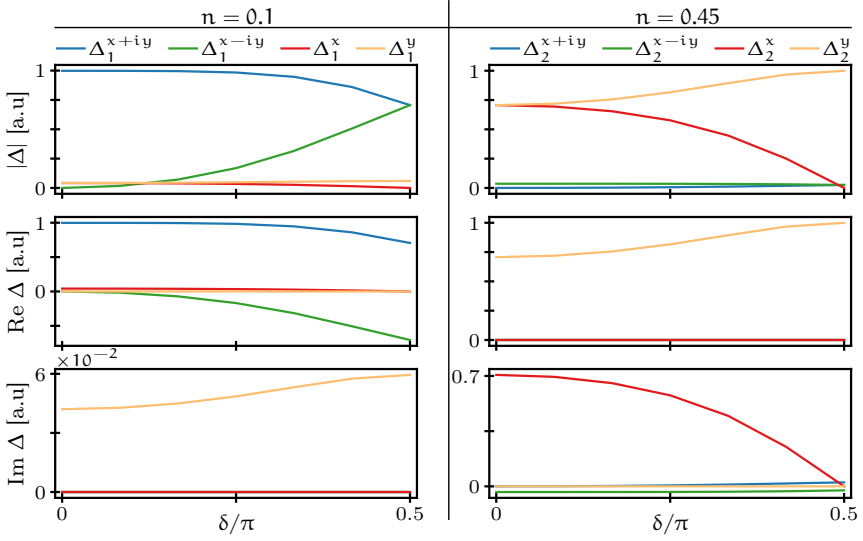


Figure 3.8: Plot of the absolute value, real and imaginary part (top to bottom) of the coefficients Δ_λ^i as a function of δ at the critical temperature for filling fractions $n = 0.1$ (left) and $n = 0.45$ (right), and $\theta = 0$. The coefficients not shown are approximately equal to zero.

the Cooper pairs have a finite center-of-mass momentum whenever the exchange field has an in-plane component [85], resulting in a Fulde-Ferrel-Larkin-Ovchinnikov [51, 52] state.

4

TOPOLOGICAL INSULATORS

This chapter serves as an introduction to the topic of topological insulators (TIs), relevant for the discussion of Papers [2–5]. We begin with a brief historical overview of the different Hall effects, leading up to the quantum spin Hall effect (QSHE) and topological insulators. Next we focus on one particular model for topological insulators, and use this model to introduce some of the features of TIs, before focusing on the TI surface states and their response to a magnetic field.

4.1 THE HALL EFFECTS

The Hall effect was discovered by Edwin Hall [111] in 1879: When running a current through a gold leaf placed in a perpendicular magnetic field, he found that there was an induced voltage difference transverse to the current direction. This can be explained from the expression for the Lorentz force on a charge q [28, 56]

$$\mathbf{F} = q(\mathbf{E} + \mathbf{v} \times \mathbf{B}), \quad (4.1)$$

where \mathbf{E} is the electric field, \mathbf{B} is the magnetic field, and \mathbf{v} is the velocity of the charged particle. Assuming a magnetic field in the z direction, and a current in the x direction, the trajectory of the electrons will initially be deflected in the negative y direction, see Fig. 4.1 for an illustration. However, in time, a negative (positive) charge density will accumulate at the lower (upper) edge, giving rise

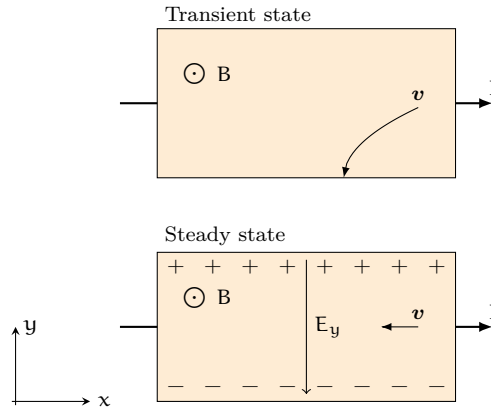


Figure 4.1: Illustration of the Hall effect with electrons as charge carriers. (top) When the current is turned on, the electrons are deflected toward the lower edge due to the perpendicular magnetic field. This leads to an induced electric field between the upper and lower edges which eventually cancels the Lorentz force due to the magnetic field (bottom). Based on similar figures in Ref. [56].

to an electric field eventually exactly counteracting the force from the magnetic field when $E_y = v_x B_z$. Thus, there is a voltage difference V_H between the upper and lower edges, where the sign of the Hall voltage is indicative of the sign of the charge carriers.

In analogy to the Hall effect, a spin Hall effect (SHE) was later theoretically predicted. In this case spin-dependent impurity scattering [112–114] or intrinsic spin-orbit coupling [115, 116] leads to a spin current transverse to an applied electric field [117, 118], and thus serves as a mechanism of converting a charge current to a spin current [89]. In the steady state we therefore have a spin imbalance instead of a charge imbalance.

In 1980 von Klitzing, Dorda and Pepper [119] reported measurements of the Hall voltage of a 2D electron gas (2DEG) in a semiconductor with a strong magnetic field at low temperature. They found that when varying the applied magnetic field, the Hall resistance did not increase linearly with the magnetic field, but had plateaus

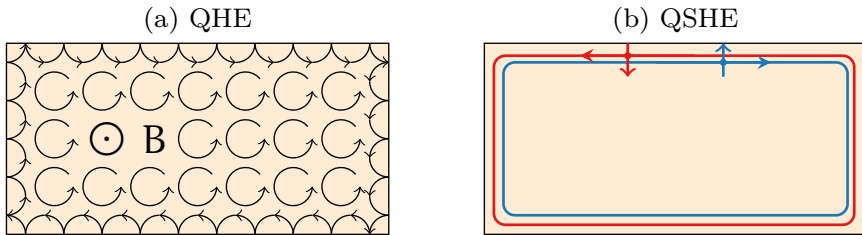


Figure 4.2: (left) Illustration of the QHE, where the electrons close to the edges cannot have complete cyclotron orbits, but instead hop along the edge, leading to metallic surface states. (right) Illustration of the QSHE, where particles with opposite spin move in opposite directions. The figures are based on similar figures in Refs. [122–125].

at quantized values $h/e^2\nu$ [41, 56, 119, 120], where h is Planck's constant, e is the electron charge, and ν is an integer. This effect has been dubbed the quantum Hall effect (QHE). The results were independent of the device geometry or material imperfections, stemming from the fact that the Hall conductance was related to a topological invariant of the system [120, 121].

One of the intriguing features of the QHE is the presence of metallic edge states, often explained in terms of broken cyclotron orbits for electrons near the edge [122, 123], see Fig. 4.2a). In 2005 Kane and Mele [126] predicted a quantum version of the spin Hall effect in graphene, the quantum spin Hall effect (QSHE) [127].¹ They predicted that the presence of spin-orbit coupling could lead to a state which was insulating in the bulk, but with gapless edge states where the momentum and spin directions are locked, see Fig. 4.2b). The states were invariant under time-reversal symmetry \mathcal{T} , and the system is classified by a nonzero topological invariant \mathbb{Z}_2 [130], as opposed to regular insulators which have $\mathbb{Z}_2 = 0$. Bernevig, Hughes and Zhang [131] later predicted that the QSHE could be observed in

¹What follows is by no means a comprehensive account of history of the quantum spin hall effect and topological insulators. For more details see e.g. Refs. [122–125, 128, 129].

mercury telluride-cadmium telluride (HgTe-CdTe) quantum wells, which due to its heavy elements has strong spin-orbit coupling [122]. This was experimentally confirmed shortly after by König *et al.* [132].

Several groups also proposed a three-dimensional version of the quantum spin hall insulator, or topological insulator [133–137], later discovered in e.g. $\text{Bi}_{1-x}\text{Sb}_x$ [138], Bi_2Se_3 [139], Bi_2Te_3 [140] and strained HgTe [141]. In order to introduce some general features of topological insulators we in the next section study the model proposed by Zhang *et al.* [137] for the three-dimensional topological insulators Bi_2Se_3 , Bi_2Te_3 and Sb_2Te_3 .

4.2 MODEL FOR TOPOLOGICAL INSULATORS

For the three-dimensional topological insulators Bi_2Se_3 , Bi_2Te_3 and Sb_2Te_3 the states lying closest to the Fermi level are the p_z orbital states of both spins, with positive and negative parity states coming from different kinds of atoms, e.g. Bi and Se respectively in Bi_2Se_3 [137]. Including only these states in an effective, low-energy model satisfying time-reversal symmetry, three-fold rotation symmetry along the z axis, and inversion symmetry, the model has the form [137],

$$H = C + D_z k_z^2 + D_{\parallel} k_{\parallel}^2 + \begin{pmatrix} \mathcal{M}(\mathbf{k}) & A_z k_z & 0 & A_{\parallel} k_{-} \\ A_z k_z & -\mathcal{M}(\mathbf{k}) & A_{\parallel} k_{-} & 0 \\ 0 & A_{\parallel} k_{+} & \mathcal{M}(\mathbf{k}) & -A_z k_z \\ A_{\parallel} k_{+} & 0 & -A_z k_z & -\mathcal{M}(\mathbf{k}) \end{pmatrix}, \quad (4.2)$$

where $k_{\parallel}^2 = k_x^2 + k_y^2$, $k_{\pm} = k_x \pm ik_y$, and $\mathcal{M}(\mathbf{k}) = M - B_z k_z^2 - B_{\parallel} k_{\parallel}^2$. A 4×4 identity matrix is implied in the first terms. The coefficients A_i , B_i , C , D_i , and M are fitting parameters determined by comparison to *ab initio* calculations [137]. The parameter M effectively tunes the strength of the spin-orbit coupling in the system. Numerically calculating the eigenvalues of this model using periodic boundary

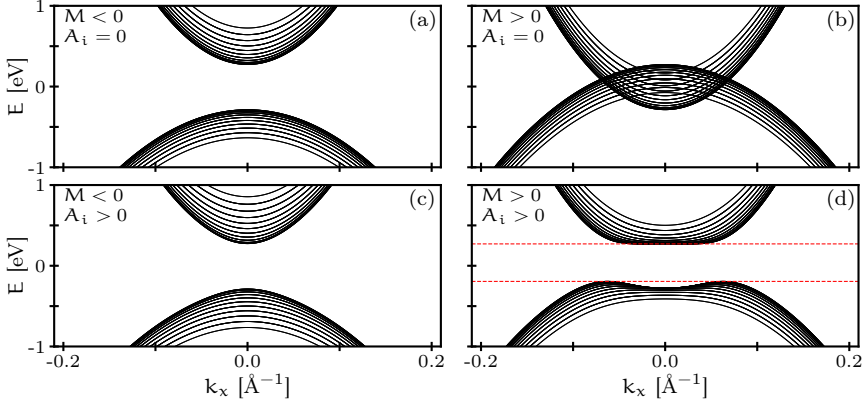


Figure 4.3: Plot of the bulk bands of the model in Eq. (4.2) for $k_y = 0$ as a function of k_x , where each line corresponds to a different value of k_z . The coefficient M is negative (positive) in the left (right) column, while the off-diagonal couplings A_i are zero (finite) in the upper (lower) plots. The red dashed lines show the edges of bulk band gap.

conditions in the $k_x - k_z$ plane, using parameter values given in Ref. [137], results in the energy bands shown in Fig. 4.3. The figure shows that changing the sign of M from negative to positive leads to a band inversion when $A_i = 0$ [Fig. 4.3b)], and the band hybridization when A_i is finite leads to an energy gap [Fig. 4.3d)].

Though there is a difference between the bulk bands in Fig. 4.3c) and d) for $M < 0$ and $M > 0$, the important difference between the two cases only becomes apparent when including an interface. Calculating the eigenvalues assuming a finite length L_z in the z direction leads to energy bands similar to Fig. 4.3c) for negative M . For positive M , however, Fig. 4.4a) shows the presence of energy states inside the bulk band gap. For small $|\mathbf{k}|$ the in-gap energy states resemble the Dirac dispersion [142] for massless electrons, with a Dirac point where the lines cross. Calculating the eigenvectors of these in-gap states with $k_y = 0$ reveals that there are two degenerate states located at either side of the material, at $z = 0$ and L_z , as seen

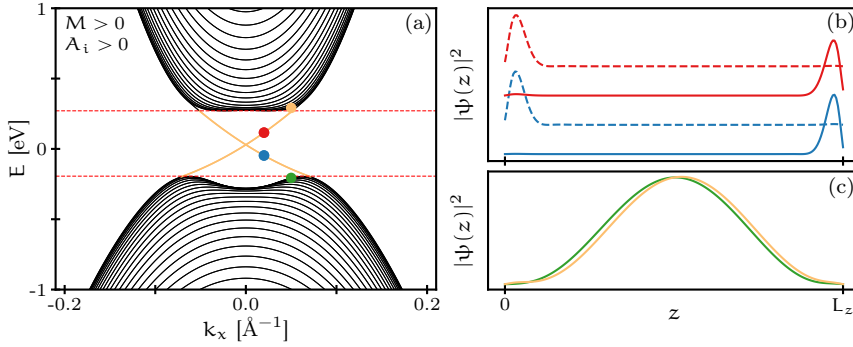


Figure 4.4: (a) Energy bands of the model in Eq. (4.2) for $k_y = 0$ as a function of k_x assuming a finite size in the z direction. There are now states inside the bulk band gap (yellow lines). Plots of the probability densities as functions of position for the indicated energy values show that the in-gap energy states are localized at either side of the material (b), which is not the case for the states outside the bulk band gap (c). The lines in panel (b) are shifted vertically to increase visibility.

by the probability density as a function of z in Fig. 4.4b). The same is not the case for states above or below the band gap, as seen in Fig. 4.4c). Hence, the metallic in-gap energy states are surface states, quite different from the insulator states in the bulk bands.

The results are similar if instead of having vacuum at $z = 0$ and $z = L_z$, the sign of M changes abruptly at $L_z/2$ while keeping $|M|$ fixed, as shown in Fig. 4.5. The surface states, now located at $L_z/2$ and L_z , are no longer degenerate due to the difference in interfaces. In both cases surface states occur where there is a change in the bulk description of the system, suggesting a connection between the existence of surface states and the bulk properties of the system.

It turns out the occurrence of edge or surface states can be predicted based on the bulk properties of a system, which can be categorized using different topological invariants. The bulk-boundary correspondence states that the number of surface states is related to the change in topological invariants [123, 129, 143–145], i.e. to

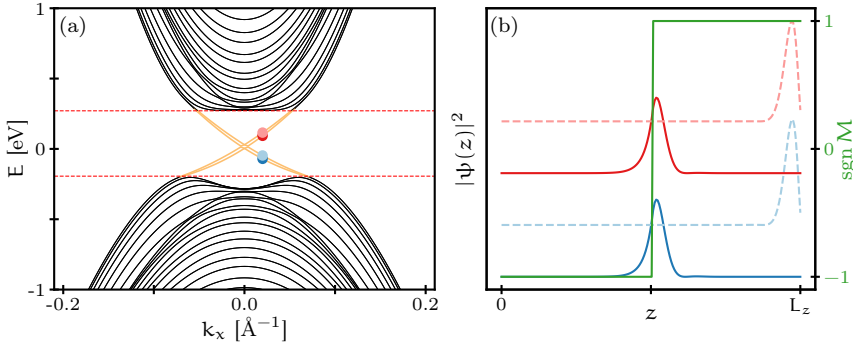


Figure 4.5: (a) Energy bands of the model in Eq. (4.2) for $k_y = 0$ as a function of k_x assuming a finite size in the z direction, and a sign change of M at $z = L_z/2$, see right axis in (b). The band structure now is a combination of the topologically trivial and nontrivial bands, with states in the middle of the bulk band gap. (b) The surface states are now located close to $L_z/2$, where M changes sign, and at L_z , the interface to vacuum.

changes in the bulk of the system. In the case of topological insulators the topological invariants are \mathbb{Z}_2 invariants [130, 133, 134, 146, 147], which are finite for TIs and zero for trivial materials and vacuum. Therefore, we have surface states at both the interface to vacuum and to topologically trivial materials, materials with $M < 0$ in the above model, see Fig. 4.5.

4.3 SURFACE STATES

We now turn our attention to the effective theory for the surface states, and study the properties of the surface states in more detail. When the chemical is inside the bulk band gap it is natural to assume that mainly the surface states contribute to the dynamics of the TI. Moreover, since surface states reside at the interface between TIs and other non-topological materials, we assume that these states are most relevant when coupling TIs to other materials, thus using only the effective surface state theories to model TIs in Papers [2–5].

In the limit $|\mathbf{k}| \rightarrow 0$ the surface states are well described by the Hamiltonian [137, 148]

$$H_{\text{surf}} = \sum_{\mathbf{k}} \Psi^\dagger(\mathbf{k}) [\hbar v_F (\sigma_x k_y - \sigma_y k_x) - \mu] \Psi(\mathbf{k}), \quad (4.3)$$

where $\Psi(\mathbf{k}) = (\psi_\uparrow(\mathbf{k}) \psi_\downarrow(\mathbf{k}))^T$, with $\psi_{\uparrow(\downarrow)}$ denoting a spin up (down) electron, and we identify $\hbar v_F = A_\parallel$. μ is the chemical potential determining the location of the Dirac point. Note that $\mathbf{k} = (k_x, k_y) = |\mathbf{k}|(\cos \phi_{\mathbf{k}}, \sin \phi_{\mathbf{k}})$, i.e. it contains only the 2D wavevectors on the surface of the TI.

The eigenenergies and eigenstates are found by solving the eigenvalue problem $Hv = \epsilon v$, resulting in the bands

$$\epsilon_\pm = \pm \hbar v_F |\mathbf{k}| - \mu, \quad (4.4)$$

and eigenvectors

$$v_+ = \frac{1}{\sqrt{2}} \begin{pmatrix} i e^{-i\phi_{\mathbf{k}}} \\ 1 \end{pmatrix}, \quad (4.5a)$$

$$v_- = \frac{1}{\sqrt{2}} \begin{pmatrix} -1 \\ -i e^{i\phi_{\mathbf{k}}} \end{pmatrix}. \quad (4.5b)$$

Calculating the spin expectation values $\langle S_\sigma \rangle_i = v_i^\dagger S_\sigma v_i$, we get

$$\langle S_x \rangle_\pm = \pm \frac{\hbar}{2} \sin \phi_{\mathbf{k}}, \quad \langle S_y \rangle_\pm = \mp \frac{\hbar}{2} \cos \phi_{\mathbf{k}}, \quad \langle S_z \rangle_\pm = 0, \quad (4.6)$$

From this we notice a few interesting features. First of all, the spin expectation value depends on the momentum. This is due to the special time-reversal symmetric form of the Hamiltonian Eq. (4.3), which leads to spin-momentum locked states, with the spin pointing normal to the momentum direction. Moreover, the spin directions are opposite for the upper (+) and lower (-) bands. This is illustrated in Fig. 4.6.

Due to the spin-momentum locking, the surface states are robust against backscattering from non-magnetic impurities [124, 129, 143].

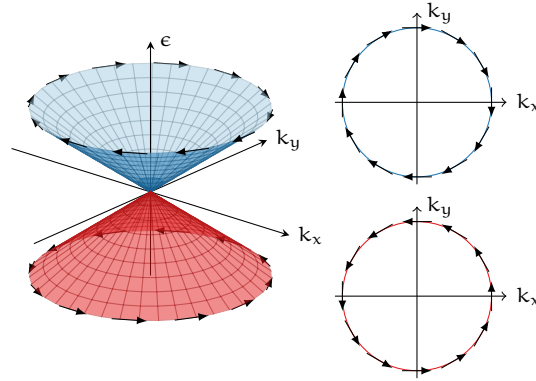


Figure 4.6: Plot of energy bands $\epsilon_{+(-)}$ in blue (red), with arrows indicating the spin structure as a function of \mathbf{k} , shown also in the $k_x - k_y$ plane to the right. The spin structure is independent of the magnitude of \mathbf{k} .

This can be explained by considering that a surface fermion can be reflected by an impurity by taking either a clockwise or counterclockwise path around the impurity. The two paths lead to spin rotations of π or $-\pi$, and thus an overall 2π rotation of the spin. Hence, there is a sign difference between the two paths, and they destructively interfere [124].

The model

$$H_{\text{surf}} = \sum_{\mathbf{k}} \Psi^\dagger(\mathbf{k}) [\hbar v_F \boldsymbol{\sigma} \cdot \mathbf{k} - \mu] \Psi(\mathbf{k}) \quad (4.7)$$

is also used for the TI surface states [123, 149]. This model has the same eigenenergies as the model in Eq. (4.3), but the spins of the surface states are rotated counterclockwise by $\pi/2$ to point along (opposite) \mathbf{k} for the $+(-)$ band. We will use both models, Eqs. (4.3) and (4.7), to model TI surface states later in the thesis.

4.4 BREAKING THE TIME-REVERSAL SYMMETRY

The degenerate states at \mathbf{k} and $-\mathbf{k}$ with opposite spin in one band (see Fig. 4.6) are Kramers pairs [41], as required by the time-reversal symmetry [150]. However, for $\mathbf{k} = 0$, each band contains only one state, and the Kramers pair is made up by the $\mathbf{k} = 0$ state from both the $+$ and $-$ band. Hence, the band crossing at the Dirac point is ensured by the time-reversal symmetry of the system [124].

Introducing a perturbation to the system that breaks time-reversal symmetry, such as a magnetic field, may therefore lift the degeneracy of the $\mathbf{k} = 0$ states, removing the Dirac point [129, 146, 151]. This becomes relevant for instance when placing a TI in proximity to a ferro- or ferrimagnet [149, 152–155], or when introducing ferromagnetically ordered magnetic dopants in the TI [156–167]. If the magnetic field has a component perpendicular to the interface, this induces a gap in the surface state dispersion, dubbed the mass gap [149] in analogy to the electron mass in the Dirac equation [142]. The surface states can nevertheless remain intact.

When adding a coupling to a magnetic field, the model for the surface states is changed to

$$H_{\text{surf}} = \sum_{\mathbf{k}} \Psi^\dagger(\mathbf{k}) [v_F k_y \sigma_x - v_F k_x \sigma_y - \mathbf{m} \cdot \boldsymbol{\sigma} - \mu] \Psi(\mathbf{k}), \quad (4.8)$$

where $\mathbf{m} = (m_x, m_y, m_z)$ is a magnetic field pointing in a general direction, with all coupling constants included in the strength $|\mathbf{m}| = m$. Calculating the surface state bands, we now get

$$\epsilon_{\pm} = \pm \sqrt{(v_F k_x + m_y)^2 + (v_F k_y - m_x)^2 + m_z^2} - \mu. \quad (4.9)$$

Hence, we see that while the in-plane components of \mathbf{m} only shift the dispersion such that it is no longer symmetric around $\mathbf{k} = 0$, the out-of-plane component creates a gap in the dispersion of $2|m_z|$, as illustrated in Fig. 4.7a).

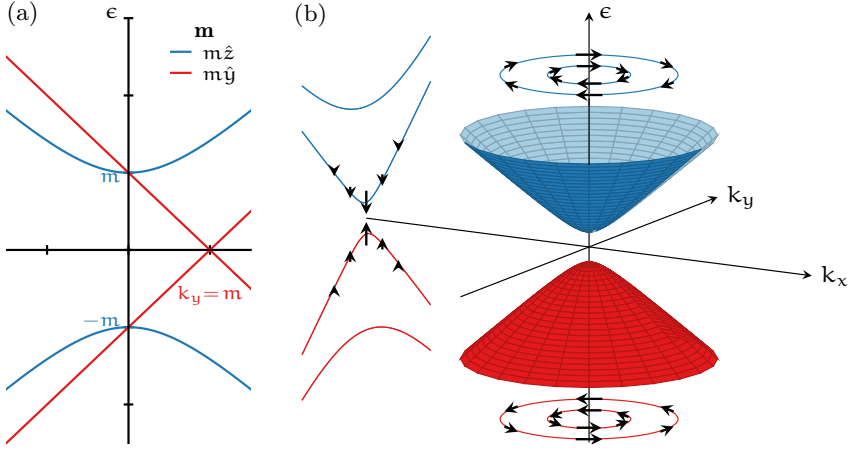


Figure 4.7: (a) Plot of energy bands ϵ_{\pm} in Eq. (4.9) for \mathbf{m} in the z and y directions. (b) Plot of energy bands $\epsilon_{+(-)}$ in blue (red) with $\mathbf{m} = m\hat{z}$, where the breaking of the time-reversal symmetry has led to a gap of $2m$. The projections to the $x - y$ plane and $y - z$ planes show energy contour lines and the spin-projections at these energies. Notice that $\langle S_z \rangle_{\pm}$ are finite in this case, but decrease for increasing $|\mathbf{k}|$.

For notational simplicity, we define $v_F \mathbf{K} = (v_F \mathbf{k} + m_y, v_F \mathbf{k} - m_x)$, and calculate the eigenvectors and spin expectation values, resulting in

$$v_+ = \frac{1}{\sqrt{n_{\mathbf{K}}}} \begin{pmatrix} v_F K_y + i v_F K_x \\ m_z + \sqrt{v_F^2 |\mathbf{K}|^2 + m_z^2} \end{pmatrix}, \quad (4.10a)$$

$$v_- = \frac{1}{\sqrt{n_{\mathbf{K}}}} \begin{pmatrix} -m_z - \sqrt{v_F^2 |\mathbf{K}|^2 + m_z^2} \\ v_F K_y - i v_F K_x \end{pmatrix}, \quad (4.10b)$$

where $n_{\mathbf{K}} = v_{\text{F}}^2 |\mathbf{K}|^2 + \left(m_z + \sqrt{v_{\text{F}}^2 |\mathbf{K}|^2 + m_z^2} \right)^2$, and

$$\langle S_x \rangle_{\pm} = \pm \frac{\hbar}{2} \frac{v_{\text{F}} K_y}{\sqrt{v_{\text{F}}^2 \mathbf{K}^2 + m_z^2}}, \quad (4.11a)$$

$$\langle S_y \rangle_{\pm} = \mp \frac{\hbar}{2} \frac{v_{\text{F}} K_x}{\sqrt{v_{\text{F}}^2 \mathbf{K}^2 + m_z^2}}, \quad (4.11b)$$

$$\langle S_z \rangle_{\pm} = \mp \frac{\hbar}{2} \frac{m_z^2 + m_z \sqrt{v_{\text{F}}^2 \mathbf{K}^2}}{v_{\text{F}}^2 \mathbf{K}^2 + m_z^2 + m_z \sqrt{v_{\text{F}}^2 \mathbf{K}^2 + m_z^2}}. \quad (4.11c)$$

For finite m_z we now have finite $\langle S_z \rangle_{\pm}$, which decreases as $|\mathbf{K}|$ increases. The spin structure is illustrated in Fig. 4.7b) for the case of $\mathbf{m} = m\hat{z}$, showing the momentum-dependence of the spin expectation values.

The influence of magnetic fields on the TI surface states is relevant for the discussion of both the proximity effect between a superconductor and TI in the next chapter, and magnon-induced superconductivity in Chapter 6.

5

TOPOLOGICAL SUPERCONDUCTING PROXIMITY EFFECT

When a non-superconducting material (M) is placed in proximity to a superconductor (S), Cooper pairs can diffuse into the non-superconducting material, leading to superconducting correlations. This is called the proximity effect [6, 15, 16, 168–171]. This in turn also weakens the superconductivity close to the S-M interface, an effect called the inverse proximity effect. The nature of the proximity effect varies greatly depending on the material M. For instance, for a normal metal in the ballistic limit the superconducting correlations decay over a length scale ξ_N , as sketched in Fig. 5.1. However, for a conventional spin-singlet superconductor in contact with a ferromagnet the pair-breaking effects lead to a much shorter oscillatory decay. One important example of the proximity effect in action is the Josephson effect [172], the presence of a supercurrent at zero voltage and finite phase difference between two superconductors separated by a thin insulator. Such Josephson junctions can be combined to create superconducting quantum interference devices (SQUIDS) used to measure magnetic fields with high precision [19].

The surface states of a topological insulator differ from normal metal electrons in many respects: The dispersion is linear, with the spin being locked to the momentum direction, meaning that any proximity-induced superconducting pairing between TI surface states may result in Cooper pairs with symmetries different from those in the superconductor. Moreover, while coupling normal metal electrons

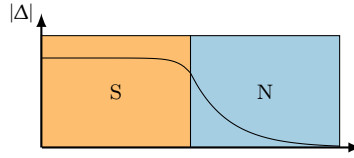


Figure 5.1: Cooper pairs leak from a superconductor into the adjacent normal metal (N), leading to a finite Cooper pair wavefunction a finite distance into the N, and a suppressed wavefunction in the S close to the interface. Based on similar figures in Refs. [15, 16, 173].

to an exchange field leads to pair-breaking effects due to the spin-splitting of the bands, we saw in the previous chapter that exchange fields do not spin-split the surface state bands, but rather open a gap or shift the bands in \mathbf{k} -space. Hence, one might expect the response of proximity-induced superconductivity to an exchange field to differ between the TI and normal metal. In this chapter we will give a brief introduction to the topological superconducting proximity effect — the proximity effect between a superconductor and topological insulator, and present the main results from Papers [2, 3].

5.1 PROXIMITY EFFECT ON THE TOPOLOGICAL INSULATOR SURFACE

The proximity effect on the surface of a topological insulator was first studied by Fu and Kane [174]. They assumed that s -wave Cooper pairs tunnel into the surface states, resulting in the effective action

$$S = \frac{1}{\beta V} \sum_{\mathbf{k}} \left\{ \Psi_{\mathbf{k}}^{\dagger} [-i\omega_n + v_F \mathbf{k} \cdot \boldsymbol{\sigma} - \mu_{\text{TI}}] \Psi_{\mathbf{k}} + \Delta \Psi_{\mathbf{k}\uparrow}^{\dagger} \Psi_{-\mathbf{k}\downarrow}^{\dagger} + \Delta^{\dagger} \Psi_{-\mathbf{k}\downarrow} \Psi_{\mathbf{k}\uparrow} \right\} \quad (5.1)$$

for the TI surface states, where $\Psi_{\mathbf{k}} = [\psi_{\mathbf{k}\uparrow} \ \psi_{\mathbf{k}\downarrow}]^T$. Switching to the diagonal basis of the non-interacting system, we find that the pairing terms are transformed to

$$\Delta\psi_{\mathbf{k}\uparrow}^\dagger\psi_{-\mathbf{k}\downarrow}^\dagger = -\frac{\Delta}{2}[e^{i\Phi_{\mathbf{k}}}\psi_{\mathbf{k},+}^\dagger\psi_{-\mathbf{k},+}^\dagger + e^{-i\Phi_{\mathbf{k}}}\psi_{\mathbf{k},-}^\dagger\psi_{-\mathbf{k},-}^\dagger], \quad (5.2)$$

where \pm denote the $+$ and $-$ helicity states. Assuming that the chemical potential is tuned far away from the superconducting gap, $\mu_{\text{TI}} \gg \Delta > 0$, we get an effective theory of a spinless $p_x + ip_y$ superconductor [174]

$$S_+ = \frac{1}{\beta V} \sum_{\mathbf{k}} \left\{ \psi_{\mathbf{k},+}^\dagger [-i\omega_n + v_F|\mathbf{k}| - \mu_{\text{TI}}] \psi_{\mathbf{k},+} - \frac{\Delta e^{i\Phi_{\mathbf{k}}}}{2} \psi_{\mathbf{k},+}^\dagger \psi_{-\mathbf{k},+}^\dagger + \text{h. c.} \right\}. \quad (5.3)$$

This result garnered much attention because of earlier predictions that Majorana zero modes could occur at the cores of vortices in such superconductors [175–177], with potential application to fault-tolerant quantum computation [178] based on non-Abelian statistics [179–182], leading to much experimental [183–195] and theoretical [196–206] work on such systems.

Irrespective of the presence of Majorana fermions, superconductivity on the surface of TIs is in itself interesting, differing from the superconducting states in both conventional and cuprate superconductors. A more detailed handling of the coupling between the TI and superconductor showed that the induced superconducting correlations in the TI are a mix of s -wave spin singlet and p -wave spin singlet correlations [197, 200, 203, 205]. Moreover, due to the similarities between the kinetic term of the TI surface states and the Zeeman coupling, the effects an exchange field on the superconducting state differs from regular superconductors, as we will see in the next section.

5.2 VORTEX SPIN VALVE

Adding a coupling to an electric potential, gauge field \mathbf{A} , and an in-plane exchange field \mathbf{m} in the action Eq. (5.1), we get the action

$$S = \int_0^\beta d\tau \int d\mathbf{r} \left\{ \Psi^\dagger [\partial_\tau - v_F(i\nabla + e\mathbf{A}) \cdot \boldsymbol{\sigma} - \mathbf{m} \cdot \boldsymbol{\sigma} - \mu_{\text{TI}} + ie\phi] \Psi - \Delta \psi_\uparrow^\dagger \psi_\downarrow^\dagger - \Delta^\dagger \psi_\downarrow \psi_\uparrow \right\}, \quad (5.4)$$

where we have switched to an imaginary time, and coordinate basis. From the above we see that the gauge and exchange fields enter the action in the same way. This equation is gauge invariant under the local transformation

$$\psi_\sigma \rightarrow \psi_\sigma e^{-i\theta}, \quad (5.5a)$$

$$e\mathbf{A} \rightarrow e\mathbf{A} - \nabla\theta, \quad (5.5b)$$

$$e\phi \rightarrow e\phi + \partial_\tau\theta, \quad (5.5c)$$

$$\Delta \rightarrow \Delta e^{-2i\theta}. \quad (5.5d)$$

The requirement that Δ must be single-valued when integrating around a contour enclosing a region with a magnetic field, leads to flux quantization with flux quantum $\Phi_0 = \pi\hbar/|e|$, see the discussion in Section 2.2. In analogy to the above transformations, we can also define another transformation

$$\psi_\sigma \rightarrow \psi_\sigma e^{-iM/v_F}, \quad (5.6a)$$

$$\Delta \rightarrow \Delta e^{-2iM/v_F}, \quad (5.6b)$$

where we have defined a time-independent function M such that $\nabla M = \mathbf{m}$. This allows us to remove the \mathbf{m} term in the action at the cost of an additional phase factor for the electron and Cooper pair fields. In a Josephson junction of length L along the x direction this leads to a cumulative phase $\varphi_0 = 2m_x L/v_F$ when integrating over the length of the junction. The current-phase relation is therefore shifted,

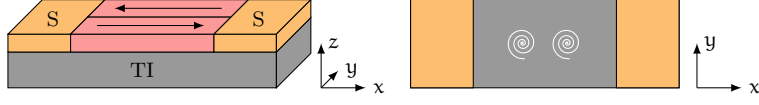


Figure 5.2: (left) Sketch of the system considered in Paper [2]: A spin valve placed on top of a TI Josephson junction. In the anti-parallel configuration the in-plane exchange field can induce vortices in the TI (right). No vortices are present in the parallel configuration.

$I \sim \sin(\varphi - \varphi_0)$ [196, 199], meaning that one can have Josephson junctions with tunable phases φ_0 other than 0 and π in the ground state.

Integrating around a contour \mathcal{C} and requiring that the gap must be single-valued, we get the requirement

$$\frac{2}{v_F} \oint_{\mathcal{C}} d\mathbf{l} \cdot \nabla M = \frac{2}{v_F} \oint_{\mathcal{C}} d\mathbf{l} \cdot \mathbf{m} = \frac{2}{v_F} \int_{\mathcal{A}} d\mathbf{S} \cdot \nabla \times \mathbf{m} = 2\pi N. \quad (5.7)$$

Defining an effective flux $\Phi_{\mathbf{m}} \equiv \int_{\mathcal{A}} d\mathbf{S} \cdot \nabla \times \mathbf{m}$, we see that this flux is quantized in terms of the new flux quantum $\Phi_0^{\mathbf{m}} = \pi v_F$. Therefore, it should be possible to induce vortices by an in-plane exchange field. This was examined in Paper [2] using the quasiclassical Usadel equation [207] for topological insulators in proximity to superconductors [208–210], showing that a spin valve structure on top of a TI Josephson junction can be used to control the presence of vortices, see Fig. 5.2.

5.3 INVERSE PROXIMITY EFFECT

The aforementioned effect depends on the fact that superconductivity is present in the system, and it is thus crucial that the inverse proximity effect is weak enough that the superconducting correlations survive when coupling to a TI. This problem was first addressed in Refs. [200, 202] and [201] for the case of 2D and 3D topological

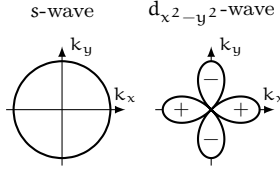


Figure 5.3: Plots of the symmetry functions $v(\mathbf{k})$ in Eq. (5.9) for the s-wave and d-wave cases.

insulators respectively,¹ showing that the superconducting correlations decayed compared to the bulk value close to the S-TI interface, but still remained finite. In Paper [3] we investigated if there exist situations where the inverse proximity effect is strong, resulting in a large decrease in the superconducting gap, by studying a model of an effectively 2D s-wave or d-wave superconductor coupled to the surface states of a TI. The bulk states were not considered, though these can also become superconducting [192, 211], meaning the chemical potential should be located inside the bulk gap of the TI. The model consists of three terms, $S = S_S + S_{\text{TI}} + S_t$, where the superconducting part reads

$$\begin{aligned}
 S_S = & \frac{1}{\beta V} \sum_{\mathbf{k}, \sigma} [-i\omega_n + \epsilon_{\mathbf{k}} - \mu] c_{\mathbf{k}\sigma}^\dagger c_{\mathbf{k}\sigma} \\
 & - \sum_{\mathbf{k}, \mathbf{k}'} \frac{V_{\mathbf{k}\mathbf{k}'}}{(\beta V)^3} c_{\mathbf{k}\uparrow}^\dagger c_{-\mathbf{k}\downarrow}^\dagger c_{-\mathbf{k}'\downarrow} c_{\mathbf{k}'\uparrow},
 \end{aligned} \tag{5.8}$$

where the interaction written in separable form [19]

$$V_{\mathbf{k}, \mathbf{k}'} = g v(\mathbf{k}) v(\mathbf{k}') \tag{5.9}$$

with $v(\mathbf{k})$ determining the symmetry of the interaction. For s-wave $v(\mathbf{k}) = 1$, while for $d_{x^2-y^2}$ -wave $v(\mathbf{k}) = \sqrt{2} \cos 2\phi_{\mathbf{k}}$, as illustrated in Fig. 5.3. The coupling strength g is finite only for $-\omega_- < \epsilon_{\mathbf{k}} - \mu <$

¹Unfortunately, I was not aware of these works when working on and writing Paper [3], and therefore failed to mention that such self-consistent calculations had already been performed.

ω_+ , where ω_{\pm} is an upper (lower) cut-off frequency. For the TI surface state theory S_{TI} we use Eq. (5.1) with $|\Delta| = 0$. The TI surface states are coupled to electrons in the superconductor by the hopping term [204, 212–214]

$$S_t = -\frac{1}{\beta V} \sum_{\mathbf{k}, \sigma} t [c_{\mathbf{k}\sigma}^\dagger \psi_{\mathbf{k}\sigma} + \psi_{\mathbf{k}\sigma}^\dagger c_{\mathbf{k}\sigma}]. \quad (5.10)$$

Integrating out the TI fermions leads to an SOC term in the effective S action [213], which for an s -wave superconductor is expected to result in p -wave correlations, see e.g. Ref. [106]. Performing a Hubbard-Stratonovich decoupling, and calculating the Green's function in the superconductor, this is exactly what we find. The anomalous Green's function has the form

$$F(\mathbf{k}) = \frac{\Delta(\mathbf{k})}{\omega_n^2 + E_{\mathbf{k}}^2} [1 + t^2 F_s(\mathbf{k}) + t^2 F_t(\mathbf{k}) \mathbf{k} \cdot \boldsymbol{\sigma}] i\sigma_y, \quad (5.11)$$

where $E_{\mathbf{k}} = \sqrt{(\epsilon_{\mathbf{k}} - \mu)^2 + |\Delta(\mathbf{k})|^2}$, indicating that the proximity to the TI has induced spin triplet p -wave (f -wave) correlations in the s -wave (d -wave) superconductor [200, 201]. The form of $F(\mathbf{k})$ is very similar to that found on the TI side of an S-TI bilayer in Ref. [203]. The anomalous Green's function does not contain odd-frequency correlations. However, adding an in-plane exchange field does result in odd-frequency correlations, in agreement with the results in Ref. [203]. Proximity-induced odd-frequency pairing was recently observed in the bulk of a TI with a magnetic field applied parallel to the interface [211].

Due to the induced spin-orbit coupling, the spin basis is no longer the eigenbasis of the S . In the normal state ($T > T_c$) we have the bands

$$\epsilon_{\lambda}^{\gamma}(\mathbf{k}) = \frac{1}{2} [\epsilon_{\mathbf{k}} - \mu + \lambda v_F |\mathbf{k}| - \mu_{\text{TI}} + \gamma \sqrt{(\epsilon_{\mathbf{k}} - \mu - \lambda v_F |\mathbf{k}| + \mu_{\text{TI}})^2 + 4t^2}], \quad (5.12)$$

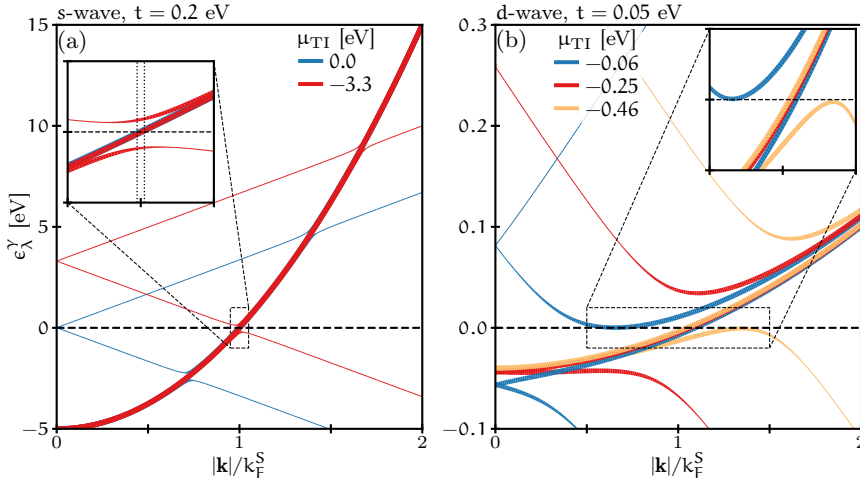


Figure 5.4: Plots of the bands $\epsilon_\lambda^\gamma(\mathbf{k})$ in Eq. (5.12) for different μ_{TI} with parameter values relevant for (a) s-wave and (b) d-wave superconductors, with line widths proportional to the spectral weights in Eq. (5.13). The dotted lines in the inset in (a) show the cut-off momenta corresponding to the cut-off frequencies ω_\pm .

with quasiparticle weights given by the residues of the Green's function,

$$w_\lambda^\gamma(\mathbf{k}) = \frac{1}{2} + \frac{\epsilon_{\mathbf{k}} - \mu - \lambda v_F |\mathbf{k}| + \mu_{\text{TI}}}{2\gamma \sqrt{(\epsilon_{\mathbf{k}} - \mu - \lambda v_F |\mathbf{k}| + \mu_{\text{TI}})^2 + 4t^2}}, \quad (5.13)$$

where $\lambda, \gamma = \pm$. The bands are plotted in Fig. 5.4 for typical parameter values for conventional s-wave and high- T_c d-wave superconductors. In both cases we see that for certain choices of μ_{TI} there is a strong hybridization of the bands close to the Fermi level, leading to only one band crossing and thus a reduced density of states at the Fermi level. This could in turn result in a reduced superconducting gap.

In the superconducting state we have the bands

$$E_{\lambda}^{\gamma}(\mathbf{k}) = \frac{1}{\sqrt{2}} \left\{ E_{\mathbf{k}}^2 + (\lambda v_F |\mathbf{k}| - \mu_{\text{TI}})^2 + 2t^2 + \gamma \{ [E_{\mathbf{k}}^2 - (\lambda v_F |\mathbf{k}| - \mu_{\text{TI}})^2]^2 + 4t^2 [(\epsilon_{\mathbf{k}} - \mu + \lambda v_F |\mathbf{k}| - \mu_{\text{TI}})^2 + |\Delta(\mathbf{k})|^2] \}^{\frac{1}{2}} \right\}^{\frac{1}{2}}, \quad (5.14)$$

where $E_{\mathbf{k}} = \sqrt{(\epsilon_{\mathbf{k}} - \mu)^2 + |\Delta(\mathbf{k})|^2}$, and $\Delta(\mathbf{k}) = \Delta v(\mathbf{k})$ is determined self-consistently from the gap equation

$$1 = \frac{g}{4V} \sum_{\mathbf{k}} \sum_{\lambda, \gamma} v(\mathbf{k})^2 \frac{E_{\lambda}^{\gamma}(\mathbf{k})^2 - (\lambda v_F |\mathbf{k}| - \mu_{\text{TI}})^2}{E_{\lambda}^{\gamma}(\mathbf{k}) [E_{\lambda}^{\gamma}(\mathbf{k})^2 - E_{\lambda}^{\bar{\gamma}}(\mathbf{k})^2]} \tanh \frac{\beta E_{\lambda}^{\gamma}(\mathbf{k})}{2}. \quad (5.15)$$

Solving the gap equation numerically, we get the dependence on μ_{TI} and t shown in Fig. 5.5a) and b) for the *s*-wave and *d*-wave cases, which we discuss in more detail in the following.

5.3.1 *s*-wave superconductors

In the *s*-wave case there is a reduction in the superconducting gap when $\mu_{\text{TI}}^{\lambda, -} < \mu_{\text{TI}} < \mu_{\text{TI}}^{\lambda, +}$, where

$$\mu_{\text{TI}}^{\lambda, \pm}(t) = \lambda \sqrt{2m v_F^2 (\mu \mp \omega_D) \pm \frac{t^2}{\omega_D}}, \quad (5.16)$$

with cut-off frequencies ω_{\pm} set to the Debye frequency ω_D . This corresponds to chemical potentials where one normal band [Eq. (5.12)] does not cross the Fermi level within a range of momenta given by the cut-off frequencies, see the inset in Fig. 5.4a). Naively we therefore expect a reduction in the gap to the value $|\Delta| = |\Delta_0| e^{-1/\lambda}$, where $\lambda = gD_0$ is the dimensionless coupling constant and D_0 is the normal density of states at the Fermi level, since this corresponds to the density of states being halved. From the inset in Fig. 5.5a) we see that this is in good agreement with the numerical results. The

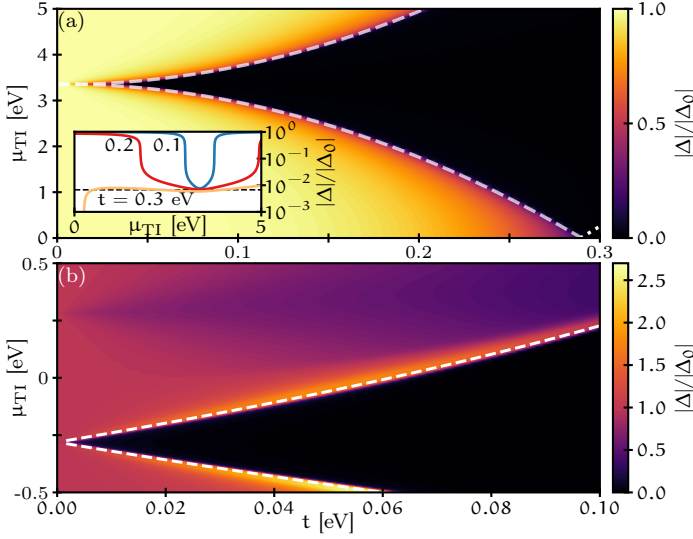


Figure 5.5: Plots of the superconducting gap at $T = 0$ normalized to the bulk value Δ_0 as a function of μ_{TI} and t for the (a) s-wave and (b) d-wave cases. The inset in (a) shows the normalized gap as a function of μ_{TI} at three specific values of t , where the dashed line indicates the value $e^{-1/\lambda}$, where λ is the dimensionless coupling constant.

reduction of Δ thus decreases for increasing λ , as seen in Fig. 5.6, consistent with the fact that the superconducting state is more robust for higher coupling constants.

For most conventional s-wave superconductors the values $\mu_{\text{TI}}^{\lambda,\pm}(t \approx 0)$ lie far outside the bulk gap of the TI due to the high chemical potential μ , meaning a strong coupling t is necessary to observe the strongly reduced gap. Since no strong inverse proximity effect has been observed, e.g. in Ref. [193], it seems that the coupling is too weak in most systems. This is also in agreement with the results in Refs. [200–202]. Moreover, since we only consider the surface states, our model is not valid for chemical potentials outside the bulk gap.

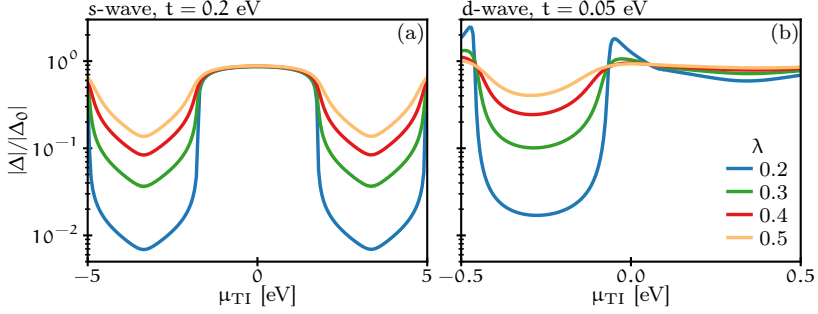


Figure 5.6: Plot of the normalized superconducting gap as a function of μ_{TI} for different effective coupling constants λ for the (a) s-wave and (b) d-wave cases, showing that the suppression decreases for increasing λ .

5.3.2 d-wave superconductors

In the case of d-wave superconductors, the chemical potential is typically much lower, leading to strong suppression for μ_{TI} inside the bulk band gap even at very low coupling, see Fig. 5.5b), and should therefore be experimentally more accessible. We here use cut-off frequencies of the order of the characteristic energies of antiferromagnetic fluctuations assumed to be relevant for high- T_c superconductors [61–63, 215–220]. The suppression now occurs when the hybridization of the bands Eq. (5.12) is so strong that the bands bend away from the Fermi level, see Fig. 5.4b), leading to a reduced number of bands crossing the Fermi level. However, when the maxima or minima of the bent bands are located close to the Fermi level the density of states is increased, thus explaining the increase in the normalized gap seen in Fig. 5.5b). In principle it could therefore be possible to tune the superconducting gap by a few orders of magnitude by small variations in μ_{TI} . From Fig. 5.6 we again see that increasing λ leads to smaller suppression of the gap, and a reduced increase at μ_{TI}^{\pm} . The inverse proximity effect between a high- T_c superconductor and a TI was also studied in Ref. [221] using dynamical mean field theory,

showing that the coupling to a TI could lead to a large suppression of the gap for certain parameter values.

6

MAGNON-MEDIATED SUPERCONDUCTIVITY

In the previous chapter we discussed superconductivity on the surface of topological insulators due to proximity to superconductors. In this chapter we will discuss another proximity system, namely a topological insulator coupled to a ferromagnetic insulator (FMI). Kargarian, Efimkin and Galitski [222] showed that the coupling between the topological surface states of the TI and the magnetic fluctuations — the magnons — in the FMI could lead to a novel type of superconductivity called Amperean pairing [223], where the momenta of the Cooper pair electrons point in the same direction, see Fig. 6.1, in contrast to regular BCS pairing where the momenta are opposite.

The idea of magnons being mediators of attractive interactions leading to superconductivity is not unique to TI-FMI systems, as it is one of the proposed mechanisms for superconductivity in certain unconventional superconductors [224, 225], where there can be either competing or coexisting magnetic and superconducting phases [61–63, 215–220, 226–231]. Moreover, there have also been

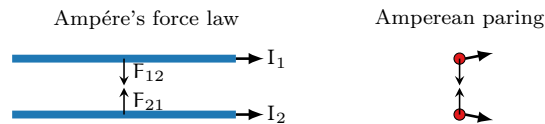


Figure 6.1: In analogy with the attractive force between two current-carrying wires, Amperean pairing is caused by attractive interactions between fermions with close to parallel momenta.

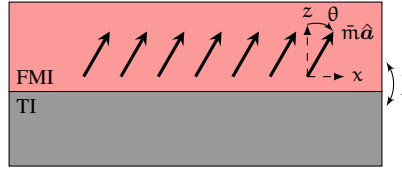


Figure 6.2: The topological surface states are coupled to the magnetic moments in the ferromagnetic insulator with magnetization direction determined by the angle θ relative to the z axis.

studies of superconductivity in systems consisting of ferromagnetic and antiferromagnetic insulators coupled to normal metals [232–236].

In this chapter we will discuss the results of Papers [4] and [5], focusing on a TI coupled to an FMI, allowing for a tilted magnetization, see Fig. 6.2. In Paper [4] we also considered coupling to an antiferromagnetic insulator (AFMI), giving similar results to that of an FMI. However, this model does not capture important differences between the FMI and AFMI cases, such as the enhanced interaction strengths due to asymmetric couplings between the AFMI sublattices [234, 236–239]. For this reason, we will focus on the FMI case for the remainder of the chapter.

6.1 FERROMAGNETIC INSULATOR

The ferromagnetic insulator is modeled using the action [222, 240]

$$S_m = \int_0^\beta d\tau \int d\mathbf{r} \left[\mathbf{b}(\mathbf{m}) \cdot i\partial_\tau \mathbf{m} + \frac{\kappa}{2} (\nabla \mathbf{m})^2 - \lambda (\mathbf{m} \cdot \hat{\mathbf{a}})^2 \right], \quad (6.1)$$

where \mathbf{m} is the magnetic moment in the FMI, and $\hat{\mathbf{a}} = \sin \theta \hat{x} + \cos \theta \hat{z}$. In general, we could also have included a y -component in $\hat{\mathbf{a}}$, but this can be shown to be equivalent with the chosen axis $\hat{\mathbf{a}}$. The first term in S_m is the Berry phase term describing how the action depends on the trajectory, and thus history, of the magnetic moment [110]. $\mathbf{b}(\mathbf{m})$ is the Berry connection satisfying $\nabla_{\mathbf{m}} \times \mathbf{b}(\mathbf{m}) = \mathbf{m}/|\mathbf{m}|^2$ [110,

p. 104], where $\nabla_{\mathbf{m}} = (\partial_{m_x}, \partial_{m_y}, \partial_{m_z})$. κ must be positive in order for the system to be stable.

Assuming no time- and space-dependence, the action is minimized by maximizing \mathbf{m} in the direction of $\hat{\mathbf{a}}$ for positive λ . Therefore, in the ground state all spins are oriented along $\hat{\mathbf{a}}$. Fixing the length of \mathbf{m} , $|\mathbf{m}| = \bar{m}$, we parametrize the magnetic moment vector in terms of fluctuations \mathbf{n} in the directions orthogonal to $\hat{\mathbf{a}}$,

$$\mathbf{m} = \sqrt{1 - \mathbf{n}^2} \bar{m} \hat{\mathbf{a}} + \bar{m} \mathbf{n}, \quad (6.2)$$

with

$$\mathbf{n} = (n_x, n_y, n_z) = n(\cos \theta \hat{x} - \sin \theta \hat{z}) + n_y \hat{y}, \quad (6.3)$$

where we assume the fluctuations are small, $|\mathbf{n}| \ll 1$. We have two independent fluctuation directions orthogonal to the axis $\hat{\mathbf{a}}$ parametrized by n and n_y . For the Berry connection, we use [222]

$$\mathbf{b} = \frac{\hat{\mathbf{a}} \times \mathbf{n}}{2}, \quad (6.4)$$

which to lowest order in fluctuations results in $\nabla_{\mathbf{m}} \times \mathbf{b} = \hat{\mathbf{a}}/\bar{m}$.

Rewriting the action in terms of the fluctuations and Fourier transforming, we get to second order in \mathbf{n}

$$S_n = \frac{\bar{m}}{\beta V} \sum_{\mathbf{q}} \left[\frac{\Omega_n}{2} [\mathbf{n}(-\mathbf{q}) \times \mathbf{n}(\mathbf{q})] \cdot \hat{\mathbf{a}} + \omega_{\mathbf{q}} \mathbf{n}(-\mathbf{q}) \cdot \mathbf{n}(\mathbf{q}) \right], \quad (6.5)$$

where we have defined the magnon dispersion

$$\omega_{\mathbf{q}} = \frac{\kappa \bar{m}}{2} \mathbf{q}^2 + \lambda \bar{m}. \quad (6.6)$$

From this we see that the magnon energy increases quadratically with increasing wavenumber, and that there is a finite energy cost $\lambda \bar{m}$ of creating any spin wave due to the easy-axis anisotropy.

In Paper [4] we used a slightly different model, where the TI surface states and the FMI magnetization are indirectly coupled by

fermions residing on the surface of the FMI [240]. This leads to a renormalization of the parameter λ in the magnon model, making negative values of λ possible for the fluctuations. We will therefore also discuss negative values of λ below, interpreting it as an effective value for the fluctuations due to a more complex underlying model, while still having an easy-axis along $\hat{\mathbf{a}}$.

6.2 MAGNON-MEDIATED INTERACTION

On the surface between the FMI and TI we couple the surface states and magnetic moments via an exchange interaction term with strength J

$$S_c = - \int_0^\beta d\tau \int d\mathbf{r} J \mathbf{m} \cdot \Psi^\dagger \boldsymbol{\sigma} \Psi, \quad (6.7)$$

where $\Psi = (\psi_\uparrow, \psi_\downarrow)^T$, where ψ_σ describe the electrons on the surface of the TI with spin $\sigma = \uparrow, \downarrow$. Fourier transforming the coupling term, and separating the mean-field and fluctuation terms we get $S_c = S_c^{\bar{\mathbf{m}}} + S_c^{\mathbf{n}}$, with

$$S_c^{\bar{\mathbf{m}}} = - \frac{J\bar{\mathbf{m}}}{\beta V} \sum_{\mathbf{k}} \Psi_{\mathbf{k}}^\dagger \hat{\mathbf{a}} \cdot \boldsymbol{\sigma} \Psi_{\mathbf{k}}, \quad (6.8a)$$

$$S_c^{\mathbf{n}} = - \frac{J\bar{\mathbf{m}}}{(\beta V)^2} \sum_{\mathbf{k}, \mathbf{q}} \Psi_{\mathbf{k}+\mathbf{q}}^\dagger \mathbf{n}(\mathbf{q}) \cdot \boldsymbol{\sigma} \Psi_{\mathbf{k}}, \quad (6.8b)$$

to leading order in \mathbf{n} . The six vertexes in Eq. (6.8b) are shown in Fig. 6.3.

Adding Eq. (6.8a) to the TI action

$$S_{\text{TI}} = \frac{1}{\beta V} \sum_{\mathbf{k}} \Psi_{\mathbf{k}}^\dagger [-i\omega_{\mathbf{n}} + v_{\text{F}}(k_x \sigma_y - k_y \sigma_x) - \mu] \Psi_{\mathbf{k}}, \quad (6.9)$$

results in a gap and/or a \mathbf{k} -space shift in the surface state dispersion of the \pm helicity states (see Section 4.4),

$$\epsilon_{\pm}(\mathbf{k}) = \pm \sqrt{v_{\text{F}}^2 k_x^2 + v_{\text{F}}^2 (k_y - K_y)^2 + M^2} - \mu, \quad (6.10)$$

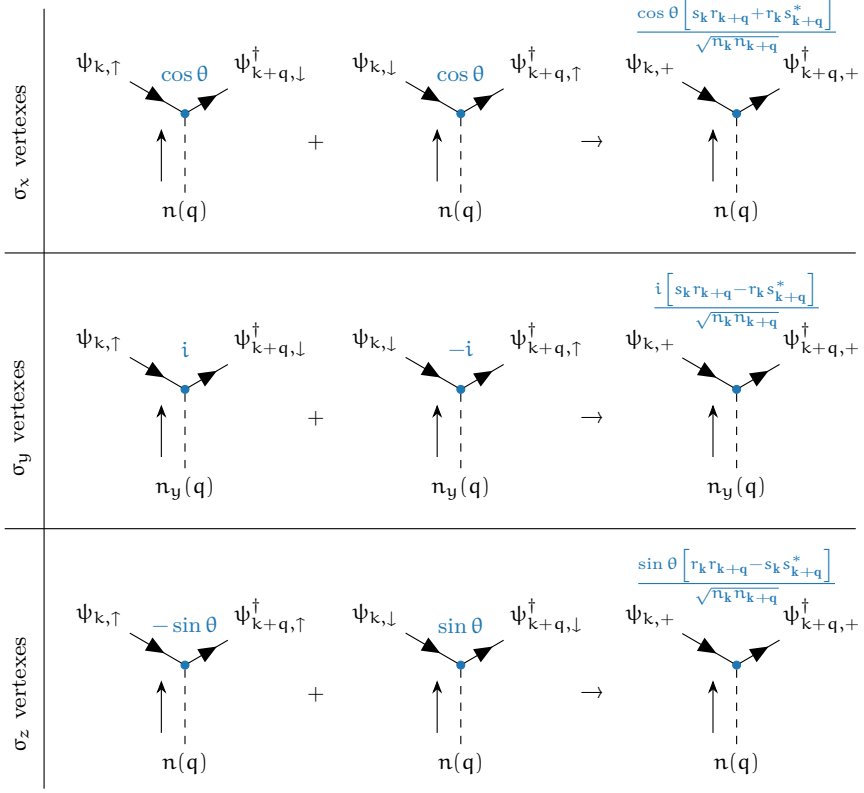


Figure 6.3: Diagrams for interaction vertices in Eq. (6.8b), and the resulting interaction vertices when projecting to the + helicity band, see Eq. (6.11). The coupling functions for each vertex is written in blue font, denoted $v_{k,k+q}^i$ with $i = x, y, z$ for the + helicity band in the rightmost column.

where we have defined $M = J\bar{m} \cos \theta$ and $v_F K_y = J\bar{m} \sin \theta$. Assuming that $\mu > 0$, only the + helicity states will contribute significantly to

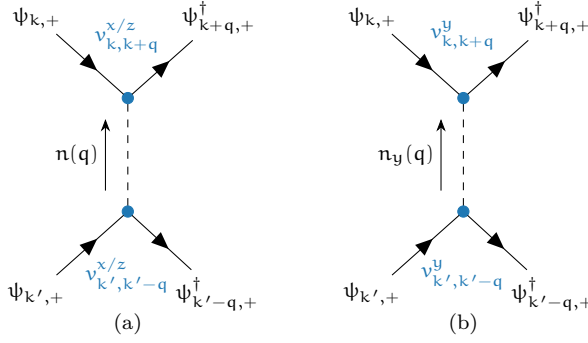


Figure 6.4: Diagrams for effective interactions mediated by (a) n and (b) n_y , constructed from the diagrams in Fig. 6.3.

any dynamical processes in the system. Hence, we get the mapping between the spin basis and the $+$ band,

$$\psi_{k\uparrow} \rightarrow \frac{s_{\mathbf{k}}}{\sqrt{n_{\mathbf{k}}}} \psi_{k,+}, \quad (6.11a)$$

$$\psi_{k\downarrow} \rightarrow \frac{r_{\mathbf{k}}}{\sqrt{n_{\mathbf{k}}}} \psi_{k,+}, \quad (6.11b)$$

where $s_{\mathbf{k}} = v_F(k_y - K_y) + iv_F k_x$, $r_{\mathbf{k}} = M + \sqrt{M^2 + |s_{\mathbf{k}}|^2}$, and $n_{\mathbf{k}} = r_{\mathbf{k}}^2 + |s_{\mathbf{k}}|^2$. Inserting this mapping into the coupling term Eq. (6.8b), the interaction vertexes are transformed as shown in Fig. 6.3, leading to new effective coupling functions between the surface states and magnon species n and n_y , denoted $v_{k,k+q}^i$ with $i = x, y, z$. These coupling functions reflect the fact that due to the spin-orbit coupling the spin-up and spin-down weights of a surface state depend on the momentum direction, and thus the scattering processes depend on the incoming and outgoing momenta of the surface states.

As with phonons in the BCS theory, the interactions between surface states and magnons lead to interactions between the surface states mediated by the n or n_y magnons, as illustrated in Fig. 6.4. Including all possible diagrams to second order in J , we get the following theory for the $+$ fermions,

$$\begin{aligned}
S_+ = & \frac{1}{\beta V} \sum_{\mathbf{k}} [-i\omega_n + \epsilon_+(\mathbf{k}) - \mu] \psi_{\mathbf{k}}^\dagger \psi_{\mathbf{k}} \\
& + \frac{1}{(\beta V)^3} \sum_{\mathbf{k}, \mathbf{k}', \mathbf{q}} V_{\mathbf{k}\mathbf{k}'}(\mathbf{q}) \psi_{\mathbf{k}+\frac{\mathbf{q}}{2}}^\dagger \psi_{-\mathbf{k}+\frac{\mathbf{q}}{2}}^\dagger \psi_{-\mathbf{k}'+\frac{\mathbf{q}}{2}} \psi_{\mathbf{k}'+\frac{\mathbf{q}}{2}},
\end{aligned} \tag{6.12}$$

where we have dropped the subscript $+$ for notational simplicity, and defined the symmetrized interaction matrix

$$V_{\mathbf{k}\mathbf{k}'}(\mathbf{q}) = -\frac{J^2 \tilde{m}}{8} [D(\mathbf{k} - \mathbf{k}') \Lambda_{\mathbf{q}}(\mathbf{k}, \mathbf{k}') - D(\mathbf{k} + \mathbf{k}') \Lambda_{\mathbf{q}}(\mathbf{k}, -\mathbf{k}')] \tag{6.13}$$

with magnon propagator

$$D(\mathbf{q}) = \frac{\omega_{\mathbf{q}}}{(\Omega_n/2)^2 + \omega_{\mathbf{q}}^2}, \tag{6.14}$$

and scattering form factor

$$\begin{aligned}
\Lambda_{\mathbf{q}}(\mathbf{k}, \mathbf{k}') = & \prod_{i,j=x,z} v_{\mathbf{k}'+\frac{\mathbf{q}}{2}, \mathbf{k}+\frac{\mathbf{q}}{2}}^i v_{-\mathbf{k}'+\frac{\mathbf{q}}{2}, -\mathbf{k}+\frac{\mathbf{q}}{2}}^j \\
& + v_{\mathbf{k}'+\frac{\mathbf{q}}{2}, \mathbf{k}+\frac{\mathbf{q}}{2}}^y v_{-\mathbf{k}'+\frac{\mathbf{q}}{2}, -\mathbf{k}+\frac{\mathbf{q}}{2}}^y.
\end{aligned} \tag{6.15}$$

6.3 THE GAP EQUATION

In the above interaction term we have allowed for a finite center-of-mass momentum \mathbf{q} , which could in principle lead to Cooper pairing with a finite center-of-mass momentum. Moreover, whenever $K_y \neq 0$, the dispersion $\epsilon_+(\mathbf{k})$ is centered at $\mathbf{k} = (0, K_y)$, meaning that Cooper pairs can have a finite center-of-mass momentum even when located at opposite sides of the Fermi surface. This would be analogous to FFLO states [51, 52], and we thus have some similarities with the Rashba spin-orbit coupled and Zeeman split system discussed in Section 3.4.

Introducing a bosonic Cooper pair field Δ through a Hubbard-Stratonovich decoupling, and deriving the gap equation along the lines sketched in Section 2.3, we arrive at

$$\Delta_{\mathbf{Q}}^{\dagger}(\mathbf{k}') = \frac{2}{\beta V} \sum_{\mathbf{k}} \frac{\Delta_{\mathbf{Q}}^{\dagger}(\mathbf{k}) V_{\mathbf{k}\mathbf{k}'}(\mathbf{Q})}{[i\omega_n - \epsilon_{\mathbf{Q}}^{\circ}(\mathbf{k}) - E_{\mathbf{Q}}(\mathbf{k})][i\omega_n - \epsilon_{\mathbf{Q}}^{\circ}(\mathbf{k}) + E_{\mathbf{Q}}(\mathbf{k})]}. \quad (6.16)$$

Here we have specialized to one center-of-mass momentum \mathbf{Q} , while the center-of-mass frequency is set to zero, meaning $Q = (0, \mathbf{Q})$. We have also defined the even and odd parts of the dispersion relation

$$\epsilon_{\mathbf{Q}}^{\circ}(\mathbf{k}) = \frac{\epsilon_+ \left(\mathbf{k} + \frac{\mathbf{Q}}{2} \right) - \epsilon_+ \left(-\mathbf{k} + \frac{\mathbf{Q}}{2} \right)}{2}, \quad (6.17a)$$

$$\epsilon_{\mathbf{Q}}^{\epsilon}(\mathbf{k}) = \frac{\epsilon_+ \left(\mathbf{k} + \frac{\mathbf{Q}}{2} \right) + \epsilon_+ \left(-\mathbf{k} + \frac{\mathbf{Q}}{2} \right)}{2}, \quad (6.17b)$$

and the function

$$E_{\mathbf{Q}}(\mathbf{k}) = \sqrt{[\epsilon_{\mathbf{Q}}^{\epsilon}(\mathbf{k})]^2 + |\Delta_{\mathbf{Q}}(\mathbf{k})|^2}. \quad (6.18)$$

Notice that $E_{\mathbf{Q}}(\mathbf{k})$ depends on the Matsubara frequency ω_n through the frequency dependence of $\Delta_{\mathbf{Q}}(\mathbf{k})$.

Since the gap function $\Delta_{\mathbf{Q}}^{\dagger}(\mathbf{k})$ describes pseudo-spin triplet Cooper pairs — the interaction is only between + helicity fermions — we see from Table 2.1 that the gap function must either be even in frequency and odd in momentum, or odd in frequency and even in momentum. From Eqs. (6.13) and (6.16) we see that the only dependence on the free frequency ω_n comes from the magnon propagator. Neglecting the frequency dependence in the propagator [228, 229, 237] thus amounts to specializing to the odd-momentum state. We will study possible superconducting states in this limit first, before later treating the frequency-dependent gap equation.

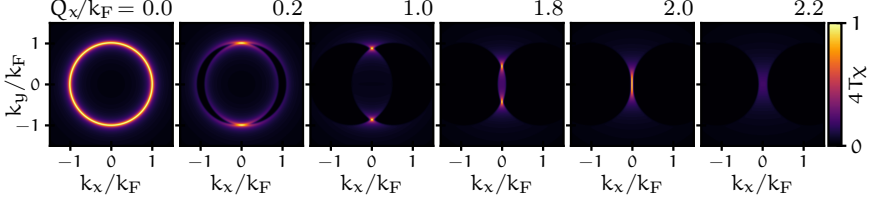


Figure 6.5: Plot of $4T\chi_{\mathbf{Q}}(\mathbf{k})$ with $\Delta_{\mathbf{Q}} = 0$ as a function of momentum for different center-of-mass momenta $\mathbf{Q} = (Q_x, 0)$. The tilt angle $\theta = 0$, resulting in $K_y = 0$, and the temperature is set to $k_B T = 2 \times 10^{-3}$ eV. We get similar results when when increasing Q_y .

6.4 ZERO FREQUENCY LIMIT

In the zero frequency limit the magnon propagator simplifies to $D(\mathbf{q}) = \omega_{\mathbf{q}}^{-1}$, leading to a simplified gap equation

$$\Delta_{\mathbf{Q}}^{\dagger}(\mathbf{k}') = -\frac{2}{V} \sum_{\mathbf{k}} V_{\mathbf{k}\mathbf{k}'}(\mathbf{Q}) \Delta_{\mathbf{Q}}^{\dagger}(\mathbf{k}) \chi_{\mathbf{Q}}(\mathbf{k}), \quad (6.19)$$

with

$$\chi_{\mathbf{Q}}(\mathbf{k}) = \frac{1}{4E_{\mathbf{Q}}(\mathbf{k})} \left\{ \begin{aligned} & \tanh \frac{\beta [\epsilon_{\mathbf{Q}}^{\circ}(\mathbf{k}) + E_{\mathbf{Q}}(\mathbf{k})]}{2} \\ & - \tanh \frac{\beta [\epsilon_{\mathbf{Q}}^{\circ}(\mathbf{k}) - E_{\mathbf{Q}}(\mathbf{k})]}{2} \end{aligned} \right\}. \quad (6.20)$$

For notational simplicity we shift $\mathbf{Q} \rightarrow \mathbf{Q} + 2\mathbf{K}$, with $\mathbf{K} = (0, K_y)$, which ensures that the dispersion $\epsilon_{\mathbf{Q}}^{\circ}(\mathbf{k})$ is always centered at the origin when $\mathbf{Q} = 0$ independent of the tilt angle θ . Plots of $\chi_{\mathbf{Q}}(\mathbf{k})$ for different center-of-mass momenta \mathbf{Q} are shown in Fig. 6.5. From the figure we see that for zero center-of-mass momentum, corresponding to the regular BCS type pairing, $\chi_{\mathbf{Q}}$ gives a large contribution around the entire Fermi surface $|\mathbf{k}| = k_F$, thus resulting in a large phase-space. The reason for this is that $\epsilon_{\mathbf{Q}}^{\circ}(\mathbf{k}) = 0$ for all \mathbf{k} in this case, giving

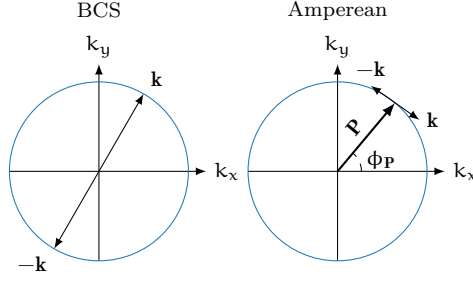


Figure 6.6: The figure shows the momentum space coordinates used when studying the BCS and Amperean cases. While both \mathbf{k} and $-\mathbf{k}$ can reside on the Fermi surface (blue) in the BCS case, it becomes increasingly difficult to place both momenta $\mathbf{P} \pm \mathbf{k}$ close to the Fermi surface when $|\mathbf{k}|$ increases in the Amperean case.

χ_Q a sharp peak at the Fermi level. Increasing Q_x shifts the zeros of $\epsilon_+(\pm\mathbf{k} + \mathbf{Q}/2)$ apart, giving a strong peak only where the Fermi surfaces intersect, thus dramatically reducing the phase-space. The points at which the two Fermi surfaces intersect are brought closer together for increasing Q_x , and coalesce to one point at $Q_x = 2k_F$, leading to an extended peak around the origin. Hence, we have the largest phase-space for $\mathbf{Q} = 0$, and a significant, but smaller phase-space for $|\mathbf{Q}| \approx 2k_F$. We therefore investigate the possibility of pairing at these two center-of-mass momenta, illustrated in Fig. 6.6.

6.4.1 BCS type pairing ($\mathbf{Q} = 0$)

Setting $\mathbf{Q} = 0$ and assuming that the gap M is small compared to the chemical potential μ , the functions $s_{\mathbf{k}}$ and $r_{\mathbf{k}}$ defined after Eq. (6.11) are simplified to $s_{\mathbf{k}} = i|\mathbf{k}|e^{-i\phi_{\mathbf{k}}}$ and $r_{\mathbf{k}} = |\mathbf{k}|$. Assuming that \mathbf{k} and \mathbf{k}' lie close to the Fermi surface, we get the scattering form factor

$$\Lambda_0(\mathbf{k}, \mathbf{k}') \approx -e^{i\phi_{\mathbf{k}} - i\phi_{\mathbf{k}'}} [1 - \sin^2 \theta \sin \phi_{\mathbf{k}} \sin \phi_{\mathbf{k}'}]. \quad (6.21)$$

As seen in Fig. 6.7a) the form factor becomes anisotropic in \mathbf{k} space when the magnetization has an in-plane component. However, the

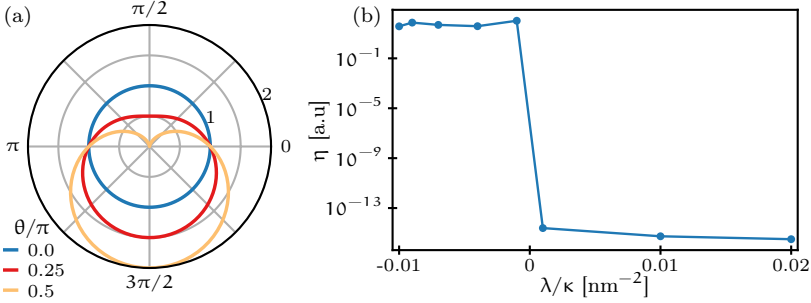


Figure 6.7: (a) Plot of the absolute value of Λ_0 in Eq. (6.21) as a function of $\phi_{\mathbf{k}}$ with $\phi_{\mathbf{k}'} = \pi/2$ for different tilt angles θ . (b) Eigenvalues η of the gap equation Eq. (6.22) as a function of λ .

expression in the square brackets never changes sign, and for $\phi_{\mathbf{k}} = \phi_{\mathbf{k}'}$ the interaction $V_{\mathbf{k}\mathbf{k}'}(0)$ is always positive for $\lambda > 0$. For negative λ , however, the magnon dispersion and thus the magnon propagator can change sign, resulting in a negative interaction potential for certain momentum values. Solving the eigenvalue problem derived from the linearized gap equation [39],

$$\eta \Delta_0^\dagger(\mathbf{k}') = - \left\langle 2V_{\mathbf{k}\mathbf{k}'}(0) \Delta_0^\dagger(\mathbf{k}) \right\rangle_{\mathbf{k}, \text{FS}} \quad (6.22)$$

where $\langle \dots \rangle_{\mathbf{k}, \text{FS}}$ denotes a Fermi surface average, we get the eigenvalues in Fig. 6.7b). The critical temperature is proportional to $e^{c/\eta}$ with some constant c , and we therefore see that we have finite critical temperatures for $\lambda < 0$. For positive λ , however, the eigenvalues are very small, and by inspecting the eigenvectors one finds that these are not actual solutions of the gap equation. Based on numerical calculations we therefore conclude that BCS pairing is possible for $\lambda < 0$ and $\mu > M$, i.e. when the Fermi momentum is finite. Moreover, remembering that the dispersion actually is shifted by \mathbf{K} even when $\mathbf{Q} = 0$, the pairing is of FFLO type whenever the magnetization has a finite in-plane component.

6.4.2 Amperean pairing ($|\mathbf{Q}| = 2k_F$)

For notational simplicity we define the vector $\mathbf{P} = k_F(\cos \phi_P, \sin \phi_P)$, where $k_F = \sqrt{\mu^2 - M^2}/v_F$, such that in the Amperean pairing case $\mathbf{Q} = 2\mathbf{P}$. To zeroth order in momenta at $\mu \gg M$, we get the scattering form factor

$$\Lambda_{2P}(\mathbf{k}, \mathbf{k}') = 1 - \sin^2 \theta \sin^2 \phi_P + \mathcal{O}(|\mathbf{k}|, |\mathbf{k}'|), \quad (6.23)$$

leading to a decrease in the scattering strength for certain center-of-mass momenta when the magnetization has an in-plane component. More importantly, the form factor has the opposite sign compared to the BCS case, and the interaction should therefore be attractive when $\lambda > 0$.

Solving the linearized gap equation numerically [241] we indeed find solutions which are odd in \mathbf{k} , as seen from Fig. 6.8a) and b)

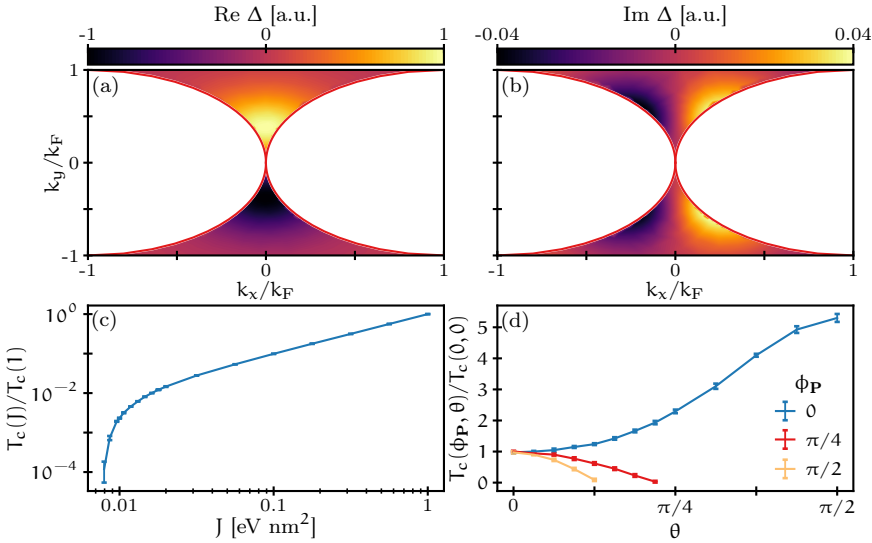


Figure 6.8: (a) Real and (b) imaginary parts of the eigenvalues of the gap equation at the critical temperature. (c) Critical temperature as a function of coupling J , and (d) tilt angle θ for different orientations of \mathbf{P} at $J = 0.01 \text{ eV nm}^2$.

for the real and imaginary part of Δ , where the critical temperature depends on the coupling J as shown in Fig. 6.8c). From Eq. (6.23) we expect the critical temperature to decrease for increasing θ when $0 < \phi_{\mathbf{P}} < \pi$, which agrees with the numerical results in Fig. 6.8d). Hence, whenever the magnetization has an in-plane component, we expect the superconducting pairing to arise for center-of-mass momenta $\mathbf{P} = (\pm k_F, 0)$. From the figure we also see that the critical temperature increases for $\phi_{\mathbf{P}} = 0$, the reason for which is not apparent from the lowest order expression Eq. (6.23), and is probably caused by higher-order terms in $\Lambda_{2\mathbf{P}}$.

6.5 FREQUENCY DEPENDENT GAP SOLUTIONS

When including the frequency dependence of the magnon propagator we can no longer neglect the frequency dependence of the superconducting gap itself. This is evident when writing out the linearized gap equation

$$\begin{aligned} \Delta_{\mathbf{Q}}^{\dagger}(N', \mathbf{k}') &= \frac{J^2 \bar{n}}{\pi V} \sum_{N, \mathbf{k}} \frac{t \Delta_{\mathbf{Q}}^{\dagger}(N, \mathbf{k})}{\left[Nt + i\epsilon_+ \left(\mathbf{k} + \frac{\mathbf{Q}}{2} \right) \right] \left[Nt - i\epsilon_+ \left(-\mathbf{k} + \frac{\mathbf{Q}}{2} \right) \right]} \\ &\times \left[\frac{\omega_{\mathbf{k}-\mathbf{k}'} \Lambda_{\mathbf{Q}}(\mathbf{k}, \mathbf{k}')}{(N - N')^2 t^2 + (2\omega_{\mathbf{k}-\mathbf{k}'})^2} - (k' \rightarrow -k') \right], \end{aligned} \quad (6.24)$$

where we have written the Matsubara frequencies as $\omega_n = Nt$ with $N = 2n + 1$ being odd numbers, and $t = \pi k_B T$ is a temperature parameter. Since the right-hand side of the equation depends on the free frequency parameter N' , the gap must also be frequency dependent. Based on the fact that the gap has the overall symmetry $\Delta_{\mathbf{Q}}(N, \mathbf{k}) = -\Delta_{\mathbf{Q}}(-N, -\mathbf{k})$, we therefore have two possible symmetry channels (see Table 2.1),

$$\Delta_{\mathbf{Q}}(N, \mathbf{k}) = \Delta_{\mathbf{Q}}^e(N, \mathbf{k}) + \Delta_{\mathbf{Q}}^o(N, \mathbf{k}), \quad (6.25)$$

where $\Delta_{\mathbf{Q}}^{e/o}(N, \mathbf{k}) = [\Delta_{\mathbf{Q}}(N, \mathbf{k}) \pm \Delta_{\mathbf{Q}}(-N, \mathbf{k})]/2$ is even (odd) in frequency and odd (even) in momentum.

Including a finite number N_ω and $N_{\mathbf{k}}$ of positive Matsubara frequencies and reciprocal lattice points respectively, we can numerically solve the gap equation as a matrix equation $\Delta = \mathcal{M}\Delta$ by finding the temperature t where the largest eigenvalue of the matrix \mathcal{M} is equal to 1. Here Δ is a vector of length $2N_\omega N_{\mathbf{k}}$ and \mathcal{M} is a $(2N_\omega N_{\mathbf{k}}) \times (2N_\omega N_{\mathbf{k}})$ matrix.

We normalize the eigenvectors such that

$$\begin{aligned} 1 &= \frac{1}{V} \sum_{n=-N_\omega}^{N_\omega} \sum_{\mathbf{k}} |\Delta_{\mathbf{Q}}(2n+1, \mathbf{k})|^2 \\ &= \frac{1}{V} \sum_{n=-N_\omega}^{N_\omega} \sum_{\mathbf{k}} [|\Delta_{\mathbf{Q}}^e(2n+1, \mathbf{k})|^2 + |\Delta_{\mathbf{Q}}^o(2n+1, \mathbf{k})|^2], \end{aligned} \quad (6.26)$$

and define the weight function for frequency index N and symmetry $i = e, o$,

$$w_i(N) = \frac{1}{V} \sum_{\mathbf{k}} [\Delta_{\mathbf{Q}}^i(N, \mathbf{k})]^\dagger \Delta_{\mathbf{Q}}(N, \mathbf{k}) = \frac{1}{V} \sum_{\mathbf{k}} |\Delta_{\mathbf{Q}}^i(N, \mathbf{k})|^2, \quad (6.27)$$

which is an even function of N . Hence, the total weight of each symmetry channel is determined by

$$W_i = \sum_{n=-N_\omega}^{N_\omega} w_i(2n+1), \quad (6.28)$$

which satisfies $W_e + W_o = 1$.

Solving the gap equation numerically in the case of Amperian pairing ($\mathbf{Q} = 2\mathbf{P}$) we find that the odd-frequency channel is the dominating channel, $W_o \gg W_e$, independent of coupling strength, tilt angle and orientation of \mathbf{P} , see Fig. 6.9. The reason for this might be that the interaction is maximized when $\mathbf{k} = 0$, a point which does not contribute to the gap equation for an even frequency, odd momentum state. The gap equation for the odd-frequency gap will therefore get a much larger contribution from the area around $\mathbf{k} = 0$ compared to

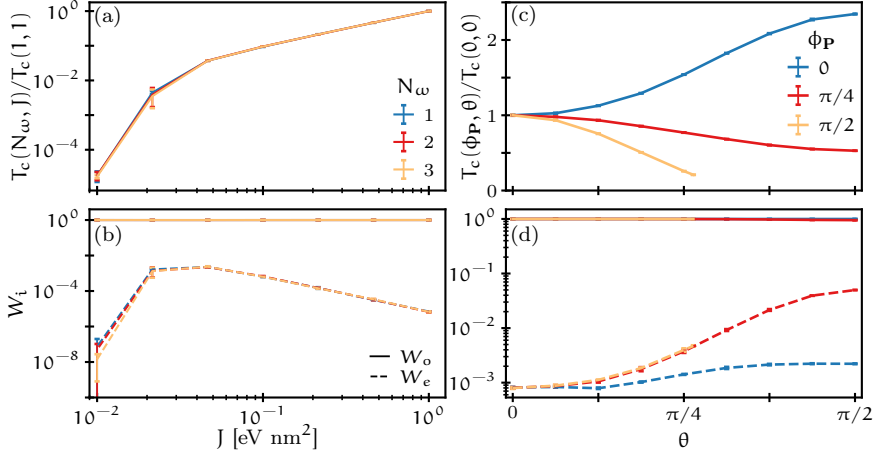


Figure 6.9: Plot of (a) critical temperature and (b) weight functions W_i as functions of coupling J for different N_ω , and (c) critical temperature and (d) weight functions as functions of tilt angle θ for different orientations of \mathbf{P} .

the even-frequency gap, enhancing its value compared to the even-frequency solution. Moreover, it has previously been shown that a finite center-of-mass momentum stabilizes odd-frequency pairing [242–244], consistent with the present results.

The fact that there is close to no change in the results for T_c when increasing N_ω [Fig. 6.9a)] probably reflects the fact that this is not a strong coupling calculation which takes the renormalization of surface state and magnon propagators into account [222]. Without this renormalization, the largest contribution to the gap equation always comes from $N = N' = \pm 1$, independent of N_ω . It would therefore be interesting to perform a strong coupling calculation using e.g. Eliashberg theory [245–247], especially for antiferromagnetic insulators which might have enhanced critical temperatures compared to ferromagnetic insulators [234, 236, 239].

OUTLOOK

In this thesis we have considered the possible superconducting states in the effectively two-dimensional systems occurring in different heterostructures, and in particular on the surface of topological insulators. While the previous chapters have introduced and summarized the work leading to the enclosed research papers, I would now like to take a brief look forward to possible future research.

The first point is rather general and applies to most, if not all the enclosed papers related to topological insulators. When modeling the TI we chose to always include only the surface states in the model. This includes only the most relevant states close to the interface to other materials, and thus simplifies the analysis greatly. It would however be interesting to consider the entire topological insulator, including the insulating bulk, not just to check the robustness of our results, but also in the hope of finding new interesting phenomena.

There are many possible avenues for further research on magnon-mediated superconductivity in TIs coupled to ferromagnetic or antiferromagnetic insulators. First of all one should investigate the possible superconducting states in a strong coupling calculation such as Eliashberg theory. Moreover, it would be interesting to examine what experimental signatures the even- and odd-frequency Amperean pairing states would have by for instance performing transport calculations, or study the Meissner response by deriving and studying the Ginzburg-Landau theory. This could give a means to distinguishing the Amperean state from the BCS state.

Common for the systems studied in Papers [1–5] is the role of spin-orbit coupling in generating interesting superconducting states, both by itself and in cooperation with exchange fields. It will be interesting to see what developments will come in this research venue, both in expanding our knowledge and hopefully in technological applications.

BIBLIOGRAPHY

1. H. G. Hugdal and A. Sudbø,
Physical Review B, **97**, 024515 (2018).
2. M. Amundsen, H. G. Hugdal, A. Sudbø and J. Linder,
Physical Review B, **98**, 144505 (2018).
3. H. G. Hugdal, M. Amundsen, J. Linder and A. Sudbø,
Physical Review B, **99**, 094505 (2019).
4. H. G. Hugdal, S. Rex, F. S. Nogueira and A. Sudbø,
Physical Review B, **97**, 195438 (2018).
5. H. G. Hugdal and A. Sudbø,
Physical Review B, **102**, 125429 (2020).
6. M. Tinkham,
Introduction to Superconductivity 2nd ed.
ISBN: 978-0-486-43503-9
(Dover Publications, Mineola, N.Y, 2004).
7. J. D. Martin,
Physics Today, **72**, 30–37 (2019).
8. P. W. Anderson,
Science, **177**, 393–396 (1972).
9. M. N. Baibich, J. M. Broto, A. Fert, F. N. Van Dau, F. Petroff,
P. Eitenne, G. Creuzet, A. Friederich and J. Chazelas,
Physical Review Letters, **61**, 2472 (1988).
10. G. Binasch, P. Grünberg, F. Saurenbach and W. Zinn,
Physical Review B, **39**, 4828 (1989).
11. The Royal Swedish Academy of Sciences,
The Nobel Prize in Physics 2007 - Information for the public (2007).
<https://www.nobelprize.org/uploads/2018/06/popular-physicsprize2007-1.pdf>.

12. V. L. Ginzburg and E. A. Andryushin,
Superconductivity Revised Ed.
ISBN: 981-238-913-X
(World Scientific Publishing, Singapore, 2004).
13. A. Hirohata, K. Yamada, Y. Nakatani, L.-I. Prejbeanu, B. Diény,
P. Pirro and B. Hillebrands,
Journal of Magnetism and Magnetic Materials, **509**, 166711 (2020).
14. A. Brataas, B. van Wees, O. Klein, G. de Loubens and M. Viret,
Physics Reports, **885**, 1–27 (2020).
15. M. Eschrig,
Physics Today, **64**, 43–49 (2011).
16. J. Linder and J. W. A. Robinson,
Nature Physics, **11**, 307–315 (2015).
17. M. Eschrig,
Reports on Progress in Physics, **78**, 104501 (2015).
18. F. Arute, K. Arya, R. Babbush, D. Bacon, J. C. Bardin, R.
Barends, R. Biswas, S. Boixo, F. G. Brandao, D. A. Buell, *et al.*,
Nature, **574**, 505–510 (2019).
19. K. Fosshem and A. Sudbø,
Superconductivity: Physics and Applications
ISBN: 9780470844526
(Wiley, Chichester, 2004).
20. H. Kamerlingh Onnes,
Communications from the Physical Laboratory at Leyden, **12**, 120
(1911).
21. W. Meissner and R. Ochsenfeld,
Naturwissenschaften, **21**, 787–788 (1933).
22. F. London and H. London,
Proceedings of the Royal Society of London A, **149**, 71–88 (1935).
23. V. L. Ginzburg and L. D. Landau,
Zhurnal Éksperimental'noĭ i Teoreticheskoi Fiziki, **20**, 1064 (1950).

24. A. L. Fetter and J. D. Walecka,
Quantum Theory of Many-Particle Systems
ISBN: 0486428273
(Dover Publications, Mineola, N.Y., 2003).
25. S. Elitzur,
Physical Review D, **12**, 3978 (1975).
26. M. Greiter,
Annals of Physics, **319**, 217–249 (2005).
27. N. R. Poniatowski,
American Journal of Physics, **87**, 436 (2019).
28. D. J. Griffiths,
Introduction to Electrodynamics 4th ed.
ISBN: 978-0-321-85656-2
(Pearson, 2013).
29. A. B. Pippard,
Proceedings of the Royal Society of London, **A216**, 547–568 (1953).
30. A. A. Abrikosov,
Doklady Akademii Nauk SSSR, **86**, 489 (1952).
31. A. A. Abrikosov,
Zhurnal Éksperimental'noĭ i Teoreticheskoi Fiziki, **32**, 1442 (1957).
Soviet Physics JETP **5**, 1174 (1957).
32. E. Maxwell,
Physical Review, **78**, 477 (1950).
33. C. A. Reynolds, B. Serin, W. H. Wright and L. B. Nesbitt,
Physical Review, **78**, 487 (1950).
34. J. Bardeen,
Physical Review, **80**, 567–574 (1950).
35. J. Bardeen, L. N. Cooper and J. R. Schrieffer,
Physical Review, **108**, 1175–1204 (1957).
36. L. N. Cooper,
Physical Review, **104**, 1189–1190 (1956).

37. L. P. Gor'kov,
Zhurnal Éksperimental'noi i Teoreticheskoi Fiziki, **36**, 1918 (1959).
Soviet Physics JETP **36**, 1364 (1959).
38. A. A. Abrikosov, L. P. Gor'kov and I. E. Dzyaloshinski,
Methods of Quantum Field Theory in Statistical Physics
ISBN: 9780486632285
(Dover Publications, New York, 1975).
39. M. Sigrist,
AIP Conference Proceedings, **789**, 165 (2005).
40. A. Altland and B. Simons,
Condensed Matter Field Theory 2nd ed.
ISBN: 978-0-521-76975-4
(Cambridge University Press, Cambridge, 2010).
41. T. Lancaster and S. Blundell,
Quantum Field Theory for the Gifted Amateur
ISBN: 9780191779435
(Oxford University Press, Oxford, 2014).
42. J. W. Negele and H. Orland,
Quantum Many-Particle Systems
ISBN: 0-7382-0052-2
(Westview Press, Boulder, Colorado, 1998).
43. H. Bruus and K. Flensberg,
Many-Body Quantum Theory in Condensed Matter Physics
ISBN: 978-0-19-856633-5
(Oxford University Press, Oxford, 2004).
44. J. Linder and A. V. Balatsky,
Reviews of Modern Physics, **91**, 045005 (2019).
45. V. L. Berezinskii,
Pis'ma v Zhurnal Éksperimental'noi i Teoreticheskoi Fiziki, **20**, 628
(1974).
JETP Letters **20**, 287 (1974).

46. A. Balatsky and E. Abrahams,
Physical Review B, **45**, 13125–13128 (1992).
47. E. Abrahams, A. Balatsky, D. J. Scalapino and J. R. Schrieffer,
Physical Review B, **52**, 1271–1278 (1995).
48. F. S. Bergeret, A. F. Volkov and K. B. Efetov,
Reviews of Modern Physics, **77**, 1321–1373 (2005).
49. Y. Tanaka, M. Sato and N. Nagaosa,
Journal of the Physical Society of Japan, **81**, 011013 (2012).
50. C. Triola and A. V. Balatsky,
Physical Review B, **94**, 094518 (2016).
51. P. Fulde and R. A. Ferrell,
Physical Review, **135**, A550 (1964).
52. I. A. Larkin and Y. N. Ovchinnikov,
Zhurnal Éksperimental'noĭ i Teoreticheskoi Fiziki, **47**, 1136 (1964).
Soviet Physics JETP **20**, 762 (1965).
53. F. Wegner,
Supermathematics and its Applications in Statistical Physics
ISBN: 978-3-662-49168-3
(Springer-Verlag Berlin Heidelberg, 2016).
54. F. N. Krohg and A. Sudbø,
Physical Review B, **98**, 014510 (2018).
55. J. A. Ouassou.
Full Proximity Effect in Spin-Textured Superconductor/Ferromagnet Bilayers
Specialization Project (Norwegian University of Science and Technology, 2014).
56. C. Kittel,
Introduction to Solid State Physics 8th ed.
ISBN: 9780471415268
(Wiley, Hoboken, N.J., 2005).

57. N. W. Ashcroft and N. D. Mermin,
Solid State Physics
ISBN: 0030839939
(Holt, Rinehart and Winston, New York, 1976).
58. F. Steglich, J. Aarts, C. D. Bredl, W. Lieke, D. Meschede, W. Franz and H. Schäfer,
Physical Review Letters, **43**, 1892 (1979).
59. M. Sigrist and K. Ueda,
Reviews of Modern Physics, **63**, 239–311 (1991).
60. J. Bednorz and K. Müller,
Zeitschrift für Physik B: Condensed Matter, **64**, 189 (1986).
61. P. Monthoux, A. V. Balatsky and D. Pines,
Physical Review Letters, **67**, 3448 (1991).
62. P. Monthoux and D. Pines,
Physical Review Letters, **69**, 961 (1992).
63. P. Monthoux, A. V. Balatsky and D. Pines,
Physical Review B, **46**, 14803 (1992).
64. W. Kohn and J. M. Luttinger,
Physical Review Letters, **15**, 524 (1965).
65. N. D. Mermin and H. Wagner,
Physical Review Letters, **17**, 1133–1136 (1966).
66. H. Nishimori and G. Ortiz,
Elements of Phase Transitions and Critical Phenomena
ISBN: 9780198754084
(Oxford University Press, Oxford, 2015).
67. V. L. Berezinskii,
Zhurnal Éksperimental'noĭ i Teoreticheskoi Fiziki, **59**, 907 (1970).
Soviet Physics JETP **32**, 493 (1971).
68. V. L. Berezinskii,
Zhurnal Éksperimental'noĭ i Teoreticheskoi Fiziki, **61**, 1144 (1971).
Soviet Physics JETP **34**, 610 (1972).

69. J. M. Kosterlitz and D. J. Thouless,
Journal of Physics C: Solid State Physics, **5**, L124 (1972).
70. J. M. Kosterlitz and D. J. Thouless,
Journal of Physics C: Solid State Physics, **6**, 1181–1203 (1973).
71. Class for Physics of the Royal Swedish Academy of Sciences,
Topological Phase Transition and Topological Phases of Matter (2016).
<https://www.nobelprize.org/uploads/2018/06/advanced-physicsprize2016.pdf>.
72. J. Pearl,
Applied Physics Letters, **5**, 65 (1964).
73. B. I. Halperin and D. R. Nelson,
Journal of Low Temperature Physics, **36**, 599–616 (1979).
74. M. R. Beasley, J. E. Mooij and T. P. Orlando,
Physical Review Letters, **42**, 1165–1168 (1979).
75. K. Epstein, A. M. Goldman and A. M. Kadin,
Physical Review Letters, **47**, 534–537 (1981).
76. S. Doniach and B. A. Huberman,
Physical Review Letters, **42**, 1169–1172 (1979).
77. Y. S. Kim, M. Brahlek, N. Bansal, E. Edrey, G. A. Kapilevich,
K. Iida, M. Tanimura, Y. Horibe, S.-W. Cheong and S. Oh,
Physical Review B, **84**, 073109 (2011).
78. A. A. Taskin, S. Sasaki, K. Segawa and Y. Ando,
Physical Review Letters, **109**, 066803 (2012).
79. S. Raghu, S. A. Kivelson and D. J. Scalapino,
Physical Review B, **81**, 224505 (2010).
80. S. Maiti and A. V. Chubukov,
AIP Conference Proceedings, **1550**, 3 (2013).
81. A. V. Chubukov and M. Yu Kagan,
Journal of Physics: Condensed Matter, **1**, 3135–3138 (1989).
82. J. M. Luttinger and W. Kohn,
Physical Review, **97**, 869–883 (1955).

83. J. R. Schrieffer and P. A. Wolff,
Physical Review, **149**, 491 (1966).
84. S. Bravyi, D. P. DiVincenzo and D. Loss,
Annals of Physics, **326**, 2793–2826 (2011).
85. E. Lake, C. Webb, D. A. Pesin and O. A. Starykh,
Physical Review B, **93**, 214516 (2016).
86. S. Raghu and S. A. Kivelson,
Physical Review B, **83**, 094518 (2011).
87. A. V. Chubukov,
Physical Review B, **48**, 1097–1104 (1993).
88. M. Y. Kagan and A. V. Chubukov,
Pis'ma v Zhurnal Éksperimental'noĭ i Teoreticheskoi Fiziki, **50**, 483 (1989).
JETP Letters **50**, 517 (1989).
89. A. Manchon, H. C. Koo, J. Nitta, S. M. Frolov and R. A. Duine,
Nature Materials, **14**, 871–882 (2015).
90. B. H. Bransden and C. J. Joachain,
Quantum Mechanics 2nd ed.
ISBN: 0-582-35691-1
(Pearson - Prentice Hall, Harlow, 2000).
91. F. Herman, C. D. Kuglin, K. F. Cuff and R. L. Kortum,
Physical Review Letters, **11**, 541–545 (1963).
92. A. Ito and K. Tanaka,
Applications of Carbon Nanotubes and Graphene in Spin Electronics in Carbon Nanotubes and Graphene
2nd ed.
(Elsevier, 2014).
ISBN: 9780080982328.
93. Y. A. Bychkov and E. I. Rashba,
Pis'ma v Zhurnal Éksperimental'noĭ i Teoreticheskoi Fiziki, **39**, 66 (1984).
JETP Letters **39**, 78 (1984).

94. O. Vafek and L. Wang,
Physical Review B, **84**, 172501 (2011).
95. L. Wang and O. Vafek,
Physica C, **497**, 6–18 (2014).
96. N. Reyren, S. Thiel, A. D. Caviglia, L. F. Kourkoutis, G. Hammerl, C. Richter, C. W. Schneider, T. Kopp, A.-S. Rüetschi, D. Jaccard, M. Gabay, D. A. Muller, J.-M. Triscone and J. Mannhart,
Science, **317**, 1196–1199 (2007).
97. A. Brinkman, M. Huijben, M. van Zalk, J. Huijben, U. Zeitler, J. C. Maan, W. G. van der Wiel, G. Rijnders, D. H. A. Blank and H. Hilgenkamp,
Nature Materials, **6**, 493–496 (2007).
98. A. D. Caviglia, S. Gariglio, N. Reyren, D. Jaccard, T. Schneider, M. Gabay, S. Thiel, G. Hammerl, J. Mannhart and J.-M. Triscone,
Nature, **456**, 624–627 (2008).
99. S. Gariglio, N. Reyren, A. D. Caviglia and J.-M. Triscone,
Journal of Physics: Condensed Matter, **21**, 164213 (2009).
100. M. Sachs, D. Rakhmilevitch, M. Ben Shalom, S. Shefler, A. Palevski and Y. Dagan,
Physica C: Superconductivity and its Applications, **470**, S746–S748 (2010).
101. D. A. Dikin, M. Mehta, C. W. Bark, C. M. Folkman, C. B. Eom and V. Chandrasekhar,
Physical Review Letters, **107**, 056802 (2011).
102. J. A. Bert, B. Kalisky, C. Bell, M. Kim, Y. Hikita, H. Y. Hwang and K. A. Moler,
Nature Physics, **7**, 767–771 (2011).
103. L. Li, C. Richter, J. Mannhart and R. C. Ashoori,
Nature Physics, **7**, 762–766 (2011).

104. M. Ben Shalom, M. Sachs, D. Rakhmilevitch, A. Palevski and Y. Dagan,
Physical Review Letters, **104**, 126802 (2010).
105. A. D. Caviglia, M. Gabay, S. Gariglio, N. Reyren, C. Cancellieri and J.-M. Triscone,
Physical Review Letters, **104**, 126803 (2010).
106. L. P. Gor'kov and E. I. Rashba,
Physical Review Letters, **87**, 037004 (2001).
107. V. Barzykin and L. P. Gor'kov,
Physical Review Letters, **89**, 227002 (2002).
108. D. F. Agterberg and R. P. Kaur,
Physical Review B, **75**, 064511 (2007).
109. F. Loder, A. P. Kampf and T. Kopp,
Journal of Physics: Condensed Matter, **25**, 362201 (2013).
110. A. Auerbach,
Interacting Electrons and Quantum Magnetism
ISBN: 978-1-4612-6928-1
(Springer, 1994).
111. E. H. Hall,
American Journal of Mathematics, **2**, 287–292 (1879).
112. M. I. D'yakonov and V. I. Perel',
Pis'ma v Zhurnal Éksperimental'noi i Teoreticheskoi Fiziki, **13**, 657 (1971).
JETP Letters **13**, 467 (1971).
113. M. I. Dyakonov and V. I. Perel,
Physics Letters A, **35**, 459 (1971).
114. J. E. Hirsch,
Physical Review Letters, **83**, 1834 (1999).
115. S. Murakami, N. Nagaosa and S.-C. Zhang,
Science, **301**, 1348 (2003).

116. J. Sinova, D. Culcer, Q. Niu, N. A. Sinitsyn, T. Jungwirth and A. H. MacDonald,
Physical Review Letters, **92**, 126603 (2004).
117. Y. K. Kato, R. C. Myers, A. C. Gossard and D. D. Awschalom,
Science, **306**, 1910 (2004).
118. J. Wunderlich, B. Kaestner, J. Sinova and T. Jungwirth,
Physical Review Letters, **94**, 047204 (2005).
119. K. von Klitzing, G. Dorda and M. Pepper,
Physical Review Letters, **45**, 494–497 (1980).
120. J. E. Avron, D. Osadchy and R. Seiler,
Physics Today, **56**, 38–42 (2003).
121. D. J. Thouless, M. Kohmoto, M. P. Nightingale and M. den Nijs,
Physical Review Letters, **49**, 405–408 (1982).
122. C. Day,
Physics Today, **61**, 19–23 (2008).
123. M. Z. Hasan and C. L. Kane,
Reviews of Modern Physics, **82**, 3045–3067 (2010).
124. X.-L. Qi and S.-C. Zhang,
Physics Today, **63**, 33 (2010).
125. X.-L. Qi and S.-C. Zhang,
Reviews of Modern Physics, **83**, 1057–1110 (2011).
126. C. L. Kane and E. J. Mele,
Physical Review Letters, **95**, 226801 (2005).
127. B. A. Bernevig and S.-C. Zhang,
Physical Review Letters, **96**, 106802 (2006).
128. J. E. Moore,
Nature, **464**, 194 (2010).
129. T. Wehling, A. Black-Schaffer and A. Balatsky,
Advances in Physics, **63**, 1–76 (2014).
130. C. L. Kane and E. J. Mele,
Physical Review Letters, **95**, 146802 (2005).

131. B. A. Bernevig, T. L. Hughes and S.-C. Zhang,
Science, **314**, 1757–1761 (2006).
132. M. König, S. Wiedmann, C. Brüne, A. Roth, H. Buhmann, L. W. Molenkamp, X.-L. Qi and S.-C. Zhang,
Science, **318**, 766–771 (2007).
133. L. Fu, C. L. Kane and E. J. Mele,
Physical Review Letters, **98**, 106803 (2007).
134. J. E. Moore and L. Balents,
Physical Review B, **75**, 121306(R) (2007).
135. R. Roy,
Physical Review B, **79**, 195322 (2009).
136. J. C. Y. Teo, L. Fu and C. L. Kane,
Physical Review B, **78**, 045426 (2008).
137. H. Zhang, C.-X. Liu, X.-L. Qi, X. Dai, Z. Fang and S.-C. Zhang,
Nature Physics, **5**, 438–442 (2009).
138. D. Hsieh, D. Qian, L. Wray, Y. Xia, Y. S. Hor, R. J. Cava and M. Z. Hasan,
Nature, **452**, 970–974 (2008).
139. Y. Xia, D. Qian, D. Hsieh, L. Wray, A. Pal, H. Lin, A. Bansil, D. Grauer, Y. S. Hor, R. J. Cava and M. Z. Hasan,
Nature Physics, **5**, 398–402 (2009).
140. Y. L. Chen, J. G. Analytis, J.-H. Chu, Z. K. Liu, S.-K. Mo, X. L. Qi, H. J. Zhang, D. H. Lu, X. Dai, Z. Fang, S. C. Zhang, I. R. Fisher, Z. Hussain and Z.-X. Shen,
Science, **325**, 178–182 (2009).
141. C. Brüne, C. X. Liu, E. G. Novik, E. M. Hankiewicz, H. Buhmann, Y. L. Chen, X. L. Qi, Z. X. Shen, S. C. Zhang and L. W. Molenkamp,
Physical Review Letters, **106**, 126809 (2011).
142. P. A. M. Dirac,
Proceedings of the Royal Society of London A: Mathematical, Physical and Engineering Sciences, **117**, 610–624 (1928).

143. S.-Q. Shen,
Topological Insulators: Dirac Equation in Condensed Matters
ISBN: 978-3-642-32858-9
(Springer-Verlag, Berlin Heidelberg, 2012).
144. C. L. Kane,
*Topological band theory and the Z_2 invariant
in Topological Insulators*
(eds. M. Franz and L. Molenkamp)
(Elsevier, 2013).
ISBN: 9780444633149.
145. J. K. Asbóth, L. Oroszlány and A. Pályi,
A Short Course on Topological Insulators
ISBN: 978-3-319-25607-8
(Springer, Cham, 2015).
146. L. Fu and C. L. Kane,
Physical Review B, **76**, 045302 (2007).
147. R. Roy,
Physical Review B, **79**, 195321 (2009).
148. C.-X. Liu, X.-L. Qi, H. Zhang, X. Dai, Z. Fang and S.-C. Zhang,
Physical Review B, **82**, 045122 (2010).
149. X.-L. Qi, T. L. Hughes and S.-C. Zhang,
Physical Review B, **78**, 195424 (2008).
150. A. Zee,
Quantum Field Theory in a Nutshell 2nd ed.
ISBN: 9780691140346
(Princeton University Press, Princeton, N.J, 2010).
151. Y. Tokura, K. Yasuda and A. Tsukazaki,
Nature Reviews Physics, **1**, 126 (2019).
152. P. Wei, F. Katmis, B. A. Assaf, H. Steinberg, P. Jarillo-Herrero,
D. Heiman and J. S. Moodera,
Physical Review Letters, **110**, 186807 (2013).

153. Q. I. Yang, M. Dolev, L. Zhang, J. Zhao, A. D. Fried, E. Schemm, M. Liu, A. Palevski, A. F. Marshall, S. H. Risbud and A. Kapitulnik,
Physical Review B, **88**, 081407(R) (2013).
154. F. Katmis, V. Lauter, F. S. Nogueira, B. A. Assaf, M. E. Jamer, P. Wei, B. Satpati, J. W. Freeland, I. Eremin, D. Heiman, P. Jarillo-Herrero and J. S. Moodera,
Nature, **533**, 513 (2016).
155. C. Tang, C. Z. Chang, G. Zhao, Y. Liu, Z. Jiang, C. X. Liu, M. R. McCartney, D. J. Smith, T. Chen, J. S. Moodera and J. Shi,
Science Advances, **3**, e1700307 (2017).
156. J. Choi, S. Choi, J. Choi, Y. Park, H. M. Park, H. W. Lee, B. C. Woo and S. Cho,
Physica Status Solidi B, **241**, 1541–1544 (2004).
157. Q. Liu, C.-X. Liu, C. Xu, X.-L. Qi and S.-C. Zhang,
Physical Review Letters, **102**, 156603 (2009).
158. Y. S. Hor, P. Roushan, H. Beidenkopf, J. Seo, D. Qu, J. G. Checkelsky, L. A. Wray, D. Hsieh, Y. Xia, S. Y. Xu, D. Qian, M. Z. Hasan, N. P. Ong, A. Yazdani and R. J. Cava,
Physical Review B, **81**, 195203 (2010).
159. Y. L. Chen, J.-H. Chu, J. G. Analytis, Z. K. Liu, K. Igarashi, H.-H. Kuo, X. L. Qi, S. K. Mo, R. G. Moore, D. H. Lu, M. Hashimoto, T. Sasagawa, S. C. Zhang, I. R. Fisher, Z. Hussain and Z. X. Shen,
Science, **329**, 659–662 (2010).
160. L. A. Wray, S. Y. Xu, Y. Xia, D. Hsieh, A. V. Fedorov, Y. S. Hor, R. J. Cava, A. Bansil, H. Lin and M. Z. Hasan,
Nature Physics, **7**, 32–37 (2011).
161. S. Y. Xu, M. Neupane, C. Liu, D. Zhang, A. Richardella, L. Andrew Wray, N. Alidoust, M. Leandersson, T. Balasubramanian, J. Sánchez-Barriga, *et al.*,
Nature Physics, **8**, 616–622 (2012).

162. C.-Z. Chang, J. Zhang, M. Liu, Z. Zhang, X. Feng, K. Li, L.-L. Wang, X. Chen, X. Dai, Z. Fang, X.-L. Qi, S.-C. Zhang, Y. Wang, K. He, X.-C. Ma and Q. -K. Xue,
Advanced Materials, **25**, 1065–1070 (2013).
163. X. Kou, L. He, M. Lang, Y. Fan, K. Wong, Y. Jiang, T. Nie, W. Jiang, P. Upadhyaya, Z. Xing, Y. Wang, F. Xiu, R. N. Schwartz and K. L. Wang,
Nano Letters, **13**, 4587–4593 (2013).
164. X. Kou, M. Lang, Y. Fan, Y. Jiang, T. Nie, J. Zhang, W. Jiang, Y. Wang, Y. Yao, L. He and K. L. Wang,
ACS Nano, **7**, 9205–9212 (2013).
165. M. Li, C. Z. Chang, L. Wu, J. Tao, W. Zhao, M. H. Chan, J. S. Moodera, J. Li and Y. Zhu,
Physical Review Letters, **114**, 146802 (2015).
166. L. Zhang, D. Zhao, Y. Zang, Y. Yuan, G. Jiang, M. Liao, D. Zhang, K. He, X. Ma and Q. Xue,
APL Materials, **5**, 076106 (2017).
167. J. Teng, N. Liu and Y. Li,
Journal of Semiconductors, **40**, 081507 (2019).
168. W. Buckel and R. Kleiner,
Superconductivity 2nd ed.
ISBN: 3-527-40349-3
(Wiley-VCH, Weinheim, 2004).
169. J. F. Annet,
Superconductivity, Superfluidity and Condensates
ISBN: 0-19-850756-9
(Oxford University Press, 2004).
170. A. I. Buzdin,
Reviews of Modern Physics, **77**, 935–976 (2005).

171. V. Chandrasekhar,
Proximity-Coupled Systems: Quasiclassical Theory of Superconductivity
in *Superconductivity: Conventional and Unconventional Superconductors*
(eds. K. H. Bennemann and J. B. Ketterson)
(Springer-Verlag Berlin Heidelberg, 2008).
ISBN: 9783540732532.
172. B. Josephson,
Physics Letters, **1**, 251–253 (1962).
173. J. B. Ketterson and S. N. Song,
Superconductivity
ISBN: 0521565626
(Cambridge University Press, Cambridge, 1999).
174. L. Fu and C. L. Kane,
Physical Review Letters, **100**, 096407 (2008).
175. G. E. Volovik,
Pis'ma v Zhurnal Éksperimental'noi i Teoreticheskoi Fiziki, **70**, 601
(1999).
JETP Letters **70**, 609 (1999).
176. N. Read and D. Green,
Physical Review B, **61**, 10267 (2000).
177. D. A. Ivanov,
Physical Review Letters, **86**, 268 (2001).
178. A. Y. Kitaev,
Annals of Physics, **303**, 2–30 (2003).
179. G. Moore and N. Read,
Nuclear Physics B, **360**, 362–396 (1991).
180. C. Nayak, S. H. Simon, A. Stern, M. Freedman and S. Das
Sarma,
Reviews of Modern Physics, **80**, 1083–1159 (2008).

181. J. Alicea,
Reports on Progress in Physics, **75**, 076501 (2012).
182. C. W. Beenakker,
Annual Review of Condensed Matter Physics, **4**, 113–136 (2013).
183. B. Sacépé, J. B. Oostinga, J. Li, A. Ubaldini, N. J. Couto, E. Giannini and A. F. Morpurgo,
Nature Communications, **2**, 575 (2011).
184. M. Veldhorst, M. Snelder, M. Hoek, T. Gang, V. K. Guduru, X. L. Wang, U. Zeitler, W. G. van der Wiel, A. A. Golubov, H. Hilgenkamp and A. Brinkman,
Nature Materials, **11**, 417 (2012).
185. M.-X. Wang, C. Liu, J.-P. Xu, F. Yang, L. Miao, M.-Y. Yao, C. L. Gao, C. Shen, X. Ma, X. Chen, Z.-A. Xu, Y. Liu, S.-C. Zhang, D. Qian, J.-F. Jia and Q.-K. Xue,
Science, **336**, 52–55 (2012).
186. F. Yang, Y. Ding, F. Qu, J. Shen, J. Chen, Z. Wei, Z. Ji, G. Liu, J. Fan, C. Yang, T. Xiang and L. Lu,
Physical Review B, **85**, 104508 (2012).
187. L. Maier, J. B. Oostinga, D. Knott, C. Brüne, P. Virtanen, G. Tkachov, E. M. Hankiewicz, C. Gould, H. Buhmann and L. W. Molenkamp,
Physical Review Letters, **109**, 186806 (2012).
188. P. Zareapour, A. Hayat, S. Y. F. Zhao, M. Kreshchuk, A. Jain, D. C. Kwok, N. Lee, S.-W. Cheong, Z. Xu, A. Yang, G. D. Gu, S. Jia, R. J. Cava and K. S. Burch,
Nature Communications, **3**, 1056 (2012).
189. E. Wang, H. Ding, A. V. Fedorov, W. Yao, Z. Li, Y.-F. Lv, K. Zhao, L.-G. Zhang, Z. Xu, J. Schneeloch, R. Zhong, S.-H. Ji, L. Wang, K. He, X. Ma, G. Gu, H. Yao, Q.-K. Xue, X. Chen and S. Zhou,
Nature Physics, **9**, 621–625 (2013).

190. I. Sochnikov, A. J. Bestwick, J. R. Williams, T. M. Lippman, I. R. Fisher, D. Goldhaber-Gordon, J. R. Kirtley and K. A. Moler, *Nano Letters*, **13**, 3086 (2013).
191. S. Cho, B. Dellabetta, A. Yang, J. Schneeloch, Z. Xu, T. Valla, G. Gu, M. J. Gilbert and N. Mason, *Nature Communications*, **4**, 1689 (2013).
192. S.-Y. Xu, N. Alidoust, I. Belopolski, A. Richardella, C. Liu, M. Neupane, G. Bian, S.-H. Huang, R. Sankar, C. Fang, B. Dellabetta, W. Dai, Q. Li, M. J. Gilbert, F. Chou, N. Samarth and M. Z. Hasan, *Nature Physics*, **10**, 943–950 (2014).
193. I. Sochnikov, L. Maier, C. A. Watson, J. R. Kirtley, C. Gould, G. Tkachov, E. M. Hankiewicz, C. Brüne, H. Buhmann, L. W. Molenkamp and K. A. Moler, *Physical Review Letters*, **114**, 066801 (2015).
194. J. Wiedenmann, E. Bocquillon, R. S. Deacon, S. Hartinger, O. Herrmann, T. M. Klapwijk, L. Maier, C. Ames, C. Brüne, C. Gould, A. Oiwa, K. Ishibashi, S. Tarucha, H. Buhmann and L. W. Molenkamp, *Nature Communications*, **7**, 10303 (2016).
195. C. X. Trang, N. Shimamura, K. Nakayama, S. Souma, K. Sugawara, I. Watanabe, K. Yamauchi, T. Oguchi, K. Segawa, T. Takahashi, Y. Ando and T. Sato, *Nature Communications*, **11**, 159 (2020).
196. Y. Tanaka, T. Yokoyama and N. Nagaosa, *Physical Review Letters*, **103**, 107002 (2009).
197. T. D. Stanescu, J. D. Sau, R. M. Lutchyn and S. Das Sarma, *Physical Review B*, **81**, 241310(R) (2010).
198. J. Linder, Y. Tanaka, T. Yokoyama, A. Sudbø and N. Nagaosa, *Physical Review Letters*, **104**, 067001 (2010).
199. J. Linder, Y. Tanaka, T. Yokoyama, A. Sudbø and N. Nagaosa, *Physical Review B*, **81**, 184525 (2010).

200. A. M. Black-Schaffer,
Physical Review B, **83**, 060504(R) (2011).
201. M. Lababidi and E. Zhao,
Physical Review B, **83**, 184511 (2011).
202. A. M. Black-Schaffer and A. V. Balatsky,
Physical Review B, **86**, 144506 (2012).
203. T. Yokoyama,
Physical Review B, **86**, 075410 (2012).
204. A. M. Black-Schaffer and A. V. Balatsky,
Physical Review B, **87**, 220506(R) (2013).
205. G. Tkachov,
Physical Review B, **87**, 245422 (2013).
206. G. Tkachov and E. M. Hankiewicz,
Physica Status Solidi B, **250**, 215–232 (2013).
207. K. D. Usadel,
Physical Review Letters, **25**, 507–509 (1970).
208. A. Zyuzin, M. Alidoust and D. Loss,
Physical Review B, **93**, 214502 (2016).
209. I. V. Bobkova, A. M. Bobkov, A. A. Zyuzin and M. Alidoust,
Physical Review B, **94**, 134506 (2016).
210. H. G. Hugdal, J. Linder and S. H. Jacobsen,
Physical Review B, **95**, 235403 (2017).
211. J. A. Krieger, A. Pertsova, S. R. Giblin, M. Döbeli, T. Prokscha,
C. W. Schneider, A. Suter, T. Hesjedal, A. V. Balatsky and Z.
Salman,
Physical Review Letters, **125**, 026802 (2020).
212. Y. Takane and R. Ando,
Journal of the Physical Society of Japan, **83**, 014706 (2014).
213. M. J. Park, J. Yang, Y. Kim and M. J. Gilbert,
Physical Review B, **96**, 064518 (2017).

214. N. Sedlmayr, E. W. Goodwin, M. Gottschalk, I. M. Dayton, C. Zhang, E. Huemiller, R. Loloee, T. C. Chasapis, M. Salehi, N. Koirala, M. G. Kanatzidis, S. Oh, D. J. V. Harlingen, A. Levchenko and S. H. Tessmer,
Dirac surface states in superconductors: a dual topological proximity effect (2018).
arXiv: 1805.12330.
215. T. Moriya, Y. Takahashi, K. Ueda, T. Moriya, Y. Takahashi and K. Ueda,
Journal of The Physical Society of Japan, **59**, 2905 (1990).
216. D. Pines,
Journal of Physics and Chemistry of Solids, **54**, 1447 (1993).
217. T. Moriya and K. Ueda,
Journal of the Physical Society of Japan, **63**, 1871 (1994).
218. T. Moriya and K. Ueda,
Advances in Physics, **49**, 555–606 (2000).
219. T. Moriya and K. Ueda,
Reports on Progress in Physics, **66**, 1299 (2003).
220. T. Moriya,
Proceedings of the Japan Academy, Series B, **82**, 1–16 (2006).
221. X. Lu and D. Sénéchal,
Physical Review B, **101**, 054512 (2020).
222. M. Kargarian, D. K. Efimkin and V. Galitski,
Physical Review Letters, **117**, 076806 (2016).
223. S.-S. Lee, P. A. Lee and T. Senthil,
Physical Review Letters, **98**, 067006 (2007).
224. D. J. Scalapino,
Reviews of Modern Physics, **84**, 1383 (2012).
225. G. R. Stewart,
Advances in Physics, **66**, 75–196 (2017).
226. T. R. Kirkpatrick, D. Belitz, T. Vojta and R. Narayanan,
Physical Review Letters, **87**, 127003 (2001).

227. H. Suhl,
Physical Review Letters, **87**, 167007 (2001).
228. T. R. Kirkpatrick and D. Belitz,
Physical Review B, **67**, 024515 (2003).
229. N. Karchev,
Physical Review B, **67**, 054416 (2003).
230. R. Kar, T. Goswami, B. C. Paul and A. Misra,
AIP Advances, **4**, 087126 (2014).
231. H. Funaki and H. Shimahara,
Journal of the Physical Society of Japan, **83**, 123704 (2014).
232. X. Gong, M. Kargarian, A. Stern, D. Yue, H. Zhou, X. Jin, M. Victor, V. M. Yakovenko, J. Xia, V. M. Galitski, V. M. Yakovenko and J. Xia,
Science Advances, **3**, e1602579 (2017).
233. N. Rohling, E. L. Fjærbu and A. Brataas,
Physical Review B, **97**, 115401 (2018).
234. E. Erlandsen, A. Kamra, A. Brataas and A. Sudbø,
Physical Review B, **100**, 100503(R) (2019).
235. E. L. Fjærbu, N. Rohling and A. Brataas,
Physical Review B, **100**, 125432 (2019).
236. E. Erlandsen and A. Sudbø,
Schwinger boson study of superconductivity mediated by antiferromagnetic spin fluctuations (2020).
arXiv: 2009.07862.
237. Ø. Johansen, A. Kamra, C. Ulloa, A. Brataas and R. A. Duine,
Physical Review Letters, **123**, 167203 (2019).
238. A. Kamra, E. Thingstad, G. Rastelli, R. A. Duine, A. Brataas, W. Belzig and A. Sudbø,
Physical Review B, **100**, 174407 (2019).
239. E. Erlandsen, A. Brataas and A. Sudbø,
Physical Review B, **101**, 094503 (2020).

240. S. Rex, F. S. Nogueira and A. Sudbø,
Physical Review B, **95**, 155430 (2017).
241. B. Nijholt, J. Weston, J. Hoofwijk and A. Akhmerov,
Adaptive: parallel active learning of mathematical functions (2020).
242. P. Coleman, E. Miranda and A. Tsvetik,
Physical Review Letters, **70**, 2960–2963 (1993).
243. P. Coleman, E. Miranda and A. Tsvetik,
Physica B, **186-188**, 362–364 (1993).
244. P. Coleman, E. Miranda and A. Tsvetik,
Physical Review B, **49**, 8955 (1994).
245. G. M. Eliashberg,
Zhurnal Éksperimental'noĭ i Teoreticheskoi Fiziki, **38**, 966 (1960).
Soviet Physics JETP **11**, 696 (1960).
246. G. M. Eliashberg,
Zhurnal Éksperimental'noĭ i Teoreticheskoi Fiziki, **39**, 1437 (1960).
Soviet Physics JETP **12**, 1000 (1961).
247. G. D. Mahan,
Many-Particle Physics 3rd ed.
ISBN: 0306463385
(Kluwer Academic / Plenum Publishers, New York, 2000).
248. J. P. Ellis,
Computer Physics Communications, **210**, 103–123 (2017).

ABBREVIATIONS

2D two-dimensional.

2DEG 2D electron gas.

3D three-dimensional.

AFMI antiferromagnetic insulator.

BCS Bardeen-Cooper-Schrieffer.

BKT Berezinskii-Kosterlitz-Thouless.

c.c. complex conjugate.

FFLO Fulde-Ferrel-Larkin-Ovchinnikov.

FMI ferromagnetic insulator.

GL Ginzburg-Landau.

h.c. Hermitian conjugate.

HS Hubbard-Stratonovich.

QHE quantum Hall effect.

QSHE quantum spin Hall effect.

S superconductor.

SHE spin Hall effect.

SOC spin-orbit coupling.

TI topological insulator.

APPENDIX

A

PATH INTEGRAL FORMALISM

We here give a brief introduction to the many-body path integral formalism, meant mostly as a reference, following the treatment in Altland and Simons [40] and Lancaster and Blundell [41].

The Schrödinger equation describes the evolution of a particle,

$$i\partial_t |\psi\rangle = \hat{H} |\psi\rangle, \quad (\text{A.1})$$

where \hat{H} is the Hamiltonian operator. Assuming that the Hamiltonian has no explicit time-dependence, we can integrate the Schrödinger equation between an initial and final time t_i and t_f respectively,

$$|\psi(t_f)\rangle = e^{-i\hat{H}(t_f-t_i)} |\psi(t_i)\rangle \equiv U(t_f, t_i) |\psi(t_i)\rangle, \quad (\text{A.2})$$

where we have defined the unitary time evolution operator $U(t', t) = e^{-i\hat{H}(t'-t)}$, which describes the evolution of state $|\psi\rangle$ from time t to t' . From this definition it is clear that U has the property $U(t'', t')U(t', t) = U(t'', t)$, from which we see that we can write $e^{-i\hat{H}(t_f-t_i)} = \left[e^{-i\hat{H}\Delta t} \right]^N$, where the time has been split into N smaller time intervals $\Delta t = (t_f - t_i)/N$.

This can be used when calculating for instance the amplitude A of a particle going from coordinate q_i at time $t_i = 0$ to coordinate q_f at time $t_f = t$,

$$\begin{aligned} A &= \langle q_f | U(t, 0) | q_i \rangle = \langle q_f | \left[e^{-i\hat{H}\Delta t} \right]^N | q_i \rangle \\ &= \langle q_f | e^{-i\hat{H}\Delta t} \dots e^{-i\hat{H}\Delta t} | q_i \rangle. \end{aligned} \quad (\text{A.3})$$

Here $|q\rangle$ is a position eigenstate, which forms a complete set and thus satisfies the identity

$$1 = \int dq |q\rangle\langle q|. \quad (\text{A.4})$$

Inserting such identities between each operator $U(\Delta t, 0)$ in the expression for A , we get

$$\begin{aligned} A &= \int dq_{N-1} \dots \int dq_1 \langle q_f | e^{-i\hat{H}\Delta t} |q_{N-1}\rangle \dots \langle q_1 | e^{-i\hat{H}\Delta t} |q_i\rangle \\ &= \int dq_{N-1} \dots \int dq_1 \prod_{n=0}^{N-1} A_n, \end{aligned} \quad (\text{A.5})$$

where $A_n = \langle q_{n+1} | e^{-i\hat{H}\Delta t} |q_n\rangle$, and we use $q_0 = q_i$ and $q_N = q_f$. We have essentially divided the trajectory between the spacetime points (t_i, q_i) and (t_f, q_f) into N independent trajectories with time intervals Δt , and then sum over all possible intermediate positions q_n between the points q_i and q_f . In other words, in the limit $N \rightarrow \infty$ we sum over all possible trajectories between (t_i, q_i) and (t_f, q_f) . This is what is often called the Feynman path integral approach. We will not proceed here with the single particle path integral, but instead focus on the path integral for many-particle systems.

In the many-body case we are interested in the quantum partition function¹

$$\mathcal{Z} = \sum_{\mathbf{n}} \langle \mathbf{n} | e^{-\beta\hat{H}} | \mathbf{n} \rangle, \quad (\text{A.6})$$

where the states $\{|\mathbf{n}\rangle\}$ represent a complete set in Fock space. Since the many-body Hamiltonian is given in terms of creation and annihilation operators, it is convenient to use states which are eigenstates of these operators, namely coherent states.

¹For notational simplicity we have included the $\mu\hat{N}$ term in \hat{H} .

A.1 COHERENT STATES

We define the coherent state $|\psi\rangle$ as an eigenstate of the annihilation operator c_α with quantum number α ,

$$c_\alpha |\psi\rangle = \psi_\alpha |\psi\rangle, \quad (\text{A.7})$$

where ψ_α is the eigenvalue. The fermionic annihilation operators anticommute, which means we must have

$$c_\alpha c_\beta |\psi\rangle = |\psi\rangle \psi_\alpha \psi_\beta = -c_\beta c_\alpha |\psi\rangle = -|\psi\rangle \psi_\beta \psi_\alpha. \quad (\text{A.8})$$

We see that the eigenvalues must also anticommute, $\psi_\alpha \psi_\beta = -\psi_\beta \psi_\alpha$, meaning they can not be ordinary complex values, but rather Grassmann numbers. The Grassmann numbers also anticommute with the fermionic operators c_α and c_α^\dagger . From the anticommutation relations we also see that $\psi_\alpha = 0$, meaning that any function of Grassmann numbers can only go up to linear order in each number ψ_α .

We now show that the fermionic coherent states are defined by

$$|\psi\rangle = e^{-\sum_\alpha \psi_\alpha c_\alpha^\dagger} |0\rangle, \quad (\text{A.9})$$

where $|0\rangle$ is the vacuum state. Operating with an operator c_β , we get

$$\begin{aligned} c_\beta |\psi\rangle &= c_\beta \sum_{k=0}^{\infty} \frac{[-\sum_\alpha \psi_\alpha c_\alpha^\dagger]^k}{k!} |0\rangle = c_\beta \prod_\alpha (1 - \psi_\alpha c_\alpha^\dagger) |0\rangle \\ &= \prod_{\alpha \neq \beta} (1 - \psi_\alpha c_\alpha^\dagger) \psi_\beta |0\rangle = \psi_\beta |\psi\rangle, \end{aligned} \quad (\text{A.10})$$

where we have used $\psi_\beta^2 = 0$ to rewrite $\psi_\beta |0\rangle = \psi_\beta (1 - \psi_\beta c_\beta^\dagger) |0\rangle$. The adjoint coherent state is given by

$$\langle\psi| = \langle 0| e^{\sum_\alpha \psi_\alpha^\dagger c_\alpha}, \quad (\text{A.11})$$

where it is important to note that ψ_α^\dagger is an independent variable, and not the hermitian conjugate of ψ_α . From this we find that the overlap between two coherent states is

$$\begin{aligned}\langle \eta | \psi \rangle &= \langle 0 | \prod_{\alpha, \beta} (1 + \eta_\alpha^\dagger c_\alpha) (1 - \psi_\beta c_\beta^\dagger) | 0 \rangle \\ &= \langle 0 | \prod_{\alpha} (1 + \eta_\alpha^\dagger \psi_\alpha c_\alpha c_\alpha^\dagger) | 0 \rangle = e^{\sum_{\alpha} \eta_\alpha^\dagger \psi_\alpha}.\end{aligned}\quad (\text{A.12})$$

Finally, the coherent states have the completeness relation

$$1 = \int d\psi^\dagger d\psi e^{-\sum_{\alpha} \psi_\alpha^\dagger \psi_\alpha} |\psi\rangle \langle \psi|, \quad (\text{A.13})$$

where $d\psi^\dagger d\psi = \prod_{\alpha} d\psi_\alpha^\dagger d\psi_\alpha$. To show that this holds, we insert the identity into

$$\begin{aligned}\langle \eta | \eta \rangle &= \int d\psi^\dagger d\psi e^{-\sum_{\alpha} \psi_\alpha^\dagger \psi_\alpha} \langle \eta | \psi \rangle \langle \psi | \eta \rangle \\ &= \int d\psi^\dagger d\psi e^{-\sum_{\alpha} \psi_\alpha^\dagger \psi_\alpha} e^{\sum_{\beta} \eta_\beta^\dagger \psi_\beta} e^{\sum_{\gamma} \psi_\gamma^\dagger \eta_\gamma} \\ &= \int d\psi^\dagger d\psi e^{-\sum_{\alpha} [\psi_\alpha^\dagger \psi_\alpha - \eta_\alpha^\dagger \psi_\alpha - \psi_\alpha^\dagger \eta_\alpha]}.\end{aligned}\quad (\text{A.14})$$

This has the form of a Gaussian integral. The Gaussian integral for Grassmann numbers is given by

$$\begin{aligned}\int d\psi^\dagger d\psi e^{-\psi^\dagger a \psi + \psi^\dagger \eta + \eta^\dagger \psi} &= \int d\psi^\dagger d\psi (1 - \psi^\dagger a \psi \\ &\quad + \psi^\dagger \eta + \eta^\dagger \psi + \psi^\dagger \eta \eta^\dagger \psi) \\ &= a + \eta^\dagger \eta = a e^{\frac{\eta^\dagger \eta}{a}},\end{aligned}\quad (\text{A.15})$$

where a is a complex number, and we have used the definitions $\int d\psi = 0$ and $\int d\psi \psi = 1$ for integration of Grassmann variables. Generalizing this to multiple Grassmann variables results in

$$\int d\psi^\dagger d\psi e^{-\psi_\alpha^\dagger A_{\alpha\beta} \psi_\beta + \psi_\alpha^\dagger \eta_\alpha + \eta_\alpha^\dagger \psi_\alpha} = \det A e^{\eta_\alpha^\dagger A_{\alpha\beta}^{-1} \eta_\beta}, \quad (\text{A.16})$$

where summation of repeated indexes is implied, and A is a complex matrix. Applying the latter equation to Eq. (A.14), we get

$$\langle \eta | \eta \rangle = e^{\sum_{\alpha} \eta_{\alpha}^{\dagger} \eta_{\alpha}}, \quad (\text{A.17})$$

which is in agreement with Eq. (A.12), showing that the completeness relation does indeed hold.

While we have here focused solely on the fermionic coherent states, the bosonic coherent states are defined in exactly the same way, and the relations above hold for both, with only a differing sign in some cases [40, p. 164]. However, since we are mostly interested in fermionic systems, we will focus on this case in the following.

A.2 COHERENT STATE PATH INTEGRAL

We now use the fermionic coherent states when constructing the path integral. Inserting the completeness relation Eq. (A.13) into the quantum partition function Eq. (A.6), we get

$$\begin{aligned} \mathcal{Z} &= \int d\psi^{\dagger} d\psi \sum_{\mathbf{n}} e^{-\sum_{\alpha} \psi_{\alpha}^{\dagger} \psi_{\alpha}} \langle \mathbf{n} | \psi \rangle \langle \psi | e^{-\beta \hat{H}} | \mathbf{n} \rangle \\ &= \int d\psi^{\dagger} d\psi e^{-\sum_{\alpha} \psi_{\alpha}^{\dagger} \psi_{\alpha}} \langle -\psi | e^{-\beta \hat{H}} | \psi \rangle. \end{aligned} \quad (\text{A.18})$$

We now follow essentially the same procedure as at the beginning of the appendix: We split the imaginary time interval β into N equally spaced segments $\Delta\tau = \beta/N$, and insert $N - 1$ copies of the completeness relation Eq. (A.13). To simplify the notation we will now use ψ to mean a vector of all ψ_{α} , such that $\psi^{\dagger} \psi \equiv \sum_{\alpha} \psi_{\alpha}^{\dagger} \psi_{\alpha}$. We also use the notation ψ_n for ψ at imaginary time $n\Delta\tau$. Hence, we have

$$\begin{aligned} \mathcal{Z} &= \int \left(\prod_{n=1}^N d\psi_n^{\dagger} d\psi_n \right) \langle \psi_N | e^{-\psi_{N-1}^{\dagger} \psi_{N-1}} e^{-\hat{H} \Delta\tau} | \psi_{N-1} \rangle \\ &\quad \times \langle \psi_{N-1} | \dots e^{-\psi_1^{\dagger} \psi_1} e^{-\hat{H} \Delta\tau} | \psi_1 \rangle \langle \psi_1 | e^{-\psi_0^{\dagger} \psi_0} e^{-\hat{H} \Delta\tau} | \psi_0 \rangle, \end{aligned} \quad (\text{A.19})$$

where $\psi_N = -\psi_0$. Using

$$\langle \psi_{n+1} | \hat{H}(c^\dagger, c) | \psi_n \rangle = H(\psi_{n+1}^\dagger, \psi_n) e^{\psi_{n+1}^\dagger \psi_n}, \quad (\text{A.20})$$

we see that the partition function gets terms in the exponential which can be written

$$\sum_{n=0}^{N-1} (\psi_n^\dagger - \psi_{n+1}^\dagger) \psi_n = \sum_{n=0}^{N-1} \psi_{n+1}^\dagger (\psi_{n+1} - \psi_n), \quad (\text{A.21})$$

where we have used $\psi_0^\dagger \psi_0 = \psi_N^\dagger \psi_N$ after shifting $n \rightarrow n+1$ in the first term. Inserting this into the partition function we get

$$\mathcal{Z} = \int \left(\prod_{n=1}^N d\psi_n^\dagger d\psi_n \right) e^{-\Delta\tau \sum_{n=0}^{N-1} \left[\psi_{n+1}^\dagger \frac{\psi_{n+1} - \psi_n}{\Delta\tau} + H(\psi_{n+1}^\dagger, \psi_n) \right]}. \quad (\text{A.22})$$

Since $\Delta\tau \rightarrow 0$ in the limit $N \rightarrow \infty$, we let

$$\Delta\tau \sum_{n=0}^{N-1} \rightarrow \int_0^\beta d\tau, \quad (\text{A.23})$$

$$H[\psi_{n+1}^\dagger, \psi_n] \rightarrow H[\psi^\dagger(n\Delta\tau), \psi(n\Delta\tau)], \quad (\text{A.24})$$

and define

$$\partial_\tau \psi(\tau) \Big|_{\tau=n\Delta\tau} \equiv \lim_{\Delta\tau \rightarrow 0} \frac{\psi_{n+1} - \psi_n}{\Delta\tau}, \quad (\text{A.25})$$

$$\mathcal{D}\psi^\dagger \mathcal{D}\psi \equiv \lim_{N \rightarrow \infty} \prod_{n=1}^N d\psi_n^\dagger d\psi_n. \quad (\text{A.26})$$

Hence, we arrive at the path integral (or functional integral)

$$\mathcal{Z} = \int \mathcal{D}\psi^\dagger \mathcal{D}\psi e^{-S[\psi^\dagger, \psi]}, \quad (\text{A.27})$$

where we have defined the action

$$S[\psi^\dagger, \psi] = \int_0^\beta d\tau \left[\psi^\dagger \partial_\tau \psi + H(\psi^\dagger, \psi) \right]. \quad (\text{A.28})$$

Though we have focused on fermionic coherent states, the result is exactly the same for bosons. The difference lies in the boundary conditions of the fields ψ^\dagger and ψ ,

$$\psi(\beta) = \pm \psi(0), \quad \psi^\dagger(\beta) = \pm \psi^\dagger(0), \quad (\text{A.29})$$

where the upper (lower) sign is for bosons (fermions).

1

Reference

H. G. Hugdal and A. Sudbø,

p-wave superconductivity in weakly repulsive 2D Hubbard model with Zeeman splitting and weak Rashba spin-orbit coupling.

Physical Review B, **97**, 024515 (2018).

Contributions

AS initiated the project. HGH performed the analytical and numerical calculations, and wrote the initial manuscript. Both authors contributed to the discussion of the results and the revisions of the final manuscript.

***p*-wave superconductivity in weakly repulsive 2D Hubbard model with Zeeman splitting and weak Rashba spin-orbit coupling**

Henning G. Hugdal^{*} and Asle Sudbø[†]

Department of Physics, NTNU, Norwegian University of Science and Technology, NO-7491 Trondheim, Norway, and Center for Quantum Spintronics, Department of Physics, Norwegian University of Science and Technology, NO-7491 Trondheim, Norway



(Received 7 November 2017; revised manuscript received 11 January 2018; published 24 January 2018)

We study the superconducting order in a two-dimensional square lattice Hubbard model with weak repulsive interactions, subject to a Zeeman field and weak Rashba spin-orbit interactions. Diagonalizing the noninteracting Hamiltonian leads to two separate bands, and by deriving an effective low-energy interaction we find the mean field gap equations for the superconducting order parameter on the bands. Solving the gap equations just below the critical temperature, we find that superconductivity is caused by Kohn-Luttinger-type interaction, while the pairing symmetry of the bands is indirectly affected by the spin-orbit coupling. The dominating attractive momentum channel of the Kohn-Luttinger term depends on the filling fraction n of the system, and it is therefore possible to change the momentum dependence of the order parameter by tuning n . Moreover, n also determines which band has the highest critical temperature. Rotating the magnetic field changes the momentum dependence from states that for small momenta reduce to a chiral $p_x \pm ip_y$ type state for out-of-plane fields, to a nodal p -wave-type state for purely in-plane fields.

DOI: [10.1103/PhysRevB.97.024515](https://doi.org/10.1103/PhysRevB.97.024515)

I. INTRODUCTION

Much attention has been paid to the possibility of unconventional superconductivity due to weak repulsive interactions, as first pointed out by Kohn and Luttinger in 1967 [1]. They found that because of oscillations in long-range interactions, a p -wave superconducting state could be formed in a three-dimensional electron gas at $O(U^2)$ in the interaction strength U . In two dimensions, no such state can be formed at $O(U^2)$ [2]; it is only present at $O(U^3)$ and zero temperature [3]. However, by applying a magnetic field the effect is present on the majority band also at second order in U [2,4].

In systems with broken inversion symmetry, either due to crystal structure or an applied electric field, one has to include the effects of spin-orbit interactions by including a Rashba spin-orbit coupling (SOC) term [5,6]. A Rashba term in the system Hamiltonian will lead to a coupling between the spin-up and spin-down Fermi surfaces, and hence opens up the possibility of proximity-induced superconductivity on the minority band [4,7]. Reference [8] provides a recent review on superconductivity in systems with broken inversion symmetry. The effects of magnetic fields and spin-orbit coupling in two-dimensional systems has been studied in various cases, in limiting cases of, e.g., the strength of the SOC or the direction of the magnetic field [4,9–14]. Recently Lake *et al.* [7] studied a weakly spin-orbit-coupled two-dimensional electron gas (2DEG) with a magnetic field which could be rotated in and out of the plane. They reported that topological $p + ip$ superconductivity is realized when the field is perpendicular

to the plane, while an in-plane magnetic field in the x direction leads to a p_y momentum dependence of the order parameter. In either case, only the majority band was found to be superconducting.

In this paper, we perform an analysis similar to that of Ref. [7] to study the superconducting order in a weakly repulsive, spin-polarized Hubbard model on a two-dimensional (2D) square lattice with weak SOC. Such systems can be realized, e.g., at the interface between LaAlO_3 and SrTiO_3 , which has been shown to exhibit a 2D superconducting state [15–17], a magnetic state [18], and coexistence of superconductivity and magnetism [19–22]. Moreover, it has been shown that the SOC at the interface can be tuned by a gate voltage or an applied electric field [23,24].

By finding the superconducting state that emerges at the critical temperature T_c , we study the dominating pairing symmetries on the two bands for different filling fractions and magnetic field orientations. We find that superconductivity can be induced on *both bands*, depending on the filling fraction. We also find that two different pairing symmetries are realized, one for nearly empty or nearly filled bands, and one close to half filling. However, the small-momentum limit of the order parameters are the same in both regions, a chiral $p_x \pm ip_y$ symmetry for purely out-of-plane fields and p -wave state state for purely in-plane fields. We also find that the Cooper pairs have a finite center-of-mass momentum [7,14,25], i.e., a Fulde-Ferrell-Larkin-Ovchinnikov state (FFLO) [26,27], whenever the magnetic field has an in-plane component.

The remainder of the paper is organized as follows: The model system is presented in Sec. II together with the derivation of the effective Hamiltonian and self-consistent equations for the mean field superconducting gap. The numerical solution strategy is discussed in Sec. III, the results of which are presented in Sec. IV. Finally, we summarize our results in Sec. V.

^{*}henning.g.hugdald@ntnu.no

[†]asle.sudbo@ntnu.no

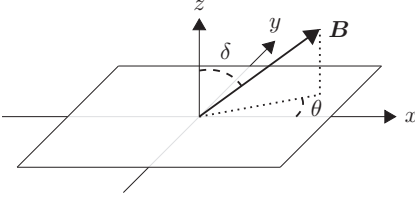


FIG. 1. Sketch of system geometry, where the 2D lattice is located in the xy plane and the magnetic field \mathbf{B} can point in any direction.

II. MODEL

Our starting point is a two-dimensional lattice in the presence of an external magnetic field, and with broken inversion symmetry such that SOC is present. A sketch of the geometry is shown in Fig. 1. We use the Hubbard model augmented by SOC to describe the fermions on the lattice, with a spin-diagonal hopping integral between nearest-neighbor lattice sites given by t , and the electrons interact via an onsite repulsion $U n_{i\uparrow} n_{i\downarrow}$, $U > 0$. We will assume that the interaction is weak, i.e., the energy scale of the Hubbard interaction is small compared to the kinetic energy, $U/t \ll 1$. Time-reversal symmetry is broken by applying an external magnetic field \mathbf{B} , which couples to the electrons via the Zeeman coupling $-g\mu_B \mathbf{B} \cdot \boldsymbol{\sigma}/2$, where g is the g factor and μ_B is the Bohr magneton. This lifts the degeneracy between the spin directions. The effect of SOC is included via a Rashba term with spin-orbit axis normal to the lattice plane, $\alpha_R(\mathbf{p} \times \boldsymbol{\sigma}) \cdot \hat{z}$, where α_R is the strength of the spin-orbit coupling. We thus obtain the total system Hamiltonian $H = H_t + H_B + H_R + H_I = H_0 + H_I$, with

$$H_t = \sum_{\mathbf{k}, \mathbf{k}'} \epsilon_{\mathbf{k}} c_{\mathbf{k}\sigma}^\dagger c_{\mathbf{k}'\sigma}, \quad (1a)$$

$$H_R = \alpha_R \sum_{\mathbf{k}} \sum_{\sigma, \sigma'} (\sigma_{\sigma\sigma'}^y \sin k_x - \sigma_{\sigma\sigma'}^x \sin k_y) c_{\mathbf{k}\sigma}^\dagger c_{\mathbf{k}\sigma'}, \quad (1b)$$

$$\begin{aligned} \epsilon_\lambda(\mathbf{k}) &= \epsilon_{\mathbf{k}} - \zeta_\lambda \sqrt{h^2 - 2h\alpha_R(\sin k_x \sin \theta - \sin k_y \cos \theta) \sin \delta + \alpha_R^2(\sin^2 k_x + \sin^2 k_y)} \\ &\approx \epsilon_{\mathbf{k}} - \zeta_\lambda \left[h - \alpha_R(\sin k_x \sin \theta - \sin k_y \cos \theta) \sin \delta + \frac{\alpha_R^2}{2h}(\sin k_x \cos \theta + \sin k_y \sin \theta)^2 \right. \\ &\quad \left. + \frac{\alpha_R^2}{2h}(\sin k_x \sin \theta - \sin k_y \cos \theta)^2 \cos^2 \delta \right], \end{aligned} \quad (4)$$

where $\zeta_{\lambda=1(2)} = +(-)1$ for the majority (minority) band. In the last line, we have kept terms only up to first order in α_R/h . In the limit $|\mathbf{k}| \ll 1$ and $\theta = 0$, this result agrees with Ref. [7]. When the magnetic field has an in-plane component, the momentum \mathbf{q} corresponding the minima of the band dispersions will shift away from the origin according to

$$q_x \approx -\frac{\zeta_\lambda \alpha_R}{2t} \sin \delta \sin \theta, \quad (5a)$$

$$q_y \approx +\frac{\zeta_\lambda \alpha_R}{2t} \sin \delta \cos \theta. \quad (5b)$$

$$H_B = -\mathbf{H} \cdot \sum_{\mathbf{k}} \sum_{\sigma, \sigma'} \boldsymbol{\sigma}_{\sigma\sigma'} c_{\mathbf{k}\sigma}^\dagger c_{\mathbf{k}\sigma'}, \quad (1c)$$

$$H_I = \frac{U}{V} \sum_{\mathbf{k}_1, \mathbf{k}_2, \mathbf{k}_3} c_{\mathbf{k}_1\uparrow}^\dagger c_{\mathbf{k}_2\downarrow}^\dagger c_{\mathbf{k}_3\downarrow} c_{\mathbf{k}_1+\mathbf{k}_2-\mathbf{k}_3, \uparrow}, \quad (1d)$$

where $\epsilon_{\mathbf{k}} \equiv -2t(\cos k_x + \cos k_y) - \mu$ is the square-lattice tight-binding dispersion relative the chemical potential μ , $\sigma = \uparrow, \downarrow$ denotes spin-up and spin-down electrons respectively, $\mathbf{H} = g\mu_B \mathbf{B}/2 = h(\cos \theta \sin \delta \hat{x} + \sin \theta \sin \delta \hat{y} + \cos \delta \hat{z})$, and V is the volume of the system. For notational simplicity, we have set \hbar and the lattice constant a to 1 throughout the paper.

A. Diagonalization of noninteracting Hamiltonian

Following Ref. [7], we will treat the SOC as a perturbation, assuming that $\alpha_R/h \ll 1$. Hence, we expect that when diagonalizing the noninteracting Hamiltonian H_0 , the lowest order expression will simply be that of a tight-binding system with spins polarized along the direction of \mathbf{H} . We therefore rotate the spin quantization axis to point along the magnetic field using the unitary rotation operator $R_n(\alpha) = \exp(-i\alpha \boldsymbol{\sigma} \cdot \hat{n}/2)$, where α is the angle of rotation about an axis \hat{n} : We first rotate an angle θ about $\hat{n} = \hat{z}$, and then an angle δ about $\hat{n} = \hat{y}$. This yields

$$H_0 = \sum_{\mathbf{k}} \sum_{\sigma, \sigma'} E_{\sigma\sigma'}(\mathbf{k}) c_{\mathbf{k}\sigma}^\dagger c_{\mathbf{k}\sigma'}, \quad (2)$$

where

$$\begin{aligned} E(\mathbf{k}) &= \epsilon_{\mathbf{k}} \sigma^0 - h \sigma^z + \alpha_R [(\sin k_x \sin \theta - \sin k_y \cos \theta) \cos \delta \sigma^x \\ &\quad + (\sin k_x \cos \theta + \sin k_y \sin \theta) \sigma^y \\ &\quad + (\sin k_y \sin \theta - \sin k_x \cos \theta) \sin \delta \sigma^z]. \end{aligned} \quad (3)$$

Diagonalizing H_0 leads to two bands with eigenenergies

This shift is illustrated in Fig. 2.

Using the eigenvalues in Eq. (4), we also find relations between the spin and band creation and annihilation operators, which to second order in α_R/h are given by

$$c_{\mathbf{k}\uparrow} = \left[1 - \frac{\alpha_R^2}{8h^2} |\gamma(\mathbf{k}, \delta, \theta)|^2 \right] a_{\mathbf{k}1} + \frac{\alpha_R}{2h} \gamma(\mathbf{k}, \delta, \theta) a_{\mathbf{k}2}, \quad (6a)$$

$$c_{\mathbf{k}\downarrow} = -\frac{\alpha_R}{2h} \gamma^\dagger(\mathbf{k}, \delta, \theta) a_{\mathbf{k}1} + \left[1 - \frac{\alpha_R^2}{8h^2} |\gamma(\mathbf{k}, \delta, \theta)|^2 \right] a_{\mathbf{k}2}, \quad (6b)$$

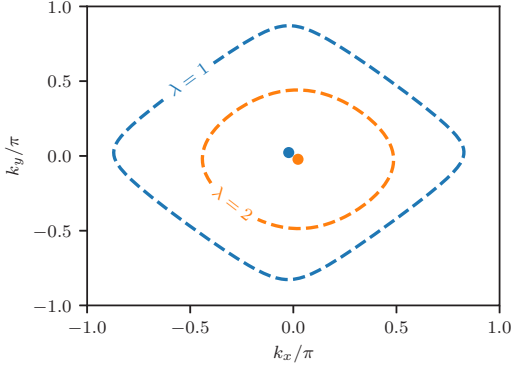


FIG. 2. Plot of the Fermi levels for an in-plane magnetic field ($\delta = \pi/2$) with angle $\theta = \pi/4$ relative to the x axis, for filling fraction $n = 0.3$, magnetic field strength $h/t = 1$, and SOC strength $\alpha_R/t = 0.2$. The momenta corresponding to the minima of the band dispersions are shifted away from the origin according to Eq. (5). Note that the shift is exaggerated compared to what will be considered throughout the paper.

where we have defined the function

$$\gamma(\mathbf{k}, \delta, \theta) = (\sin k_x \sin \theta - \sin k_y \cos \theta) \cos \delta - i(\sin k_x \cos \theta + \sin k_y \sin \theta)$$

and $a_{\mathbf{k}\lambda}^\dagger$ and $a_{\mathbf{k}\lambda}$ are the creation and annihilation operators for band λ respectively. Using these relations, we find that the expectation value of the z component of the spin is $1/2$ for the majority $\lambda = 1$ band and $-1/2$ for the minority $\lambda = 2$ band, with the corrections being second order in α_R/h . Hence, to lowest order, the majority and minority bands consist of spin-up and spin-down particles, respectively. This has consequences for the momentum dependence of any intraband interaction which could lead to superconductivity. In the next section, we will transform the interaction Hamiltonian using the above operator relations and obtain an effective low-energy theory using a Schrieffer-Wolff transformation [28].

B. Transformation of the interaction Hamiltonian

Since the interaction Hamiltonian H_I is proportional to U , where we have assumed that the interaction is weak, $U/t \ll 1$, we have to consider what powers of U and α_R/h to keep when transforming the Hamiltonian to the eigenbasis according to Eq. (6). Following Ref. [7], we keep terms of $O(U^2/t^2)$ and $O(U\alpha_R^2/th^2)$, while disregarding terms of $O(U^2\alpha_R/t^2h)$; i.e., we assume $\alpha_R/h \gg U/t$.

Transforming the creation and annihilation operators in H_I , we get four main types of terms: intraband and pair-hopping terms $a_{\mathbf{k}_1\lambda}^\dagger a_{\mathbf{k}_2\lambda}^\dagger a_{\mathbf{k}_3\mu} a_{\mathbf{k}_4\mu}$ of $O(U\alpha_R^2/h^2)$; interband terms $a_{\mathbf{k}_1\lambda}^\dagger a_{\mathbf{k}_2\bar{\lambda}}^\dagger a_{\mathbf{k}_3\bar{\lambda}} a_{\mathbf{k}_4\lambda}$ of $O(U)$; and mixed terms such as $a_{\mathbf{k}_1\lambda}^\dagger a_{\mathbf{k}_2\lambda}^\dagger a_{\mathbf{k}_3\bar{\lambda}} a_{\mathbf{k}_4\bar{\lambda}}$ of $O(U\alpha_R/h)$ and higher. The notation $\bar{\lambda}$ denotes the opposite band of λ . We collect the intraband and

pair-hopping terms in H_1 and the remaining terms in H_2 :

$$H_1 = \sum_{\mathbf{k}, \mathbf{k}', \mathbf{q}} \sum_{\lambda, \mu} \frac{U\alpha_R^2}{4Vh^2} \Gamma_\lambda(\mathbf{k} + \frac{\mathbf{q}}{2}) \Gamma_\mu^\dagger(\mathbf{k}' + \frac{\mathbf{q}}{2}) \times a_{-\mathbf{k} + \frac{\mathbf{q}}{2}, \lambda}^\dagger a_{\mathbf{k} + \frac{\mathbf{q}}{2}, \lambda}^\dagger a_{\mathbf{k}' + \frac{\mathbf{q}}{2}, \mu} a_{-\mathbf{k}' + \frac{\mathbf{q}}{2}, \mu}, \quad (7)$$

where

$$\Gamma_\lambda(\mathbf{k}) = \zeta_\lambda [\sin k_x \cos \theta + \sin k_y \sin \theta + i\zeta_\lambda (\sin k_x \sin \theta - \sin k_y \cos \theta) \cos \delta] \quad (8)$$

and

$$H_2 = \frac{U}{2V} \sum_{\mathbf{k}_1, \mathbf{k}_2, \mathbf{k}_3} \sum_{\lambda} a_{\mathbf{k}_1\lambda}^\dagger a_{\mathbf{k}_2\bar{\lambda}}^\dagger a_{\mathbf{k}_3\bar{\lambda}} a_{\mathbf{k}_1 + \mathbf{k}_2 - \mathbf{k}_3, \lambda} + O\left(\frac{U\alpha_R}{h}\right). \quad (9)$$

The terms in H_2 correspond to processes where the resulting quasiparticles are on different bands, and including such interactions in a mean-field treatment would require order parameters with mixed-band indices. In order to get a form of the interaction suitable for analysis within a mean-field theory, we perform a Schrieffer-Wolff transformation; see, e.g., Ref. [29] for a review. This enables us to get rid of the lowest order processes in H_2 while still including the effects of H_2 to higher order, such as an intraband process at $O(U^2)$. This is obtained by the unitary transformation

$$H' = e^{-S} H e^S = H_0 + H_1 + H_2 + [H_0 + H_1 + H_2, S] + \frac{1}{2} [[H_0 + H_1 + H_2, S], S] + \dots, \quad (10)$$

where S is an antiunitary operator chosen such that $[H_0, S] = -H_2$. The lowest order term in S is necessarily of $O(U/t)$, and this is the only contributing term to the order we are working. Using as an ansatz $S = \sum_{\mathbf{k}_1, \mathbf{k}_2, \mathbf{k}_3} \sum_{\lambda} C_\lambda(\mathbf{k}_1, \mathbf{k}_2, \mathbf{k}_3, \mathbf{k}_4) a_{\mathbf{k}_1\lambda}^\dagger a_{\mathbf{k}_2\bar{\lambda}}^\dagger a_{\mathbf{k}_3\bar{\lambda}} a_{\mathbf{k}_4\lambda}$, where $\mathbf{k}_4 = \mathbf{k}_1 + \mathbf{k}_2 - \mathbf{k}_3$, we find

$$S = \frac{U}{2V} \sum_{\mathbf{k}_1, \mathbf{k}_2, \mathbf{k}_3, \mathbf{k}_4} \sum_{\lambda} \frac{a_{\mathbf{k}_1\lambda}^\dagger a_{\mathbf{k}_2\bar{\lambda}}^\dagger a_{\mathbf{k}_3\bar{\lambda}} a_{\mathbf{k}_4\lambda} \delta(\mathbf{k}_1 + \mathbf{k}_2 - \mathbf{k}_3 - \mathbf{k}_4)}{\epsilon_\lambda(\mathbf{k}_4) + \epsilon_\lambda(\mathbf{k}_3) - \epsilon_\lambda(\mathbf{k}_2) - \epsilon_\lambda(\mathbf{k}_1)}. \quad (11)$$

Since S comes with a factor U , we can neglect most of the terms in the transformed Hamiltonian, leaving us with $H' = H_0 + H_1 + [H_2, S]/2$. Hence, the contributing higher order processes due to H_2 are found by calculating the commutator between H_2 and S .

The commutator leads to two kinds of terms of relevant order: a four-operator interband term proportional to $a_\lambda^\dagger a_\lambda^\dagger a_{\bar{\lambda}} a_{\bar{\lambda}}$ and six-operator terms $a_\lambda^\dagger a_\lambda^\dagger a_{\bar{\lambda}} a_{\bar{\lambda}} a_\lambda^\dagger a_{\bar{\lambda}}$, both of $O(U^2/t^2)$. However, since the interactions must conserve momentum, and the interacting particles are close to the Fermi level, the phase space of the interband interaction is severely limited, as illustrated in Fig. 3. Although the figure does not include the shifts in the minima of the dispersions away from the origin, Eq. (5), these shifts are small when $\alpha_R/h \ll 1$, and the argument should still hold. Hence we will neglect this term, and include only the six-operator terms.

An effective intraband process on band λ is obtained from the six-operator terms $a_\lambda^\dagger a_\lambda^\dagger a_\lambda a_\lambda a_\lambda^\dagger a_\lambda^\dagger$ by projecting the

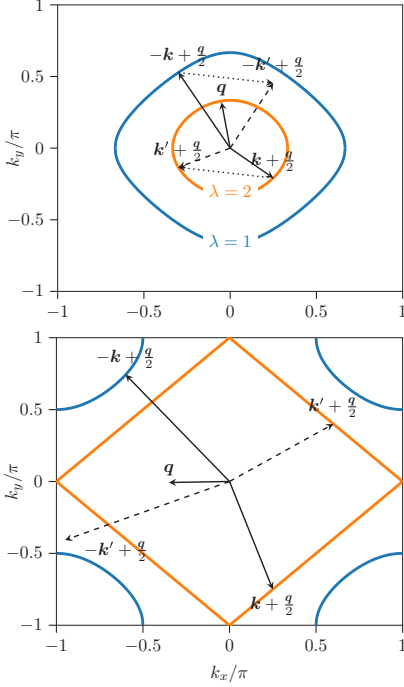


FIG. 3. The figures illustrate that the interband scattering from $\mathbf{k} + \mathbf{q}/2$ and $-\mathbf{k} + \mathbf{q}/2$ to $\mathbf{k}' + \mathbf{q}/2$ and $-\mathbf{k}' + \mathbf{q}/2$ has a very limited phase space for both low (top) and high (bottom) filling fractions n . Here we have not included the shifts in center-of-mass momenta, since the shifts are small when $\alpha_R/h \ll 1$.

operators $a_{\lambda}^{\dagger} a_{\bar{\lambda}}$ to the noninteracting $\bar{\lambda}$ band, which results in a replacement $a_{\lambda}^{\dagger} a_{\bar{\lambda}} \rightarrow \delta(\mathbf{k} - \mathbf{k}') f(\epsilon_{\bar{\lambda}}(\mathbf{k}))$ [4,7]. Here, $f(\epsilon)$ is the Fermi-Dirac distribution function. Since the shifts in center-of-mass momenta are small, including them in the interaction terms leads to a correction of higher order than we are considering. We therefore specialize to the case where the total momentum of the particles interacting is zero, which yields the result for the commutator

$$\frac{1}{2}[H_2, S] = \frac{U^2}{2V} \sum_{\mathbf{k}, \mathbf{k}'} \sum_{\lambda} \chi_{\bar{\lambda}}(\mathbf{k} - \mathbf{k}') a_{-\mathbf{k}', \lambda}^{\dagger} a_{\mathbf{k}', \lambda}^{\dagger} a_{\mathbf{k}, \lambda} a_{-\mathbf{k}, \lambda}, \quad (12)$$

where we have defined the susceptibility

$$\chi_{\lambda}(\mathbf{q}) = \frac{1}{V} \sum_{\mathbf{p}} \frac{f(\epsilon_{\lambda}(\mathbf{p} + \mathbf{q})) - f(\epsilon_{\lambda}(\mathbf{p}))}{\epsilon_{\lambda}(\mathbf{p} + \mathbf{q}) - \epsilon_{\lambda}(\mathbf{p})}. \quad (13)$$

In contrast to the 2DEG case [4,7], we have not been able to calculate the susceptibility analytically for the lattice model. However, a numerical calculation is possible, the results of which will be discussed in Sec. III A.

Setting the total momentum of an interacting pair of particles to zero also in H_1 , and collecting all terms, we arrive at

the effective low-energy Hamiltonian

$$H' = H_0 + \sum_{\mathbf{k}, \mathbf{k}'} \sum_{\lambda, \mu} g_{\lambda, \mu}(\mathbf{k}, \mathbf{k}') a_{-\mathbf{k}, \lambda}^{\dagger} a_{\mathbf{k}', \lambda}^{\dagger} a_{\mathbf{k}', \mu} a_{-\mathbf{k}, \mu}, \quad (14)$$

where we have defined the interaction matrix

$$g_{\lambda, \mu}(\mathbf{k}, \mathbf{k}') = \frac{U^2}{2V} \delta_{\lambda, \mu} \chi_{\bar{\lambda}}(\mathbf{k}' - \mathbf{k}) + \frac{U \alpha_R^2}{4V h^2} \Gamma_{\lambda}(\mathbf{k}) \Gamma_{\mu}^{\dagger}(\mathbf{k}'), \quad (15)$$

where $\Gamma_{\lambda}(\mathbf{k})$ is defined in Eq. (8). The first term in Eq. (15) is an intraband interaction due to the Kohn-Luttinger mechanism. The second term, which is caused by the SOC, contains both intraband and pair-hopping terms, with opposite signs due to the factors $\zeta_{\lambda} \zeta_{\mu}$. We thus expect the two terms in Eq. (15) to give rise to different superconducting states. The first term gives rise to uncoupled ordered states on the two bands with different T_c , while the second term couples the order parameters and should lead to simultaneous superconductivity on both bands.

C. Mean-field treatment

Defining the mean-field order parameters (gap functions)

$$\Delta_{\lambda}(\mathbf{k}) = - \sum_{\mathbf{k}', \mu} 2g_{\lambda, \mu}(\mathbf{k}, \mathbf{k}') \langle a_{\mathbf{k}', \mu} a_{-\mathbf{k}', \mu} \rangle, \quad (16)$$

$$\Delta_{\mu}^{\dagger}(\mathbf{k}) = - \sum_{\mathbf{k}', \lambda} 2g_{\lambda, \mu}(\mathbf{k}', \mathbf{k}) \langle a_{-\mathbf{k}', \lambda}^{\dagger} a_{\mathbf{k}', \lambda}^{\dagger} \rangle, \quad (17)$$

we rewrite the Hamiltonian in the standard way

$$H' = \sum_{\mathbf{k}, \lambda} \frac{1}{2} \{ [\epsilon_{\lambda}(-\mathbf{k}) - \mu] + \Delta_{\lambda}(\mathbf{k}) \langle a_{-\mathbf{k}, \lambda}^{\dagger} a_{\mathbf{k}, \lambda}^{\dagger} \rangle \} + \frac{1}{2} \sum_{\mathbf{k}, \lambda} \psi_{\mathbf{k}, \lambda}^{\dagger} \mathcal{E}_{\lambda}(\mathbf{k}) \psi_{\mathbf{k}, \lambda}. \quad (18)$$

Here, we have defined the Nambu spinors $\psi_{\mathbf{k}, \lambda} = (a_{\mathbf{k}, \lambda} \ a_{-\mathbf{k}, \lambda}^{\dagger})^T$ and the matrix

$$\mathcal{E}_{\lambda}(\mathbf{k}) = \begin{pmatrix} \epsilon_{\lambda}(\mathbf{k}) - \mu & \Delta_{\lambda}(\mathbf{k}) \\ \Delta_{\lambda}^{\dagger}(\mathbf{k}) & -\epsilon_{\lambda}(-\mathbf{k}) + \mu \end{pmatrix}. \quad (19)$$

Performing a Bogoliubov transformation yields

$$H' = E_0 + \sum_{\mathbf{k}, \lambda} \left[\frac{\epsilon_{\lambda}(\mathbf{k}) - \epsilon_{\lambda}(-\mathbf{k})}{2} + E_{\lambda}(\mathbf{k}) \right] n_{\mathbf{k}, \lambda}, \quad (20)$$

where $n_{\mathbf{k}, \lambda}$ is the number operator of the Bogoliubov quasiparticles in the rotated basis and

$$E_{\lambda}(\mathbf{k}) = \sqrt{\xi_{\lambda}^2(\mathbf{k}) + |\Delta_{\lambda}(\mathbf{k})|^2} \quad (21)$$

is the approximate quasiparticle dispersion with $\xi_{\lambda}(\mathbf{k}) \equiv [\epsilon_{\lambda}(\mathbf{k}) + \epsilon_{\lambda}(-\mathbf{k})]/2$. Moreover,

$$E_0 = \frac{1}{2} \sum_{\mathbf{k}, \lambda} [\xi_{\lambda}(\mathbf{k}) - E_{\lambda}(\mathbf{k}) + \Delta_{\lambda}(\mathbf{k}) \langle a_{-\mathbf{k}, \lambda}^{\dagger} a_{\mathbf{k}, \lambda}^{\dagger} \rangle]. \quad (22)$$

Since the SOC term in the system Hamiltonian is the only term which breaks inversion symmetry, we have $[\epsilon_{\lambda}(\mathbf{k}) - \epsilon_{\lambda}(-\mathbf{k})]/2 \sim \alpha_R$. The $[\epsilon_{\lambda}(\mathbf{k}) - \epsilon_{\lambda}(-\mathbf{k})]$ term in the diagonalized Hamiltonian thus leads to higher order corrections and will therefore be neglected. Minimizing the free energy with

respect to $\Delta_\lambda^\dagger(\mathbf{k})$ yields the gap equations

$$\Delta_\lambda(\mathbf{k}) = - \sum_{\mathbf{k}', \mu} \frac{g_{\lambda\mu}(\mathbf{k}, \mathbf{k}') \Delta_\mu(\mathbf{k}')}{E_\mu(\mathbf{k}')} \tanh\left(\frac{\beta E_\mu(\mathbf{k}')}{2}\right), \quad (23)$$

where $\beta = 1/k_B T$. Note that we have set $\alpha_R = 0$ in $E_\lambda(\mathbf{k})$, since including the effects of the SOC in the dispersion give rise to terms of higher order than what we are considering.

III. NUMERICAL SOLUTION STRATEGY

A. Calculation of the susceptibility

The susceptibility is obtained numerically from Eq. (13) in the zero-temperature limit. Since the susceptibility enters the gap equations Eq. (23) with a prefactor proportional to U^2 , we can neglect the effects of SOC and thus set $\alpha_R = 0$ in the calculations. The results for the majority band for three different n are shown in Fig. 4, together with the analytical result for the 2DEG with Zeeman splitting treated in Refs. [4,7]. For low n , the susceptibility is isotropic and resembles the 2DEG result. Closer to half-filling, the susceptibility becomes more anisotropic due to the anisotropy of the dispersion.

In order to find the dominating attractive pairing channels due to the Kohn-Luttinger term in the gap equations, we expand the results for the susceptibility in square lattice harmonics; see the Appendix for details. Considering only the dominant attractive pairing channels, we find that the susceptibility to

good approximation can be written

$$\begin{aligned} \chi_\lambda(\mathbf{k} - \mathbf{k}') &= \chi_\lambda^1 [g_{x+iy}(\mathbf{k}) g_{x-iy}(\mathbf{k}') + g_{x-iy}(\mathbf{k}) g_{x+iy}(\mathbf{k}')] \\ &+ \chi_\lambda^2 [g_x(\mathbf{k}) g_x(\mathbf{k}') + g_y(\mathbf{k}) g_y(\mathbf{k}')] \\ &+ \chi_\lambda^3 [g_x(k_x, 2k_y) g_x(k'_x, 2k'_y) + g_y(k_x, 2k_y) g_y(k'_x, 2k'_y) \\ &+ g_x(2k_x, k_y) g_x(2k'_x, k'_y) + g_y(2k_x, k_y) g_y(2k'_x, k'_y)], \quad (24) \end{aligned}$$

where we have defined the functions

$$2\pi g_{x+iy}(\mathbf{k}) = \sin k_x + i \sin k_y, \quad (25a)$$

$$2\pi g_{x-iy}(\mathbf{k}) = \sin k_x - i \sin k_y, \quad (25b)$$

$$2\pi g_x(\mathbf{k}) = 2\pi g_x(k_x, k_y) = 2 \sin k_x \cos k_y, \quad (25c)$$

$$2\pi g_y(\mathbf{k}) = 2\pi g_y(k_x, k_y) = 2 \cos k_x \sin k_y. \quad (25d)$$

These functions are orthonormal, i.e., $\int_{\text{1BZ}} d\mathbf{k} g_i(\mathbf{k}) g_j^\dagger(\mathbf{k}) = \delta_{ij}$.

The values for the expansion coefficients χ_λ^i for different filling fractions n are shown in Fig. 5 for $h = 0.2t$ at zero temperature. Notice that $\chi_\lambda^i(n) = \chi_\lambda^i(1-n)$. We will in the following focus on filling fractions where the first two terms in Eq. (24) suffice to describe the most attractive pairing channel, i.e., the channel with the most negative coefficient χ_λ^i . Regions where this does not simultaneously hold for both susceptibilities, because of significant or dominant

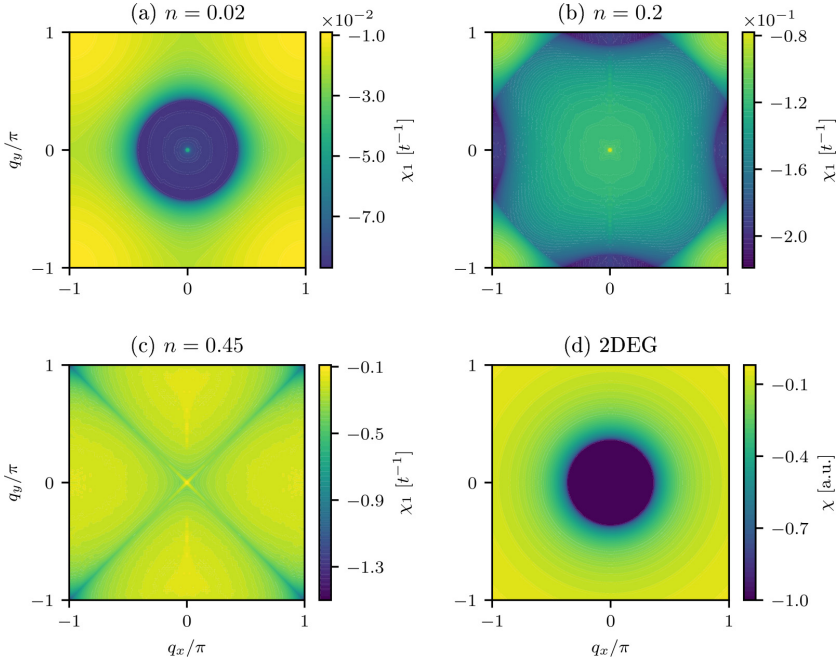


FIG. 4. Plot of numerically calculated susceptibilities for the majority band at filling fraction (a) $n = 0.02$, (b) $n = 0.2$, and (c) $n = 0.45$, which is close to half-filling of the band. The spikes at $\mathbf{q} = 0$ are numerical divergences that do not contribute to the results when expanding in square lattice harmonics. The susceptibility in the 2DEG case with Zeeman splitting treated in Refs. [4,7], $\chi(\mathbf{q}) \propto -1 + \text{Re}\sqrt{q^2 - (2k_F)^2}/q$, is shown in panel (d) with $k_F/\pi = 0.2$ for comparison.

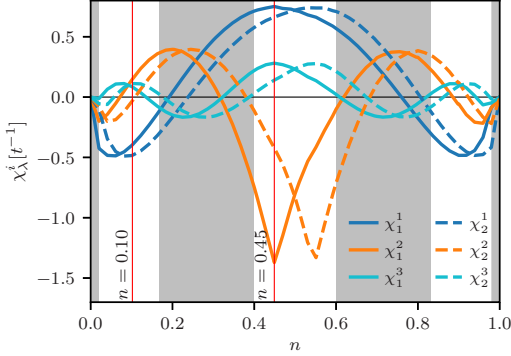


FIG. 5. Plot of expansion coefficients χ_λ^i in Eq. (24) as a function of filling fraction n for $h = 0.2t$ at zero temperature. Filling fraction $n = 0$ corresponds to a completely empty system, and $n = 1$ to two completely filled bands. The gray regions indicate where keeping only the first two terms in the expansion in Eq. (24) is not sufficient due to dominant contributions to attractive pairing from other square lattice harmonics, such as the χ_λ^3 term in Eq. (24).

contributions from other channels, are indicated by the gray regions in the figure. The coefficients χ_λ^i should, strictly speaking, be calculated at the temperature of the system, but we expect the superconducting transition temperature to be sufficiently low for this to be a good approximation.

The plots of the coefficients χ_λ^i in Fig. 5 illustrate two important points. First, the dominant attractive Kohn-Luttinger pairing channel depends strongly on the filling fraction. For instance, the dominant attractive channel for intermediate filling fractions differs from low and high filling fractions. This is related to the shape of the Fermi surfaces in these regions and could lead to significantly different \mathbf{k} dependences of the order parameters in these regions. Second, the plots also show that the majority and minority bands have the most negative expansion coefficient in different filling fraction intervals. Therefore, there exists a possibility that there can be a switching between bands with the highest T_c .

B. Momentum dependence of the order parameter

From the preceding subsection, we found that the potentially dominating momentum dependence of the superconducting gap due to the Kohn-Luttinger term in the interaction Eq. (15) could be any of the four functions in Eq. (25). If, however, the solution were to be determined by the second term in Eq. (15), the solution should be proportional to $\Gamma_\lambda(\mathbf{k})$ in Eq. (8), which can be rewritten in terms of $g_{x\pm iy}(\mathbf{k})$,

$$\Gamma_\lambda(\mathbf{k}) = \pi g_{x+iy}(\mathbf{k})(\xi_\lambda - \cos \delta)(\cos \theta - i \sin \theta) + \pi g_{x-iy}(\mathbf{k})(\xi_\lambda + \cos \delta)(\cos \theta + i \sin \theta). \quad (26)$$

Therefore, keeping only the dominant terms, the superconducting gap can be expanded using the four functions in Eq. (25),

$$\Delta_\lambda(\mathbf{k}) = \Delta_\lambda^{x+iy} g_{x+iy}(\mathbf{k}) + \Delta_\lambda^{x-iy} g_{x-iy}(\mathbf{k}) + \Delta_\lambda^x g_x(\mathbf{k}) + \Delta_\lambda^y g_y(\mathbf{k}). \quad (27)$$

C. Solutions close to the critical temperature T_c

The physically realizable solution of the gap equations is the solution which corresponds to a global minimum of the free energy. However, when solving the gap equations numerically using, e.g., a root solver, the solution might just as well correspond to a local minimum of the free energy. These solutions will have a lower T_c and will therefore not be realized when cooling down the system. In order to circumvent this problem, we instead calculate T_c and find the corresponding solution.

Close to and below T_c , we linearize the gap equations,

$$\Delta_\lambda(\mathbf{k}, T_c^-) = - \sum_{\mathbf{k}'\mu} \frac{g_{\lambda\mu}(\mathbf{k}, \mathbf{k}') \Delta_\mu(\mathbf{k}', T_c^-)}{|\xi_\mu(\mathbf{k}')|} \tanh\left(\frac{\beta_c |\xi_\mu(\mathbf{k}')|}{2}\right). \quad (28)$$

By multiplying this equation by $(2\pi)^2 g_j^\dagger(\mathbf{k})/V$, where $j = \{x + iy, x - iy, x, y\}$, and summing over the first Brillouin zone, we get a system of linear equations

$$\Delta_\lambda^i = \sum_j \sum_\mu \mathcal{M}_{\lambda\mu}^{ij}(T_c) \Delta_\mu^j, \quad (29)$$

where

$$\mathcal{M}_{\lambda\mu}^{ij}(T_c) = - \frac{(2\pi)^2}{V} \sum_{\mathbf{k}'} \left[\left(\sum_{\mathbf{k}} g_{\lambda\mu}(\mathbf{k}, \mathbf{k}') g_j^\dagger(\mathbf{k}) \right) \times \frac{g_i(\mathbf{k}')}{|\xi_\mu(\mathbf{k}')|} \tanh\left(\frac{\beta_c |\xi_\mu(\mathbf{k}')|}{2}\right) \right], \quad (30)$$

which may conveniently be written in the form

$$\vec{\Delta} = \mathcal{M}(T_c) \vec{\Delta}. \quad (31)$$

Here, $\vec{\Delta} = (\Delta_1^{x+iy}, \Delta_1^{x-iy}, \dots, \Delta_2^y)^T$. Thus, for a nontrivial solution to exist we require that $\det(\mathcal{M}(T_c)) = 0$, which allows for a computation of T_c . In cases where this holds for multiple temperatures, the highest T_c corresponds to the channel where superconductivity actually occurs. When T_c is determined, $\vec{\Delta}$ is found by calculating the eigenvector of $\mathcal{M}(T_c)$ corresponding to eigenvalue 1. The eigenvector only gives information about the relative size of the coefficients in Eq. (27), not the absolute scale. This is nonetheless enough information to determine the dominant momentum dependence of the order parameter close to T_c , and hence in which channel superconductivity first appears upon cooling.

IV. RESULTS AND DISCUSSION

Using the procedure described in the previous section, we have calculated the eigenvector of $\mathcal{M}(T_c)$, focusing on filling fractions $n = 0.1$ and $n = 0.45$. These values are indicated in Fig. 5. All results are obtained with $h = 0.2t$. For $n = 0.1$, the results as a function of tilt angle δ at $\theta = 0$ is shown in Fig. 6. We see that for a pure out-of-plane field, $\delta = 0$, $\Delta_1(\mathbf{k}) \propto \sin k_x + i \sin k_y$, which for small momenta corresponds to a chiral $k_x + ik_y$ order parameter. For a pure in-plane field in the x direction, $\Delta_1(\mathbf{k}) \propto \sin k_y$, which corresponds to a k_y dependence in the low- $|\mathbf{k}|$ limit. This is in agreement with the results of Lake *et al.* [7]. It is important to note that when calculating the eigenvectors at T_c , we do not get information

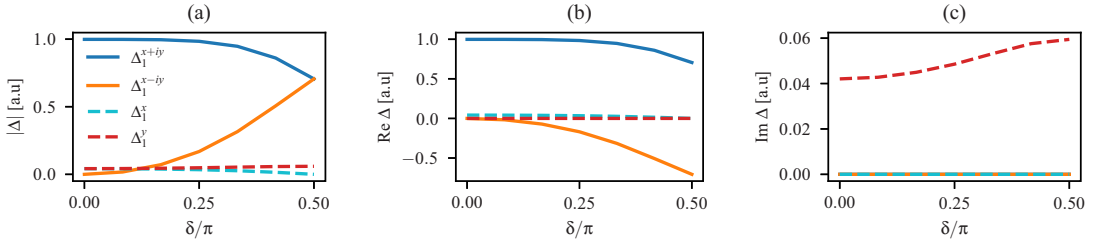


FIG. 6. Plot of the (a) absolute value, (b) real part, and (c) imaginary part of the dominant elements of the eigenvector of $\mathcal{M}(T_c)$ corresponding to eigenvalue 1 as a function of δ for $n = 0.1$ and $\theta = 0$. The terms proportional to the function $g_{x\pm iy}(\mathbf{k})$ are the dominant terms in $\Delta_1(\mathbf{k})$. $\Delta_2(\mathbf{k}) = 0$, not shown in the plot.

about the absolute value of the gaps, nor the relative size of the gap coefficients between, e.g., $\delta = 0$ and $\delta = \pi$.

Rotating the magnetic field in the xy plane, the \mathbf{k} dependence of the gap also changes accordingly, from a pure $\sin k_y$ dependence for $\theta = 0$, to a pure $\sin k_x$ dependence for $\theta = \pi/2$, as seen from the values of the coefficients in Fig. 7(a). This change coincides with the rotation of the center momentum \mathbf{q} in Eq. (5). The reason for this might be that the superconducting state is of FFLO kind whenever there is an in-plane component of the field. In the above calculations, we

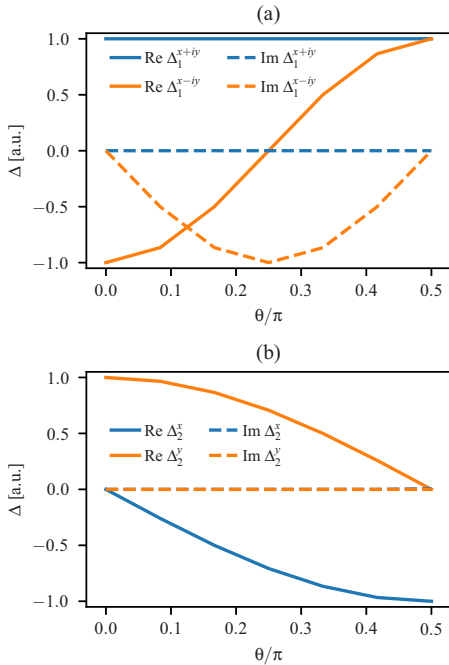


FIG. 7. Plot of dominating terms of the eigenvector as a function of θ for pure in-plane magnetic field and filling fraction (a) $n = 0.1$ and (b) $n = 0.45$. In the small- $|\mathbf{k}|$ limit, the \mathbf{k} dependence is changed from pure k_y to a pure k_x as the field is rotated. The overall phase is chosen such that the dominating contribution at $\theta = 0$ is real.

neglected the shift in the center momentum of the Fermi levels, Eq. (5), since they lead to higher order corrections. However, since the Fermi levels in fact are shifted, the Cooper pairs have a finite center momentum $2\mathbf{q}$ and thus are FFLO Cooper pairs. This is in agreement with Ref. [7].

Though the majority band has the highest T_c here, we see from Fig. 5 that also the minority band is attractive in the $g_{x\pm iy}$ channel for low filling fractions, in contrast to what has been found in other studies with quadratic dispersions [4,7]. Instead of being completely flat for $|\mathbf{k} - \mathbf{k}'| < 2|\mathbf{k}_{F\lambda}|$, as in the quadratic case, the susceptibility develops a dome in this region when increasing the filling fraction. In this way, the susceptibility on the majority band also becomes \mathbf{k} -dependent for interactions between particles close to the Fermi surface on the minority band, leading to the possibility of attractive interactions. We therefore expect that the minority band becomes superconducting at some finite temperature lower than T_c on the majority band.

Performing similar calculations close to half-filling, with $n = 0.45$, we find that the momentum dependence for the order parameter is dominated by the functions $g_x(\mathbf{k})$ and $g_y(\mathbf{k})$. Moreover, superconductivity is now induced on the minority band at T_c , as shown in Fig. 8. The value $n = 0.45$ is close to the filling fraction for which the majority band is half-filled, which corresponds to a van Hove singularity in the density of states of the majority band. The fact that the minority band has the highest T_c can thus be explained by the vast number of particles on the majority band which can mediate an effective intraband interaction. Again, the functional form of the gap is changed by rotating the magnetic field: When $\delta = 0$, $\Delta_2(\mathbf{k}) \propto \sin k_x \cos k_y - i \cos k_x \sin k_y$, which in the small- $|\mathbf{k}|$ limit corresponds to $k_x - ik_y$, and thus has the opposite chirality compared to the $n = 0.1$ case. For a pure in-plane field, we get $\Delta_2(\mathbf{k}) \propto \cos k_x \sin k_y$, which for small momenta corresponds to a pure k_y dependence. As for $n = 0.1$, rotating the field in-plane changes the \mathbf{k} dependence, as shown in Fig. 7(b).

Since the coefficients χ_λ^i have the symmetry $\chi_\lambda^i(n) = \chi_\lambda^i(1-n)$, we have also performed the above analysis for $n = 0.9$ and $n = 0.55$. In both cases, superconductivity is now present on the opposite band compared to the $n = 0.1$ and $n = 0.45$ cases, again with helicity $k_x + ik_y$ for $\lambda = 1$ and $k_x - ik_y$ for $\lambda = 2$. Therefore, it appears that a superconducting state with the same helicity as the band is favored [7].

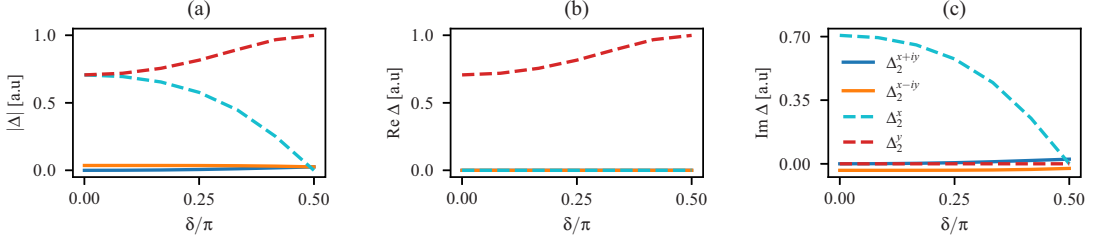


FIG. 8. Plot of the (a) absolute value, (b) real part, and (c) imaginary part of the dominant elements of the eigenvector of $\mathcal{M}(T_c)$ corresponding to eigenvalue 1 as a function of δ for $n = 0.45$ and $\theta = 0$. The terms proportional to the functions $g_x(\mathbf{k})$ and $g_y(\mathbf{k})$ are the dominant terms in $\Delta_2(\mathbf{k})$, which differs from the $n = 0.1$ case in Fig. 6. $\Delta_1(\mathbf{k}) = 0$, not shown in the plot.

In both previous cases, only one band is superconducting at T_c . This indicates that the second term in Eq. (15) does not contribute significantly to the superconducting pairing, as this would lead to simultaneous superconductivity on both bands. Moreover, from the form of $\Gamma_\lambda(\mathbf{k})$, we see that this term should lead to superconductivity of opposite chirality of what was found here, $k_x \mp ik_y$ on the majority/minority band [7]. Notice also that it is in principle possible to read off the dominating functional form of the superconducting gap directly from Fig. 5.

Finally, we have found that the value of α_R/h has no impact on T_c , while it depends strongly on the value of U/t . These are indications that the Kohn-Luttinger term in the interaction is responsible for the physically realizable superconducting order, and thus due to pure intraband interactions. This allows to make some predictions regarding parts of the gray regions in Fig. 5, where the χ_λ^3 term is the dominating attractive term. From the above results, it is reasonable to assume that the solution in these regions is of the form $\Delta_\lambda(\mathbf{k}) = \Delta_\lambda^{x,2y} g_x(k_x, 2k_y) + \Delta_\lambda^{y,2y} g_y(k_x, 2k_y) + \Delta_\lambda^{x,2x} g_x(2k_x, k_y) + \Delta_\lambda^{y,2x} g_y(2k_x, k_y)$, with the same small- $|\mathbf{k}|$ functional form as found above. This, however, has not been checked explicitly.

The fact that superconductivity is not proximity induced on the opposite band by the second term in Eq. (15), requires that $\Delta_\lambda(\mathbf{k})$ satisfies

$$\sum_{\mathbf{k}} \frac{\Gamma_\lambda^\dagger(\mathbf{k}) \Delta_\lambda(\mathbf{k})}{|\xi_\lambda(\mathbf{k})|} \tanh\left(\frac{\beta |\xi_\lambda(\mathbf{k})|}{2}\right) = 0. \quad (32)$$

Using this requirement, we derive an ansatz for the functional form of the superconducting gaps,

$$\begin{aligned} \Delta_1(\mathbf{k}) = & \Delta_1^1 \left[\frac{1 + \cos \delta}{\sqrt{2(1 + \cos^2 \delta)}} (\cos \theta - i \sin \theta) g_{x+iy}(\mathbf{k}) \right. \\ & \left. - \frac{1 - \cos \delta}{\sqrt{2(1 + \cos^2 \delta)}} (\cos \theta + i \sin \theta) g_{x-iy}(\mathbf{k}) \right] \\ & + \Delta_1^2 \left[\frac{\cos \theta - i \cos \delta \sin \theta}{\sqrt{1 + \cos^2 \delta}} g_y(\mathbf{k}) \right. \\ & \left. - \frac{\sin \theta + i \cos \delta \cos \theta}{\sqrt{1 + \cos^2 \delta}} g_x(\mathbf{k}) \right], \end{aligned} \quad (33a)$$

$$\begin{aligned} \Delta_2(\mathbf{k}) = & \Delta_2^1 \left[\frac{1 + \cos \delta}{\sqrt{2(1 + \cos^2 \delta)}} (\cos \theta + i \sin \theta) g_{x-iy}(\mathbf{k}) \right. \\ & \left. - \frac{1 - \cos \delta}{\sqrt{2(1 + \cos^2 \delta)}} (\cos \theta - i \sin \theta) g_{x+iy}(\mathbf{k}) \right] \\ & + \Delta_2^2 \left[\frac{\cos \theta + i \cos \delta \sin \theta}{\sqrt{1 + \cos^2 \delta}} g_y(\mathbf{k}) \right. \\ & \left. - \frac{\sin \theta - i \cos \delta \cos \theta}{\sqrt{1 + \cos^2 \delta}} g_x(\mathbf{k}) \right], \end{aligned} \quad (33b)$$

where Δ_λ^i in general can depend on the field alignment angle. Using this ansatz to find T_c and the solution eigenvectors, we find the same results as presented above. Hence, we see that even though the results do not depend directly on the SOC strength, the fact that SOC is present affects the realized pairing symmetry [7]. The results of Ref. [14] indicate that this conclusion might not hold for all values of α_R/h , and an interesting development would therefore be to study this system for general SOC strengths.

The T_c quickly decreases with decreasing U/t , and for values in the regime set by the derivation of the gap equations, a numerical solution is impossible. Hence, we have performed the above analysis for a range of values of U/t and α_R/h , and found that the results were qualitatively unchanged. The facts that the results agree with Ref. [7] for small filling fractions and that T_c depends only on U/t indicate that the results presented above should be valid also for realistic values of U/t and α_R/h .

There could in principle exist a transition to a magnetic state, such as the antiferromagnetic phase found for the 2D repulsive Hubbard model at half-filling in the weak-coupling limit [30]. However, applying a Zeeman field splits the degenerate spin bands, and we therefore expect that no antiferromagnetic ordering can exist as long as $h > U$. Though the application of a Zeeman field could favor a ferromagnetic phase, other studies have indicated that ferromagnetic ordering does not appear in the weak-coupling limit of the 2D Hubbard model [30,31], a result we expect to hold also in the present case.

V. CONCLUSION

We have investigated the role of a weak spin-orbit coupling on a spin-polarized weakly repulsive Hubbard system on a square lattice. Performing an analysis along the same lines as done by Lake *et al.* [7] for the 2D electron gas, we found that

the superconducting order was caused by the SOC-independent Kohn-Luttinger term in the interaction. The pairing symmetry was, however, indirectly determined by the SOC: The realized superconducting gap has the same chirality as the band. We also found that the momentum dependence of the superconducting gap could be tuned by rotating the magnetic field and changing the filling fraction. The filling fraction also determines which band has the highest T_c .

ACKNOWLEDGMENTS

H.G.H. would like to thank F. N. Krogh for useful discussions. This work was supported by the Research Council of Norway through Grant No. 250985, ‘‘Fundamentals of Low-Dissipative Topological Matter’’, and through Grant No. 262633 Center of Excellence, ‘‘Center for Quantum Spintronics’’.

APPENDIX: EXPANSION OF SUSCEPTIBILITY IN SQUARE LATTICE HARMONICS

To the order we are working, we can set $\alpha_R = 0$ when calculating the susceptibility, Eq. (13). In this case, the dispersion in Eq. (4) has the symmetries of the C_{4v} group and is invariant under spatial inversion, $\mathbf{k} \rightarrow -\mathbf{k}$, 4-fold rotations, $(k_x, k_y) \rightarrow (k_y, -k_x)$, mirror operations, $(k_x, k_y) \rightarrow (-k_x, k_y)$, etc. Since we in Eq. (13) sum over the 1 BZ, it can be shown that the susceptibility has the same symmetries. The expansion of the susceptibility thus has to be invariant under the same operations, which greatly reduces the possible terms in the expansion. Since the susceptibility is even under inversions (only the SOC term breaks inversion symmetry, which is neglected here), the expansion must contain only even terms, which we write in a general form [32] as

$$\chi(\mathbf{q}) = \sum_{m,n} a_{mn} \cos(mq_x + nq_y), \quad (\text{A1})$$

where m and n are integers, and the band index has been dropped for notational simplicity. From the requirement $\chi(q_x, q_y) = \chi(-q_x, q_y)$, we find $a_{mn} = a_{m,-n} = a_{-m,n}$, and similarly from $\chi(q_x, q_y) = \chi(q_y, -q_x)$ we find $a_{mn} = a_{-n,m} = a_{nm}$. Using these relations, we simplify the above equation:

$$\chi(\mathbf{q}) = a_{00} + \sum_{(m,n)>0} 2a_{mn} [\cos(mq_x + nq_y) + \cos(mq_x - nq_y)]. \quad (\text{A2})$$

Separating the terms according to if $m = n$ or not, we get

$$\chi(\mathbf{q}) = D_{00}G_{00} + \sum_{m>n>0} D_{mn}G_{mn}(\mathbf{q}) + \sum_{m>0} [D_{0m}G_{0m}(\mathbf{q}) + D_{mm}G_{mm}(\mathbf{q})], \quad (\text{A3})$$

where we have redefined the expansion coefficients a_{mn} and defined the orthonormal functions

$$G_{00} = \frac{1}{2\pi}, \quad (\text{A4a})$$

$$G_{0m}(\mathbf{q}) = \frac{\cos mq_x + \cos mq_y}{2\pi}, \quad (\text{A4b})$$

$$G_{mm}(\mathbf{q}) = \frac{\cos mq_x \cos mq_y}{\pi}, \quad (\text{A4c})$$

$$G_{mn}(\mathbf{q}) = \frac{\cos mq_x \cos nq_y + \cos nq_x \cos mq_y}{\sqrt{2}\pi}. \quad (\text{A4d})$$

We now insert $\mathbf{q} = \mathbf{k} - \mathbf{k}'$ and rewrite the above functions in terms of products of functions of \mathbf{k} or \mathbf{k}' separately,

$$4\pi G_{0m}(\mathbf{k} - \mathbf{k}') = [(\sin mk_x + i \sin mk_y)(\sin mk'_x - i \sin mk'_y) + \text{H.c.}] + [\sin \rightarrow \cos],$$

$$\pi G_{mm}(\mathbf{k} - \mathbf{k}') = [(\cos mk_x \cos mk_y)(\cos mk'_x \cos mk'_y) + (\cos mk_x \sin mk_y)(\cos mk'_x \sin mk'_y)] + [\sin \leftrightarrow \cos],$$

$$\sqrt{2}\pi G_{mn}(\mathbf{k} - \mathbf{k}') = [(\cos mk_x \cos nk_y)(\cos mk'_x \cos nk'_y) + (\cos mk_x \sin nk_y)(\cos mk'_x \sin nk'_y) + (\sin mk_x \cos nk_y)(\sin mk'_x \cos nk'_y) + (\sin mk_x \sin nk_y)(\sin mk'_x \sin nk'_y)] + [n \leftrightarrow m].$$

Since the SOC is weak, the interaction can be regarded to be between particles of equal spin to the order we are working. Hence, the interaction must be odd in \mathbf{k} and \mathbf{k}' . In this way, we can neglect most of the above terms and are left with an expansion of the form

$$\chi(\mathbf{k} - \mathbf{k}') = \sum_m \chi^{0m} [g_{x+iy}(m\mathbf{k})g_{x-iy}(m\mathbf{k}') + \text{H.c.}] + \sum_m \chi^{mm} [g_x(m\mathbf{k})g_x(m\mathbf{k}') + g_y(m\mathbf{k})g_y(m\mathbf{k}')] + \sum_{m>n} \chi^{mn} [g_x(mk_x, nk_y)g_x(mk'_x, nk'_y) + g_y(mk_x, nk_y)g_y(mk'_x, nk'_y) + m \leftrightarrow n], \quad (\text{A5})$$

where $m, n > 0$ and we have used the functions defined in Eq. (25). The leading-order terms included in Eq. (24) correspond to the χ^{01} , χ^{11} , and χ^{21} terms in the above equation.

[1] W. Kohn and J. M. Luttinger, *Phys. Rev. Lett.* **15**, 524 (1965).
 [2] M. Yu. Kagan and A. V. Chubukov, *JETP Lett.* **50**, 517 (1989).
 [3] A. V. Chubukov, *Phys. Rev. B* **48**, 1097 (1993).
 [4] S. Raghu and S. A. Kivelson, *Phys. Rev. B* **83**, 094518 (2011).

[5] Yu. A. Bychkov and E. I. Rashba, *JETP Lett.* **39**, 78 (1984).
 [6] A. Manchon, H. C. Koo, J. Nitta, S. M. Frolov, and R. A. Duine, *Nat. Mater.* **14**, 871 (2015).
 [7] E. Lake, C. Webb, D. A. Pesin, and O. A. Starykh, *Phys. Rev. B* **93**, 214516 (2016).

- [8] M. Smidman, M. B. Salamon, H. Q. Yuan, and D. F. Agterberg, *Rep. Prog. Phys.* **80**, 36501 (2017).
- [9] L. P. Gor'kov and E. I. Rashba, *Phys. Rev. Lett.* **87**, 037004 (2001).
- [10] V. Barzykin and L. P. Gor'kov, *Phys. Rev. Lett.* **89**, 227002 (2002).
- [11] D. F. Agterberg and R. P. Kaur, *Phys. Rev. B* **75**, 064511 (2007).
- [12] O. Vafek and L. Wang, *Phys. Rev. B* **84**, 172501 (2011).
- [13] S. Raghu, S. A. Kivelson, and D. J. Scalapino, *Phys. Rev. B* **81**, 224505 (2010).
- [14] F. Loder, A. P. Kampf, and T. Kopp, *J. Phys.: Condens. Matter* **25**, 362201 (2013).
- [15] N. Reyren, S. Thiel, A. D. Caviglia, L. Fitting Kourkoutis, G. Hammerl, C. Richter, C. W. Schneider, T. Kopp, A.-S. Rüetschi, D. Jaccard, M. Gabay, D. A. Muller, J.-M. Triscone, and J. Mannhart, *Science* **317**, 1196 (2007).
- [16] A. D. Caviglia, S. Gariglio, N. Reyren, D. Jaccard, T. Schneider, M. Gabay, S. Thiel, G. Hammerl, J. Mannhart, and J.-M. Triscone, *Nature (London)* **456**, 624 (2008).
- [17] S. Gariglio, N. Reyren, A. D. Caviglia, and J. Triscone, *J. Phys. Condens. Matter* **21**, 164213 (2009).
- [18] A. Brinkman, M. Huijben, M. van Zalk, J. Huijben, U. Zeitler, J. C. Maan, W. G. van der Wiel, G. Rijnders, D. H. A. Blank, and H. Hilgenkamp, *Nat. Mater.* **6**, 493 (2007).
- [19] J. A. Bert, B. Kalisky, C. Bell, M. Kim, Y. Hikita, H. Y. Hwang, and K. A. Moler, *Nat. Phys.* **7**, 767 (2011).
- [20] L. Li, C. Richter, J. Mannhart, and R. C. Ashoori, *Nat. Phys.* **7**, 762 (2011).
- [21] M. Sachs, D. Rakhmilevitch, M. B. Shalom, S. Shefler, A. Palevski, and Y. Dagan, *Phys. C* **470**, S746 (2010).
- [22] D. A. Dikin, M. Mehta, C. W. Bark, C. M. Folkman, C. B. Eom, and V. Chandrasekhar, *Phys. Rev. Lett.* **107**, 056802 (2011).
- [23] M. B. Shalom, M. Sachs, D. Rakhmilevitch, A. Palevski, and Y. Dagan, *Phys. Rev. Lett.* **104**, 126802 (2010).
- [24] A. D. Caviglia, M. Gabay, S. Gariglio, N. Reyren, C. Cancellieri, and J. M. Triscone, *Phys. Rev. Lett.* **104**, 126803 (2010).
- [25] K. Michaeli, A. C. Potter, and P. A. Lee, *Phys. Rev. Lett.* **108**, 117003 (2012).
- [26] P. Fulde and R. A. Ferrell, *Phys. Rev.* **135**, A550 (1964).
- [27] A. Larkin and Y. Ovchinnikov, *Sov. Phys. JETP* **20**, 762 (1965).
- [28] J. R. Schrieffer and P. A. Wolff, *Phys. Rev.* **149**, 491 (1966).
- [29] S. Bravyi, D. P. Di Vincenzo, and D. Loss, *Ann. Phys. (NY)* **326**, 2793 (2011).
- [30] J. E. Hirsch, *Phys. Rev. B* **31**, 4403 (1985).
- [31] H. Q. Lin and J. E. Hirsch, *Phys. Rev. B* **35**, 3359 (1987).
- [32] E. Otnes, M.Sc. thesis, Norwegian University of Science and Technology, Trondheim, Norway, 1997.

Reference

M. Amundsen, H. G. Hugdal, A. Sudbø and J. Linder,
Vortex spin valve on a topological insulator.
Physical Review B, **98**, 144505 (2018).

Contributions

MA performed the 2D numerical simulations, based on a formalism developed by HGH, with support from HGH, AS and JL. MA drafted the manuscript. All authors contributed to the discussions of the physics and the revision of the final manuscript. HGH had a minor supporting role in this collaboration, assisting with the interpretation and discussion of the results, and contributing to the revision of the final manuscript.

Vortex spin valve on a topological insulatorMorten Amundsen,^{*} Henning G. Hugdal, Asle Sudbø, and Jacob Linder*Center for Quantum Spintronics, Department of Physics, Norwegian University of Science and Technology, NO-7491 Trondheim, Norway*

(Received 11 June 2018; published 5 October 2018)

Spin-valve structures are usually associated with the ability to modify the resistance of electrical currents. We here demonstrate a profoundly different effect of a spin-valve. In combination with a topological insulator and superconducting materials, we show that a spin-valve can be used to toggle quantum vortices in and out of existence. In the antiparallel configuration, the spin valve causes superconducting vortex nucleation. In the parallel configuration, however, no vortices appear. This switching effect suggests a new way to control quantum vortices.

DOI: [10.1103/PhysRevB.98.144505](https://doi.org/10.1103/PhysRevB.98.144505)**I. INTRODUCTION**

Topological insulators (TI) are fascinating materials which are insulating in their bulk, but have topologically protected conducting surface states [1]. When a conventional s -wave superconductor is placed in contact with a topological insulator, the superconducting correlations induced on the TI surface gain a topological character [2]. This may give rise to a range of exotic phenomena, such as the appearance of Majorana bound states at vortices [3], which provides an exciting avenue toward non-Abelian statistics and topological quantum computation [4].

A particularly interesting property of the surface states of a TI is the presence of spin-momentum locking. By proximity coupling both superconducting and ferromagnetic elements to the topological insulator, this may be used to create complex supercurrent density distributions [5]. A key observation is that the exchange field enters the Hamiltonian for the surface states of a TI in the same way as the magnetic vector potential does, due to the spin-momentum locking. Because of this, one might expect that quantum vortices with a phase-winding could be induced by an exchange field alone on the surface of a TI in contact with a superconductor, without the need of any external magnetic flux. The study of superconducting vortices induced in nonsuperconducting materials via proximity has recently attracted attention both theoretically [5–9] and experimentally [10].

In this paper, we show that a spin-valve structure combined with a topological insulator and superconducting materials can be used to toggle quantum vortices in and out of existence. These vortices behave in the exact same way as conventional proximity-induced vortices in superconducting heterostructures, except for the crucial difference of being generated by an inhomogeneous in-plane exchange field, rather than the orbital effect of an applied magnetic flux. Indeed, we will show that vortex nucleation may be understood in terms of the presence of an effective flux created by the exchange field, completely analogously to the flux produced by a magnetic vector potential. An advantage of using an exchange

field to generate vortices is that it provides greater freedom in studying inhomogeneous effective flux densities than is possible with an applied perpendicular magnetic field, and hence may give rise to more complex vortex patterns. The spin valve consists of two ferromagnetic layers which can be either in a parallel (P) or antiparallel (AP) configuration. In the P configuration, the spin valve does not cause superconducting vortex nucleation. In contrast, vortices can exist in the AP configuration. This switching effect suggests a new way to control quantum vortices in heterostructures. The precise conditions under which this can occur will be detailed below.

II. THEORY AND MODEL

To demonstrate the spin-valve effect, we consider the system shown in Fig. 1. Two superconductors are placed on top of a topological insulator, maintaining a good electrical contact to induce a measurable proximity effect. This can, for instance, be a Nb-Bi₂Te₃-Nb heterostructure, in which the presence of a Josephson effect has been experimentally verified [11]. Between the superconductors is placed a pair of ferromagnets. This creates an effective SFS Josephson weak link on the two-dimensional surface of the TI via the proximity effect. The distance between the superconductors is $L = 2\xi$, where ξ is the superconducting coherence length, which is assumed to also be the width of the system. The exchange field in the ferromagnet is directed along the x axis (between the superconductors). The magnitude of the exchange field is constant in the x direction, but can be toggled between either a P or AP configuration. Such a system can be experimentally designed by separating the two ferromagnets by a thin nonmagnetic spacer layer. If the ferromagnets have different coercive fields, one may toggle between configurations, for instance, by heating the system to above the critical temperature of the superconductors, T_c , apply a magnetic field in the x direction large enough to switch the magnetization in one of the layers, and then cool the system to below T_c . To ensure different coercive fields, the ferromagnets may either be different materials or have different sizes.

The surface of the three-dimensional diffusive topological insulator here considered may be described by using quasiclassical theory [12,13]. In the following, we use units

^{*}Corresponding author: morten.amundsen@ntnu.no

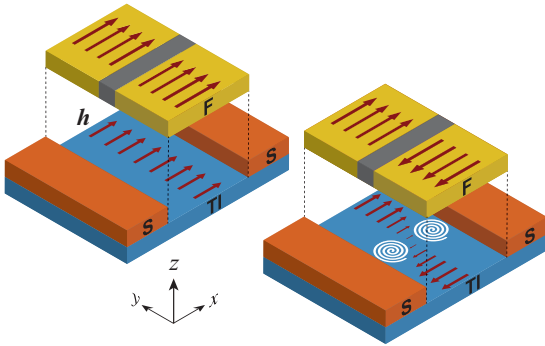


FIG. 1. The geometry considered. Two superconductors and a spin valve are placed on top of a topological insulator. The spatial variation of the exchange field induced by the antiparallel configuration of the ferromagnets creates vortices in the TI. The spin valve is shown lifted for clarity.

where $\hbar = 1$. In equilibrium, all physical observables may be computed from the 2×2 retarded Green's function

$$G = \begin{pmatrix} g & f \\ \tilde{f} & -g \end{pmatrix}, \quad (1)$$

where g and f are the normal and anomalous Green's functions, respectively, and $\tilde{f}(\varepsilon) = f^*(-\varepsilon)$. G has structure only in particle-hole space, and the spin structure has been factored out by a unitary transformation to take the spin-momentum locking into account. A detailed description of this procedure is given in Ref. [14]. In the diffusive limit, the Green's function is governed by the Usadel equation [15]

$$2D\hat{\nabla} \cdot (G\hat{\nabla}G) = [\varepsilon\sigma_3, G], \quad (2)$$

where $\hat{\nabla}G = \nabla G - \frac{i}{v_F}[\mathbf{h}\sigma_3, G]$, \mathbf{h} is the in-plane exchange field, D is the diffusion constant, ε is the quasiparticle energy, v_F is the Fermi velocity, and σ_3 is the third Pauli matrix. We solve Eq. (2) in the region of the TI located between the superconductors, which we consider as large enough to be described by their bulk expressions, G_{BCS} , as given in Ref. [14]. The numerical method we employ is described in detail in Ref. [16], and only slight modifications are necessary to adapt it to topological insulators. We neglect the inverse proximity effect, which is a good approximation as long as the Fermi level μ_{TI} in the TI is substantially different from $\pm\sqrt{2m v_F^2 \mu_S}$, where m and μ_S are the electron mass and Fermi level in the superconductor, respectively [17]. We further assume transparent boundary conditions to the superconductors, while the vacuum interfaces are described by the Neumann boundary condition $\hat{\nabla}G = 0$. We note in particular that the in-plane exchange field enters Eq. (2) in precisely the same way as does the vector potential in a normal metal. A consequence of this is that the system will react to a spatial variation in \mathbf{h} in the same way as if an effective flux $\Phi_h = \int_A \nabla \times \mathbf{h} \, d\mathbf{r}$ is applied, where A is the area of the TI surface. This means that for a sufficiently large inhomogeneous exchange field, vortices may appear. Note that for a curl-free inhomogeneous \mathbf{h} , vortices do not appear. An analogy to an SNS junction with a uniform applied magnetic flux is found by considering an

exchange field $\mathbf{h} = -h_0 y \hat{x}$. In the Fraunhofer limit, where the width of the junction (in the y direction) is much larger than its length, the number of vortices in the system is equal to the number of flux quanta that is applied. The relevant flux quantum for the exchange-field-induced vortices in the present paper is then $\Phi_0 = \pi v_F$. The square geometry of the system studied herein influences the number and position of the vortices. However, the number of flux quanta produced by the effective flux Φ_h still remains a good estimate for the number of vortices.

From the retarded Green's function, G , the density of states, normalized by its value at the Fermi level, may be computed as $N(\mathbf{r}, \varepsilon) = \text{Re } g(\mathbf{r}, \varepsilon)$, with $g(\mathbf{r}, \varepsilon)$ defined in Eq. (1). Furthermore, the pair correlation in the TI, which is a measure of the strength of the superconducting correlations induced by the proximity effect, may be computed from

$$\Psi(\mathbf{r}) = N_0 \int d\varepsilon [f(\mathbf{r}, \varepsilon) - f(\mathbf{r}, -\varepsilon)] \tanh \frac{\beta\varepsilon}{2}, \quad (3)$$

where $\beta = 1/k_B T$, T is the temperature and N_0 is the density of states at the Fermi level. Finally, the current density is given as

$$\mathbf{J}(\mathbf{r}) = J_0 \int d\varepsilon \text{Re} \left[f \nabla \tilde{f} - \tilde{f} \nabla f - \frac{4i}{v_F} \mathbf{h} f \tilde{f} \right] \tanh \frac{\beta\varepsilon}{2}, \quad (4)$$

with $J_0 = N_0 e D$.

III. RESULTS AND DISCUSSION

We consider an in-plane exchange field and set $\mathbf{h} = h_x(y)\hat{x}$. The necessary (but not sufficient) requirement for inducing vortices is then that $\partial_y h_x \neq 0$. To be specific, we assume that the AP configuration of the ferromagnets induces an antisymmetric exchange field with a spatial variation given by $\mathbf{h} = h_0 \tanh(\alpha y/L)\hat{x}$, where α is a shape factor which determines the size of the transition region. We note that the size of the effective flux Φ_h , and thus the net number of vortices introduced, does not depend on the specific shape of the exchange field since, by the fundamental theorem of calculus, $\Phi_h = L[h(L/2) - h(-L/2)]$. To model the P configuration, a constant exchange field $\mathbf{h} = h_0 \hat{x}$ is assumed.

The two configurations show markedly different behaviors, as is shown in Fig. 2 where we set $\alpha = 20$ (the results are qualitatively the same for all $\alpha \gg 1$, which corresponds to the magnetization saturating before it reaches the outer edges of the magnetic regions). The uniform exchange field in the P configuration introduces a phase shift between the superconductors, so that a net supercurrent flows between them. Otherwise, the system is unaffected. The pair correlation decays towards the center of the TI, but remains nonzero everywhere, as seen in Fig. 2(a). In the AP configuration, there is no net current due to the antisymmetry of the exchange field, which induces an antisymmetric current-density distribution. Furthermore, the exchange field produces a net effective flux $\Phi_h \simeq 2h_0 L$, which may cause vortex nucleation. This is shown in Fig. 2(b) for $h_0 = 2v_F/\xi$. In this case, two vortices appear along the x axis—the region of largest effective flux density. Figures 2(c) and 2(d) show the spatial distribution of the density of states at zero energy for the two configurations. In the P configuration, $N(\mathbf{r}, 0)$ is clearly uniformly

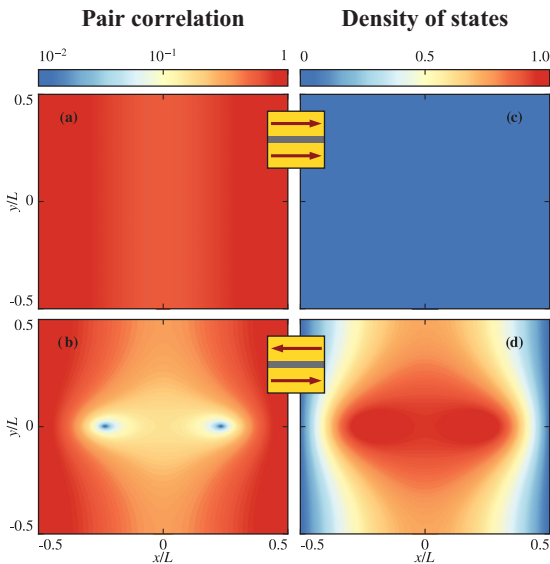


FIG. 2. A comparison of the results for the parallel (upper row) and antiparallel (lower row) configuration of the spin valve. (a) and (b) show the absolute value of the pair correlation for the two configurations, as given by Eq. (3). The localized zeros in the antiparallel case indicate vortices. (c) and (d) show the density of states N at zero energy, which is gapped in the parallel configuration and admits a normal state solution at the location of the vortices in the antiparallel configuration.

suppressed throughout the entire system, as is expected due to the presence of a proximity-induced energy gap. In the AP configuration, on the other hand, the presence of the vortices, which have normal cores, leads to a more complicated topography of the density of states, wherein a normal state value of $N = 1$ is found in localized regions surrounding the vortices. The topological nature of these vortices is illustrated by the phase of the pair correlation, which is shown in Fig. 3(a). It is seen that for any closed contour around a vortex, it is necessary to traverse two discontinuous jumps of value π , giving a total winding of 2π . This is the hallmark of a vortex. Another signature of vortices is circulating supercurrents, as is shown in Fig. 3(b), in which streamlines of the current density, as given by Eq. (4), are plotted. Since the eddies produce an out-of-plane magnetic field, which should be detectable using, for instance, a scanning nanoSQUID device [18], this provides means for experimentally verifying the presence of vortices. It is interesting to note that there are currents circulating around the origin of the system, as seen in Fig. 3(b). A conventional vortex has a phase gradient that goes like $\nabla\phi \sim \frac{2\pi n}{r}$, where n is the winding number of the vortex, and r is the radius from its center. This means that the phase gradient diverges at the vortex core, leading to a suppression of the pair correlation. The observed flow pattern in the present case is not accompanied by such a suppression, and is hence not a vortex in the topological sense. Rather, it is caused by an accidental cancellation of the phase gradient at the origin due to the applied exchange field. This can be seen from the current density

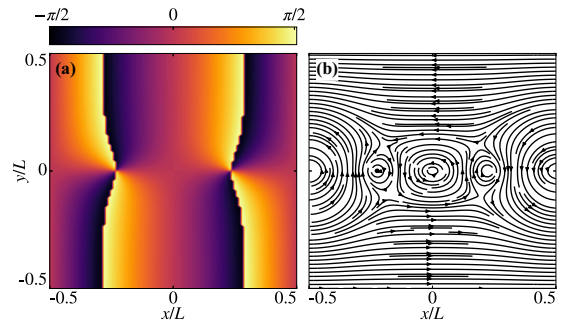


FIG. 3. Evidence of vortex nucleation. (a) The phase of the pair correlation, showing a winding of 2π around each of the vortices. (b) Streamlines of the current density, as given by Eq. (4), which gives its direction at every point, showing that supercurrents circulate around the vortices.

$\mathbf{J} \sim \nabla\phi$. The x component, J_x , is antisymmetric about the x axis due to the antisymmetric exchange field. It therefore vanishes along the x axis. The y component on the other hand, must change direction as one moves along the x axis from one vortex to the other. J_y is therefore zero in the origin as well. This means that the magnitude of the current is zero at this point, thereby producing the observed current pattern. We emphasize that this eddy is not topologically protected, and may be removed by minor perturbations of the exchange field.

The behavior of the vortices is greatly influenced by the symmetries of the system. The model considered herein is symmetric about the y axis, and either symmetric or antisymmetric about the x axis, depending on the applied exchange field. This means that a single vortex pair can only be located on symmetrically opposite sides of the origin, along either the x or the y axis without breaking the symmetries of the system. For an increasing exchange field amplitude, h_0 , the AP configuration will lead to the appearance of an increasing number of vortices. The vortices enter the system from the vacuum edges, and must do so in pairs from opposite sides. Due to the low flux density near the vacuum edges, even the slightest additional increase in h_0 will cause the vortices to translate along the y axis, meet at the origin, and stabilize at a location along the x axis, as shown in Fig. 2. As h_0 is increased further, vortices accumulate along the x axis. This will, in turn, result in a complete suppression of the density of states in their vicinity, whereas superconductivity will still be present closer to the vacuum edges. We point out that while the present discussion relies on the symmetry, the symmetry is not crucial to observe the spin-valve effect. The only requirement is the ability to switch between a rotational and an irrotational exchange field. Another interesting feature of the inhomogeneous effective flux density is that it leads to significant vortex pinning. Indeed, if the superconducting leads are given a phase difference, for instance by applying a current bias, so that a net supercurrent flows between them, the vortex positions are only slightly perturbed. This is in contrast to the behavior of conventional SNS Josephson weak links with an applied magnetic flux, where a phase difference leads to a transversal shift of the vortex positions [6, 7].

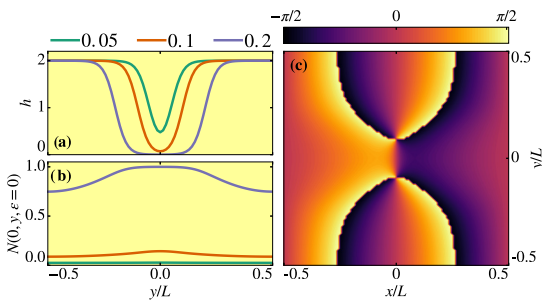


FIG. 4. An analysis of the effect of the spacer layer. (a) The transversal distribution of the exchange field h for increasing size δ of the central region of suppressed magnetization. (b) The zero-energy density of states along the y axis for the exchange fields in (a). (c) The phase of the pair correlation for the case where $\delta = 0.2$, showing the appearance of a vortex–antivortex pair.

The exchange field induced on the topological insulator is assumed generated by two separate ferromagnets with an intermediate spacer layer. In the P configuration, this will likely create a suppression of the induced exchange field beneath the spacer. The resulting $\partial_y h_x \neq 0$ could in itself induce vortices in the system, in addition to the switching-effect we have described above. To investigate this, we consider a P exchange field $\mathbf{h}(y) = h_0\{1 + 0.5(\tanh[\alpha(y/L - \delta)] - \tanh[\alpha(y/L + \delta)])\}\hat{x}$, where δ is another shape factor indicating the width of the central dip in $h(y)$. The exchange field is plotted along the transversal direction y for increasing δ in Fig. 4(a). Since the exchange field is symmetric, the effective flux $\Phi_h = 0$. Nonetheless, topological excitations in the form of vortex–antivortex pairs may be induced. It is clear that this can happen if an effective flux greater than Φ_0 passes through any subdomain of the system within which vortex nucleation is allowed by symmetry. The central dip in the exchange field will cause vortices to nucleate where $\nabla \times \mathbf{h}$ is largest and positive, at $y = \delta L$, whereas antivortices will nucleate at $y = -\delta L$, where the largest negative effective flux

density is found. To conserve the symmetry of the system, a single vortex–antivortex pair must appear along the y axis. The first appearance of such a pair may therefore be gauged from the zero-energy density of states along this line, as is shown in Fig. 4(b). It is seen that N remains gapped for a sufficiently small dip, as exemplified by $\delta = 0.05$ and $\delta = 0.1$. This shows that the vortex spin-valve effect is robust against small deviations from a constant exchange field due to the presence of the spacer layer. For $\delta = 0.2$, however, a vortex–antivortex pair appears, and the gap in the density of states closes. This is verified from the phase of the pair correlation, shown in Fig. 4(c), where the two vortices along the y axis are seen to have opposite windings.

IV. CONCLUSION

We have considered a Josephson weak link made on the surface of a topological insulator, onto which is proximity coupled two ferromagnets separated by a spacer. By using microscopic calculations, we have shown that it is possible to switch vortices on and off in this system solely by toggling between an AP and P configuration of the ferromagnets, respectively. We further show that this vortex spin-valve effect is robust against small deviations in the induced exchange field caused by the spacer layer.

An interesting direction for future work would be to study the effect of an electrically induced phase gradient in the superconducting leads, which has recently been shown to generate vortices in proximitized normal metals [9].

ACKNOWLEDGMENTS

J.L. and A.S. acknowledge funding from the Research Council of Norway Center of Excellence Grant No. 262633, Center for Quantum Spintronics. J.L. and M.A. also acknowledge funding from the NV faculty at the Norwegian University of Science and Technology. A.S. and H.G.H. acknowledge funding from the Research Council of Norway Grant No. 250985. J.L. acknowledges funding from Research Council of Norway Grant No. 240806.

- [1] M. Z. Hasan and C. L. Kane, *Rev. Mod. Phys.* **82**, 3045 (2010).
- [2] X.-L. Qi and S.-C. Zhang, *Rev. Mod. Phys.* **83**, 1057 (2011).
- [3] L. Fu and C. L. Kane, *Phys. Rev. Lett.* **100**, 096407 (2008).
- [4] C. Nayak, S. H. Simon, A. Stern, M. Freedman, and S. Das Sarma, *Rev. Mod. Phys.* **80**, 1083 (2008).
- [5] A. Zyuzin, M. Alidoust, and D. Loss, *Phys. Rev. B* **93**, 214502 (2016).
- [6] J. C. Cuevas and F. S. Bergeret, *Phys. Rev. Lett.* **99**, 217002 (2007).
- [7] F. S. Bergeret and J. C. Cuevas, *J. Low Temp. Phys.* **153**, 304 (2008).
- [8] V. P. Ostrokh, B. Baxevanis, A. R. Akhmerov, and C. W. J. Beenakker, *Phys. Rev. B* **94**, 094514 (2016).
- [9] M. Amundsen, J. A. Ouassou, and J. Linder, *Phys. Rev. Lett.* **120**, 207001 (2018).
- [10] D. Roditchev, C. Brun, L. Serrier-Garcia, J. C. Cuevas, V. H. L. Bessa, M. V. Milošević, F. Debontridder, V. Stolyarov, and T. Cren, *Nat. Phys.* **11**, 332 (2015).
- [11] M. Veldhorst, M. Snelder, M. Hoek, T. Gang, V. K. Guduru, X. L. Wang, U. Zeitler, W. G. van der Wiel, A. A. Golubov, H. Hilgenkamp, and A. Brinkman, *Nat. Mater.* **11**, 417 (2012).
- [12] J. Rammer and H. Smith, *Rev. Mod. Phys.* **58**, 323 (1986).
- [13] W. Belzig, F. K. Wilhelm, C. Bruder, G. Schön, and A. D. Zaikin, *Superlattices Microst.* **25**, 1251 (1999).
- [14] H. G. Hugdal, J. Linder, and S. H. Jacobsen, *Phys. Rev. B* **95**, 235403 (2017).
- [15] K. D. Usadel, *Phys. Rev. Lett.* **25**, 507 (1970).
- [16] M. Amundsen and J. Linder, *Sci. Rep.* **6**, 22765 (2016).
- [17] H. G. Hugdal, M. Amundsen, J. Linder, and A. Sudbø, [arXiv:1808.03650](https://arxiv.org/abs/1808.03650).
- [18] D. Vasyukov, Y. Anahory, L. Embon, D. Halbertal, J. Cuppens, L. Neeman, A. Finkler, Y. Segev, Y. Myasoedov, M. L. Rappaport, M. E. Huber, and E. Zeldov, *Nat. Nanotech.* **8**, 639 (2013).

3

Reference

H. G. Hugdal, M. Amundsen, J. Linder and A. Sudbø,

Inverse proximity effect in s-wave and d-wave superconductors coupled to topological insulators.

Physical Review B, **99**, 094505 (2019).

Contributions

HGH performed the analytical and numerical calculations with support from MA, AS and JL. HGH drafted the manuscript. All authors contributed to the discussions of the physics and the revision of the final manuscript.

Inverse proximity effect in *s*-wave and *d*-wave superconductors coupled to topological insulators

Henning G. Hugdal, Morten Amundsen, Jacob Linder, and Asle Sudbø*
*Center for Quantum Spintronics, Department of Physics, NTNU,
 Norwegian University of Science and Technology, NO-7491 Trondheim, Norway*

 (Received 9 August 2018; published 7 March 2019)

We study the inverse proximity effect in a bilayer consisting of a thin *s*- or *d*-wave superconductor (S) and a topological insulator (TI). Integrating out the topological fermions of the TI, we find that spin-orbit coupling is induced in the S, which leads to spin-triplet *p*-wave (*f*-wave) correlations in the anomalous Green's function for an *s*-wave (*d*-wave) superconductor. Solving the self-consistency equation for the superconducting order parameter, we find that the inverse proximity effect can be strong for parameters for which the Fermi momenta of the S and TI coincide. The suppression of the gap is approximately proportional to $e^{-1/\lambda}$, where λ is the dimensionless superconducting coupling constant. This is consistent with the fact that a higher λ gives a more robust superconducting state. For an *s*-wave S, the interval of TI chemical potentials for which the suppression of the gap is strong is centered at $\mu_{\text{TI}} = \pm\sqrt{2mv_{\text{F}}^2\mu}$, and increases quadratically with the hopping parameter t . Since the S chemical potential μ typically is high for conventional superconductors, the inverse proximity effect is negligible except for t above a critical value. For sufficiently low t , however, the inverse proximity effect is negligible, in agreement with what has thus far been assumed in most works studying the proximity effect in S-TI structures. In superconductors with low Fermi energies, such as high- T_c cuprates with *d*-wave symmetry, we again find a suppression of the order parameter. However, since μ is much smaller in this case, a strong inverse proximity effect can occur at $\mu_{\text{TI}} = 0$ for much lower values of t . Moreover, the onset of a strong inverse proximity effect is preceded by an increase in the order parameter, allowing the gap to be tuned by several orders of magnitude by small variations in μ_{TI} .

DOI: [10.1103/PhysRevB.99.094505](https://doi.org/10.1103/PhysRevB.99.094505)

I. INTRODUCTION

Topological insulators (TIs) are insulating in the bulk, but host metallic surface states protected by the topology of the material [1–3]. For three-dimensional topological insulators, the two-dimensional (2D) surface states can be described by a massless analog of the relativistic Dirac equation, having linear dispersions and spin-momentum locking. Many interesting phenomena are predicted to occur by coupling the TI to a superconductor, thus inducing a superconducting gap in the TI [4]. For instance, such systems have been predicted to host Majorana bound states [5], which could be used for topological quantum computing. Moreover, the Dirac-like Hamiltonian $\sigma \cdot \mathbf{k}$ has consequences for the response to exchange fields, allowing the phase difference in a Josephson junction to be tuned by an in-plane magnetization to values other than 0 and π [6], and inducing vortices by an in-plane magnetic field [7,8].

Numerous papers have studied the interesting phenomena that have been discovered in topological insulators with proximity-induced superconductivity [9–22]. To our knowledge, however, much less attention has been paid to the inverse superconducting, or topological [23], proximity effect, i.e., the effect that the topological insulator has on the superconductor order parameter. There have been indications that superconductivity might be suppressed [17], while other

studies have found no suppression [20]. One recent study demonstrated that the proximity to the TI induces spin-orbit coupling in the superconductor (S), possibly making a Fulde-Ferrel [24] superconducting state energetically more favorable near the interface of a magnetically doped TI [25]. Another study showed that the TI surface states can leak into the superconductor, resulting in a Dirac cone in the density of states [26]. In this paper, we focus on the superconducting gap itself and study under what circumstances the inverse proximity effect is negligible, as is often assumed in theoretical works.

Using a field-theoretical approach, we study an atomically thin Bardeen-Cooper-Schrieffer (BCS) *s*-wave superconductor and *d*-wave superconductor coupled to a TI. While this is an approximation for most conventional and high- T_c superconductors such as, e.g., Nb, Al, and $\text{YBa}_2\text{Cu}_3\text{O}_7$, superconductivity has been observed in, e.g., single-layer NbSe_2 [27] and FeSe [28–30]. Integrating out the TI fermions, we obtain an effective action for the S electrons. Due to the induced spin-orbit coupling, spin-triplet *p*-wave (*f*-wave) correlations are induced in the *s*-wave (*d*-wave) superconductor.

Solving the mean-field equations, using parameters valid for both conventional *s*-wave superconductors and high- T_c *d*-wave superconductors, we find that in both cases a strong suppression of the superconducting gap is possible. For conventional superconductors, where the Fermi energy μ is high compared to the cut-off frequency, the coupling between the S and the TI has to be quite large in order for the inverse proximity effect to be strong for relevant TI chemical potentials μ_{TI} . This can explain the lack of any inverse proximity effect in

*Corresponding author: asle.sudbo@ntnu.no

experiments [20]. In high- T_c d -wave superconductors, on the other hand, where the Fermi energy is much smaller, we find a strong gap suppression at much lower coupling strengths, which might therefore be experimentally observable. For these systems, we also find an increase in the gap for μ_{TI} just outside the region of strong inverse proximity effect.

The remainder of the paper is organized as follows: The model system is presented in Sec. II, and the effective action for the S fermions and order parameter is derived in Sec. III. In Sec. IV we derive the mean-field gap equations for the order parameter. Numerical results for the superconducting gap are presented and discussed in Sec. V, and summarized in Sec. VI. Further details on the calculation of the criteria for strong proximity effect, the Nambu space field integral, the zero-temperature, noninteracting gap solutions, and the numerical methods used, are presented in the Appendices.

II. MODEL

We model the bilayer consisting of a thin superconductor (S) coupled to a TI by the action

$$S = S_S + S_{\text{TI}} + S_t. \quad (1)$$

In Matsubara and reciprocal space, the superconductor is described by

$$S_S = \frac{1}{\beta V} \sum_k c^\dagger(k) \left(-i\omega_n + \frac{\mathbf{k}^2}{2m} - \mu \right) c(k) - \sum_{k,k',q} \frac{V_{\mathbf{k},\mathbf{k}'}}{(\beta V)^3} c^\dagger(k') c^\dagger(-k' + q) c_\downarrow(-k + q) c_\uparrow(k), \quad (2)$$

where $c(k) = [c_\uparrow(k) c_\downarrow(k)]^T$ with $c_{\uparrow(\downarrow)}(k)$ denoting the annihilation operator for spin-up (spin-down) electrons, m is the electron mass, and μ is the chemical potential in the S. $\beta = 1/k_B T$ and $V = L_x L_y$ are the inverse temperature and system area, respectively. We have used the notation $k = (\omega_n, \mathbf{k})$ [$q = (\Omega_n, \mathbf{q})$], where ω_n (Ω_n) is a fermionic (bosonic) Matsubara frequency, and \mathbf{k} (\mathbf{q}) the fermionic (bosonic) in-plane wave vector. $V_{\mathbf{k},\mathbf{k}'}$ is the pairing potential, which can be written [31]

$$V_{\mathbf{k},\mathbf{k}'} = gv(\mathbf{k})v(\mathbf{k}'), \quad (3)$$

where $v(\mathbf{k}) = 1$ for s -wave pairing, and $v(\mathbf{k}) = \sqrt{2} \cos(2\phi_{\mathbf{k}})$ for $d_{x^2-y^2}$ -wave pairing, where $\phi_{\mathbf{k}}$ is the angle of \mathbf{k} relative to the k_x axis. The coupling constant g is assumed to be nonzero only when $-\omega_- < \mathbf{k}^2/2m - \mu < \omega_+$, where $\pm\omega_\pm$ is the upper (lower) cut-off frequency. For conventional s -wave superconductors this is typically taken to be the characteristic frequency ω_D of the phonons, while the cut-off frequencies in high- T_c superconductors are of the order of the characteristic energy of the antiferromagnetic fluctuations present in these materials [32–35]. We will set $\hbar = 1$ throughout the paper. For the TI we use the Dirac action

$$S_{\text{TI}} = \frac{1}{\beta V} \sum_k \Psi^\dagger(k) (-i\omega_n + v_F \mathbf{k} \cdot \boldsymbol{\sigma} - \mu_{\text{TI}}) \Psi(k), \quad (4)$$

where $\Psi(\mathbf{r}) = [\psi_\uparrow(\mathbf{r}) \psi_\downarrow(\mathbf{r})]^T$ describes the TI fermions, v_F is the Fermi velocity, and μ_{TI} is the TI chemical potential. The

S and TI layers are coupled by a hopping term [25,26,36,37]

$$S_t = -\frac{1}{\beta V} \sum_k t [c^\dagger(k) \Psi(k) + \Psi^\dagger(k) c(k)]. \quad (5)$$

Similar models were recently used in Refs. [25,26] when studying similar systems with an s -wave S. The full partition function of the system is therefore

$$Z = \int \mathcal{D}[c^\dagger, c] e^{-S_S} \left(\int \mathcal{D}[\Psi^\dagger, \Psi] e^{-S_{\text{TI}} - S_t} \right). \quad (6)$$

III. EFFECTIVE ACTION

As we are interested in the inverse proximity effect in the S and its consequences for the superconducting gap, we integrate out the TI fermions by performing the functional integral $Z_{\text{TI},t} = \int \mathcal{D}[\Psi^\dagger, \Psi] e^{-S_{\text{TI},t}}$, where

$$S_{\text{TI},t} = \frac{1}{\beta V} \sum_k \left\{ \Psi^\dagger(k) (-G_{\text{TI}}^{-1}) \Psi(k) - t [c^\dagger(k) \Psi(k) + \Psi^\dagger(k) c(k)] \right\}. \quad (7)$$

Here, we have defined the matrix $G_{\text{TI}}^{-1} = i\omega_n - v_F \mathbf{k} \cdot \boldsymbol{\sigma} + \mu_{\text{TI}}$. Performing the functional integration leads to an additional term in the S action,

$$\delta S_S = \frac{t^2}{\beta V} \sum_k c^\dagger(k) G_{\text{TI}} c(k), \quad (8)$$

with the TI Green's function

$$G_{\text{TI}} = \frac{i\omega_n + \mu_{\text{TI}} + v_F \mathbf{k} \cdot \boldsymbol{\sigma}}{(i\omega_n + \mu_{\text{TI}})^2 - v_F^2 \mathbf{k}^2}. \quad (9)$$

The effective S action thus reads

$$S_S^{\text{eff}} = -\frac{1}{\beta V} \sum_k c^\dagger(k) G_0^{-1} c(k) - \sum_{k,k',q} \frac{V_{\mathbf{k},\mathbf{k}'}}{(\beta V)^3} c^\dagger(k') \times c^\dagger(-k' + q) c_\downarrow(-k + q) c_\uparrow(k), \quad (10)$$

where we have defined the inverse noninteracting Green's function

$$G_0^{-1} = i\omega_n - \frac{\mathbf{k}^2}{2m} + \mu - t^2 G_{\text{TI}}. \quad (11)$$

From this we see that the coupling to G_{TI} in Eq. (9) leads to an induced spin-orbit coupling $\sim \mathbf{k} \cdot \boldsymbol{\sigma}$ in the S, in agreement with Ref. [25].

Performing a Hubbard-Stratonovich decoupling [38], the four-fermion term in the S action can be rewritten in terms of bosonic fields $\varphi(q)$ and $\varphi^\dagger(q)$,

$$-\sum_{k,k',q} \frac{V_{\mathbf{k},\mathbf{k}'}}{(\beta V)^3} c^\dagger(k') c^\dagger(-k' + q) c_\downarrow(-k + q) c_\uparrow(k) \rightarrow -\frac{1}{\beta V} \times \sum_{k,q} [\varphi(q) v(\mathbf{k}) c^\dagger(k) c^\dagger(-k + q) + \text{H.c.}]. \quad (12)$$

This also leads to an additional term in the total system action

$$S_\varphi^0 = \frac{\beta V}{g} \sum_q \varphi^\dagger(q) \varphi(q), \quad (13)$$

and a functional integration of the bosonic fields in the partition function. Note that the decoupling is performed such that the bosonic fields have units of energy.

By defining the Nambu spinor

$$\mathcal{C}(k) = [c_\uparrow(k) c_\downarrow(k) c_\uparrow^\dagger(-k) c_\downarrow^\dagger(-k)]^T, \quad (14)$$

the effective S action can be written

$$S_S^{\text{eff}} = -\frac{1}{2\beta V} \sum_{k,k'} \mathcal{C}^\dagger(k) \mathcal{G}^{-1}(k,k') \mathcal{C}(k'), \quad (15)$$

where

$$\mathcal{G}^{-1}(k,k') = \begin{pmatrix} G_0^{-1}(k) \delta_{k,k'} & \varphi(k-k') v(\mathbf{k}) i\sigma_y \\ -\varphi^\dagger(-k+k') v(\mathbf{k}) i\sigma_y & -[G_0^{-1}(-k)]^T \delta_{k,k'} \end{pmatrix}. \quad (16)$$

Performing the functional integration over the fermionic fields, we arrive at the effective action for the bosonic fields

$$S_\varphi = \frac{\beta V}{g} \sum_q \varphi^\dagger(q) \varphi(q) - \frac{1}{2} \text{Tr} \ln(-\mathcal{G}^{-1}). \quad (17)$$

The additional factor 1/2 in front of the trace is due to the change in integration measure when changing to the Nambu

spinor notation (see Appendix B and, e.g., Ref. [39] for details).

IV. MEAN-FIELD THEORY

Since $G_0^{-1}(i\omega_n, \mathbf{k})$ is still inversion symmetric in the diagonal basis (see below), we assume that the bosonic field $\varphi(q)$ is temporally and spatially homogeneous as in the regular BCS case. However, a recent study has shown that introducing in-plane magnetic fields in the TI breaks this symmetry and can make a Fulde-Ferrel [24] order parameter energetically more favorable in an *s*-wave S [25]. Calculating the matrix $\mathcal{G}(k)$ assuming a spatially homogeneous bosonic field $\phi(q) = \delta_{q,0} \Delta$, and defining the superconducting order parameter $\Delta(\mathbf{k}) = \Delta \cdot v(\mathbf{k})$, we get

$$\mathcal{G}(k) = \begin{pmatrix} G(k) & F(k) \\ F^\dagger(k) & -G^T(-k) \end{pmatrix}, \quad (18)$$

where to leading order in t

$$G(k) = -\frac{\epsilon_{\mathbf{k}} + i\omega_n}{\xi_{\mathbf{k}}^2 + \omega_n^2} - t^2 \frac{(\epsilon_{\mathbf{k}} + i\omega_n)^2 [(i\omega_n + \mu_{\text{TI}}) + v_{\text{F}} \mathbf{k} \cdot \boldsymbol{\sigma}]}{(\xi_{\mathbf{k}}^2 + \omega_n^2)^2 [v_{\text{F}}^2 \mathbf{k}^2 - (i\omega_n + \mu_{\text{TI}})^2]} - t^2 \frac{|\Delta(\mathbf{k})|^2 [(i\omega_n - \mu_{\text{TI}}) - v_{\text{F}} \mathbf{k} \cdot \boldsymbol{\sigma}]}{(\xi_{\mathbf{k}}^2 + \omega_n^2)^2 [v_{\text{F}}^2 \mathbf{k}^2 - (i\omega_n - \mu_{\text{TI}})^2]}, \quad (19)$$

$$F(k) = \frac{\Delta(\mathbf{k})}{\xi_{\mathbf{k}}^2 + \omega_n^2} \left\{ 1 + 2t^2 \frac{(v_{\text{F}}^2 \mathbf{k}^2 - \mu_{\text{TI}}^2 - \omega_n^2) \epsilon_{\mathbf{k}} \mu_{\text{TI}} - \omega_n^2 (v_{\text{F}}^2 \mathbf{k}^2 + \mu_{\text{TI}}^2 + \omega_n^2)}{(\xi_{\mathbf{k}}^2 + \omega_n^2) [(v_{\text{F}} |\mathbf{k}| - \mu_{\text{TI}})^2 + \omega_n^2] [(v_{\text{F}} |\mathbf{k}| + \mu_{\text{TI}})^2 + \omega_n^2]} \right. \\ \left. + 2t^2 \frac{(v_{\text{F}}^2 \mathbf{k}^2 - \mu_{\text{TI}}^2 - \omega_n^2) \epsilon_{\mathbf{k}} - 2\omega_n^2 \mu_{\text{TI}}}{(\xi_{\mathbf{k}}^2 + \omega_n^2) [(v_{\text{F}} |\mathbf{k}| - \mu_{\text{TI}})^2 + \omega_n^2] [(v_{\text{F}} |\mathbf{k}| + \mu_{\text{TI}})^2 + \omega_n^2]} v_{\text{F}} \mathbf{k} \cdot \boldsymbol{\sigma} \right\} i\sigma_y, \quad (20)$$

with $\epsilon_{\mathbf{k}} = \mathbf{k}^2/2m - \mu$ and $\xi_{\mathbf{k}} = \sqrt{\epsilon_{\mathbf{k}}^2 + |\Delta(\mathbf{k})|^2}$. As mentioned above, the proximity-induced spin-orbit coupling leads to nondiagonal terms in $G(k)$. Moreover, $F(k)$ now has diagonal terms $\propto \mathbf{k} \cdot \boldsymbol{\sigma} i\sigma_y$, signaling that *p*-wave (*f*-wave) triplet superconducting correlations are induced in the *s*-wave (*d*-wave) superconductor. This has been shown to be the case in *s*-wave superconductors when the spin degeneracy is lifted by spin-orbit coupling [40]. A similar expression was found for the anomalous Green's function on the TI side of an S-TI bilayer in Ref. [41]. The results in Ref. [41] also suggest that odd-frequency triplet pairing could be induced in the S by including a magnetic exchange term $\mathbf{m} \cdot \boldsymbol{\sigma}$ in the TI Lagrangian.

Gap equation

While the above Green's functions contain information about the correlations in the superconductor, the superconducting gap must be determined self-consistently. We first change to the basis which diagonalizes the nonsuperconducting normal inverse Green's function G_0^{-1} . We find $G_{d,0}^{-1}(k) = P(k) G_0^{-1}(k) P^\dagger(k)$, where $G_{d,0}^{-1}(k) = \text{diag}[G_{+,0}^{-1}(k), G_{-,0}^{-1}(k)]$,

with

$$G_{\pm,0}^{-1}(k) = i\omega_n - \epsilon_{\mathbf{k}} - \frac{t^2}{i\omega_n + \mu_{\text{TI}} \mp v_{\text{F}} |\mathbf{k}|} \quad (21)$$

and

$$P(k) = \frac{1}{\sqrt{2}} \begin{pmatrix} 1 & e^{-i\phi_{\mathbf{k}}} \\ 1 & -e^{-i\phi_{\mathbf{k}}} \end{pmatrix} t. \quad (22)$$

Here $\phi_{\mathbf{k}}$ is the angle of \mathbf{k} relative to the k_x axis. + (−) here denotes the Green's function for positive (negative) chirality states. Inverting $G_{d,0}^{-1}$ we find the Green's functions

$$G_{\pm,0}(k) = \frac{i\omega_n \mp v_{\text{F}} |\mathbf{k}| + \mu_{\text{TI}}}{[i\omega_n - \epsilon_{\pm}^+(\mathbf{k})][i\omega_n - \epsilon_{\pm}^-(\mathbf{k})]}, \quad (23)$$

where

$$\epsilon_{\alpha}^{\gamma}(\mathbf{k}) = \frac{1}{2} [\epsilon_{\mathbf{k}} + \alpha v_{\text{F}} |\mathbf{k}| - \mu_{\text{TI}} \\ + \gamma \sqrt{(\epsilon_{\mathbf{k}} - \alpha v_{\text{F}} |\mathbf{k}| + \mu_{\text{TI}})^2 + 4t^2}], \quad (24)$$

with $\alpha, \gamma = \pm 1$. The Green's function has residues

$$w_\alpha^\gamma(\mathbf{k}) = \frac{1}{2} + \frac{\epsilon_{\mathbf{k}} - \alpha v_F |\mathbf{k}| + \mu_{\text{TI}}}{2\gamma \sqrt{(\epsilon_{\mathbf{k}} - \alpha v_F |\mathbf{k}| + \mu_{\text{TI}})^2 + 4t^2}}. \quad (25)$$

We next transform the entire inverse Green's function \mathcal{G} using $\mathcal{G}_d^{-1}(k) = \mathcal{P}(k)\mathcal{G}^{-1}(k)\mathcal{P}^\dagger(k)$, where

$$\mathcal{P}(k) = \begin{pmatrix} P(k) & 0 \\ 0 & P^*(-k) \end{pmatrix}, \quad (26)$$

$$G_\pm(k) = \frac{[i\omega_n + \epsilon_\pm^+(\mathbf{k})][i\omega_n + \epsilon_\pm^-(\mathbf{k})][i\omega_n \mp v_F |\mathbf{k}| + \mu_{\text{TI}}]}{[i\omega_n - \xi_\pm^+(\mathbf{k})][i\omega_n + \xi_\pm^+(\mathbf{k})][i\omega_n - \xi_\pm^-(\mathbf{k})][i\omega_n + \xi_\pm^-(\mathbf{k})]}, \quad (29a)$$

$$F_\pm(k) = \pm \frac{\Delta(\mathbf{k})e^{-i\phi_{\mathbf{k}}}[(i\omega_n)^2 - (\pm v_F |\mathbf{k}| - \mu_{\text{TI}})^2]}{[i\omega_n - \xi_\pm^+(\mathbf{k})][i\omega_n + \xi_\pm^+(\mathbf{k})][i\omega_n - \xi_\pm^-(\mathbf{k})][i\omega_n + \xi_\pm^-(\mathbf{k})]}. \quad (29b)$$

The eigenenergies of the system are now given by the poles in the above equation, where

$$\xi_\alpha^\gamma(\mathbf{k}) = \frac{1}{\sqrt{2}} \left\{ \xi_{\mathbf{k}}^2 + (\alpha v_F |\mathbf{k}| - \mu_{\text{TI}})^2 + 2t^2 + \gamma \sqrt{[\xi_{\mathbf{k}}^2 - (\alpha v_F |\mathbf{k}| - \mu_{\text{TI}})^2]^2 + 4t^2[(\epsilon_{\mathbf{k}} + \alpha v_F |\mathbf{k}| - \mu_{\text{TI}})^2 + |\Delta(\mathbf{k})|^2]} \right\}^{1/2}. \quad (30)$$

The gap equation for the amplitude Δ is found by requiring $\frac{\delta s_{\text{eff}}}{\delta \Delta} = 0$ [38], which yields

$$\Delta^\dagger = -\frac{g}{2\beta V} \sum_k \text{tr} F_d^\dagger(k) v(\mathbf{k}) \sigma_z e^{-i\phi_{\mathbf{k}}}. \quad (31)$$

Inserting the Hermitian conjugate of Eq. (29b) and performing the sum over Matsubara frequencies, we get the gap equation,

$$1 = \frac{g}{4V} \sum_{\mathbf{k}} v(\mathbf{k})^2 \left\{ \frac{\xi_+^+(\mathbf{k})^2 - (v_F |\mathbf{k}| - \mu_{\text{TI}})^2}{\xi_+^+(\mathbf{k})[\xi_+^+(\mathbf{k})^2 - \xi_+^-(\mathbf{k})^2]} \tanh \frac{\beta \xi_+^+(\mathbf{k})}{2} - \frac{\xi_+^-(\mathbf{k})^2 - (v_F |\mathbf{k}| - \mu_{\text{TI}})^2}{\xi_+^-(\mathbf{k})[\xi_+^+(\mathbf{k})^2 - \xi_+^-(\mathbf{k})^2]} \tanh \frac{\beta \xi_+^-(\mathbf{k})}{2} + \frac{\xi_+^+(\mathbf{k})^2 - (v_F |\mathbf{k}| + \mu_{\text{TI}})^2}{\xi_+^+(\mathbf{k})[\xi_+^+(\mathbf{k})^2 - \xi_-^-(\mathbf{k})^2]} \tanh \frac{\beta \xi_+^+(\mathbf{k})}{2} - \frac{\xi_-^-(\mathbf{k})^2 - (v_F |\mathbf{k}| + \mu_{\text{TI}})^2}{\xi_-^-(\mathbf{k})[\xi_+^+(\mathbf{k})^2 - \xi_-^-(\mathbf{k})^2]} \tanh \frac{\beta \xi_-^-(\mathbf{k})}{2} \right\}. \quad (32)$$

Setting $t = 0$ simply yields the regular BCS gap equation, which results in a gap $\Delta_0 = 2\omega_D e^{-1/\lambda}$ in the s -wave case [42], where $\lambda = gD_0/V$ is a dimensionless coupling constant, and D_0 is the density of states at the Fermi level. d -wave pairing results in a slightly smaller gap for the same values for λ and the cut-off frequencies (see Appendix C for details). For $t \neq 0$, the above equation can be expressed in terms of an energy integral over $\epsilon_{\mathbf{k}}$ using $v_F |\mathbf{k}| = v_F \sqrt{2m(\epsilon_{\mathbf{k}} + \mu)}$.

V. RESULTS AND DISCUSSION

From the expressions for the system eigenenergies in the nonsuperconducting case, Eq. (24), we see that the S and TI bands have hybridized, leading to avoided crossings. The effect of this hybridization is largest when the chemical

which yields

$$\mathcal{G}_d^{-1}(k) = \begin{pmatrix} G_{d,0}^{-1}(k) & -\Delta(\mathbf{k})e^{-i\phi_{\mathbf{k}}} \sigma_z \\ -\Delta^\dagger(\mathbf{k})e^{i\phi_{\mathbf{k}}} \sigma_z & -G_{d,0}^{-1}(-k) \end{pmatrix}. \quad (27)$$

Hence the full Green's function matrix for the superconductor is

$$\mathcal{G}_d(k) = \begin{pmatrix} G_d(k) & F_d(k) \\ F_d^\dagger(k) & -G_d(-k) \end{pmatrix}, \quad (28)$$

where we have defined the 2×2 matrices $G_d(k) = \text{diag}[G_+(k), G_-(k)]$ and $F_d(k) = \text{diag}[F_+(k), F_-(k)]$, and Green's functions

potential of both the S and TI is tuned such that the Fermi momenta coincide, i.e., for $\mu_{\text{TI}} = \pm \sqrt{2m}v_F^2\mu$. A possibly strong proximity effect should therefore be expected to occur in a region close to these values of μ_{TI} , the size of which increases with increased hopping t . In the following we numerically solve the gap equations for both s - and d -wave superconductors for relevant parameter values.

A. s -wave pairing

Using numerical values $\mu \sim 5$ eV, a cutoff corresponding to the Debye frequency, $\hbar\omega_{\pm} = \hbar\omega_D \sim 25$ meV [43], $\hbar^2/2m \sim 40$ meV nm², $\hbar v_F \sim 300$ meV nm [20,44], and $\lambda = 0.2$, we solve the gap equation in Eq. (32) for different values of t and μ_{TI} at $T = 0$ for an s -wave superconductor. The results in Fig. 1(a) show that the absolute value of the gap is not changed significantly due to the inverse proximity effect for small t , except for μ_{TI} close to $\sqrt{2m}v_F^2\mu$. Both for μ_{TI} above and below this region, the inverse proximity effect is small, signifying that the disappearing gap in the region where the inverse proximity effect is strong cannot be simply related to the increasing density of states in the TI. For increasing t , the region where superconductivity is suppressed increases quadratically with t , eventually leading to suppressed superconductivity also at $\mu_{\text{TI}} = 0$.

The strong suppression of the order parameter can be understood from the fact that the pairing potential is attractive only when $|\mathbf{k}^2/2m - \mu| \leq \omega_D$, corresponding to wave vectors between $k_{\pm} \equiv \sqrt{2m(\mu \pm \omega_{\pm})}$. This means that the Fermi wave vectors k_F of the bands in Eq. (24), the value of $|\mathbf{k}|$ for which $\epsilon_{\alpha}^{\gamma}(\mathbf{k}) = 0$, have to satisfy $k_- < k_F < k_+$ in order to contribute significantly to the integral in the gap equations and thus give a finite gap. This can be seen by comparing the left panels in Fig. 1(b), where the upper left panel shows

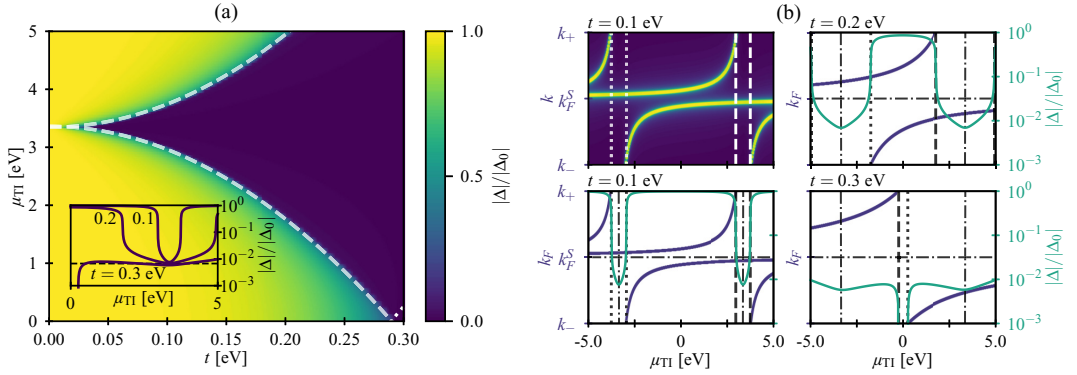


FIG. 1. (a) Plot of the superconducting gap at $T = 0$ for an *s*-wave superconductor as a function of μ_{TI} and t and with an upper cutoff $\omega_+ = 0.0025$ eV, normalized to the bulk value $|\Delta_0|$ for parameter values relevant for Nb-HgTe bilayers. The k_{F} values for the TI appear vertical on this plot as a function of μ_{TI} due to the small value of the cutoff ω_+ . The numerical results show that the zero-temperature gap essentially is unaffected by the proximity to the TI for small values of t , where the suppression is severe only for values of μ_{TI} close to $\sqrt{2m v_{\text{F}}^2 \mu}$, a value far too large to be experimentally achievable. However, for increasing t , the region where superconductivity is suppressed increases quadratically with t , eventually leading to a suppression also for $\mu_{\text{TI}} = 0$. The inset shows the normalized gap at $t = 0.1, 0.2$, and 0.3 eV, indicating that the gap is not suppressed entirely in most cases, but rather to a reduced value of $\Delta_0 e^{-1/\lambda}$ (dashed line), consistent with there being only one band contributing to superconductivity in this region. The exception is close to $\mu_{\text{TI}} = 0$ for $t = 0.3$ eV, where there are no bands with Fermi wave vector between k_- and k_+ , resulting in $\Delta = 0$. This is the case in the area restricted by the dotted line in the main figure. (b) The upper left panel is a plot of the integrand in the gap equation, Eq. (32), evaluated at Δ_0 for wave vectors $k_- < |\mathbf{k}| < k_+$ and $t = 0.1$ eV, where light colors correspond to high values of the integrand. The three remaining panels show the magnitude of the Fermi wave vectors k_{F} of the bands defined in Eq. (24) in the same interval at $t = 0.1, 0.2$ and 0.3 eV, and the normalized gap (right axis). Notice that the plots are close to symmetric around $\mu_{\text{TI}} = 0$ since $\omega_D \ll \mu$. The dash-dotted lines are k_{F}^{S} and $k_{\text{F}}^{\text{TI}}(\mu_{\text{TI}})$, the Fermi wave vectors of the S and TI for $t = 0$, respectively. Comparing the two left panels it is clear that the main contribution to the integral in the gap equation comes from wave vectors close to the Fermi wave vectors of the bands in the relevant $|\mathbf{k}|$ interval. $\mu_{\text{TI}}^{\alpha, \pm}(t)$ are plotted as dashed ($\alpha = 1$) and dotted ($\alpha = -1$) lines in all plots, indicating the onset of the region in parameter space where superconductivity is greatly suppressed.

the integrand of the gap equation, Eq. (32), and the lower left panel plots k_{F} for the bands in Eq. (24) as a function of μ_{TI} . The main contribution to the gap equation clearly comes from the values $|\mathbf{k}| = k_{\text{F}}$. From Fig. 1(b) we also see that as μ_{TI} approaches $\pm\sqrt{2m v_{\text{F}}^2 \mu}$, the value where the Fermi wave vectors for the bare S and TI bands, k_{F}^{S} and $k_{\text{F}}^{\text{TI}}(\mu_{\text{TI}})$ cross, the wave vector of one of the bands exceeds k_+ and thus does not contribute to the gap equation. Now there is only one nondegenerate band inside the relevant region, meaning that the density of states and thus λ is halved compared to the $t = 0$ case, where the band is doubly degenerate. Hence the resulting gap is suppressed to $\Delta_0 e^{-1/\lambda} = 2\omega_D e^{-2/\lambda}$, in good agreement with the numerical results, as shown by the dashed line in the inset in Fig. 1(a). This also means that the suppression is less severe for higher λ , which we have confirmed by numerical simulations.

For positive μ_{TI} , the Fermi wave vector in one band exits the integration interval $[k_-, k_+]$ at $\mu_{\text{TI}} = \mu_{\text{TI}}^{+, -}$, while a new band enters this region at $\mu_{\text{TI}} = \mu_{\text{TI}}^{+, +}$, where we have defined

$$\mu_{\text{TI}}^{\alpha, \pm}(t) = \alpha \sqrt{2m v_{\text{F}}^2 (\mu \mp \omega_D)} \pm \frac{t^2}{\omega_D} \quad (33)$$

(see Appendix A for details). A similar argument holds for negative μ_{TI} , and hence superconductivity is strongly suppressed for

$$\mu_{\text{TI}}^{\alpha, -} < \mu_{\text{TI}} < \mu_{\text{TI}}^{\alpha, +}, \quad (34)$$

indicated by the dashed and dotted lines in Fig. 1. If the hopping parameter is large enough, $t^2 > \omega_D \sqrt{2m v_{\text{F}}^2 (\mu \mp \omega_D)} \equiv (t_{\mp})^2$, $\mu_{\text{TI}}^{+, +}$ and $\mu_{\text{TI}}^{+, -}$ change sign. Hence, for $|t| > |t_+| > |t_-|$ and $\mu_{\text{TI}}^{+, -} < \mu_{\text{TI}} < \mu_{\text{TI}}^{+, +}$, no bands have a Fermi wave vector between k_- and k_+ , resulting in $\Delta = 0$, as seen for $t \approx 0.3$ eV and low μ_{TI} in Fig. 1. Since $\mu \gg \omega_D$, all results are close to symmetric about $\mu_{\text{TI}} = 0$, as seen in Fig. 1(b).

In order for strong suppression to occur for some value of μ_{TI} , we must require $\mu_{\text{TI}}^{\alpha, -} < \mu_{\text{TI}}^{\alpha, +}$. For $\alpha = -1$ this always holds, while for $\alpha = +1$ we get a lower limit for t^2 ,

$$t^2 > \omega_D \left[\sqrt{2m v_{\text{F}}^2 (\mu + \omega_D)} - \sqrt{2m v_{\text{F}}^2 (\mu - \omega_D)} \right]. \quad (35)$$

For conventional *s*-wave superconductors $\mu \gg \omega_D$, meaning strong suppression can occur even at low values of t , though for TI chemical potentials close to $\pm\sqrt{2m v_{\text{F}}^2 \mu}$.

While this result is strictly only valid in the limit of an atomically thin superconductor, we expect that this effect in principle could reduce the zero-temperature gap and thus also reduce the critical temperature in superconducting thin films. However, for typical parameter values in TIs and *s*-wave superconductors, the values of μ_{TI} where superconductivity vanishes is inaccessible, tuning μ_{TI} by several eV would place the Fermi level inside the bulk bands of the TI, where our model is no longer valid. The only exception from this is when $|t| \gtrsim |t_-|$, when superconductivity is suppressed even at $\mu_{\text{TI}} = 0$. The fact that no strong inverse proximity effect

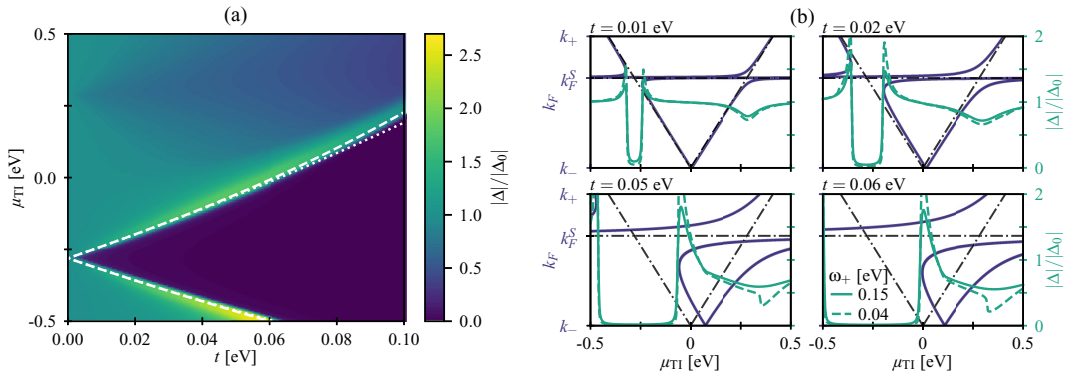


FIG. 2. (a) Plot of the superconducting gap at $T = 0$ for a d -wave superconductor as a function of μ_{TI} and t with upper cutoff $\omega_+ = 0.15$ eV, normalized to the bulk value $|\Delta_0|$ for parameter values relevant for bilayers consisting of HgTe and high- T_c superconductors. The gap is strongly suppressed for $\mu_{\text{TI}}^- < \mu_{\text{TI}} < \mu_{\text{TI}}^+$, where the approximate (exact numerical) functions $\mu_{\text{TI}}^\pm(t)$ in Eq. (36) are plotted as dotted (dashed) lines. The approximate solution is only valid for $k_F \approx k_F^S$, corresponding to small t . For $\mu_{\text{TI}} \approx \mu_{\text{TI}}^\pm(t)$ the gap increases beyond Δ_0 . (b) Plot of the magnitude of the Fermi wave vectors of the bands in Eq. (24) in the interval $k_- < k_F < k_+$ (left axis), together with the normalized gap (right axis) for $\omega_+ = 0.15$ and 0.04 eV. The upper limit k_+ in the left axis corresponds to $\omega_+ = 0.04$ eV. The black dash-dotted lines show the S and TI Fermi wave vectors for $t = 0$. As for the s -wave case, the strong suppression of the gap is due to only one band having a Fermi wave vector in the integration interval. Note how the values of $k_F(\mu_{\text{TI}})$ of the hybridized bands (originating with the left $t = 0$ crossing of the k_F 's of the TI and the S) bend back in a pronounced way as a function of μ_{TI} (k_F is a multivalued function of μ_{TI} since there are four bands). This leads to an enhanced density of states for these values of μ_{TI} . This in turn gives an enhancement of the gap in the immediate vicinity of the region of μ_{TI} where the gap is suppressed by the disappearance of bands crossing the TI Fermi surface. This effect is not seen in the s -wave case, where the pronounced back bending of $k_F(\mu_{\text{TI}})$ does not occur inside the integration interval with the much lower values of ω_\pm [see Fig. 3(a)].

has been observed, e.g., in Ref. [20], might indicate that the coupling constant t is below this limit, meaning that an unphysical high chemical potential is needed in the TI to observe the vanishing of superconductivity. Since conventional s -wave superconductors have high Fermi energies, it might not be possible to reach the parameter regions where superconductivity vanishes, unless the chemical potential in the S can be lowered significantly, the Fermi velocity of the TI is lowered by renormalization, as was proposed in Ref. [26], or the coupling between the layers can be increased beyond t_- . However, as we show below, similar effects are present also for unconventional, high- T_c superconductors, for which the Fermi energy is lower. Examples of such superconductors would be the high- T_c cuprates and the heavy-fermion superconductors.¹

B. d -wave pairing

Using a much lower chemical potential in the S, $\mu \sim 35$ meV [45], and an upper cut-off frequency comparable to the spin fluctuation energy in the high- T_c cuprates, $\omega_+ \sim 0.04$ – 0.15 eV [32,33,46], $\omega_- = \mu$, and parameters otherwise as for the s -wave case, we solve the gap equations for a d -wave superconductor. First of all, the effect of the d -wave gap structure, compared to an s -wave gap, is an overall change in scaling, just as is the case for Δ_0 (see Appendix C). Hence, the results for $\Delta^{s\text{-wave}}/\Delta_0^{s\text{-wave}}$ are identical to $\Delta^{d\text{-wave}}/\Delta_0^{d\text{-wave}}$

when using the same parameters, and we have therefore solved the numerically more efficient s -wave gap equations with parameters valid for high- T_c superconductors.

Figure 2(a) shows the numerical results for the normalized gap as a function of μ_{TI} and t . The most prominent difference compared to the results in Fig. 1 is that the results are no longer symmetric about $\mu_{\text{TI}} = 0$, which can be understood from the fact that ω_\pm is of the same order of magnitude or larger than μ . Due to the anticrossing of the Fermi wave vectors at negative μ_{TI} , there is only one Fermi wave vector between k_- and k_+ for $\mu_{\text{TI}}^- < \mu_{\text{TI}} < \mu_{\text{TI}}^+$ [dashed lines in Fig. 2(a)], leading to strong suppression for negative μ_{TI} . This is illustrated in Fig. 2(b), where we plot the Fermi wave vectors of the bands together with the normalized gap as a function of μ_{TI} for different values of t . The figure also shows how the regions of strong mixing between the bands increases with increasing t . Interestingly, the suppression of the gap is preceded by an increased Δ at μ_{TI}^\pm , due to the bending of the Fermi wave vectors away from the crossing point of k_F^S and $k_F^{\text{TI}}(\mu_{\text{TI}})$, which leads to an increase in the density of states at the Fermi level. This is illustrated in Fig. 3(b), where for TI chemical potentials μ_{TI}^\pm the bands have a minimum (maximum) at the Fermi level, resulting in high densities of states. The difference in the gap enhancement between μ_{TI}^+ and μ_{TI}^- is due to the combined effects of different spectral weights, indicated by the linewidths in Fig. 3(b), and the size of the Fermi surface, leading to a net larger increase in $|\Delta|$ at μ_{TI}^- . In the small t limit, we find the approximate expressions

$$\mu_{\text{TI}}^\pm = -\sqrt{2mv_F^2\mu} \pm 2\left(\frac{mv_F^2}{2\mu}\right)^{1/4} t + \frac{1}{4\mu} t^2. \quad (36)$$

¹Although heavy-fermion superconductors nominally have a quite low critical temperature in absolute terms, they are nevertheless high- T_c superconductors. Their critical temperatures are a significant fraction of their Fermi-temperatures.

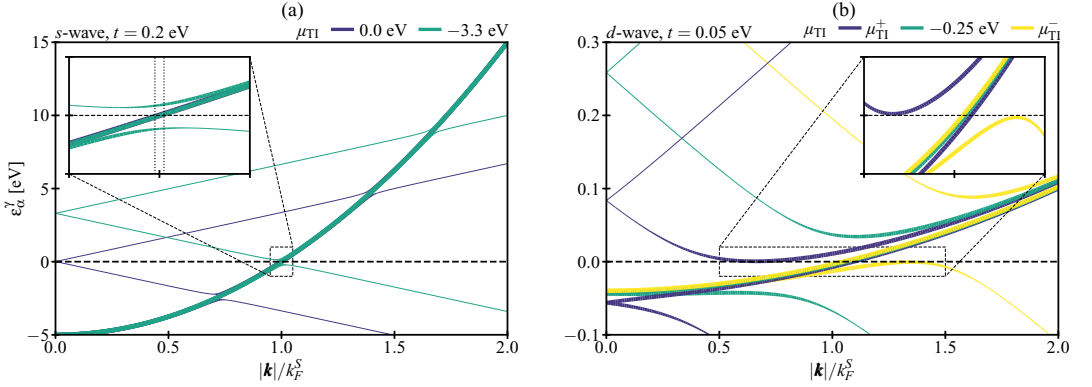


FIG. 3. Plots of the bands $\epsilon_\alpha^\gamma(\mathbf{k})$ in Eq. (24) for (a) *s*-wave and (b) *d*-wave parameter values and different values of μ_{TI} . The linewidths are proportional to the spectral weights $w_\alpha^\gamma(\mathbf{k})$ of the bands [see Eq. (25)]. In (a) the values of μ_{TI} correspond to a barely suppressed ($\mu_{\text{TI}} = 0.0$ eV) and strongly suppressed ($\mu_{\text{TI}} = -3.3$ eV $\approx -\sqrt{2}mv_F^2\mu$) gap for coupling $t = 0.2$ eV. The inset shows that there is no hybridization of bands close to the Fermi level (dashed line) for the lowest μ_{TI} , while the strong hybridization for $\mu_{\text{TI}} = 3.3$ eV leads to only one band crossing the Fermi level in the interval $[k_-, k_+]$ (dotted lines). In (b) we see that only one band crosses the Fermi level for $\mu_{\text{TI}} = -0.25$ eV, explaining the strong suppression in this case. At $\mu_{\text{TI}} = \mu_{\text{TI}}^\pm$ we have an increase in $|\Delta|$, which can be explained by the bands having minima/maxima at the Fermi level in these cases, leading to high densities of states.

These lines are plotted in Fig. 2(a) (dotted lines) together with the exact numerical solutions (dashed lines) (see Appendix A for details). This increase in $|\Delta|$ is not due to the the *d*-wave symmetry, and should therefore be present for $\mu_{\text{TI}} = \mu_{\text{TI}}^\pm$ whenever the interval $[k_-, k_+]$ includes either of the points $k_F^S \pm |\delta k_F|$, where δk_F is defined in Eq. (A7).

For positive μ_{TI} there is a small reduction in Δ close to $\mu_{\text{TI}} = \sqrt{2}mv_F^2\mu$, even though there are three bands with $k_F \in [k_-, k_+]$. However, since the numerator of each term in the gap equation, Eq. (32), can be written $\xi_\alpha^\pm(\mathbf{k})^2 - (\alpha v_F |\mathbf{k}| - \mu_{\text{TI}})^2$, regions where $\xi_\alpha^\pm(\mathbf{k})$ are similar to the bare TI bands contribute little to the gap equations, resulting in a small decrease of Δ .

The effect of using a lower upper cutoff in the solution of the gap equations is also shown in Fig. 2. Comparing the $\omega_+ = 0.15$ and 0.04 eV lines, we see that for high t , the mixing of the *S* and *TI* bands is still significant at $k_F = k_+$, leading to abrupt changes in Δ . For the negative μ_{TI} the main effect of lowering the upper cutoff ω_+ is a further increase of Δ at μ_{TI}^\pm .

From the above results, it is clear that a strong suppression of the gap is more probable in *S*-*TI* bilayers consisting of a high- T_c *S*, where both the chemical potential $-\sqrt{2}mv_F^2\mu$ corresponding to $k_F^S = k_F^{\text{TI}}(\mu_{\text{TI}})$ and the hopping strength needed for strong suppression at $\mu_{\text{TI}} = 0$ is much lower. Hence, we may expect a strong inverse proximity effect in such systems, with a strength determined by λ , as illustrated in Fig. 4 for both the *s*- and the *d*-wave case. Increasing λ leads to a reduced suppression of the gap, consistent with the fact that the superconducting state is more robust for higher λ . For the *s*-wave case, the suppression is proportional to $e^{-1/\lambda}$. This holds only approximately for the *d*-wave case due to other factors than Fermi level crossings affecting the suppression, such as changes in the spectral densities at the Fermi level and changes in the size of the Fermi surface (see Fig. 3), effects which are small in the *s*-wave case. From the results in Fig. 2 we also see that it should be possible to change Δ by several

orders of magnitude by small changes in μ_{TI} , again depending on the value of λ as illustrated in Fig. 4.

VI. SUMMARY

We have theoretically studied the inverse superconducting proximity effect between a thin *s*-wave or *d*-wave superconductor and a topological insulator. Using a field-theoretical approach, we have found that in both cases there are regions in parameter space where the inverse proximity effect is strong, leading to a strong suppression of the gap approximately proportional to $e^{-1/\lambda}$. The suppression can be related to the

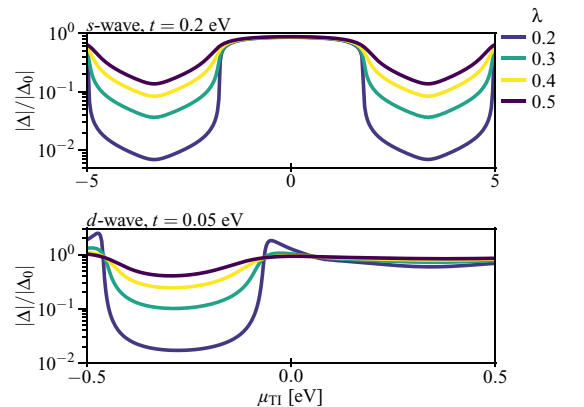


FIG. 4. The figure shows how the dimensionless coupling constant λ affects the suppression of the superconducting gap for *s*-wave *S* with $t = 0.2$ eV (top) and *d*-wave *S* with $t = 0.05$ eV and $\omega_+ = 0.15$ eV (bottom). Increasing λ makes the superconducting state more robust, reducing both the suppression of Δ , and also the increase in Δ at μ_{TI}^\pm in the *d*-wave case.

hybridization of the TI and S bands, and the large degree of mixing which occurs when the Fermi wave vectors of the S and TI coincide for chemical potential $\mu_{\text{TI}} = \pm\sqrt{2mv_{\text{F}}^2}\mu$. A larger value of λ results in a more robust superconducting state, and hence less suppression.

For parameter values relevant for s -wave superconductors, the interval of suppression grows quadratically with the hopping t , and eventually leads to strong suppression even at $\mu_{\text{TI}} = 0$. However, since there have been no experimental indications of a strong inverse proximity effect, we must conclude that the hopping is too weak to lead to suppression for experimentally accessible values of μ_{TI} . Neglecting the inverse proximity effect regarding the stability of the superconducting order therefore seems to be a good approximation for conventional s -wave superconductors.

A similar effect of suppressed superconductivity is also present for d -wave superconductors with parameter values relevant for the high- T_c superconductors. In this case the strong suppression is found for TI chemical potentials close to $-\sqrt{2mv_{\text{F}}^2}\mu$, where the interval of strong suppression of the gap grows approximately linearly with t . Since the Fermi energy μ is much lower for high- T_c superconductors, both the magnitude of the chemical potential $-\sqrt{2mv_{\text{F}}^2}\mu$, and the hopping strength needed for strong suppression at $\mu_{\text{TI}} = 0$ is much lower, making a strong inverse proximity effect more probable in such systems. In contrast to the s -wave case, the region of strong suppression was preceded by an increase in Δ above Δ_0 . This is, however, not a consequence of the pairing symmetry, but rather the difference in system parameters. For large enough cut-off frequencies, the integration region will include a band minimum/maximum just touching the Fermi level, leading to a large increase in the density of states, and thus increased gap.

We also find that the spin-triplet p -wave (f -wave) superconducting correlations are induced in the s -wave (d -wave) S due to the proximity-induced spin-orbit coupling. Possible further work could include breaking the translation symmetry in the x or y direction and probing the density of states normal to the z axis, possibly revealing signatures of p -wave or f -wave pairing. Moreover, it could be interesting to study the spatial variation of the order parameter in a superconductor with finite thickness.

ACKNOWLEDGMENTS

J.L. and A.S. acknowledge funding from the Research Council of Norway Center of Excellence Grant No. 262633, Center for Quantum Spintronics. A.S. and H.G.H. also acknowledge funding from the Research Council of Norway Grant No. 250985. J.L. acknowledges funding from Research Council of Norway Grant No. 240806. J.L. and M.A. also acknowledge funding from the NV-faculty at the Norwegian University of Science and Technology. H.G.H. thanks F. N. Krogh for useful discussions.

APPENDIX A: CRITERIA FOR STRONG PROXIMITY EFFECT

For superconductivity to occur, the Fermi wave vector of at least one of the bands has to lie within the interval

of attractive pairing, which for s -wave superconductors is $\sqrt{2m(\mu - \omega_D)} < |\mathbf{k}| < \sqrt{2m(\mu + \omega_D)}$. We find the Fermi wave vector of the energy bands by setting $\epsilon_{\alpha}^{\nu}(\mathbf{k}) = 0$, which yields the equation

$$[\alpha v_{\text{F}}|\mathbf{k}| - \mu_{\text{TI}}]\epsilon_{\mathbf{k}} - t^2 = 0. \quad (\text{A1})$$

Inserting $|\mathbf{k}| = k_{\pm}$ we get the value of μ_{TI} for which the Fermi wave vector of a band enters or leaves the interval of attractive pairing,

$$\mu_{\text{TI}}^{\alpha,\pm}(t) = \alpha\sqrt{2mv_{\text{F}}^2(\mu \mp \omega_D)} \pm \frac{t^2}{\omega_D}. \quad (\text{A2})$$

The Fermi wave vectors of the bands $\epsilon_{\alpha}^{-}(\mathbf{k})$ exceed k_+ at $\mu_{\text{TI}}^{\alpha,-}$, while the Fermi wave vectors of $\epsilon_{\alpha}^{+}(\mathbf{k})$ enter the interval $[k_-, k_+]$ at $\mu_{\text{TI}}^{\alpha,+}$. $\mu_{\text{TI}}^{\alpha,+}$ ($\mu_{\text{TI}}^{\alpha,-}$) is always positive (negative), while $\mu_{\text{TI}}^{\alpha,+}$ and $\mu_{\text{TI}}^{\alpha,-}$ change sign when $t^2 > \omega_D\sqrt{2mv_{\text{F}}^2(\mu + \omega_D)} \equiv (t_0^+)^2$ and $t^2 > \omega_D\sqrt{2mv_{\text{F}}^2(\mu - \omega_D)} \equiv (t_0^-)^2$, respectively, where $|t_0^+| > |t_0^-|$.

Hence we have strong suppression when

$$\mu_{\text{TI}}^{\alpha,-} < \mu_{\text{TI}} < \mu_{\text{TI}}^{\alpha,+}, \quad (\text{A3})$$

which for $\alpha = +1$ requires

$$t^2 > \omega[\sqrt{2mv_{\text{F}}^2(\mu + \omega_D)} - \sqrt{2mv_{\text{F}}^2(\mu - \omega)}].$$

Moreover, for $|t| > |t_+|$ and $\mu_{\text{TI}}^{\alpha,-} < \mu_{\text{TI}} < \mu_{\text{TI}}^{\alpha,+}$ no bands have a Fermi wave vector inside the relevant interval, and the gap is zero.

For the d -wave S we find an increase in the gap function for certain values of μ_{TI} . An increase in the gap would occur in regions where the Fermi wave vectors of two bands approach each other and finally coincide as a function of μ_{TI} , resulting in a region of closely spaced Fermi wave vectors. This can be seen to happen in Fig. 2(b). To find the value of μ_{TI} corresponding to the increase in Δ we find the local minima of

$$\mu_{\text{TI}}(k_{\text{F}}) = \alpha v_{\text{F}}k_{\text{F}} - \frac{t^2}{\epsilon_{k_{\text{F}}}} \quad (\text{A4})$$

by requiring $\partial_{k_{\text{F}}}\mu_{\text{TI}}(k_{\text{F}}) = 0$, from which we get the equation for k_{F} ,

$$\alpha v_{\text{F}} + \frac{t^2 k_{\text{F}}}{m\epsilon_{k_{\text{F}}}^2} = 0. \quad (\text{A5})$$

Solving this equation numerically with $\alpha = -1$ and inserting the results into Eq. (A4) yields the dashed lines in Fig. 2, in good agreement with the numerical results of the gap equation. To get an approximate analytical expression, we assume that $k_{\text{F}} = k_{\text{F}}^{\text{S}} + \delta k_{\text{F}}$, where $\delta k_{\text{F}} \ll k_{\text{F}}^{\text{S}}$, which is valid for sufficiently small t . Neglecting terms of $O(\delta k_{\text{F}}^3)$ and higher, we get

$$\delta k_{\text{F}}^2 + \frac{t^2 m}{\alpha v_{\text{F}} k_{\text{F}}^{\text{S}}} + \frac{t^2 m}{\alpha v_{\text{F}} (k_{\text{F}}^{\text{S}})^2} \delta k_{\text{F}} = 0. \quad (\text{A6})$$

Neglecting the last term yields, effectively keeping terms up to $O(t^2)$, results in

$$\delta k_{\text{F}} = \pm \sqrt{-\frac{1}{\alpha} \left(\frac{m}{2v_{\text{F}}^2\mu} \right)^{1/4}} t, \quad (\text{A7})$$

from which it is clear that we only have solutions for $\alpha = -1$. Inserting this expression into Eq. (A4), we get to $O(t^2)$

$$\mu_{\text{T1}}^{\pm} \approx -\sqrt{2mv_{\text{F}}^2\mu} \pm 2\left(\frac{mv_{\text{F}}^2}{2\mu}\right)^{1/4} t + \frac{1}{4\mu}t^2. \quad (\text{A8})$$

This result is plotted as dotted lines in Fig. 2(a), and is in good agreement with the exact numerical results for small t . For $\mu_{\text{T1}}^- < \mu_{\text{T1}} < \mu_{\text{T1}}^+$, there is only one Fermi wave vector in the integration region, leading to a suppressed gap.

APPENDIX B: FUNCTIONAL INTEGRAL IN NAMBU SPINOR NOTATION

We begin by considering the Gaussian integral over Grassmann variables [47],

$$I = \left(\prod_i \int da_i \right) e^{-1/2 \sum_{i,j} a_i M_{ij} a_j} = \left(\prod_i \int da_i \right) \prod_{i,j} \left(1 - \frac{1}{2} a_i M_{ij} a_j \right) = \text{Pf} \left(\frac{M - M^T}{2} \right), \quad (\text{B1})$$

where $\text{Pf}[(M - M^T)/2]$ is the Pfaffian of the antisymmetric part of M , where $\text{Pf}(A)^2 = \det(A)$. As an example we consider only two variables, a_1 and a_2 . In this case, terms containing M_{ii} disappear, since $a_i^2 = 0$, as do second-order terms in M . For the above integral we therefore get

$$I = \int da_1 da_2 \frac{1}{2} (-a_1 M_{12} a_2 - a_2 M_{21} a_1) = \frac{M_{12} - M_{21}}{2} = \sqrt{\det \frac{M - M^T}{2}} = \sqrt{\det M^A} = \text{Pf}(M^A). \quad (\text{B2})$$

Here, M^A is the antisymmetric part of M .

Applying this to the problem of integrating $\exp(-S_S^{\text{eff}})$, we first write the action in terms of the Nambu spinor \mathcal{C} :

$$\begin{aligned} S_S^{\text{eff}} &= -\frac{1}{\beta V} \sum_{k,k'} \mathcal{C}^T(-k) \begin{pmatrix} \varphi^\dagger(k'-k) \frac{\sigma_x - i\sigma_y}{2} & 0 \\ \mathcal{G}_0^{-1}(k) \delta_{k,k'} & \varphi(k-k') \frac{\sigma_x + i\sigma_y}{2} \end{pmatrix} \mathcal{C}(k') \equiv -\frac{1}{2\beta V} \sum_{k,k'} \mathcal{C}^T(-k) A(k,k') \mathcal{C}(k') \\ &= -\frac{1}{\beta V} \sum_{k,k'} \mathcal{C}^T(k) \begin{pmatrix} -\varphi^\dagger(k-k) \frac{\sigma_x + i\sigma_y}{2} & -[\mathcal{G}_0^{-1}(k)]^T \delta_{k,k'} \\ 0 & -\varphi(k'-k) \frac{\sigma_x - i\sigma_y}{2} \end{pmatrix} \mathcal{C}(-k') \equiv -\frac{1}{2\beta V} \sum_{k,k'} \mathcal{C}^T(k) [-A(k',k)]^T \mathcal{C}(-k'). \end{aligned}$$

Combining these two expressions, we get

$$\begin{aligned} S_S^{\text{eff}} &= -\frac{1}{2\beta V} \sum_{k,k'} \mathcal{C}^T(-k) \begin{pmatrix} -\varphi^\dagger(k'-k) i\sigma_y & -[\mathcal{G}_0^{-1}(-k)]^T \delta_{k,k'} \\ \mathcal{G}_0^{-1}(k) \delta_{k,k'} & \varphi(k-k') i\sigma_y \end{pmatrix} \mathcal{C}(k') \\ &= -\frac{1}{2\beta V} \sum_{k,k'} \mathcal{C}^T(-k) \frac{A(k,k') - A^T(-k',-k)}{2} \mathcal{C}(k') = -\frac{1}{2\beta V} \sum_{k,k'} \mathcal{C}^T(-k) A^A(k,k') \mathcal{C}(k'), \end{aligned} \quad (\text{B3})$$

where $A^A(k,k')$ denotes the antisymmetric part of A . This is exactly equal to Eq. (15), as can be seen by the following manipulations. For notational simplicity we use the two-vector notation

$$\mathcal{C}(k) = \begin{pmatrix} c(k) \\ c^*(-k) \end{pmatrix}, \quad (\text{B4})$$

i.e., $[\mathcal{C}(k)]_1 = c(k)$, $[\mathcal{C}(k)]_2 = c^*(-k)$. Hence the matrix multiplication in Eq. (B3) can be written

$$\begin{aligned} \sum_{ij} [\mathcal{C}^T(-k)]_i [A^A(k,k')]_{ij} [\mathcal{C}(k')]_j &= -[\mathcal{C}^T(-k)]_1 \varphi^\dagger(k'-k) i\sigma_y [\mathcal{C}(k')]_1 - [\mathcal{C}^T(-k)]_1 [\mathcal{G}_0^{-1}(-k) \delta_{k,k'}]^T [\mathcal{C}(k')]_2 \\ &\quad + [\mathcal{C}^T(-k)]_2 \mathcal{G}_0^{-1}(-k) \delta_{k,k'} [\mathcal{C}(k')]_1 + [\mathcal{C}^T(-k)]_2 \varphi(k-k') i\sigma_y [\mathcal{C}(k')]_2. \end{aligned} \quad (\text{B5})$$

We use the fact that $[\mathcal{C}^\dagger(k)]_1 = [\mathcal{C}^T(-k)]_2$ and $[\mathcal{C}^\dagger(k)]_2 = [\mathcal{C}^T(-k)]_1$, and relate the remaining factors to the elements of $\mathcal{G}^{-1}(k,k')$ in Eq. (16),

$$\begin{aligned} \mathcal{C}^T(-k) A^A(k,k') \mathcal{C}(k') &= [\mathcal{C}^\dagger(k)]_2 [\mathcal{G}^{-1}(k,k')]_{21} [\mathcal{C}(k')]_1 + [\mathcal{C}^\dagger(k)]_2 [\mathcal{G}^{-1}(k,k')]_{22} [\mathcal{C}(k')]_2 + [\mathcal{C}^\dagger(k)]_1 [\mathcal{G}^{-1}(k,k')]_{11} [\mathcal{C}(k')]_1 \\ &\quad + [\mathcal{C}^\dagger(k)]_1 [\mathcal{G}^{-1}(k,k')]_{12} [\mathcal{C}(k')]_2 \\ &= \mathcal{C}^\dagger(k) \mathcal{G}^{-1}(k,k') \mathcal{C}(k'), \end{aligned} \quad (\text{B6})$$

which shows that Eqs. (B3) and (15) are equivalent. Using Eq. (B1), the functional integral of the action in Eq. (B3) results in

$$Z = \int \mathcal{D}c^\dagger \mathcal{D}c e^{-S_S^{\text{eff}}} = \sqrt{\det[-A^A]}, \quad (\text{B7})$$

where we have neglected various numerical constants. By interchanging an even number of rows, it can be shown that $A^A(k, k') \rightarrow \mathcal{G}^{-1}(k, k')$, and since the determinant is invariant under an even number of interchanges, we find [39]

$$Z = e^{1/2 \text{Tr} \ln(-\mathcal{G}^{-1})}. \quad (\text{B8})$$

APPENDIX C: ZERO-TEMPERATURE GAP FOR $t = 0$

When $t = 0$, the gap equation, Eq. (32), reduces to

$$1 = \frac{g}{2V} \sum_{\mathbf{k}} \frac{v^2(\mathbf{k})}{\sqrt{\epsilon_{\mathbf{k}} + |\Delta_0(\mathbf{k})|^2}} \quad (\text{C1})$$

in the zero-temperature limit. Transforming this to an integration over $\phi_{\mathbf{k}}$ and energy, we get

$$1 = \frac{\lambda}{2} \int_{-\omega_-}^{\omega_+} d\epsilon \int_0^{2\pi} \frac{d\phi_{\mathbf{k}}}{2\pi} \frac{v^2(\phi_{\mathbf{k}})}{\sqrt{\epsilon + |\Delta_0(\phi_{\mathbf{k}})|^2}}, \quad (\text{C2})$$

where ω_{\pm} are positive. Performing the energy integral we get

$$1 = \frac{\lambda}{2} \int_0^{2\pi} \frac{d\phi_{\mathbf{k}}}{2\pi} v^2(\phi_{\mathbf{k}}) \ln \frac{\sqrt{|\Delta_0(\phi_{\mathbf{k}})|^2 + \omega_+^2} + \omega_+}{\sqrt{|\Delta_0(\phi_{\mathbf{k}})|^2 + \omega_-^2} - \omega_-} \\ \approx \frac{\lambda}{2} \int_0^{2\pi} \frac{d\phi_{\mathbf{k}}}{2\pi} v^2(\phi_{\mathbf{k}}) \left[\ln \frac{4\omega_- \omega_+}{\Delta_0^2} - 2 \ln |v(\phi_{\mathbf{k}})| \right], \quad (\text{C3})$$

where we in the last line have assumed that the gap is small compared to the cut-off energy. For an s -wave superconductor $v(\phi_{\mathbf{k}}) = 1$, and we get simply $\Delta_0 = 2\sqrt{\omega_- \omega_+} e^{-1/\lambda}$. For

d -wave pairing we can instead write the gap as

$$\Delta_0 = 2\sqrt{\omega_- \omega_+} e^{-(1/\lambda) - I}, \quad (\text{C4})$$

where we have defined the integral

$$I = \int_0^{2\pi} \frac{d\phi_{\mathbf{k}}}{2\pi} v^2(\phi_{\mathbf{k}}) \ln |v(\phi_{\mathbf{k}})| = \frac{1 - \ln 2}{2} \approx 0.153426. \quad (\text{C5})$$

Hence, the maximum d -wave gap amplitude is marginally smaller than the s -wave gap for the same values of λ and ω_{\pm} .

APPENDIX D: NUMERICAL INTEGRATION PROCEDURES

When solving the gap equation numerically, the \mathbf{k} sum is rewritten in terms of an energy integral over $\epsilon_{\mathbf{k}}$ and an integral over $\phi_{\mathbf{k}}$, which in the s -wave case is simply equal to 2π . In the s -wave case we therefore only have to perform the energy integral for energies in the interval $[-\omega_-, \omega_+]$, in our case using Python and the implementation TRAPZ of the trapezoidal method in the SCIPY library. In the d -wave case, we use the QUADPY library's implementation of the numerical integration method in Ref. [48] when calculating the 2D integral in the $\epsilon_{\mathbf{k}}\text{-}\phi_{\mathbf{k}}$ plane.

-
- [1] M. Z. Hasan and C. L. Kane, *Rev. Mod. Phys.* **82**, 3045 (2010).
[2] X. L. Qi and S. C. Zhang, *Rev. Mod. Phys.* **83**, 1057 (2011).
[3] T. O. Wehling, A. M. Black-Schaffer, and A. V. Balatsky, *Adv. Phys.* **63**, 1 (2014).
[4] J. Alicea, *Rep. Prog. Phys.* **75**, 076501 (2012).
[5] L. Fu and C. L. Kane, *Phys. Rev. Lett.* **100**, 096407 (2008).
[6] Y. Tanaka, T. Yokoyama, and N. Nagaosa, *Phys. Rev. Lett.* **103**, 107002 (2009).
[7] A. Zyuzin, M. Alidoust, and D. Loss, *Phys. Rev. B* **93**, 214502 (2016).
[8] M. Amundsen, H. G. Hugdal, A. Sudbø, and J. Linder, *Phys. Rev. B* **98**, 144505 (2018).
[9] L. Fu and C. L. Kane, *Phys. Rev. Lett.* **102**, 216403 (2009).
[10] A. R. Akhmerov, J. Nilsson, and C. W. J. Beenakker, *Phys. Rev. Lett.* **102**, 216404 (2009).
[11] J. Linder, Y. Tanaka, T. Yokoyama, A. Sudbø, and N. Nagaosa, *Phys. Rev. Lett.* **104**, 067001 (2010).
[12] J. Linder, Y. Tanaka, T. Yokoyama, A. Sudbø, and N. Nagaosa, *Phys. Rev. B* **81**, 184525 (2010).
[13] D. Zhang, J. Wang, A. M. DaSilva, J. S. Lee, H. R. Gutierrez, M. H. W. Chan, J. Jain, and N. Samarth, *Phys. Rev. B* **84**, 165120 (2011).
[14] A. Cook and M. Franz, *Phys. Rev. B* **84**, 201105 (2011).
[15] F. Qu, F. Yang, J. Shen, Y. Ding, J. Chen, Z. Ji, G. Liu, J. Fan, X. Jing, C. Yang, and L. Lu, *Sci. Rep.* **2**, 339 (2012).
[16] A. M. Cook, M. M. Vazifeh, and M. Franz, *Phys. Rev. B* **86**, 155431 (2012).
[17] I. Sochnikov, A. J. Bestwick, J. R. Williams, T. M. Lippman, I. R. Fisher, D. Goldhaber-Gordon, J. R. Kirtley, and K. A. Moler, *Nano Lett.* **13**, 3086 (2013).
[18] G. Koren, T. Kirzhner, Y. Kalcheim, and O. Millo, *Europhys. Lett.* **103**, 67010 (2013).
[19] L. Galletti, S. Charpentier, M. Iavarone, P. Lucignano, D. Massarotti, R. Arpaia, Y. Suzuki, K. Kadowaki, T. Bauch, A. Tagliacozzo, F. Tafuri, and F. Lombardi, *Phys. Rev. B* **89**, 134512 (2014).
[20] I. Sochnikov, L. Maier, C. A. Watson, J. R. Kirtley, C. Gould, G. Tkachov, E. M. Hankiewicz, C. Brüne, H. Buhmann, L. W. Molenkamp, and K. A. Moler, *Phys. Rev. Lett.* **114**, 066801 (2015).
[21] Z.-Z. Li, F.-C. Zhang, and Q.-H. Wang, *Sci. Rep.* **4**, 6363 (2015).
[22] Y. Kim, T. M. Philip, M. J. Park, and M. J. Gilbert, *Phys. Rev. B* **94**, 235434 (2016).
[23] T. Shoman, A. Takayama, T. Sato, S. Souma, T. Takahashi, T. Oguchi, K. Segawa, and Y. Ando, *Nat. Commun.* **6**, 6547 (2015).
[24] P. Fulde and R. A. Ferrell, *Phys. Rev.* **135**, A550 (1964).
[25] M. J. Park, J. Yang, Y. Kim, and M. J. Gilbert, *Phys. Rev. B* **96**, 064518 (2017).
[26] N. Sedlmayr, E. W. Goodwin, M. Gottschalk, I. M. Dayton, C. Zhang, E. Huemiller, R. Loloee, T. C. Chasapis, M. Salehi, N. Koirala, M. G. Kanatzidis, S. Oh, D. J. Van Harlingen, A. Levchenko, and S. H. Tessmer, *arXiv:1805.12330*.

- [27] M. M. Ugeda, A. J. Bradley, Y. Zhang, S. Onishi, Y. Chen, W. Ruan, C. Ojeda-Aristizabal, H. Ryu, M. T. Edmonds, H.-Z. Tsai, A. Riss, S.-K. Mo, D. Lee, A. Zettl, Z. Hussain, Z.-X. Shen, and M. F. Crommie, *Nat. Phys.* **12**, 92 (2016).
- [28] Q.-Y. Wang, Z. Li, W.-H. Zhang, Z.-C. Zhang, J.-S. Zhang, W. Li, H. Ding, Y.-B. Ou, P. Deng, K. Chang, J. Wen, C.-L. Song, K. He, J.-F. Jia, S.-H. Ji, Y.-Y. Wang, L.-L. Wang, X. Chen, X.-C. Ma, and Q.-K. Xue, *Chin. Phys. Lett.* **29**, 037402 (2012).
- [29] D. Liu, W. Zhang, D. Mou, J. He, Y.-B. Ou, Q.-Y. Wang, Z. Li, L. Wang, L. Zhao, S. He, Y. Peng, X. Liu, C. Chen, L. Yu, G. Liu, X. Dong, J. Zhang, C. Chen, Z. Xu, J. Hu, X. Chen, X. Ma, Q. Xue, and X. J. Zhou, *Nat. Commun.* **3**, 931 (2012).
- [30] S. He, J. He, W. Zhang, L. Zhao, D. Liu, X. Liu, D. Mou, Y.-B. Ou, Q.-Y. Wang, Z. Li, L. Wang, Y. Peng, Y. Liu, C. Chen, L. Yu, G. Liu, X. Dong, J. Zhang, C. Chen, Z. Xu, X. Chen, X. Ma, Q. Xue, and X. J. Zhou, *Nat. Mater.* **12**, 605 (2013).
- [31] K. Fossheim and A. Sudbø, *Superconductivity: Physics and Applications* (Wiley, Chichester, 2004).
- [32] T. Moryia, Y. Takahashi, and K. Ueda, *J. Phys. Soc. Jpn.* **59**, 2905 (1990).
- [33] P. Monthoux, A. V. Balatsky, and D. Pines, *Phys. Rev. B* **46**, 14803 (1992).
- [34] D. Pines, *J. Phys. Chem. Solids* **54**, 1447 (1993).
- [35] T. Moryia and K. Ueda, *J. Phys. Soc. Jpn.* **63**, 1871 (1994).
- [36] A. M. Black-Schaffer and A. V. Balatsky, *Phys. Rev. B* **87**, 220506(R) (2013).
- [37] Y. Takane and R. Ando, *J. Phys. Soc. Jpn.* **83**, 014706 (2014).
- [38] A. Altland and B. Simons, *Condensed Matter Field Theory*, 2nd ed. (Cambridge University Press, Cambridge, 2010).
- [39] F. N. Krogh and A. Sudbø, *Phys. Rev. B* **98**, 014510 (2018).
- [40] L. P. Gor'kov and E. I. Rashba, *Phys. Rev. Lett.* **87**, 037004 (2001).
- [41] T. Yokoyama, *Phys. Rev. B* **86**, 075410 (2012).
- [42] J. Bardeen, L. N. Cooper, and J. R. Schrieffer, *Phys. Rev.* **108**, 1175 (1957).
- [43] N. W. Ashcroft and N. D. Mermin, *Solid State Physics* (Holt, Rinehart and Winston, New York, 1976).
- [44] C. Brüne, C. X. Liu, E. G. Novik, E. M. Hankiewicz, H. Buhmann, Y. L. Chen, X. L. Qi, Z. X. Shen, S. C. Zhang, and L. W. Molenkamp, *Phys. Rev. Lett.* **106**, 126803 (2011).
- [45] Y. M. Gerbstein, N. E. Timoschenko, and F. A. Chudnovskii, *Phys. C* **162–164**, 961 (1989).
- [46] N. Nagaosa, *Science* **275**, 1078 (1997).
- [47] F. Wegner, *Supermathematics and its Applications in Statistical Physics: Grassmann Variables and the Method of Supersymmetry* (Springer, Berlin/Heidelberg, 2016), Chap. 5.
- [48] H. Xiao and Z. Gimbutas, *Comput. Math. Appl.* **59**, 663 (2010).

4

Reference

H. G. Hugdal, S. Rex, F. S. Nogueira and A. Sudbø,

Magnon-induced superconductivity in a topological insulator coupled to ferromagnetic and antiferromagnetic insulators.

Physical Review B, **97**, 195438 (2018).

Contributions

AS and SR initiated the project. HGH performed the analytical and numerical calculations with input from AS, SR and FSN, and wrote the initial manuscript. All authors contributed to the discussion of the results and revision of the manuscript.

Magnon-induced superconductivity in a topological insulator coupled to ferromagnetic and antiferromagnetic insulators

Henning G. Hugdal,^{1,2} Stefan Rex,^{3,4} Flavio S. Nogueira,⁵ and Asle Sudbø^{1,2,*}

¹*Department of Physics, NTNU, Norwegian University of Science and Technology, NO-7491 Trondheim, Norway*

²*Center for Quantum Spintronics, Norwegian University of Science and Technology, NO-7491 Trondheim, Norway*

³*Institut für Nanotechnologie, Karlsruhe Institute of Technology, 76021 Karlsruhe, Germany*

⁴*Institut für Theorie der Kondensierten Materie, Karlsruhe Institute of Technology, 76128 Karlsruhe, Germany*

⁵*Institute for Theoretical Solid State Physics, IFW Dresden, PF 270116, D-01171 Dresden, Germany*



(Received 26 February 2018; published 23 May 2018)

We study the effective interactions between Dirac fermions on the surface of a three-dimensional topological insulator due to the proximity coupling to the magnetic fluctuations in a ferromagnetic or antiferromagnetic insulator. Our results show that the magnetic fluctuations can mediate attractive interactions between Dirac fermions of both Amperean and BCS types. In the ferromagnetic case, we find pairing between fermions with parallel momenta, so-called Amperean pairing, whenever the effective Lagrangian for the magnetic fluctuations does not contain a quadratic term. The pairing interaction also increases with increasing Fermi momentum and is in agreement with previous studies in the limit of high chemical potential. If a quadratic term is present, the pairing is instead of BCS type above a certain chemical potential. In the antiferromagnetic case, BCS pairing occurs when the ferromagnetic coupling between magnons on the same sublattice exceeds the antiferromagnetic coupling between magnons on different sublattices. Outside this region in parameter space, we again find that Amperean pairing is realized.

DOI: [10.1103/PhysRevB.97.195438](https://doi.org/10.1103/PhysRevB.97.195438)

I. INTRODUCTION

Topological insulators (TIs) have attracted much attention since their discovery a decade ago [1,2]. Although being insulating in the bulk, the surface of a three-dimensional TI has topologically protected metallic surface states. These metallic surface states are well described by the two-dimensional (2D) massless Dirac equation, having linear dispersions and spin-momentum locking, and are therefore often called Dirac fermions [3]. A gap in the dispersion, analogous to the mass gap for massive relativistic fermions, can be opened by breaking the time-reversal symmetry of the system, for instance, by applying a magnetic field normal to the TI surface or by proximity coupling to a magnetic insulator [4–8].

Many theoretical works have studied heterostructures consisting of TIs and ferromagnetic (FM) insulators, focusing in particular on the effects on the magnetization in the magnetic layer [9–20]. One recent study focused instead on the effective interactions between Dirac fermions on the surface of a TI coupled to a FM insulator with mean-field magnetization perpendicular to the TI surface [21]. It showed that interactions between the Dirac fermions and the transverse magnons in the FM lead to an effective attractive pairing between fermions with parallel momenta, so-called Amperean pairing [22,23]. In the presence of spin-momentum locking, this exotic pairing also implies that the pairs will form spin triplets. However, the chemical potential was assumed to be tuned far away

from the gap thus neglecting the effects of the mass gap in the Dirac fermion dispersion. This raises the question how the pairing is affected when the chemical potential is tuned towards the gap as the pairing must disappear in the absence of a Fermi surface. Moreover, the pairing mediated by fluctuations in other magnetic configurations than FM order have not yet been studied. Bilayer systems of antiferromagnetic (AFM) insulators and TI films, for instance, are also under experimental investigation [24].

Rex *et al.* [20] recently studied the effective theory for the magnetic moments in a bipartite magnetic insulator (BMI) coupled to the Dirac fermions on a TI surface. Their model allows to continuously tune the magnet from a FM to an AFM configuration. In the present paper we will use the same model, restricted to the limiting FM and AFM cases, to study the effective interactions between the Dirac fermions induced by the magnetic fluctuations, including the effects of the mass gap. Possible material choices for such systems are Bi₂Se₃ or Bi₂Te₃ as the TI, EuS as FM [4,25], and NiO or CoO as AFM [26–30]. In both cases, we find that pairing between Dirac fermions is possible in certain regions of parameter space. For coupling to ferromagnetic fluctuations, the pairing is of the Amperean type whenever there is no quadratic coupling term between the magnons, in agreement with Ref. [21] in the limit of high chemical potential. However, as the Fermi level is moved towards the gap, the pairing decreases, vanishing when the chemical potential is tuned inside the gap. We also find that pairing of the Bardeen-Cooper-Schrieffer (BCS) type, i.e., where the interacting particles have momenta in opposite directions, is possible in certain regions of the parameter space.

*Corresponding author: asle.sudbo@ntnu.no

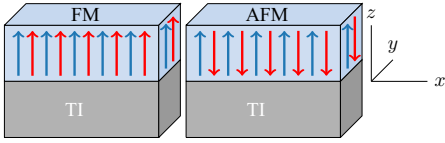


FIG. 1. Bilayer heterostructures consisting of ferromagnetic and antiferromagnetic insulators proximity coupled to a TI are modeled using a bipartite magnetic insulator with tunable mean-field magnetizations [20]. The surface of the TI is placed in the xy plane, and the mean-field magnetization of the magnetic insulators is perpendicular to the interface.

In the antiferromagnetic case we again find pairing of both types, depending on the relative strength between the intra- and interlattice couplings. Hence, we find that, for both magnetic configurations, magnon-induced superconductivity due to the attractive interactions is possible.

The remainder of the article is organized as follows: The model is presented in Sec. II together with the derivation of the effective action for the TI surface fermions. Subsequently, the effective pairing interaction on the TI surface is discussed for the FM and AFM cases in Secs. III and IV, respectively. The results are summarized in Sec. V. Further details regarding the derivation of the effective TI action are presented in the Appendix.

II. MODEL

The bilayer heterostructures are described by taking into account the surface of the TI and magnetic insulator, the bulk of the magnetic insulators, and hopping across the interface due to the proximity [20]. In order to treat heterostructures with FM and AFM insulators simultaneously, we will consider a BMI consisting of two FMs with lattice magnetizations \mathbf{m}_1 and \mathbf{m}_2 as is illustrated in Fig. 1. We set $\hbar = 1$ throughout the paper and work close to zero temperature utilizing the zero-temperature Matsubara frequency formalism. The bulk of the magnetic insulator is described by the Lagrangian $\mathcal{L}_{\text{BMI}} = \mathcal{L}_1 + \mathcal{L}_2 + \mathcal{L}_{\text{ex}}$, where

$$\mathcal{L}_i = -\mathbf{b}(\mathbf{m}_i) \cdot \partial_t \mathbf{m}_i - \frac{\kappa}{2} (\nabla \mathbf{m}_i)^2 \quad (1)$$

amounts to a continuum description of each of the two sublattices with $i = 1, 2$, whereas

$$\mathcal{L}_{\text{ex}} = -\lambda \mathbf{m}_1 \cdot \mathbf{m}_2 \quad (2)$$

describes the exchange interaction. $\kappa > 0$ is the ferromagnetic exchange-coupling constant, whereas the coupling between the two lattices is ferromagnetic or antiferromagnetic for $\lambda < 0$ or $\lambda > 0$, respectively. \mathbf{b} denotes the Berry connection, satisfying $\nabla_{\mathbf{m}_i} \times \mathbf{b}(\mathbf{m}_i) = \mathbf{m}_i / m_i^2$.

The surface of the TI is described by the 2D Dirac Lagrangian together with a weak quadratic term in the derivatives leading to particle-hole asymmetry [31–34],

$$\mathcal{L}_{\text{TI}} = \Psi^\dagger [i \partial_t - i v_F (\sigma_y \partial_x - \sigma_x \partial_y) + E_0 (\partial_x^2 + \partial_y^2) + \mu] \Psi, \quad (3)$$

where $\Psi = (\psi_\uparrow, \psi_\downarrow)^T$ is the spinor of the Dirac fermions, \uparrow, \downarrow label the spin in the z direction, v_F is the Fermi velocity, and μ is the chemical potential. The second derivative term is assumed small compared to the Dirac term. We have not included the fluctuating Coulomb interactions between the Dirac fermions since this interaction is screened whenever we have a Fermi surface. For the ferromagnetic case, there will also be a demagnetizing field outside the ferromagnet, resulting in a coupling to a mostly in-plane vector potential in the TI Hamiltonian [35]. This coupling in turn leads to circular orbits with radii of the order of the magnetic length $l \sim \sqrt{e \mu_0 |\mathbf{M}| / \hbar}$ [33] where \mathbf{M} is the magnetization, μ_0 is the vacuum permeability, and e is the electron charge. This coupling can only be neglected when the motion of the TI fermions is unaffected on the relevant length scale, which for superconductivity is the coherence length ξ , i.e., we must have $l \gg \xi$. Using $\xi \sim \hbar v_F / k_B T_c$ [36] where T_c is the critical temperature, we get the requirement that $|\mathbf{M}| \ll e \mu_0 k_B^2 T_c^2 / \hbar v_F^2$. We will assume that this holds in the following. Since antiferromagnets have close to zero stray fields [37,38], the coupling to the vector potential can be safely disregarded in the AFM case.

In order to couple the TI fermions and BMI magnetization, Rex *et al.* [20] introduced auxiliary fermionic fields $\chi_i = (\chi_\uparrow, \chi_\downarrow)^T$ on the surface of the magnet for the two sublattices $i = 1, 2$. These fields can be interpreted as electrons in the magnetic insulator, which are localized in the atomic limit. Their spins $\mathbf{S}_i = \frac{1}{2} \chi_i^\dagger \boldsymbol{\sigma} \chi_i$ are coupled to the magnetization of the corresponding sublattice, and in proximity to the TI, hopping across the interface is taken into account. Thus, the Hamiltonian of χ_1, χ_2 is

$$H_{\text{surf}} = -t (\chi_1^\dagger \chi_2 + \chi_2^\dagger \chi_1) - J \sum_{i=1,2} \chi_i^\dagger \mathbf{m}_i \cdot \boldsymbol{\sigma} \chi_i - h [\Psi^\dagger (\chi_1 + \chi_2) + (\chi_1^\dagger + \chi_2^\dagger) \Psi]. \quad (4)$$

Here, t is the coupling between the surface fermions, J and h are the strengths of the coupling to the magnetization \mathbf{m}_i at $z = 0$ and to the Dirac fermions, respectively, and $\boldsymbol{\sigma}$ is the Pauli matrix vector.

A. Integration of magnetic moments

By integrating out the χ_i fermions, an effective theory for the Dirac fermions and magnetizations was obtained in Ref. [20], including effective couplings between Ψ and \mathbf{m}_i . In the following, we will assume that the length of the magnetizations \mathbf{m}_i is fixed to the mean-field value of $|\mathbf{m}_i| = \pm \bar{m}_i$ and write the magnetization vector as [21]

$$\mathbf{m}_i = \bar{m}_i \hat{z} \sqrt{1 - \frac{\tilde{\mathbf{m}}_i^2}{\bar{m}_i^2}} + \tilde{\mathbf{m}}_i, \quad (5)$$

where $\tilde{\mathbf{m}}_i = \tilde{m}_i^x \hat{x} + \tilde{m}_i^y \hat{y}$. By fixing the length in this way, the fluctuations in the z direction are of second order in $|\tilde{\mathbf{m}}_i|$. Working to second order in $\tilde{m}_i^{x/y}$, we get the Berry connection,

$$\mathbf{b}(\mathbf{m}_i) = -\frac{\tilde{m}_i^y \hat{x} - \tilde{m}_i^x \hat{y}}{2\bar{m}_i}, \quad (6)$$

and the effective Lagrangian for the magnetic fluctuations can be written as

$$\begin{aligned} \mathcal{L}_{\tilde{\mathbf{m}}} = & \sum_{i=1,2} \left\{ - \left(\frac{1}{2\tilde{m}_i} - 2D_i^{0z} \right) \hat{z} \cdot (\tilde{\mathbf{m}}_i \times \partial_t \tilde{\mathbf{m}}_i) - \frac{\kappa}{2} (\nabla \tilde{\mathbf{m}}_i)^2 \right. \\ & + \frac{1}{2} \left[\frac{\tilde{m}_{3-i}}{\tilde{m}_i} \lambda - 2J^2 (D_i^{00} - D_i^{zz}) \right] \tilde{\mathbf{m}}_i \cdot \tilde{\mathbf{m}}_i \\ & + \Psi^\dagger J_i \tilde{\mathbf{m}}_i \cdot \boldsymbol{\sigma} \Psi \left. \right\} - [\lambda + 2J^2 (T^{00} - T^{zz})] \tilde{\mathbf{m}}_1 \cdot \tilde{\mathbf{m}}_2 \\ & + 2J^2 \mathcal{T}^{0z} \hat{z} \cdot (\tilde{\mathbf{m}}_1 \times \partial_t \tilde{\mathbf{m}}_2 + \tilde{\mathbf{m}}_2 \times \partial_t \tilde{\mathbf{m}}_1), \end{aligned} \quad (7)$$

where

$$J_i = \frac{h^2 J}{(t^2 - J^2 \tilde{m}_{3-i} \tilde{m}_2)^2} (J^2 \tilde{m}_{3-i}^2 - t^2) \quad (8)$$

is the effective magnetic coupling of the TI surface states to $\tilde{\mathbf{m}}_i$. The coefficients D_i^{00} , D_i^{zz} , \mathcal{D}_i^{0z} , T^{00} , T^{zz} , and \mathcal{T}^{0z} depend only on the model parameters and are described in detail in Ref. [20]. Since h is assumed small compared to

t and $J\tilde{m}_i$ [20], we have neglected terms of $O(h^2|\tilde{\mathbf{m}}_i|^2)$ in Eq. (7). Note that the exchange couplings between fluctuations are renormalized in the above Lagrangian,

$$\tilde{\lambda}_i = \frac{\tilde{m}_{3-i}}{2\tilde{m}_i} \lambda - J^2 (D_i^{00} - D_i^{zz}), \quad (9a)$$

$$\lambda_{\text{eff}} = \lambda + 2J^2 (T^{00} - T^{zz}). \quad (9b)$$

Integration of the χ fermions also results in an additional term in the Dirac Lagrangian due to the mean-field magnetizations in the BMI,

$$\delta\mathcal{L}_{\text{MF}} = \Psi^\dagger (J_1 \tilde{m}_1 \sigma_z + J_2 \tilde{m}_2 \sigma_z) \Psi. \quad (10)$$

As will be shown in the next section, this term can create a gap in the Dirac fermion dispersion.

Specializing to the ferromagnetic ($\tilde{m}_2 = \tilde{m}_1 = \tilde{m}$) and antiferromagnetic ($\tilde{m}_2 = -\tilde{m}_1 = -\tilde{m}$) cases, we define $\nu = \tilde{m}_2/\tilde{m}_1 = \pm 1$ for notational simplicity. In both cases the magnetic couplings in Eq. (8) are identical on the two sublattices $J_1 = J_2 \equiv J$. Transforming to imaginary time $T = it$ in the zero-temperature limit and Fourier transforming both the time and the space variables [44], we arrive at the functional integral in the magnon fields,

$$Z = \int \mathcal{D}[M] e^{-S_{\text{mag}}}, \quad (11)$$

where

$$S_{\text{mag}} = \int \frac{d^3q}{(2\pi)^3} \left\{ M^T(-q) \mathcal{K}(q) M(q) - \frac{1}{2} [\mathcal{J}^T(q) M(q) + M^T(-q) \mathcal{J}(-q)] \right\}. \quad (12)$$

Here, we have defined the matrix,

$$\mathcal{K}(q) = \begin{pmatrix} \frac{\kappa}{2} \mathbf{q}^2 - \frac{\lambda\nu}{2} + J^2 D - \frac{i\sigma_y}{2m^*} \Omega & \frac{\lambda}{2} + J^2 T + J^2 (1 + \nu) \mathcal{T}^{0z} i\sigma_y \Omega \\ \frac{\lambda}{2} + J^2 T + J^2 (1 + \nu) \mathcal{T}^{0z} i\sigma_y \Omega & \frac{\kappa}{2} \mathbf{q}^2 - \frac{\lambda}{2\nu} + J^2 D - \frac{i\sigma_y}{2\nu m^*} \Omega \end{pmatrix}, \quad (13)$$

and the four-component fluctuation vectors,

$$M(q) = [\tilde{\mathbf{m}}_1^x(q) \tilde{\mathbf{m}}_1^y(q) \tilde{\mathbf{m}}_2^x(q) \tilde{\mathbf{m}}_2^y(q)]^T, \quad (14)$$

and

$$\mathcal{J}(q) = \int \frac{d^3k}{(2\pi)^3} \begin{pmatrix} \bar{J} \Psi^\dagger(k) \sigma_x \Psi(k - q) \\ \bar{J} \Psi^\dagger(k) \sigma_y \Psi(k - q) \\ \bar{J} \Psi^\dagger(k) \sigma_x \Psi(k - q) \\ \bar{J} \Psi^\dagger(k) \sigma_y \Psi(k - q) \end{pmatrix}. \quad (15)$$

The functions D , T , and m^* are defined in the Appendix. We have also used the notation $q = (\Omega, \mathbf{q})$ and $k = (\omega, \mathbf{k})$ for the bosonic and fermionic fields, respectively. Performing the functional integral, we get the additional contribution to the Dirac action,

$$\delta S_{\text{TI}} = -\frac{1}{4} \int \frac{d^3q}{(2\pi)^3} \mathcal{J}^T(q) \mathcal{K}^{-1}(q) \mathcal{J}(-q). \quad (16)$$

After calculating \mathcal{K}^{-1} , details of which are given in the Appendix, the effective action in the FM and AFM cases can be calculated separately. However, the resulting magnon-mediated interaction between the Ψ fermions is given in the

chirality basis rather than the spin basis. Therefore, we will derive the corresponding operator transformations for the Ψ operators entering Eq. (16) through the current vector \mathcal{J} in Eq. (15).

B. Diagonalization of the TI Hamiltonian

The operator transformations are derived by diagonalizing the TI Hamiltonian including the interaction with the mean-field magnetizations in Eq. (10),

$$\begin{aligned} H_{\text{TI}} = & \int d^2r \Psi^\dagger [i v_F (\sigma_y \partial_x - \sigma_x \partial_y) - E_0 \nabla^2 \\ & - \mu - \bar{J} (1 + \nu) \tilde{m} \sigma_z] \Psi, \\ = & \int d^2r \Psi^\dagger \mathcal{H}_{\text{TI}} \Psi. \end{aligned} \quad (17)$$

Fourier transforming the Hamiltonian and solving the eigenvalue problem $\mathcal{H}_{\text{TI}} \Psi_\pm = E \Psi_\pm$, we find the eigenenergies,

$$E_\pm(\mathbf{k}) = E_0 \mathbf{k}^2 \pm \sqrt{\bar{J}^2 \tilde{m}^2 (1 + \nu)^2 + v_F^2 \mathbf{k}^2} - \mu, \quad (18)$$

and eigenvectors,

$$\Psi_{\pm}(\mathbf{k}) = \begin{pmatrix} \psi_{+}(\mathbf{k}) \\ \psi_{-}(\mathbf{k}) \end{pmatrix} = \frac{1}{\sqrt{N_{\mathbf{k}}}} \begin{pmatrix} s_{\mathbf{k}}^{*} & r_{\mathbf{k}} \\ -r_{\mathbf{k}} & s_{\mathbf{k}} \end{pmatrix} \Psi(\mathbf{k}), \quad (19)$$

where we have defined the functions,

$$s_{\mathbf{k}} = v_F(k_y + ik_x), \quad (20a)$$

$$r_{\mathbf{k}} = \bar{J}\bar{m}(1 + \nu) + \sqrt{\bar{J}^2\bar{m}^2(1 + \nu)^2 + v_F^2|\mathbf{k}|^2}, \quad (20b)$$

$$N_{\mathbf{k}} = r_{\mathbf{k}}^2 + |s_{\mathbf{k}}|^2. \quad (20c)$$

The subscripts $+$ and $-$ denote Dirac fermions with positive and negative chiralities, respectively. Note that the eigenvectors of \mathcal{H}_{TI} are unaffected by the value of E_0 since this is a diagonal term. If $\mu > 0$, the conduction band will consist of ψ_{+} fermions. Considering only the fermions which are free to interact, i.e., projecting onto the conduction band, allows us to make the substitutions,

$$\psi_{\uparrow}(k) \rightarrow \frac{s_{\mathbf{k}}}{\sqrt{N_{\mathbf{k}}}} \psi_{+}(k) \quad \text{and} \quad \psi_{\downarrow}(k) \rightarrow \frac{r_{\mathbf{k}}}{\sqrt{N_{\mathbf{k}}}} \psi_{+}(k), \quad (21)$$

in the effective action δS_{TI} . This results in a momentum-dependent scattering form factor $\Lambda_{\mathbf{k}\mathbf{k}'}(\mathbf{q})$ characterizing the interaction between the fermions in the effective action, which we write as

$$\delta S_{\text{TI}} = \int \frac{d^3q}{(2\pi)^3} \int \frac{d^3k}{(2\pi)^3} \int \frac{d^3k'}{(2\pi)^3} \times V_{kk'}(q) \psi^{\dagger}(k + q) \psi^{\dagger}(k' - q) \psi(k') \psi(k). \quad (22)$$

with the interaction matrix defined as

$$V_{kk'}(q) = -\bar{J}^2 D(q) \Lambda_{\mathbf{k}\mathbf{k}'}(\mathbf{q}), \quad (23)$$

where $D(q)$ is the magnon propagator. We refer to the Appendix for further details. If the effective action leads to an attractive interaction, it can be shown that this results in a superconducting instability, e.g., by performing a mean-field treatment of the effective theory. We will, however, not perform such an analysis but rather focus on the type of effective interaction that arises due to the proximity to the magnetic layer. In the following two sections, we will analyze the effective action in the FM and AFM cases separately.

III. FERROMAGNETIC CASE

In the ferromagnetic case, the magnon propagator is given by

$$D^{\text{FM}}(q) = \frac{\frac{\kappa}{2}q^2 - \frac{J}{2a^2\bar{m}}\Theta(1 - \tau)}{\left(\frac{\Omega}{2m}\right)^2 + \left(\frac{\kappa}{2}q^2 - \frac{J}{2a^2\bar{m}}\Theta(1 - \tau)\right)^2}, \quad (24)$$

where we have used the definitions of $D_i^{\alpha\alpha}$ and $T^{\alpha\alpha}$ given in Ref. [20] and m is defined in the Appendix. Here, a is the lattice constant, introduced when using π/a as a cutoff in diverging momentum integrals [20], $\Theta(x)$ is the Heaviside step function, and $\tau = t^2/\bar{J}^2\bar{m}^2$ is a dimensionless parameter signifying the strength of the coupling between χ_1 and χ_2 relative to the coupling between χ_i and the magnetic moments, see Eq. (4). Assuming that the Dirac fermions move at speeds higher than the ferromagnetic magnons, which certainly holds for small momentum transfers $|\mathbf{q}|$, we set Ω to zero in the

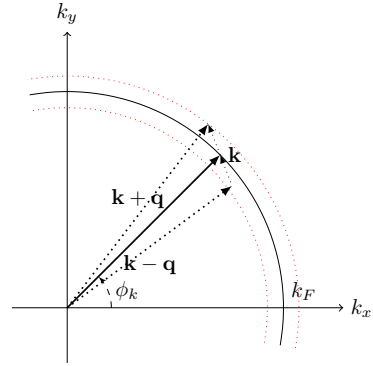


FIG. 2. The figure shows parts of the Fermi surface and the momenta of the interacting particles $\mathbf{k} = \mathbf{k}'$, $\mathbf{k} + \mathbf{q}$, and $\mathbf{k} - \mathbf{q}$. The figure illustrates that only small momentum transfers $|\mathbf{q}|$ compared to k_F are kinematically allowed since the momenta must lie within a thin shell (red dotted lines) around k_F (black line). This also implies that a process with momentum transfer $-\mathbf{q}$ is necessarily kinematically allowed if the process with \mathbf{q} is allowed.

magnon propagator. This yields

$$D^{\text{FM}}(0, |\mathbf{q}|) = \frac{1}{\frac{\kappa}{2}q^2 - \frac{J}{2a^2\bar{m}}\Theta(1 - \tau)}. \quad (25)$$

Note that if $\tau > 1$, $D^{\text{FM}}(0, |\mathbf{q}|)$ is positive for any \mathbf{q} . Because the coupling constants $D_i^{\alpha\beta}$ and $T^{\alpha\beta}$ are discontinuous at $\nu = \tau$ [20], values of $\tau \approx 1$ are excluded from the analysis in the ferromagnetic case.

Kargarian *et al.* [21] found attractive interactions between particles with parallel momenta, dubbed Amperian pairing [22], in the high-doping regime. We expand this analysis to also include the gap in the Dirac fermion dispersion, i.e., by not setting $\bar{m} = 0$ in the operator transformations, Eqs. (19) and (20). Since $\mathbf{k} \approx \mathbf{k}'$ for Amperian pairing, a process is only possible if both $\mathbf{k} + \mathbf{q}$ and $\mathbf{k} - \mathbf{q}$ lie within a thin shell of the Fermi level. This restricts the kinematically allowed values of \mathbf{q} to those with small $|\mathbf{q}|$ as illustrated in Fig. 2. Moreover, if a process with momentum transfer \mathbf{q} is possible, the process with momentum transfer $-\mathbf{q}$ is necessarily also possible. Thus, any term linear in \mathbf{q} in the form factor disappears when performing the \mathbf{q} integration in δS_{TI} . Expanding the form factor in $v_F|\mathbf{q}|/|\bar{J}\bar{m}|$ and neglecting linear terms in \mathbf{q} , we get to leading order,

$$\Lambda(\phi_k, \phi_{k'}) = \frac{v_F^2 k_F^2 (2\bar{J}\bar{m} + \sqrt{(2\bar{J}\bar{m})^2 + k_F^2})^2 \cos(\phi_k - \phi_{k'})}{2[v_F^2 k_F^2 + (2\bar{J}\bar{m})^2 + 2\bar{J}\bar{m}\sqrt{(2\bar{J}\bar{m})^2 + v_F^2 k_F^2}]^2}, \quad (26)$$

where we have set $|\mathbf{k}| = |\mathbf{k}'| = k_F$ and introduced the polar angle ϕ_k of each momentum in the xy plane. Setting $\bar{m} = 0$, we get $\Lambda = \cos(\phi_k - \phi_{k'})/2$, which is in agreement with Ref. [21]. This corresponds to the limit $v_F k_F \gg |\bar{J}\bar{m}|$ for which the interaction is strongest. The interaction strength decreases for decreasing k_F and disappears at $k_F = 0$, as illustrated in

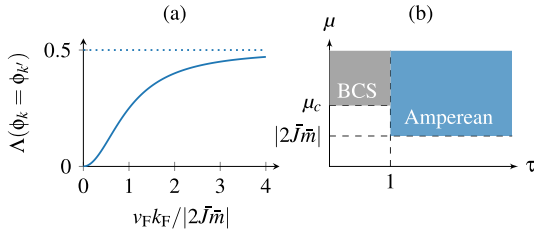


FIG. 3. (a) Variation of $\Lambda(\phi_k = \phi_{k'})$ in Eq. (26). The form factor increases when increasing k_F , corresponding to moving the Fermi level away from the gap in the dispersion. $\Lambda(\phi_k = \phi_{k'})$ approaches 1/2 in the limit $v_F k_F \gg |2\bar{J}\bar{m}|$. (b) A diagram showing the regions in parameter space where Amperean or BCS pairing is possible for TI surface states coupled to a ferromagnet. $\mu = |2\bar{J}\bar{m}|$ corresponds to $k_F = 0$.

Fig. 3(a). This is as expected since there must be a Fermi surface in the conduction band in order for interactions to be possible.

From the above results of the form factor and integrated magnon propagator, we see that the overall interaction matrix $V_{kk'}$ is negative for all kinematically allowed \mathbf{q} if $\tau > 1$ and \mathbf{k} and \mathbf{k}' are parallel. Hence, superconductivity with Amperean pairing is possible if $\tau > 1$. This is in agreement with the results in Ref. [21], which treats an analogous situation. Setting $\bar{\mathbf{m}}_1 = \bar{\mathbf{m}}_2$ in the magnon Lagrangian Eq. (7), we note that the ferromagnetic coupling between magnons,

$$\begin{aligned} \tilde{\lambda}_1 + \tilde{\lambda}_2 - \lambda_{\text{eff}} &= -2J^2(D_1^{00} - D_1^{zz} - T^{00} + T^{zz}) \\ &= \frac{J}{a^2\bar{m}}\Theta(1 - \tau) \end{aligned} \quad (27)$$

disappears when $\tau > 1$, which is, again, similar to the situation discussed in Ref. [21].

For $\tau < 1$, $D^{\text{FM}}(0, |\mathbf{q}|)$ is negative for $|\mathbf{q}| < \sqrt{J/a^2\bar{m}\kappa}$, resulting in repulsive interactions, and changes sign as $|\mathbf{q}|$ is increased. Since Amperean pairing is kinematically possible only for small $|\mathbf{q}|$, Amperean pairing is suppressed for increasing $J/\bar{m}\kappa$. However, note that for small $|\mathbf{q}|$ and $\phi_k - \phi_{k'} \approx \pi$, corresponding to normal BCS pairing, the interaction matrix is attractive. Therefore, the possibility of BCS pairing is investigated further.

In the BCS case $\mathbf{k}' = -\mathbf{k}$, the length of \mathbf{q} is less restricted since $|\mathbf{k}' - \mathbf{q}| = |\mathbf{k} + \mathbf{q}| \approx k_F$ is satisfied for the same momentum transfer \mathbf{q} . Requiring $|\mathbf{k}| = |\mathbf{k} + \mathbf{q}| = k_F$, we find

$$|\mathbf{q}| = \begin{cases} -2k_F \cos(\phi_k - \phi_q), & \text{if } \pi \geq |\phi_k - \phi_q| \geq \frac{\pi}{2}, \\ 0, & \text{otherwise.} \end{cases} \quad (28)$$

Inserted into the form factor, we find

$$\begin{aligned} \Lambda^{\text{BCS}}(\phi_k, \phi_q) &= \frac{v_F^2 k_F^2 e^{2i(\phi_k - \phi_q)} [2\bar{J}\bar{m} + \sqrt{v_F^2 k_F^2 + (2\bar{J}\bar{m})^2}]^2}{2[v_F^2 k_F^2 + (2\bar{J}\bar{m})^2 + 2\bar{J}\bar{m}\sqrt{v_F^2 k_F^2 + (2\bar{J}\bar{m})^2}]^2}. \end{aligned} \quad (29)$$

Since the signs of $D^{\text{FM}}(0, |\mathbf{q}|)$ with kinematically allowed $|\mathbf{q}|$, and $\Lambda^{\text{BCS}}(\phi_k, \phi_q)$ both vary with $\phi_k - \phi_q$, the overall sign of

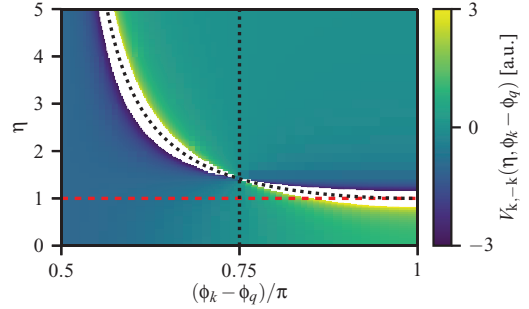


FIG. 4. Plot of $V_{\mathbf{k}, -\mathbf{k}}$ in Eq. (30) as a function of η and $\phi_k - \phi_q$, showing that the BCS pairing is attractive only for certain scattering angles ϕ_q . The black dotted lines show where the interaction changes sign. For $\eta > 1$, shown by the red dashed line, integrating over the scattering angle gives a dominantly attractive pairing.

the real part of the interaction matrix will depend on $\phi_k - \phi_q$ as

$$V_{\mathbf{k}, -\mathbf{k}} \propto -\frac{2a^2\bar{m}}{J} \frac{\cos 2(\phi_k - \phi_q)}{\eta^2 \cos^2(\phi_k - \phi_q) - 1}, \quad (30)$$

if $\pi \geq |\phi_k - \phi_q| \geq \frac{\pi}{2}$, where $\eta \equiv 2k_F/\sqrt{J/a^2\bar{m}\kappa}$. This quantity is plotted in Fig. 4 where it is clear that a BCS-type interaction is both attractive and repulsive depending on the scattering angle. Integrating $V_{\mathbf{k}, -\mathbf{k}}$ over ϕ_q gives a measure to whether most scattering angles are attractive or repulsive and in this way gives a conservative estimate of when BCS pairing is possible. The results show that the overall interaction is attractive whenever $\eta > 1$, i.e., when $2k_F > \sqrt{J/a^2\bar{m}\kappa}$, which corresponds to chemical potential $\mu > \mu_c$, where

$$\mu_c = \frac{E_0 J}{4a^2\bar{m}\kappa} + \sqrt{(2\bar{J}\bar{m})^2 + \frac{v_F^2 J}{4a^2\bar{m}\kappa}}. \quad (31)$$

Hence BCS pairing is possible for $\tau < 1$ and $\mu > \mu_c$. The attractive pairing is most dominant close to μ_c and decreases for increasing chemical potential. It is however important to note that the phase space of the pairing is reduced since not all scattering angles give attractive interactions, and the overall pairing is thus weakened compared to a normal BCS pairing.

To summarize, we find that, for $\tau > 1$, which corresponds to a disappearing $\bar{\mathbf{m}}^2$ term in the magnon Lagrangian, superconductivity with Amperean pairing occurs. For $\tau < 1$ and $\mu > \mu_c$ we instead have BCS pairing. The pairing strength decreases for decreasing k_F in the Amperean case, vanishing when the Fermi level lies inside the mass gap, whereas the BCS pairing is strongest close to μ_c . A simplified diagram showing for which parameter values Amperean and BCS pairings occur is presented in Fig. 3(b).

IV. ANTIFERROMAGNETIC CASE

In the antiferromagnetic case, the net mean-field magnetization is zero, and hence a gap is not opened in the dispersion. This also gives significantly simplified operator

transformations, resulting in a scattering form factor,

$$\Lambda_{\mathbf{k}\mathbf{k}'}(\mathbf{q}) = \frac{2\mathbf{k} \cdot \mathbf{k}' - i(\mathbf{k} \times \mathbf{q} - \mathbf{k}' \times \mathbf{q}) \cdot \hat{z} - \mathbf{k} \cdot \mathbf{q} + \mathbf{k}' \cdot \mathbf{q}}{4|\mathbf{k}||\mathbf{k}'|}, \quad (32)$$

where we have used $|\mathbf{k} + \mathbf{q}| \approx |\mathbf{k}|$. The magnon propagator in the antiferromagnetic case is given by

$$D^{\text{AFM}}(q) = \frac{\frac{\kappa}{2}\mathbf{q}^2 - \frac{J}{2a^2\bar{m}\sqrt{1+\tau}}}{\left(\frac{\Omega}{2\bar{m}}\right)^2 + \left(\frac{\kappa}{2}\mathbf{q}^2 - \frac{J}{2a^2\bar{m}\sqrt{1+\tau}}\right)\left(\frac{\kappa}{2}\mathbf{q}^2 - \frac{J}{2a^2\bar{m}(1+\tau)^{3/2}} + \lambda\right)}. \quad (33)$$

The frequency of antiferromagnetic magnons typically lies in the microwave range [39] and can therefore also be considered slow compared to the TI fermions, which have group velocities $v_F \sim 10^5$ m/s (see, e.g., Ref. [40]). Setting $\Omega = 0$ in the above propagator yields

$$D^{\text{AFM}}(0, |\mathbf{q}|) = \frac{1}{\frac{\kappa}{2}\mathbf{q}^2 - \frac{J}{2a^2\bar{m}(1+\tau)^{3/2}} + \lambda}. \quad (34)$$

Plots of D^{AFM} as a function of $|\mathbf{q}|$ and τ for $\lambda > J/2a^2\bar{m}$ and $\lambda < J/2a^2\bar{m}$ are shown in Fig. 5. From the figure we see that the propagator is positive for all $|\mathbf{q}|$ and τ when $\lambda > J/2a^2\bar{m}$. For $\lambda < J/2a^2\bar{m}$ the propagator is positive for all $|\mathbf{q}|$ if $\tau > \tau_c$, where

$$\tau_c = \left(\frac{|J/2a^2\bar{m}|}{\lambda}\right)^{2/3} - 1, \quad (35)$$

and for $|\mathbf{q}| > q_c$ if $\tau < \tau_c$, where

$$q_c = \sqrt{\left|\frac{J}{2a^2\bar{m}\kappa}\right| \frac{2}{(1+\tau)^{3/2}} - 2\frac{\lambda}{\kappa}}, \quad \tau < \tau_c. \quad (36)$$

In the Amperean case we are again restricted to small momentum transfers, which to lowest order gives the form factor $\Lambda^{\text{Amp}} = 1/2$. Hence magnon-induced Amperean pairing between Dirac fermions is possible either when $\lambda > J/2a^2\bar{m}$ or when $\lambda < J/2a^2\bar{m}$ and $\tau > \tau_c$.

For BCS pairing, however, we get the form factor $\Lambda^{\text{BCS}} = e^{2i(\phi_k - \phi_q)}/2$, which corresponds to setting $\bar{m} = 0$ in Eq. (29). The real part of the overall interaction can then be written

$$V_{\mathbf{k}, -\mathbf{k}} \propto -\left(\frac{J}{2a^2\bar{m}(1+\tau)^{3/2}} - \lambda\right)^{-1} \frac{\cos 2(\phi_k - \phi_q)}{\eta^2 \cos^2(\phi_k - \phi_q) - 1} \quad (37)$$

for $\pi/2 < |\phi_k - \phi_q| < \pi$. Here we have used Eq. (28) and defined $\eta = 2k_F/\sqrt{J/a^2\bar{m}(1+\tau)^{3/2}\kappa - 2\lambda/\kappa}$. Again, the sign of the interaction depends on the parameter η and the scattering angle $\phi_k - \phi_q$ in exactly the same way as in the FM case. Therefore the interaction is dominantly attractive when $\eta > 1$, which corresponds to $\mu > \mu_c(\tau)$, where $\mu_c(\tau) = E_0 q_c(\tau)^2/4 + v_F q_c(\tau)/2$. Hence, BCS pairing can be realized when $\lambda < J/2a^2\bar{m}$, $\tau < \tau_c$, and $\mu > \mu_c$. This is a conservative limit as there are attractive regions of phase space also when $\mu < \mu_c$. The type of pairing realized for different values of τ and μ is shown in Fig. 6.

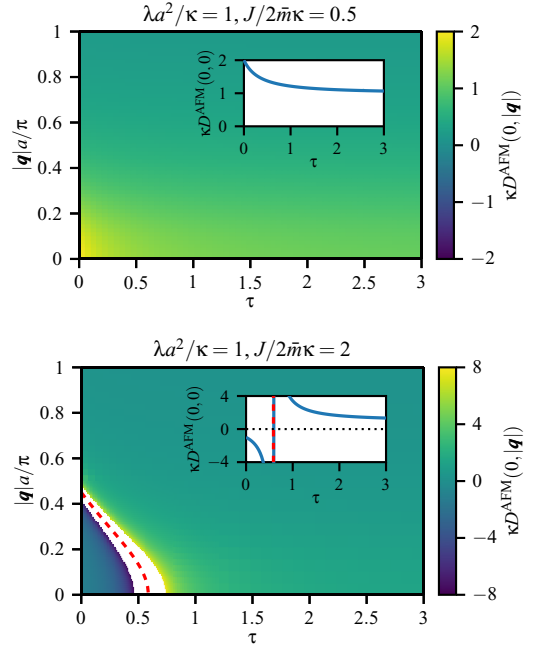


FIG. 5. Plot of D^{AFM} as a function of $|\mathbf{q}|$ and τ for $\lambda > J/2a^2\bar{m}$ (top) and $\lambda < J/2a^2\bar{m}$ (bottom). In the former case $D^{\text{AFM}} \geq 0$ for all \mathbf{q} and τ . In the latter case however, the integrated propagator is negative in a region around $|\mathbf{q}| = 0$ and $\tau = 0$. This region is bounded by the curve $q_c(\tau)$ (dashed red) given in Eq. (36) and increases for increasing $J/2a^2\bar{m}\lambda$. The white region indicates values outside the color bar range. The propagator for $|\mathbf{q}| = 0$ is plotted in the insets.

τ_c corresponds to the value where $\tilde{\lambda}_1 + \tilde{\lambda}_2 - \lambda_{\text{eff}}$, see Eq. (9), changes sign from positive to negative, i.e., the point where the ferromagnetic coupling between spins on each of the two sublattices becomes weaker than the antiferromagnetic coupling between spins on different sublattices. Thus, for both the FM and the AFM cases, BCS pairing seems to be possible

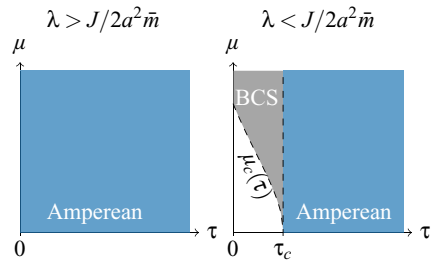


FIG. 6. Diagram showing the regions in parameter space where BCS or Amperean pairing is possible for TI surface states coupled to an antiferromagnet. BCS pairing is possible only when $\lambda < J/2a^2\bar{m}$ when $\tau < \tau_c$ and $\mu > \mu_c(\tau)$.

when the quadratic $\bar{\mathbf{m}}^2$ term dominates over the interlattice coupling.

V. SUMMARY

We have studied the possible electron pairing due to magnetic fluctuations at the interface of a TI and a FM or AFM insulator. In the FM case, we have expanded the results of Ref. [21] to be valid also for chemical potentials close to the gap in the TI fermion dispersion. We find that for $\tau > 1$, which corresponds to a vanishing quadratic term $\propto \bar{\mathbf{m}}^2$ in the magnon Lagrangian, Amperean pairing occurs. The pairing strength decreases for decreasing k_F and vanishes when the chemical potential lies inside the mass gap. For $\tau < 1$, Amperean pairing is suppressed for increasing $J/\bar{m}\kappa$, and instead BCS pairing occurs above a critical chemical potential. In the AFM case BCS pairing is realized only when the ferromagnetic coupling between magnons on the same sublattice exceeds the antiferromagnetic coupling between magnons on different sublattices. For other parameter values, Amperean pairing is realized with an interaction strength independent of the chemical potential. In both the FM and the AFM cases, the BCS pairing has a limited phase space compared to the regular BCS

interaction and could therefore be a weak effect depending on the chemical potential of the system.

In conclusion, magnetic fluctuations at the interface between a TI and a magnetic insulator can mediate attractive interactions between Dirac fermions, giving pairing of both BCS and Amperean types, depending on the degree of anisotropy of the magnetic fluctuations in the system. Investigating other magnetic configurations, such as ferrimagnetic insulators, would be an interesting further development. We also leave it for future work to consider bilayers involving magnetic metals where a similar pairing mechanism is likely to remain in effect. For the metallic FM case, non-*s*-wave pairing has already been reported in recent experiments on superconducting Ni-Bi bilayers [41–43].

ACKNOWLEDGMENTS

H.G.H. and A.S. were supported by the Research Council of Norway through Grant No. 250985, “Fundamentals of Low-dissipative Topological Matter” and the Center of Excellence Grant No. 262633, Center for Quantum Spintronics. S.R. was supported by DFG through Grant No. SPP 1666, “Topological Insulators: Materials-Fundamental Properties-Devices.”

APPENDIX: CALCULATION OF EFFECTIVE TI ACTION

In the cases $\bar{m}_2/\bar{m}_1 = \nu = \pm 1$, we have the relations $D_1^{00} = D_2^{00}$, $D_1^{zz} = D_2^{zz}$, and $\mathcal{D}_1^{0z} = \nu \mathcal{D}_2^{0z}$, whereas T^{zz} and \mathcal{T}^{0z} are zero in the antiferromagnetic case. To handle this, we write $T^{zz} = (1 + \nu)T^{zz}/2$ and $\mathcal{T}^{0z} = (1 + \nu)\mathcal{T}^{0z}/2$. Inserting this into the magnon action and rewriting in vector form, we defined the matrix \mathcal{K} in Eq. (13) using the functions,

$$D = D_1^{00} - D_1^{zz}, \quad (\text{A1a})$$

$$T = T^{00} - \frac{1 + \nu}{2} T^{zz}, \quad (\text{A1b})$$

$$\frac{1}{2m^*} = \frac{1}{2\bar{m}} - 2J^2 \mathcal{D}_1^{0z} \quad (\text{A1c})$$

for notational simplicity.

The inverse of \mathcal{K} can be written in the form

$$\mathcal{K}^{-1} = \frac{1}{\det \mathcal{K}} \begin{pmatrix} A_0 + A_y i \sigma_y & B_0 + B_y i \sigma_y \\ B_0 + B_y i \sigma_y & A_0 + \nu A_y i \sigma_y \end{pmatrix}, \quad (\text{A2})$$

where

$$\begin{aligned} \det \mathcal{K} = & \left(\frac{\kappa}{2} \mathbf{q}^2 + J^2 D \right)^2 \left\{ \left[\left(\frac{\kappa}{2} \mathbf{q}^2 + J^2 D \right) - \nu \lambda \right]^2 + 2 \left[\left(\frac{\Omega}{2m^*} \right)^2 + (1 + \nu)^2 (\mathcal{T}^{0z} \Omega)^2 \right] - 2\lambda T - 2T^2 \right\} \\ & + 2 \left(\frac{\kappa}{2} \mathbf{q}^2 + J^2 D \right) \left[\nu \lambda T (\lambda + T) + 4T(1 + \nu) \frac{\mathcal{T}^{0z} \Omega^2}{2m^*} - \lambda \nu \left(\frac{\Omega}{2m^*} - (1 + \nu) \mathcal{T}^{0z} \Omega \right)^2 \right] \\ & + T^2 \left[(T + \lambda)^2 + 2\nu \left(\frac{\Omega}{2m^*} \right)^2 + 2(1 + \nu)^2 (\mathcal{T}^{0z} \Omega)^2 \right] + (1 + \nu)^2 \frac{\lambda^2}{2^2} \left(\frac{\Omega}{2m^*} - 2\mathcal{T}^{0z} \Omega \right)^2 \\ & + 2\lambda \nu T \left(\frac{\Omega}{2m^*} - (1 + \nu) \mathcal{T}^{0z} \Omega \right)^2 + \left[\left(\frac{\Omega}{2m^*} \right)^2 - (1 + \nu)^2 (\mathcal{T}^{0z} \Omega)^2 \right]^2, \quad (\text{A3}) \end{aligned}$$

and

$$A_0 = \left(\frac{\kappa}{2}\mathbf{q}^2 + J^2D\right)^3 - \frac{3\nu\lambda}{2}\left(\frac{\kappa}{2}\mathbf{q}^2 + J^2D\right)^2 + \left(\frac{\kappa}{2}\mathbf{q}^2 + J^2D\right)\left[\frac{\lambda^2}{2} - \lambda T - T^2 + \left(\frac{\Omega}{2m^*}\right)^2 + (1+\nu)^2(\mathcal{T}^{0z}\Omega)^2\right] \\ + \frac{\nu}{2}\lambda T(\lambda + T) + 2(1+\nu)T\frac{\mathcal{T}^{0z}\Omega^2}{2m^*} - \frac{\nu\lambda}{2}\left(\frac{\Omega}{2m^*} - (1+\nu)\mathcal{T}^{0z}\Omega\right)^2, \quad (\text{A4a})$$

$$A_y = \left(\frac{\kappa}{2}\mathbf{q}^2 + J^2D\right)\frac{\Omega}{2m^*} + \left(\frac{\kappa}{2}\mathbf{q}^2 + J^2D\right)\left[(1+\nu)(2T+\lambda)\mathcal{T}^{0z}\Omega - \nu\lambda\frac{\Omega}{2m^*}\right] \\ + \frac{\Omega}{2m^*}\left[\left(\frac{\Omega}{2m^*}\right)^2 - (1+\nu)^2(\mathcal{T}^{0z}\Omega)^2 + \nu T^2 + (1+\nu)\frac{\lambda^2}{4} + \nu\lambda T\right] - (1+\nu)\frac{\lambda}{2}(\lambda + 2T)\mathcal{T}^{0z}\Omega, \quad (\text{A4b})$$

$$B_0 = -\frac{1}{2}\left(\frac{\kappa}{2}\mathbf{q}^2 + J^2D\right)^2(\lambda + 2T) + \left(\frac{\kappa}{2}\mathbf{q}^2 + J^2D\right)\left[\frac{\lambda}{2}(\lambda + 2T) + (1+\nu)^2\frac{\mathcal{T}^{0z}\Omega^2}{2m^*}\right] + \frac{1}{2}\lambda^2 T \\ + \nu T\left[\left(\frac{\Omega}{2m^*}\right)^2 + (1+\nu)^2(\mathcal{T}^{0z}\Omega)^2\right] + T^2\left(T + \frac{3}{2}\lambda\right) + \nu\frac{\lambda}{2}\left[\frac{\Omega}{2m^*} - (1+\nu)\mathcal{T}^{0z}\Omega\right]^2, \quad (\text{A4c})$$

$$B_y = -\frac{\Omega}{2m^*}(1+\nu)\left(\frac{\lambda}{2} + T\right)\left(\frac{\kappa}{2}\mathbf{q}^2 + J^2D - \frac{\lambda}{2}\right) - (1+\nu)\mathcal{T}^{0z}\Omega \\ \times \left[(1+\nu)^2(\mathcal{T}^{0z}\Omega)^2 + \left(\frac{\kappa}{2}\mathbf{q}^2 + J^2D - \frac{\lambda}{2}\right)^2 + \left(\frac{\lambda}{2} + T\right)^2 - \left(\frac{\Omega}{2m^*}\right)^2\right]. \quad (\text{A4d})$$

The above equations have been simplified using $v^2 = 1$ and $1/\nu = \nu$ and are therefore valid only when $\bar{m}_2 = \pm\bar{m}_1$.

Performing the matrix multiplication in Eq. (16) using the above form of \mathcal{K}^{-1} and the definition of $\mathcal{J}(q)$ in Eq. (15), we get

$$\delta S_{\Pi} = -\bar{J}^2 \int \frac{d^3q}{(2\pi)^3} \int \frac{d^3k}{(2\pi)^3} \int \frac{d^3k'}{(2\pi)^3} \left\{ \frac{A_0 + B_0}{\det \mathcal{K}} [\psi_{\uparrow}^{\dagger}(k)\psi_{\downarrow}^{\dagger}(k')\psi_{\uparrow}(k'+q)\psi_{\downarrow}(k-q) + \psi_{\downarrow}^{\dagger}(k)\psi_{\uparrow}^{\dagger}(k')\psi_{\downarrow}(k'+q)\psi_{\uparrow}(k-q)] \right. \\ \left. + i\frac{A_y(1+\nu) + 2B_y}{2\det \mathcal{K}} [\psi_{\uparrow}^{\dagger}(k)\psi_{\downarrow}^{\dagger}(k')\psi_{\uparrow}(k'+q)\psi_{\downarrow}(k-q) - \psi_{\downarrow}^{\dagger}(k)\psi_{\uparrow}^{\dagger}(k')\psi_{\downarrow}(k'+q)\psi_{\uparrow}(k-q)] \right\}. \quad (\text{A5})$$

In the antiferromagnetic case, $A_y(1+\nu) + 2B_y$ is exactly equal to zero. In the ferromagnetic case however, this term has an overall factor of Ω , making it less divergent in the low-frequency limit. We will therefore neglect this term [21].

Projecting onto the conduction band using Eq. (21), we get the effective action,

$$\delta S_{\Pi} = -\bar{J}^2 \int \frac{d^3q}{(2\pi)^3} \int \frac{d^3k}{(2\pi)^3} \int \frac{d^3k'}{(2\pi)^3} D(q)\Lambda_{\mathbf{k}\mathbf{k}'}(\mathbf{q})\psi^{\dagger}(k+q)\psi^{\dagger}(k'-q)\psi(k')\psi(k), \quad (\text{A6})$$

where we have dropped the subscript $+$ for notational simplicity and defined the magnon propagator,

$$D(q) = \frac{A_0(q) + B_0(q)}{\det \mathcal{K}(q)}, \quad (\text{A7})$$

and the scattering form factor,

$$\Lambda_{\mathbf{k}\mathbf{k}'}(\mathbf{q}) = \frac{s_{\mathbf{k}+\mathbf{q}}^* r_{\mathbf{k}'-\mathbf{q}} s_{\mathbf{k}'} r_{\mathbf{k}} + r_{\mathbf{k}+\mathbf{q}} s_{\mathbf{k}'-\mathbf{q}}^* r_{\mathbf{k}'} s_{\mathbf{k}}}{\sqrt{N_{\mathbf{k}} N_{\mathbf{k}'} N_{\mathbf{k}-\mathbf{q}} N_{\mathbf{k}'+\mathbf{q}}}}. \quad (\text{A8})$$

Defining the parameter m such that

$$\frac{1}{m} = \frac{1}{2\bar{m}} - 2J^2\mathcal{D}_1^{0z} - J^2(1+\nu)\mathcal{T}^{0z}, \quad (\text{A9})$$

and using the results in Eqs. (A4a) and (A4c), we get the ferromagnetic propagator ($\nu = 1$),

$$D^{\text{FM}}(q) = \frac{\frac{\kappa}{2}\mathbf{q}^2 + J^2(D+T)}{\left(\frac{\Omega}{2m}\right)^2 + \left(\frac{\kappa}{2}\mathbf{q}^2 + J^2(D+T)\right)^2}, \quad (\text{A10})$$

and the antiferromagnetic propagator ($\nu = -1$),

$$D^{\text{AFM}}(q) = \frac{\frac{\kappa}{2}\mathbf{q}^2 + J^2(D-T)}{\left(\frac{\Omega}{2m}\right)^2 + \left(\frac{\kappa}{2}\mathbf{q}^2 + J^2(D-T)\right)\left(\frac{\kappa}{2}\mathbf{q}^2 + J^2(D+T) + \lambda\right)}. \quad (\text{A11})$$

- [1] M. Z. Hasan and C. L. Kane, *Rev. Mod. Phys.* **82**, 3045 (2010).
- [2] X. L. Qi and S. C. Zhang, *Rev. Mod. Phys.* **83**, 1057 (2011).
- [3] T. O. Wehling, A. M. Black-Schaffer, and A. V. Balatsky, *Adv. Phys.* **63**, 1 (2014).
- [4] P. Wei, F. Katmis, B. A. Assaf, H. Steinberg, P. Jarillo-Herrero, D. Heiman, and J. S. Moodera, *Phys. Rev. Lett.* **110**, 186807 (2013).
- [5] Q. I. Yang, M. Dolev, L. Zhang, J. Zhao, A. D. Fried, E. Schemm, M. Liu, A. Palevski, A. F. Marshall, S. H. Risbud, and A. Kapitulnik, *Phys. Rev. B* **88**, 081407(R) (2013).
- [6] W. Liu, L. He, Y. Xu, K. Murata, M. C. Onbasli, M. Lang, N. J. Maltby, S. Li, X. Wang, C. A. Ross, P. Bencok, G. Van Der Laan, R. Zhang, and K. L. Wang, *Nano Lett.* **15**, 764 (2015).
- [7] F. Katmis, V. Lauter, F. S. Nogueira, B. A. Assaf, M. E. Jamer, P. Wei, B. Satpati, J. W. Freeland, I. Eremin, D. Heiman, P. Jarillo-Herrero, and J. S. Moodera, *Nature (London)* **533**, 513 (2016).
- [8] C. Tang, C.-Z. Chang, G. Zhao, Y. Liu, Z. Jiang, C.-X. Liu, M. R. McCartney, D. J. Smith, T. Chen, J. S. Moodera, and J. Shi, *Sci. Adv.* **3**, e1700307 (2017).
- [9] I. Garate and M. Franz, *Phys. Rev. Lett.* **104**, 146802 (2010).
- [10] K. Nomura and N. Nagaosa, *Phys. Rev. B* **82**, 161401(R) (2010).
- [11] Y. Tserkovnyak and D. Loss, *Phys. Rev. Lett.* **108**, 187201 (2012).
- [12] Y. G. Semenov, X. Duan, and K. W. Kim, *Phys. Rev. B* **86**, 161406(R) (2012).
- [13] Y. Ferreiros and A. Cortijo, *Phys. Rev. B* **89**, 024413 (2014).
- [14] J. Linder, *Phys. Rev. B* **90**, 041412(R) (2014).
- [15] Y. G. Semenov, X. Duan, and K. W. Kim, *Phys. Rev. B* **89**, 201405(R) (2014).
- [16] Y. Ferreiros, F. J. Buijnsters, and M. I. Katsnelson, *Phys. Rev. B* **92**, 085416 (2015).
- [17] X. Duan, X. L. Li, Y. G. Semenov, and K. W. Kim, *Phys. Rev. B* **92**, 115429 (2015).
- [18] S. Rex, F. S. Nogueira, and A. Sudbø, *Phys. Rev. B* **93**, 014404 (2016).
- [19] S. Rex, F. S. Nogueira, and A. Sudbø, *Phys. Rev. B* **94**, 020404(R) (2016).
- [20] S. Rex, F. S. Nogueira, and A. Sudbø, *Phys. Rev. B* **95**, 155430 (2017).
- [21] M. Kargarian, D. K. Efimkin, and V. Galitski, *Phys. Rev. Lett.* **117**, 076806 (2016).
- [22] S.-S. Lee, P. A. Lee, and T. Senthil, *Phys. Rev. Lett.* **98**, 067006 (2007).
- [23] P. A. Lee, *Phys. Rev. X* **4**, 031017 (2014).
- [24] Q.-L. He, X. Kou, A. J. Grutter, G. Yin, L. Pan, X. Che, Y. Liu, T. Nie, B. Zhang, S. M. Disseler, B. J. Kirby, W. Ratcliff II, Q. Shao, K. Murata, X. Zhu, G. Yu, Y. Fan, M. Montazeri, X. Han, J. A. Borchers, and K. L. Wang, *Nat. Mater.* **16**, 94 (2017).
- [25] M. Li, C.-Z. Chang, B. J. Kirby, M. E. Jamer, W. Cui, L. Wu, P. Wei, Y. Zhu, D. Heiman, J. Li, and J. S. Moodera, *Phys. Rev. Lett.* **115**, 087201 (2015).
- [26] H. Wang, C. Du, P. C. Hammel, and F. Yang, *Phys. Rev. Lett.* **113**, 097202 (2014).
- [27] C. Hahn, G. de Loubens, V. V. Naletov, J. Ben Youssef, O. Klein, and M. Viret, *Europhys. Lett.* **108**, 57005 (2014).
- [28] T. Moriyama, S. Takei, M. Nagata, Y. Yoshimura, N. Matsuzaki, T. Terashima, Y. Tserkovnyak, and T. Ono, *Appl. Phys. Lett.* **106**, 162406 (2015).
- [29] H. Wang, C. Du, P. C. Hammel, and F. Yang, *Phys. Rev. B* **91**, 220410(R) (2015).
- [30] W. Lin, K. Chen, S. Zhang, and C. L. Chien, *Phys. Rev. Lett.* **116**, 186601 (2016).
- [31] A. A. Taskin and Y. Ando, *Phys. Rev. B* **84**, 035301 (2011).
- [32] A. R. Wright and R. H. McKenzie, *Phys. Rev. B* **87**, 085411 (2013).
- [33] Z. Li and J. P. Carbotte, *Phys. Rev. B* **88**, 045414 (2013).
- [34] J. P. F. LeBlanc and J. P. Carbotte, *Phys. Rev. B* **89**, 035419 (2014).
- [35] D. J. Griffiths, *Introduction to Electrodynamics*, 4th ed. (Pearson, Upper Saddle River, NJ, 2013).
- [36] H. Bruus and K. Flensberg, *Many-Body Quantum Theory in Condensed Matter Physics* (Oxford University Press, Oxford, 2004).
- [37] X. Marti, I. Fina, C. Frontera, J. Liu, P. Wadley, Q. He, R. J. Paull, J. D. Clarkson, J. Kudrnovský, I. Turek, J. Kunes, D. Yi, J. H. Chu, C. T. Nelson, L. You, E. Arenholz, S. Salahuddin, J. Fontcuberta, T. Jungwirth, and R. Ramesh, *Nat. Mater.* **13**, 367 (2014).
- [38] X. Marti, I. Fina, and T. Jungwirth, *IEEE Trans. Magn.* **51**, 2900104 (2015).
- [39] C. Kittel, *Quantum Theory of Solids* (Wiley, New York, 1963).
- [40] H. Zhang, C.-X. Liu, X.-L. Qi, X. Dai, Z. Fang, and S.-C. Zhang, *Nat. Phys.* **5**, 438 (2009).
- [41] X.-X. Gong, H.-X. Zhou, P.-C. Xu, D. Yue, K. Zhu, X.-F. Jin, H. Tian, G.-J. Zhao, and T.-Y. Chen, *Chin. Phys. Lett.* **32**, 067402 (2015).
- [42] X.-X. Gong, M. Kargarian, A. Stern, D. Yue, H. Zhou, X. Jin, V. M. Galitski, V. M. Yakovenko, and J. Xia, *Sci. Adv.* **3**, e1602579 (2017).
- [43] J. Wang, X. Gong, G. Yang, Z. Lyu, Y. Pang, G. Liu, Z. Ji, J. Fan, X. Jing, C. Yang, F. Qu, X. Jin, and L. Lu, *Phys. Rev. B* **96**, 054519 (2017).
- [44] We have used the sign convention,
- $$f(\mathbf{k}, \omega) = \int dT \int d^2r e^{-i\mathbf{k}\cdot\mathbf{r} - i\omega T} f(T, \mathbf{r}), \quad (\text{A12})$$
- when Fourier transforming.

Reference

H. G. Hugdal and A. Sudbø,

Possible odd-frequency Amperean magnon-mediated superconductivity in topological insulator – ferromagnetic insulator bilayer.

Physical Review B, **102**, 125429 (2020).


Contributions

HGH initiated the project, performed the analytical and numerical calculations with input from AS, and wrote the initial manuscript. Both authors contributed to the discussion of the physics and revision of the final manuscript.

Possible odd-frequency Amperean magnon-mediated superconductivity in topological insulator–ferromagnetic insulator bilayer

Henning G. Hugdal  and Asle Sudbø 

Center for Quantum Spintronics, Department of Physics, NTNU, Norwegian University of Science and Technology, NO-7491 Trondheim, Norway

 (Received 1 July 2020; revised 9 September 2020; accepted 9 September 2020; published 23 September 2020)

We study the magnon-mediated pairing between fermions on the surface of a topological insulator (TI) coupled to a ferromagnetic insulator with a tilted mean field magnetization. Tilting the magnetization toward the interfacial plane reduces the magnetic band gap and leads to a shift in the effective TI dispersions. We derive and solve the self-consistency equation for the superconducting gap in two different situations, where we neglect or include the frequency dependence of the magnon propagator. Neglecting the frequency dependence results in p -wave Amperean solutions. We also find that tilting the magnetization into the interface plane favors Cooper pairs with center-of-mass momenta parallel to the magnetization vector, increasing T_c compared to the out-of-plane case. Including the frequency dependence of the magnon propagator, and solving for a low number of Matsubara frequencies, we find that the eigenvectors of the Amperean solutions at the critical temperature are dominantly odd in frequency and even in momentum, thus opening the possibility for odd-frequency Amperean pairing.

DOI: [10.1103/PhysRevB.102.125429](https://doi.org/10.1103/PhysRevB.102.125429)

I. INTRODUCTION

Spin fluctuations are one of the proposed mechanisms for superconductivity in unconventional superconductors [1,2], for which the phase diagrams often have both antiferromagnetic and superconducting regions [3–9], or where ferromagnetism and superconductivity appear simultaneously [10–15]. Recently, there have been studies focusing on the possibility of magnon-mediated superconductivity in heterostructures consisting of magnetic insulators and a normal metal or topological insulator (TI) [16–22], where the electrons couple to magnetic fluctuations at the interface. In TIs the superconductivity can be between fermions with parallel momenta, so-called Amperean pairing [23]. It has also been shown that a coupling to magnons can lead to indirect exciton condensation [24].

Coupling the magnetic insulator to the TI surface states [25,26] has a few interesting consequences compared to coupling to the electrons in a normal metal. First of all, the metallic states are restricted to the surface, locating them close to the spin fluctuations, ensuring a strong coupling. Moreover, due to the spin-momentum locking in the TI, the response to the magnetization is very different compared to a normal metal. While an exchange field leads to a band splitting and thus pair-breaking effects for any spin-0 Cooper pairs in a normal metal, the exchange field in a TI leads only to a gap and/or shift in the surface state dispersions, but no band splitting. Hence, the Fermi level only crosses one band, and the Cooper pairs must necessarily be pseudospin triplets.

In this work we study a TI exchange coupled to a ferromagnetic insulator (FMI) with a mean field magnetization that can be tilted toward the plane of the interface between the TI and

FMI. We derive the gap equation for the static gap, and study the possibility of both Bardeen–Cooper–Schrieffer (BCS) [27] type superconductivity and Amperean superconductivity, focusing on the changes due to the in-plane component of the magnetization. We also derive the gap equation including the frequency dependence of the magnon propagator, and solve these equations including only a few Matsubara frequencies. Our results show that the eigenvectors are mostly odd in frequency [28–36], thus showing the possibility for magnon-mediated *odd-frequency Amperean superconductivity*.

The remainder of the paper is organized as follows: The model is presented in Sec. II, as is the derivation of the effective magnon-mediated action. The general gap equations are derived in Sec. III, and specifically studied for the static and frequency-dependent cases in Secs. IV and V. Finally, the main results are summarized in Sec. VI. Further details regarding the derivations and material parameters are presented in the Appendix.

II. MODEL

A sketch of the system is shown in Fig. 1. We model the FMI using the Lagrangian

$$\mathcal{L}_m = -\mathbf{b}(\mathbf{m}) \cdot \partial_t \mathbf{m} - \frac{\kappa}{2} (\nabla \mathbf{m})^2 + \lambda (\mathbf{m} \cdot \hat{\mathbf{a}})^2, \quad (1)$$

where $\hat{\mathbf{a}}$ is the direction of the mean field magnetization, parametrized by $\hat{\mathbf{a}} = \sin \theta \hat{x} + \cos \theta \hat{z}$, and $\lambda > 0$. A general mean field magnetization including a y component can be shown to be equivalent to considering only an xz -plane magnetization by rotating the spin-quantization axis and the coordinate system. $\mathbf{b}(\mathbf{m})$ is the Berry connection, satisfying

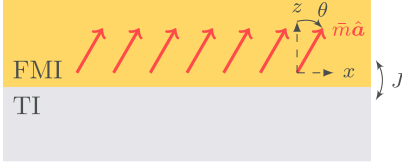


FIG. 1. Sketch of the system consisting of TI coupled to a FMI with a mean field magnetization tilted in the xz plane by angle θ with respect to the z axis. J is the strength of the exchange coupling.

$\nabla_{\mathbf{m}} \times \mathbf{b}(\mathbf{m}) = \mathbf{m}/\bar{m}^2$ [37], where $\nabla_{\mathbf{m}} = (\partial_{m_x}, \partial_{m_y}, \partial_{m_z})$. Here \bar{m} is the length of the mean field magnetization along $\hat{\mathbf{a}}$. We have set $\hbar = 1$ throughout the paper. The Lagrangian of the TI surface states reads as

$$\mathcal{L}_{\text{TI}} = \Psi^\dagger [i\partial_t - iv_F(\sigma_y \partial_x - \sigma_x \partial_y) + \mu] \Psi, \quad (2)$$

where $\Psi = (\psi_\uparrow, \psi_\downarrow)^T$ is a vector of spin-up and spin-down electrons in the TI, v_F is the Fermi velocity, and μ is the chemical potential. The TI and FMI are coupled by the exchange coupling term

$$\mathcal{L}_c = J \Psi^\dagger \mathbf{m} \cdot \boldsymbol{\sigma} \Psi, \quad (3)$$

where J is the coupling strength.

We fix the length of the magnetization vector to \bar{m} , and thus write

$$\mathbf{m} = \sqrt{1 - n^2} \bar{m} \hat{\mathbf{a}} + \bar{m} \mathbf{n}, \quad (4)$$

where \mathbf{n} is the fluctuation vector perpendicular to $\hat{\mathbf{a}}$,

$$\mathbf{n} = n(\cos \theta \hat{x} - \sin \theta \hat{z}) + n_y \hat{y}. \quad (5)$$

We assume that $n, n_y \ll 1$.

We next calculate the Berry connection by generalizing the leading-order expression $\mathbf{b} = (\hat{z} \times \mathbf{n})/2$ [16] to a mean field direction along $\hat{\mathbf{a}}$:

$$\mathbf{b} = \frac{\hat{\mathbf{a}} \times \mathbf{n}}{2} = -\frac{n_y \cos \theta \hat{x} - n \hat{y} - n_y \sin \theta \hat{z}}{2}. \quad (6)$$

Hence, to lowest order, we have

$$\nabla_{\mathbf{m}} \times \mathbf{b} = \frac{\hat{\mathbf{a}}}{\bar{m}}. \quad (7)$$

Switching to imaginary time $\tau = it$ and Fourier transforming,¹ we get the three contributions to the action:

$$\begin{aligned} S_m &= \frac{1}{\beta V} \sum_q \left\{ \left[\frac{\kappa \bar{m}^2}{2} \mathbf{q}^2 + \lambda \bar{m}^2 \right] N(-q) \cdot \mathbf{n}(q) \right. \\ &\quad \left. - \frac{\Omega_n \bar{m}}{2} [n_y(-q)n(q) - n(-q)n_y(q)] \right\}, \end{aligned} \quad (8)$$

¹We use the convention

$$f(\tau, \mathbf{r}) = \frac{1}{\beta V} \sum_{\omega_n, \mathbf{k}} f(\omega_n, \mathbf{k}) e^{i\mathbf{k} \cdot \mathbf{r} - i\omega_n \tau}$$

for the Fourier transform.

$$S_{\text{TI}} = \frac{1}{\beta V} \sum_k \Psi^\dagger(k) [-i\omega_n - v_F(k_x \sigma_y - k_y \sigma_x) - \mu] \Psi(k), \quad (9)$$

$$\begin{aligned} S_c &= S_c^{\bar{m}} + S_c^n \\ &= -\frac{J \bar{m}}{\beta V} \sum_k \Psi^\dagger(k) \hat{\mathbf{a}} \cdot \boldsymbol{\sigma} \Psi(k) \\ &\quad - \frac{J \bar{m}}{(\beta V)^2} \sum_{q, k} \Psi^\dagger(k+q) \mathbf{n}(q) \cdot \boldsymbol{\sigma} \Psi(k). \end{aligned} \quad (10)$$

Here, we have used the notation $q = (\Omega_n, \mathbf{q})$ and $k = (\omega_n, \mathbf{k})$ for bosonic and fermionic Matsubara frequencies and momenta, respectively. We have also kept only leading-order terms in the fluctuations in the coupling term. Using a more general model as a starting point, such as the one in Ref. [38], λ could in principle be renormalized to take negative values, meaning that an antiferromagnetic alignment between the magnetic fluctuations \mathbf{n} could be favored.

A. Integrating out the magnons

To obtain the effective, magnon-mediated interaction between Dirac electrons, we need to integrate out the magnons. This can be done by rewriting the full magnon action $S_n = S_m + S_c^n$ by introducing the vectors $N(q) = (n(q), n_y(q))^T$ and

$$j(q) = \frac{J \bar{m}}{\beta V} \sum_k \begin{pmatrix} \Psi^\dagger(k+q) (\cos \theta \sigma_x - \sin \theta \sigma_z) \Psi(k) \\ \Psi^\dagger(k+q) \sigma_y \Psi(k) \end{pmatrix}, \quad (11)$$

resulting in

$$\begin{aligned} S_n &= \frac{1}{\beta V} \sum_q \left\{ N(-q)^T \left[\frac{\kappa \bar{m}^2}{2} \mathbf{q}^2 + \bar{m}^2 \lambda + \frac{i \Omega_n \bar{m} \sigma_y}{2} \right] N(q) \right. \\ &\quad \left. - \frac{N^T(-q) j(-q) + j^T(q) N(q)}{2} \right\}. \end{aligned} \quad (12)$$

Performing the functional integral, we get an additional term in the TI action:

$$\delta S_{\text{TI}} = -\frac{1}{4\beta V \bar{m}} \sum_q j^T(q) \frac{\frac{\kappa \bar{m}}{2} \mathbf{q}^2 + \bar{m} \lambda - 4 \frac{i \Omega_n}{2} \sigma_y}{\left(\frac{\Omega_n}{2}\right)^2 + \left(\frac{\kappa \bar{m}}{2} \mathbf{q}^2 + \bar{m} \lambda\right)^2} j(-q). \quad (13)$$

In the low-frequency limit, the last term in the numerator is less singular than the other two terms, and we therefore neglect it in the following [16]. We therefore get

$$\delta S_{\text{TI}} = -\frac{1}{4\beta V \bar{m}} \sum_q \frac{\omega_{\mathbf{q}}}{\left(\frac{\Omega_n}{2}\right)^2 + \omega_{\mathbf{q}}^2} j^T(q) j(-q), \quad (14)$$

where we have defined the magnon dispersion

$$\omega_{\mathbf{q}} = \frac{\kappa \bar{m}}{2} \mathbf{q}^2 + \bar{m} \lambda. \quad (15)$$

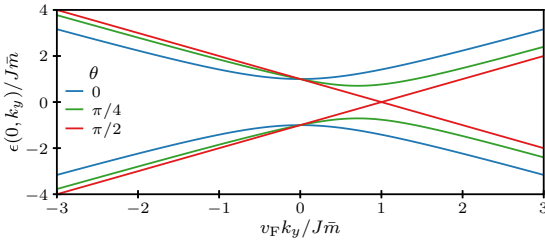


FIG. 2. Plot of eigenenergies in Eq. (23) as a function of k_y with $k_x = 0$ and $\mu = 0$ for different values of θ . Increasing θ toward $\pi/2$ reduces the mass gap and shifts the center of the dispersion away from $k_y = 0$. At $\pi/2$ we have a Dirac point located at $k_y = J\bar{m}/v_F$.

B. Diagonalization of mean field TI action

We next diagonalize the mean field TI action

$$S_{\text{TI}}^{\text{mf}} = -\frac{1}{\beta V} \sum_k \Psi^\dagger(k) G^{-1}(k) \Psi, \quad (16)$$

where we have defined the inverse Green's function

$$G^{-1}(k) = i\omega_n + \mu + M\sigma_z + v_F k_x \sigma_y - v_F(k_y - K_y)\sigma_x, \quad (17)$$

where $M = J\bar{m} \cos \theta$ and $K_y = J\bar{m} \sin \theta / v_F$. Diagonalizing the Green's function results in

$$G_d^{-1} = P_{\mathbf{k}} G^{-1} P_{\mathbf{k}}^\dagger = \text{diag}(\lambda_+, \lambda_-), \quad (18)$$

where the diagonal entries are

$$\lambda_{\pm} = i\omega_n + \mu \mp \sqrt{v_F^2 k_x^2 + v_F^2 (k_y - K_y)^2 + M^2}, \quad (19)$$

and the Green's function is diagonalized by the matrix

$$P_{\mathbf{k}} = \frac{1}{\sqrt{n_{\mathbf{k}}}} \begin{pmatrix} s_{\mathbf{k}} & r_{\mathbf{k}} \\ -r_{\mathbf{k}} & s_{\mathbf{k}} \end{pmatrix}, \quad (20)$$

where

$$s_{\mathbf{k}} = v_F(k_y - K_y) + i v_F k_x, \quad (21a)$$

$$r_{\mathbf{k}} = M + \sqrt{|s_{\mathbf{k}}|^2 + M^2}, \quad (21b)$$

$$n_{\mathbf{k}} = r_{\mathbf{k}}^2 + |s_{\mathbf{k}}|^2. \quad (21c)$$

The eigenvectors $\Psi_{\pm}(k)$ in the helicity basis are given by a transformation from the spin basis $\Psi(k)$, defined below Eq. (2), as follows:

$$\Psi_{\pm}(k) \equiv \begin{pmatrix} \psi_+ \\ \psi_- \end{pmatrix} = P_{\mathbf{k}} \Psi(k), \quad (22)$$

where the helicity index is denoted by + or -. The eigenenergies are given by the zeros of the diagonal entries

$$\epsilon_{\pm}(\mathbf{k}) = \pm \sqrt{v_F^2 k_x^2 + v_F^2 (k_y - K_y)^2 + M^2} - \mu. \quad (23)$$

Hence, M leads to a gap in the dispersion, while K_y shifts the dispersion along the k_y axis. This is illustrated in Fig. 2.

C. Magnon-mediated interaction

We now rewrite the effective action in Eq. (14) in terms of the Dirac fermions defined by Eq. (22), assuming that $\mu > M$

and thus restricting the problem to only considering the ψ_+ fermions. This results in (see Appendix A for details)

$$\delta S_{\text{TI}} = -\frac{J^2 \bar{m}}{4(\beta V)^3} \sum_{q,k,k'} D(q) \Lambda_{\mathbf{k}'\mathbf{k}}(\mathbf{q}) \times \psi^\dagger(k' + q) \psi^\dagger(k - q) \psi(k) \psi(k'), \quad (24)$$

where we for notational simplicity have dropped the subscript + on the fields ψ_+ , and defined the magnon propagator

$$D(q) = \frac{\omega_{\mathbf{q}}}{(\Omega_n/2)^2 + \omega_{\mathbf{q}}^2}, \quad (25)$$

and the scattering form factor $\Lambda_{\mathbf{k}'\mathbf{k}}(\mathbf{q}) = \Lambda_{\mathbf{k}'\mathbf{k}}^0(\mathbf{q}) + \Lambda_{\mathbf{k}'\mathbf{k}}^x(\mathbf{q}) + \Lambda_{\mathbf{k}'\mathbf{k}}^{xz}(\mathbf{q})$, with

$$\Lambda_{\mathbf{k}'\mathbf{k}}^0(\mathbf{q}) = \frac{\cos^2 \theta + 1}{\sqrt{n_{\mathbf{k}} n_{\mathbf{k}-\mathbf{q}} n_{\mathbf{k}'+\mathbf{q}}}} \times [s_{\mathbf{k}'} s_{\mathbf{k}-\mathbf{q}}^* r_{\mathbf{k}'+\mathbf{q}} r_{\mathbf{k}} + s_{\mathbf{k}} s_{\mathbf{k}'+\mathbf{q}}^* r_{\mathbf{k}'} r_{\mathbf{k}-\mathbf{q}}], \quad (26)$$

$$\Lambda_{\mathbf{k}'\mathbf{k}}^x(\mathbf{q}) = \frac{\sin^2 \theta}{\sqrt{n_{\mathbf{k}} n_{\mathbf{k}-\mathbf{q}} n_{\mathbf{k}'+\mathbf{q}}}} \times [s_{\mathbf{k}'} s_{\mathbf{k}} s_{\mathbf{k}'+\mathbf{q}}^* s_{\mathbf{k}-\mathbf{q}}^* - s_{\mathbf{k}'} s_{\mathbf{k}'+\mathbf{q}}^* r_{\mathbf{k}'} r_{\mathbf{k}-\mathbf{q}} - s_{\mathbf{k}} s_{\mathbf{k}-\mathbf{q}}^* r_{\mathbf{k}'} r_{\mathbf{k}'+\mathbf{q}} + r_{\mathbf{k}} r_{\mathbf{k}-\mathbf{q}} r_{\mathbf{k}'} r_{\mathbf{k}'+\mathbf{q}} - s_{\mathbf{k}'} s_{\mathbf{k}} r_{\mathbf{k}'+\mathbf{q}} r_{\mathbf{k}-\mathbf{q}} - s_{\mathbf{k}'+\mathbf{q}}^* s_{\mathbf{k}-\mathbf{q}}^* r_{\mathbf{k}'} r_{\mathbf{k}}], \quad (27)$$

$$\Lambda_{\mathbf{k}'\mathbf{k}}^{xz}(\mathbf{q}) = -\frac{\cos \theta \sin \theta}{\sqrt{n_{\mathbf{k}} n_{\mathbf{k}-\mathbf{q}} n_{\mathbf{k}'+\mathbf{q}}}} \times [s_{\mathbf{k}'} s_{\mathbf{k}} s_{\mathbf{k}-\mathbf{q}}^* r_{\mathbf{k}'+\mathbf{q}} + s_{\mathbf{k}} s_{\mathbf{k}'} s_{\mathbf{k}'+\mathbf{q}}^* r_{\mathbf{k}-\mathbf{q}} + s_{\mathbf{k}} s_{\mathbf{k}-\mathbf{q}}^* s_{\mathbf{k}'+\mathbf{q}}^* r_{\mathbf{k}'} + s_{\mathbf{k}'} s_{\mathbf{k}'+\mathbf{q}}^* s_{\mathbf{k}-\mathbf{q}}^* r_{\mathbf{k}} - s_{\mathbf{k}'} r_{\mathbf{k}'+\mathbf{q}} r_{\mathbf{k}'} r_{\mathbf{k}-\mathbf{q}} - s_{\mathbf{k}} r_{\mathbf{k}-\mathbf{q}} r_{\mathbf{k}'} r_{\mathbf{k}'+\mathbf{q}} - s_{\mathbf{k}'+\mathbf{q}}^* r_{\mathbf{k}'} r_{\mathbf{k}-\mathbf{q}} - s_{\mathbf{k}-\mathbf{q}}^* r_{\mathbf{k}'} r_{\mathbf{k}'+\mathbf{q}}]. \quad (28)$$

The first expression is the same expression as was analyzed in Refs. [16,19], except it now has a θ dependence and an overall multiplicative factor of 2 when $\theta = 0$. This term is, however, always nonzero. The other two expressions were not present in Refs. [16,19], as they both require an x component in the mean field magnetization. The last expression also requires a finite z component. Hence, we may have differences in the pairing depending on the angle of the mean field direction, which will be analyzed after calculating the gap equations for the system.

III. Gapequations

Including the symmetrized magnon-mediated interaction in the action, we get the following effective action for the + fermions:

$$S_+ = -\frac{1}{\beta V} \sum_k \psi^\dagger(k) \lambda_+(k) \psi(k) + \frac{1}{(\beta V)^3} \sum_{k,k',q} V_{k'k}(q) \times \psi^\dagger\left(k' + \frac{q}{2}\right) \psi^\dagger\left(-k' + \frac{q}{2}\right) \psi\left(-k + \frac{q}{2}\right) \psi\left(k + \frac{q}{2}\right), \quad (29)$$

with the symmetrized interaction

$$V_{k'k}(q) = -\frac{J^2 \bar{m}}{8} [D(k' - k) \Lambda_{\mathbf{q}}(\mathbf{k}', \mathbf{k}) - D(k' + k) \Lambda_{\mathbf{q}}(\mathbf{k}', -\mathbf{k})]. \quad (30)$$

For notational simplicity we have defined

$$\Lambda_{\mathbf{q}}(\mathbf{k}', \mathbf{k}) \equiv \Lambda_{\mathbf{k}+\frac{\mathbf{q}}{2}, -\mathbf{k}+\frac{\mathbf{q}}{2}}(\mathbf{k}' - \mathbf{k}). \quad (31)$$

We have also relabeled the momenta to allow for a finite center-of-mass momentum \mathbf{q} for the Cooper pairs, which is necessary for Amperean pairing. Moreover, since the minimum of the dispersion is shifted away from $\mathbf{k} = 0$ for nonzero θ there is also the possibility of BCS Cooper pairs with finite center-of-mass momentum, i.e., a Fulde-Ferrell-Larkin-Ovchinnikov (FFLO) state [39,40]. As such, the system has some similarities to two-dimensional normal metal systems with Rashba spin-orbit coupling coupled to a Zeemann field with an in-plane component, leading to a shift in the dispersion and thus the possibility of a FFLO state [41–46].

We now perform a Hubbard-Stratonovich decoupling [47] by introducing bosonic fields φ_q and ϕ_q^\dagger (see Appendix B for details), resulting in the functional integral

$$Z = \int \mathcal{D}\psi^\dagger \mathcal{D}\psi e^{-S'} \int \mathcal{D}\varphi_q^\dagger \mathcal{D}\varphi_q e^{-S_\phi^0}, \quad (32)$$

where we have the fermionic action containing the coupling to the bosonic fields

$$S' = -\frac{1}{\beta V} \sum_k \left\{ \psi^\dagger(k) \lambda_+(k) \psi(k) + \sum_q \left[\varphi_q^\dagger(k) \psi\left(-k + \frac{q}{2}\right) \psi\left(k + \frac{q}{2}\right) + \psi^\dagger\left(k + \frac{q}{2}\right) \psi^\dagger\left(-k + \frac{q}{2}\right) \varphi_q(k) \right] \right\}, \quad (33)$$

and the additional bosonic action

$$S_\phi^0 = -\beta V \sum_{q, k'} \varphi_q^\dagger(k') [V_{k'k}(q)]^{-1} \varphi_q(k). \quad (34)$$

Before proceeding any further, we will assume that the mean field bosonic field is of the form

$$\varphi_q(k) = \frac{1}{2} \delta_{\mathbf{q}, \mathbf{Q}} \delta_{\Omega_n, 0} \Delta_{\mathbf{Q}}(k). \quad (35)$$

This effectively restricts the analysis to only consider Cooper pairs with one common center-of-mass momentum. In general, these will couple to Cooper pairs with other center-of-mass momenta. However, since any interaction between them does not conserve momentum, the couplings are likely to be small, and we therefore focus on only one \mathbf{Q} in the following.

In order to integrate out the fermions, we rewrite the action using the vector

$$\Psi_{\mathbf{Q}}(k) = \begin{pmatrix} \psi(k) \\ \psi^\dagger(-k + \mathbf{Q}) \end{pmatrix}, \quad (36)$$

where $\mathbf{Q} = (0, \mathbf{Q})$, leading to

$$S' = -\frac{1}{2\beta V} \sum_k \Psi_{\mathbf{Q}}^\dagger\left(k + \frac{\mathbf{Q}}{2}\right) \mathcal{G}_{\mathbf{Q}}^{-1}(k) \Psi_{\mathbf{Q}}\left(k + \frac{\mathbf{Q}}{2}\right), \quad (37)$$

where we have defined the inverse Green's function matrix

$$\mathcal{G}_{\mathbf{Q}}^{-1}(k) = \begin{pmatrix} \lambda_+(k + \frac{\mathbf{Q}}{2}) & \Delta_{\mathbf{Q}}(k) \\ \Delta_{\mathbf{Q}}^\dagger(k) & -\lambda_+(-k + \frac{\mathbf{Q}}{2}) \end{pmatrix}. \quad (38)$$

Integrating out the fermions, we finally get the effective action for the bosonic fields

$$S_\phi = -\frac{\beta V}{4} \sum_{k'} \Delta_{\mathbf{Q}}^\dagger(k') [V_{k'k}(\mathbf{Q})]^{-1} \Delta_{\mathbf{Q}}(k) - \frac{1}{2} \text{Tr} \ln(-\mathcal{G}_{\mathbf{Q}}^{-1}). \quad (39)$$

The gap equation follows from using the saddle-point approximation [47]

$$\frac{\delta S_\phi}{\delta \Delta_{\mathbf{Q}}(p)} = 0, \quad (40)$$

resulting in

$$\frac{\beta V}{4} \sum_{k'} \Delta_{\mathbf{Q}}^\dagger(k') [V_{k'p}(\mathbf{Q})]^{-1} = \frac{\Delta_{\mathbf{Q}}^\dagger(p)}{2 \det \mathcal{G}_{\mathbf{Q}}^{-1}(p)}, \quad (41)$$

where $\det \mathcal{G}_{\mathbf{Q}}^{-1}(k) = -\lambda_+(k + \mathbf{Q}/2) \lambda_+(-k + \mathbf{Q}/2) - |\Delta_{\mathbf{Q}}(k)|^2$. Multiplying both sides with $V_{pk}(\mathbf{Q})/\beta V$ and summing over p , we get

$$\Delta_{\mathbf{Q}}^\dagger(k) = \frac{2}{\beta V} \sum_{\omega_n, \mathbf{k}'} \frac{\Delta_{\mathbf{Q}}^\dagger(k') V_{k'k}(\mathbf{Q})}{[i\omega_n - \epsilon_{\mathbf{Q}}^o(\mathbf{k}') - E_{\mathbf{Q}}(k')] [i\omega_n - \epsilon_{\mathbf{Q}}^o(\mathbf{k}') + E_{\mathbf{Q}}(k')]}, \quad (42)$$

where we have defined

$$\epsilon_{\mathbf{Q}}^o(\mathbf{k}') = \frac{\epsilon_+(\mathbf{k}' + \frac{\mathbf{Q}}{2}) - \epsilon_+(-\mathbf{k}' + \frac{\mathbf{Q}}{2})}{2}, \quad (43)$$

$$\epsilon_{\mathbf{Q}}^e(\mathbf{k}') = \frac{\epsilon_+(\mathbf{k}' + \frac{\mathbf{Q}}{2}) + \epsilon_+(-\mathbf{k}' + \frac{\mathbf{Q}}{2})}{2}, \quad (44)$$

$$E_{\mathbf{Q}}(k') = \sqrt{[\epsilon_{\mathbf{Q}}^e(\mathbf{k}')]^2 + |\Delta_{\mathbf{Q}}(k')|^2}. \quad (45)$$

It is important to point out that since we have included only the ψ_+ states in the analysis, the gap equation is for pseudospin triplets, the ‘‘spin’’ in this case being the helicity index $+$ or $-$. The physical spin is not a good quantum number because of the spin-orbit coupling in the system. Therefore, following the symmetry analysis in, e.g., Ref. [36], the gap function has to be odd in ω_n and even in \mathbf{k} , or even in ω_n and odd in \mathbf{k} .

We will now treat the gap equation in two different ways:

(1) We neglect the frequency dependence of the magnon

propagator in Eq. (25) [12,13,19,24] and study the static limit, and (2) we use an approach similar to the Eliashberg equations [48–50], solving the gap equations directly including only a low number of Matsubara frequencies.

IV. FREQUENCY-INDEPENDENT SOLUTION

In the static limit, we set the frequency to zero in the magnon propagator,

$$D(q) \rightarrow D(\mathbf{q}) = \frac{1}{\omega_{\mathbf{q}}}, \quad (46)$$

such that the interaction now only depends on the momenta $V_{k'k}(q) \rightarrow V_{k'k}(\mathbf{q})$. Hence, there is no longer a free frequency in the gap equation, and we can perform the remaining Matsubara sum, resulting in

$$\Delta_{\mathbf{Q}}^{\dagger}(\mathbf{k}) = -\frac{2}{V} \sum_{\mathbf{k}'} V_{k'k}(\mathbf{Q}) \Delta_{\mathbf{Q}}(\mathbf{k}') \chi_{\mathbf{Q}}(\mathbf{k}'), \quad (47)$$

with

$$\chi_{\mathbf{Q}}(\mathbf{k}) = \frac{1}{4E_{\mathbf{Q}}(\mathbf{k}')} \left[\tanh \frac{\beta(\epsilon_{\mathbf{Q}}^{\circ}(\mathbf{k}) + E_{\mathbf{Q}}(\mathbf{k}))}{2} - \tanh \frac{\beta(\epsilon_{\mathbf{Q}}^{\circ}(\mathbf{k}) - E_{\mathbf{Q}}(\mathbf{k}))}{2} \right], \quad (48)$$

where $\beta = 1/k_{\text{B}}T$. Since the surface states are pseudospin triples, and we have neglected the frequency dependence, $\Delta_{\mathbf{Q}}(\mathbf{k})$ must now be an odd function of \mathbf{k} [36], which is evident also from the interaction. For simplicity, we now define $\mathbf{K} = (0, K_y)$, and let $\mathbf{Q} = 2\mathbf{K} + 2\mathbf{P}$, such that the center of the Fermi surface is at the origin when $\mathbf{P} = 0$ independent of the angle θ .

A. BCS pairing

We first study the case $\mathbf{P} = 0$, which resembles the regular BCS pairing case with circular Fermi surface. Now, $\epsilon_{2\mathbf{K}}^{\circ}(\mathbf{k}) = \mathbf{0}$ for all \mathbf{k} , and the temperature-dependent factor in the gap equation simplifies to

$$\chi_{2\mathbf{K}}(\mathbf{k}) = \frac{1}{2E_{2\mathbf{K}}(\mathbf{k})} \tanh \frac{\beta E_{2\mathbf{K}}(\mathbf{k})}{2}, \quad (49)$$

which is peaked at the minima of $E_{2\mathbf{K}}$, at Fermi momenta $v_{\text{F}}k_{\text{F}} = \sqrt{\mu^2 - M^2}$. Instead of solving the gap equation directly, we write the linearized gap equation [51]

$$\Delta_{2\mathbf{K}}^{\dagger}(\mathbf{k}) = -\langle 2V_{k'k}(2\mathbf{K})\Delta_{2\mathbf{K}}(k') \rangle_{k',\text{FS}} \int \frac{dk'}{2\pi} k' \chi_{2\mathbf{K}}(k'), \quad (50)$$

which can be written as an eigenvalue problem

$$\eta \Delta_{2\mathbf{K}}(k') = -\langle 2V_{k'k}(2\mathbf{K})\Delta_{2\mathbf{K}}(k') \rangle_{k',\text{FS}}, \quad (51)$$

where FS denotes an average over the Fermi surface. The critical temperature is then proportional to $e^{-c/\eta}$, where η is the highest positive eigenvalue [51], and c is some constant.

TABLE I. Material parameters used unless otherwise stated.

$\hbar v_{\text{F}}$	0.4 eV nm [57]
μ	0.2 eV [58]
a	0.4 nm [57]
$J\bar{m}$	10 meV [59,60]
$\bar{m}\kappa$	0.03 meV nm ² [61]
λ/κ	0.01 nm ⁻²

Assuming $M \ll \mu$, we get for the scattering form factor

$$\Delta_{2\mathbf{K}}(\mathbf{k}', \mathbf{k}) \approx -e^{-i\phi_{\mathbf{k}} + i\phi_{\mathbf{k}'}} [1 - \sin^2 \theta \sin \phi_{\mathbf{k}} \sin \phi_{\mathbf{k}'}]. \quad (52)$$

The expression in the square brackets never changes sign, but introduces anisotropy in \mathbf{k} space. Hence, for $\phi_{\mathbf{k}} = \phi_{\mathbf{k}'}$, the interaction $V_{k'k}(2\mathbf{K})$ is always positive as long as the easy-axis parameter $\lambda > 0$ [see Eq. (1)], giving the wrong overall sign in order for a nontrivial solution of the gap equation to be possible. To verify this, we solve Eq. (51) numerically as a function of λ using the parameter values in Table I, resulting in the eigenvalues shown in Fig. 3 for tilt angle $\theta = 0$. The figure shows that η is very small for positive values of λ . We also calculated the eigenvectors, which were randomly fluctuating for positive λ . For other tilt angles, the results are qualitatively the same. Hence, we conclude that BCS pairing is not possible in the static limit for $\lambda > 0$. For $\lambda < 0$ we find finite eigenvalues η and smooth eigenvectors, meaning that the system has a superconducting instability in this case, the reason being that the magnon propagator, and thus the interaction potential, now can change sign. This is consistent with the results in Ref. [19]. In systems where $\lambda < 0$ and $\theta \neq 0$ is possible, this would lead to FFLO Cooper pairs with momentum $2\mathbf{K}$. However, for the present system, we have assumed that $\lambda > 0$, thus, we do not find a solution to the gap equation in the BCS-type case.

B. Amperean pairing

As has been shown in previous work [16,19,22], it is possible to get a superconducting instability where the Cooper pairs reside on the same side of the Fermi surface, and the Cooper

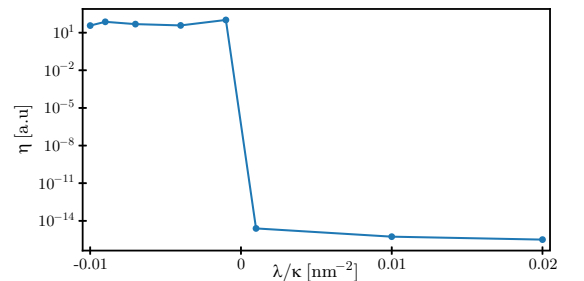


FIG. 3. Plot of solutions to the eigenvalue problem (51) as a function of λ for $\theta = 0$ and $J = 0.01 \text{ eV nm}^2$. We see that the eigenvalues are very small for $\lambda > 0$, indicative of the gap equation not having solutions. For $\lambda < 0$, however, we get finite eigenvalues, meaning that the gap equation has solutions for negative λ .

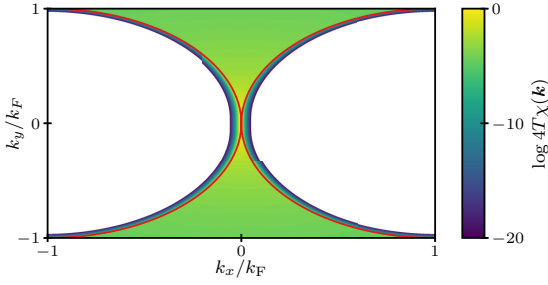


FIG. 4. Plot of the logarithm of $4T\chi_{\mathbf{Q}}(\mathbf{k})$ with $\mathbf{Q} = 2\mathbf{K} + 2\mathbf{P}$ for $\mathbf{P} = (k_F, 0)$, $k_B T = 5 \times 10^{-4}$ eV, and $\Delta_{\mathbf{Q}} = 0$. The white areas are outside the range of the color bar. The red lines indicate $k_{\parallel}^2 + k_{\perp}^2 \pm 2k_{\parallel}k_F = 0$.

pairs thus have a finite center-of-mass momentum of $2k_F$. In the present case, this means setting $\mathbf{Q} = 2\mathbf{K} + 2\mathbf{P}$, where $|\mathbf{P}| = k_F$. In the limit $T \rightarrow 0$, $\chi(\mathbf{k})$ quickly drops off to zero when the $\epsilon_{2\mathbf{K}+2\mathbf{P}}^e(\mathbf{k})$ term in the tanh terms dominates over the $\epsilon_{2\mathbf{K}+2\mathbf{P}}^e(\mathbf{k})$ term in the $\Delta = 0$ limit, i.e., approximately when

$$k_{\parallel}^2 + k_{\perp}^2 \pm 2k_{\parallel}k_F > 0, \quad (53)$$

where k_{\perp} (k_{\parallel}) is perpendicular to (parallel with) \mathbf{P} [23] (see Fig. 4). Even inside this region, we see that $\chi(\mathbf{k})$ is largest for small $|\mathbf{k}|$. In the limit $|\mathbf{k}|, |\mathbf{k}'| \ll |\mathbf{P}|$ the form factor to lowest order is

$$\Lambda_{2\mathbf{K}+2\mathbf{P}}(0, 0) = \frac{v_F^2 k_F^2 (1 - \sin^2 \phi_P \sin^2 \theta) + M^2 \sin^2 \theta}{M^2 + v_F^2 k_F^2}, \quad (54)$$

a plot of which is shown in Fig. 5. The figure shows that as θ increases toward $\pi/2$, the isotropy in the xy plane is broken, and pairing of particles with \mathbf{P} pointing along the x axis becomes increasingly more favored. Importantly, the sign

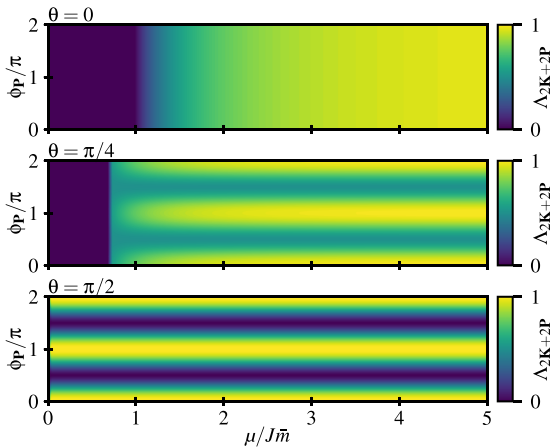


FIG. 5. Plot of $\Lambda_{2\mathbf{K}+2\mathbf{P}}(0, 0)$ for different tilt angles θ as a function of ϕ_P and chemical potential μ . The pairing is zero for $\mu < M = J\bar{m} \cos \theta$ since we have no Fermi surface in this case.

is opposite compared to the BCS case studied above. Solving the linearized gap equation numerically in the Amperean pairing case as a function of tilt angle θ for different orientations of $\mathbf{P} = k_F(\cos \phi_P, \sin \phi_P)$, we get the results shown in Fig. 6(a). As expected from Fig. 5 the critical temperature decreases when θ increases toward $\pi/2$ when $\phi_P = \pi/4$ and $\pi/2$ compared to $\phi_P = 0$. For $\phi_P = 0$, the critical temperature increases for increasing θ , meaning that Amperean superconductivity might be easier to detect in a system where the FMI magnetization lies in the interface plane. It must be noted that the change in T_c due to changes in J [see Fig. 6(b)] is quite large for $J \sim 0.01$ eV nm², and might explain the rather large relative increase in T_c for $\phi_P = 0$ when tuning the magnetization into the plane. Figures 6(c) and 6(d) show the real and imaginary parts of the eigenvector, showing that the eigenvector is odd in \mathbf{k} . The eigenvector is similar to that obtained in Ref. [22] for a topological insulator coupled to an antiferromagnetic insulator.

For systems with a finite in-plane component of the magnetization, the system no longer has many degenerate solutions for all the possible choices of the vector \mathbf{P} . The highest T_c will be for $\mathbf{P} = (\pm k_F, 0)$, and hence we expect the system to condense to either or both of these \mathbf{P} vectors. Although condensing with $\mathbf{P} = (\pm k_F, 0)$ is equally probable, there is still an overall shift $2\mathbf{K}$ in the center-of-mass momentum, meaning we always have a net shift in the Cooper pair center-of-mass momentum.

V. FREQUENCY-DEPENDENT TREATMENT

We next solve the gap equations including the frequency dependence of the gap function and magnon propagator. In this way we allow for both even-frequency/odd-momentum solutions, and odd-frequency/even-momentum solutions. The latter has, to our knowledge, not been considered in the context of Amperean pairing in other works. Writing out the interaction potential in Eq. (42), we get

$$\Delta_{\mathbf{Q}}^{\dagger}(i\omega_n, \mathbf{k}) = \frac{J^2 \bar{m}}{\beta V} \sum_{\omega_n, \mathbf{k}'} \sum_{\gamma} \gamma \omega_{\mathbf{k}' - \gamma \mathbf{k}} \Lambda_{\mathbf{Q}}(\mathbf{k}', \gamma \mathbf{k}) \Delta_{\mathbf{Q}}^{\dagger}(i\omega_n', \mathbf{k}') \times \frac{1}{[i\omega_n' - z_1][i\omega_n' - z_2][i\omega_n' - z_{\gamma}^+][i\omega_n' - z_{\gamma}^-]}, \quad (55)$$

where $\gamma = \pm 1$, and the poles are given by

$$z_{1,2} = \epsilon_{\mathbf{Q}}^o(\mathbf{k}') \pm E_{\mathbf{Q}}(k'), \quad (56a)$$

$$z_{\gamma}^{\pm} = \gamma i\omega_n \pm 2\omega_{\mathbf{k}' - \gamma \mathbf{k}}. \quad (56b)$$

To find T_c we linearize the above gap equation, and define the indices $N = 2n + 1$ and $M = 2n' + 1$, and the temperature parameter $t = \pi k_B T$, such that the Matsubara frequencies can be written $\omega_n = Nt$ and $\omega_n' = Mt$. For notational simplicity, we also define $\Delta_{\mathbf{Q}}^{\dagger}(N, \mathbf{k}) = \Delta_{\mathbf{Q}}^{\dagger}(i\omega_n, \mathbf{k})$. Inserted into the

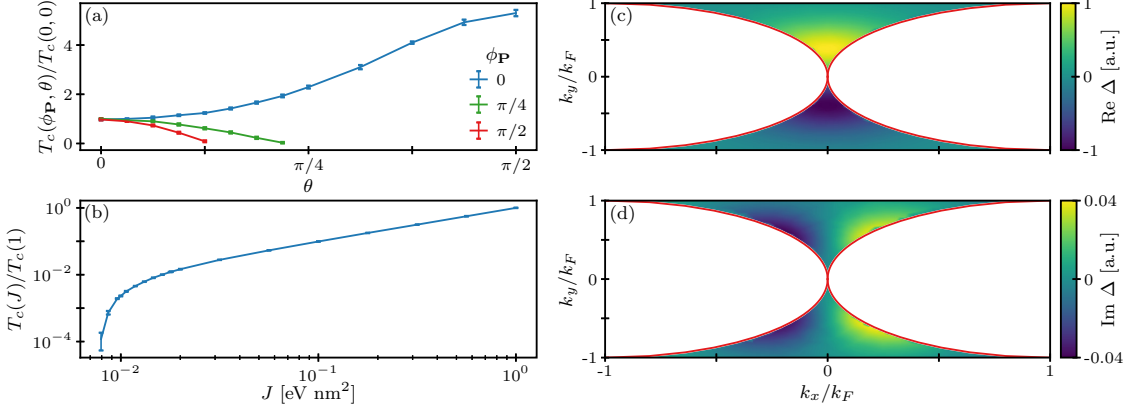


FIG. 6. (a) Plot of T_c normalized to that at $\phi_{\mathbf{P}} = 0$ and $\theta = 0$ for $J = 0.01 \text{ eV nm}^2$. We see that as the tilt angle θ increases, the critical temperature is no longer the same for different \mathbf{P} : It decreases for θ increasing toward $\pi/2$ for $\phi_{\mathbf{P}} = \pi/4$ and $\pi/2$, as we would expect from Fig. 5. For $\phi_{\mathbf{P}} = 0$ it actually increases for increasing θ . We use a momentum cutoff of $3k_F$ for k_x and k_y . (b) Plot of T_c as a function of J normalized to the value of T_c at $J = 1 \text{ eV nm}^2$, showing a very sharp decrease in the critical temperature for $J < 0.01 \text{ eV nm}^2$. The error bar shows the sample standard deviation for five calculations of T_c . (c), (d) Show the real and imaginary parts of the eigenvector Δ at T_c for $\phi_{\mathbf{P}} = 0$, $\theta = 0$, and clearly shows that the eigenvector is odd in \mathbf{k} .

linearized equation, we get

$$\begin{aligned} \Delta_{\mathbf{Q}}^{\dagger}(N, \mathbf{k}) &= \frac{J^2 \bar{m}}{\pi V} t \sum_{M, \mathbf{k}'} \\ &\times \frac{\Delta_{\mathbf{Q}}^{\dagger}(M, \mathbf{k}')}{\left[M t + i \epsilon_+ \left(\mathbf{k}' + \frac{\mathbf{Q}}{2} \right) \right] \left[M t - i \epsilon_+ \left(-\mathbf{k}' + \frac{\mathbf{Q}}{2} \right) \right]} \\ &\times \left[\frac{\omega_{\mathbf{k}' - \mathbf{k}} \Lambda_{\mathbf{Q}}(\mathbf{k}', \mathbf{k})}{(M - N)^2 t^2 + (2\omega_{\mathbf{k}' - \mathbf{k}})^2} \right. \\ &\left. - \frac{\omega_{\mathbf{k}' + \mathbf{k}} \Lambda_{\mathbf{Q}}(\mathbf{k}', -\mathbf{k})}{(M + N)^2 t^2 + (2\omega_{\mathbf{k}' + \mathbf{k}})^2} \right]. \end{aligned} \quad (57)$$

Including a finite number N_{ω} of positive Matsubara frequencies, and $N_{\mathbf{k}}$ reciprocal lattice points \mathbf{k} , we can write this as a matrix equation $\Delta = \mathcal{M}(t)\Delta$, where $\mathcal{M}(t)$ is a $(2N_{\omega}N_{\mathbf{k}}) \times (2N_{\omega}N_{\mathbf{k}})$ matrix. Hence, the critical temperature is given by the value of t such that the highest eigenvalue of \mathcal{M} is 1.

Since we did not find any BCS-type solutions, except for $\lambda < 0$ in the frequency-independent treatment above, we will focus only on Amperean pairing. Solving the eigenvalue problem numerically for the Amperean case with $\mathbf{Q} = 2\mathbf{K} + 2\mathbf{P}$, $\mathbf{P} = (k_F, 0)$ for $\theta = 0$, we find the dependence on coupling J as shown in Fig. 7(a) for $N_{\omega} = 1, 2$, and 3. The critical temperature does not change significantly by increasing the number of Matsubara frequencies included in the calculation. The reason for this is that this is not a strong coupling calculation, and thus the renormalization of the fermion propagator is not included. Hence, the largest eigenvalues of \mathcal{M} are given by $M = N = \pm 1$, and necessarily do not change when including more frequencies.

We also calculate the eigenvalues $\Delta(N, \mathbf{k})$ at T_c when solving the matrix equation. Under particle exchange, we must

have $\Delta(N, \mathbf{k}) = -\Delta(-N, -\mathbf{k})$ [36] which means the eigenvectors can be written in the form

$$\Delta(N, \mathbf{k}) = \Delta_e(N, \mathbf{k}) + \Delta_o(N, \mathbf{k}), \quad (58)$$

where $\Delta_{e/o}$ is even/odd in the frequency index N . Hence, we have

$$\Delta_e(N, \mathbf{k}) = \frac{\Delta(N, \mathbf{k}) + \Delta(-N, \mathbf{k})}{2}, \quad (59a)$$

$$\Delta_o(N, \mathbf{k}) = \frac{\Delta(N, \mathbf{k}) - \Delta(-N, \mathbf{k})}{2}, \quad (59b)$$

where $\Delta_{e/o}$ necessarily is odd/even under $\mathbf{k} \rightarrow -\mathbf{k}$. Numerically, we normalize the eigenvectors such that

$$\begin{aligned} 1 &= \frac{1}{V} \sum_{n=-N_{\omega}}^{N_{\omega}} \sum_{\mathbf{k}} |\Delta(2n+1, \mathbf{k})|^2 \\ &= \frac{1}{V} \sum_{n=-N_{\omega}}^{N_{\omega}} \sum_{\mathbf{k}} [|\Delta_e(2n+1, \mathbf{k})|^2 + |\Delta_o(2n+1, \mathbf{k})|^2]. \end{aligned} \quad (60)$$

For an index N , we define the weighting function for odd- or even-frequency pairing

$$\begin{aligned} w_i(N) &= \frac{1}{V} \sum_{\mathbf{k}} \Delta_i^{\dagger}(N, \mathbf{k}) \Delta(N, \mathbf{k}) \\ &= \frac{1}{V} \sum_{\mathbf{k}} \Delta_i^{\dagger}(N, \mathbf{k}) [\Delta_e(N, \mathbf{k}) + \Delta_o(N, \mathbf{k})] \\ &= \frac{1}{V} \sum_{\mathbf{k}} |\Delta_i(N, \mathbf{k})|^2 = w_i(-N), \end{aligned} \quad (61)$$

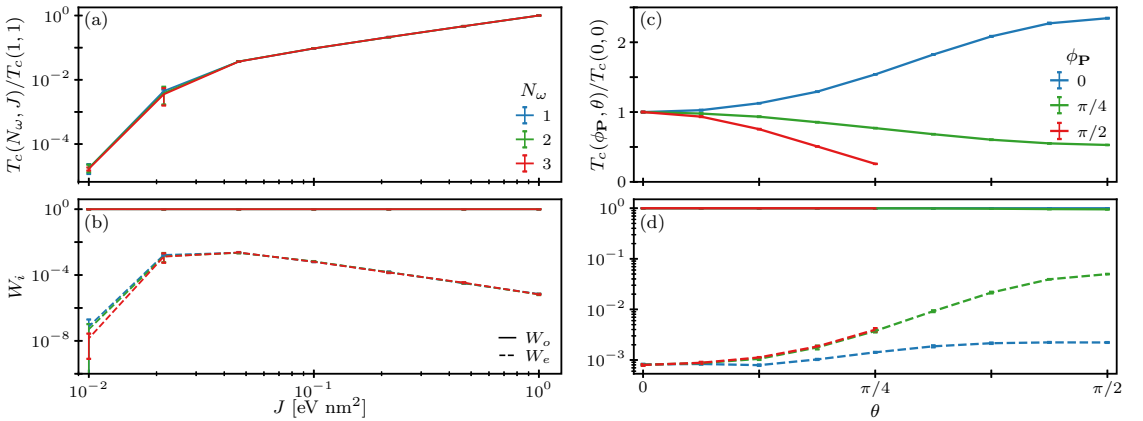


FIG. 7. (a) Plot of the critical temperature for different couplings J and N_ω normalized to that at $J = 1 \text{ eV nm}^2$ and $N_\omega = 1$. (b) Plot of the total weight W_i for odd- (solid) and even- (dashed) frequency solutions as a function of J for different N_ω . For the entire range of couplings, the eigenvectors are dominantly odd in frequency. For both plots we see that there is no significant difference between the plots for different N_ω . (c) Plot of T_c normalized to that at $\phi_{\mathbf{P}} = \theta = 0$ and (d) the total weight W_i as functions of tilt angle θ for different \mathbf{P} orientations for $J = 10^{-1} \text{ eV nm}^2$ and $N_\omega = 1$. The error bars show the sample standard deviation for 5 runs with momentum cutoff k_F .

where $i = e/o$, and the total weight for each symmetry is defined as

$$W_i = \sum_{n=-N_\omega}^{N_\omega} w_i(2n+1). \quad (62)$$

Hence, we must have

$$1 = \sum_{n=-N_\omega}^{N_\omega} [w_e(2n+1) + w_o(2n+1)] = W_e + W_o. \quad (63)$$

A plot of W_i is shown in Fig. 7(b), and shows that the odd-frequency part of the eigenvectors dominates the even-frequency part. Hence, this points to the possibility of magnon-mediated odd-frequency Amperean pairing, which is consistent with the fact that pairing at finite momentum has been shown to stabilize odd-frequency superconductivity [30–32]. Moreover, the reason odd-frequency solutions are favored might be understood from the fact that s -wave solutions allow for a finite gap close to $\mathbf{k} = 0$, corresponding to a maximum of the first term in Eq. (57). The even-frequency p -wave solution, however, has to be zero at $\mathbf{k} = 0$, and thus gets a much smaller contribution from these areas of \mathbf{k} space.

Again, we see negligible change when increasing N_ω . Figure 8 shows the effects of increasing the number of momentum-space grid points on the critical temperature and weights W_i , showing that T_c converges quickly for the given parameter values. For lower couplings J (not shown), the convergence is slower due to the increasing sharpness of the potential when the temperature decreases. However, the qualitative picture still remains the same independent of the number of grid points, namely, that the odd-frequency solution dominates.

Figures 7(c) and 7(d) show the critical temperature and weight functions W_i as functions of tilt angle θ for different orientations of \mathbf{P} for $J = 10^{-1} \text{ eV nm}^2$. The overall θ dependence is similar to that in Fig. 6(a), which is expected since

the θ dependence of T_c is determined by the scattering form factor. Compared to Fig. 6(a) the changes in T_c are somewhat less pronounced due to the fact that T_c changes less rapidly as a function of pairing strength in this case, as seen when comparing Figs. 7(a) and 6(b).

VI. SUMMARY

We have derived and solved the gap equation for magnon-mediated superconductivity in a TI/FMI bilayer for a

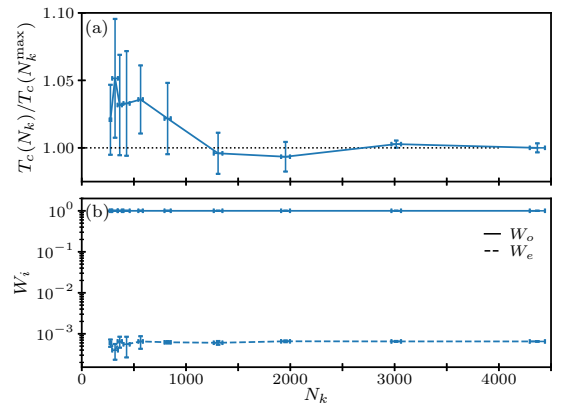


FIG. 8. (a) Plot of the critical temperature and (b) weights W_i as functions of the total number of grid points N_k used in the numerical calculation, for $\phi_{\mathbf{P}} = \theta = 0$, $J = 0.1 \text{ eV nm}^2$, and momentum cutoff k_F . The critical temperature is normalized to the value at the highest number of grid points. The figures show an average over five runs, with the error bars showing the sample standard deviation. The deviation in the number N_k is due to the way the number of grid points is set by the adaptive Python library [52].

general magnetization direction. Neglecting the frequency dependence of the magnon propagator, we found that only Amperean-type pairing was possible for easy-axis anisotropy coupling $\lambda > 0$. Tilting the magnetization toward the interface plane led to an overall shift in the Cooper pair center-of-mass momenta, and an increase in T_c for Cooper pairs with \mathbf{P} parallel to the magnetization vector.

Including the frequency dependence of the magnon propagator, we found that odd-frequency, even-momentum solutions to the gap equations dominated, thus leading to odd-frequency Amperean pairing. If odd-frequency pairing is found in such a system, it is an example of a naturally occurring odd-frequency superconductor, in contrast to odd-frequency pairing due to superconductors coupled to magnetic or spin-orbit-coupled materials [53–55]. This possibility should be further investigated by performing a strong coupling Eliashberg calculation, where also the frequency-dependent renormalization of the fermion propagator is taken into account. In addition, there are many other properties that should be calculated, such as the Meissner response [56] and the transport properties of the system, which might yield interesting results.

ACKNOWLEDGMENTS

We acknowledge funding from the Research Council of Norway Project No. 250985 ‘‘Fundamentals of Low-dissipative Topological Matter’’ and the Research Council of Norway through its Centres of Excellence funding scheme, Project No. 262633, ‘‘QuSpin.’’ H.G.H. thanks E. Erlandsen, E. Thingstad, and J. Linder for useful discussions. Most of the numerics utilized the Python library ADAPTIVE [52] to generate the \mathbf{k} -space points.

APPENDIX A: DETAILS OF THE CALCULATION OF THE MAGNON-MEDIATED INTERACTION

We rewrite the effective action in Eq. (14) in terms of the Dirac fermions defined by Eq. (22). We first get

$$j(q) = \frac{J}{\beta V} \sum_k \begin{pmatrix} \Psi_{\pm}^{\dagger}(k+q) P_{\mathbf{k}+q} (\cos \theta \sigma_x - \sin \theta \sigma_z) P_{\mathbf{k}}^{\dagger} \Psi_{\pm}(k) \\ \Psi_{\pm}^{\dagger}(k+q) P_{\mathbf{k}+q} \sigma_y P_{\mathbf{k}}^{\dagger} \Psi_{\pm}(k) \end{pmatrix}, \quad (\text{A1})$$

and performing the matrix calculations results in

$$\begin{aligned} P_{\mathbf{k}+q} \sigma_x P_{\mathbf{k}} &= \frac{1}{\sqrt{n_{\mathbf{k}} n_{\mathbf{k}+q}}} \begin{pmatrix} s_{\mathbf{k}} r_{\mathbf{k}+q} + s_{\mathbf{k}+q}^* r_{\mathbf{k}} & s_{\mathbf{k}}^* s_{\mathbf{k}+q}^* - r_{\mathbf{k}} r_{\mathbf{k}+q} \\ s_{\mathbf{k}} s_{\mathbf{k}+q} - r_{\mathbf{k}} r_{\mathbf{k}+q} & -s_{\mathbf{k}}^* r_{\mathbf{k}+q} - s_{\mathbf{k}+q} r_{\mathbf{k}} \end{pmatrix}, \\ P_{\mathbf{k}+q} \sigma_y P_{\mathbf{k}} &= \frac{i}{\sqrt{n_{\mathbf{k}} n_{\mathbf{k}+q}}} \begin{pmatrix} s_{\mathbf{k}} r_{\mathbf{k}+q} - s_{\mathbf{k}+q}^* r_{\mathbf{k}} & -s_{\mathbf{k}}^* s_{\mathbf{k}+q} - r_{\mathbf{k}} r_{\mathbf{k}+q} \\ s_{\mathbf{k}} s_{\mathbf{k}+q} + r_{\mathbf{k}} r_{\mathbf{k}+q} & -s_{\mathbf{k}}^* r_{\mathbf{k}+q} + s_{\mathbf{k}+q} r_{\mathbf{k}} \end{pmatrix}, \\ P_{\mathbf{k}+q} \sigma_z P_{\mathbf{k}} &= \frac{1}{\sqrt{n_{\mathbf{k}} n_{\mathbf{k}+q}}} \begin{pmatrix} s_{\mathbf{k}} s_{\mathbf{k}+q}^* - r_{\mathbf{k}} r_{\mathbf{k}+q} & -s_{\mathbf{k}}^* r_{\mathbf{k}+q} - s_{\mathbf{k}+q}^* r_{\mathbf{k}} \\ -s_{\mathbf{k}} r_{\mathbf{k}+q} - s_{\mathbf{k}+q} r_{\mathbf{k}} & -s_{\mathbf{k}+q} s_{\mathbf{k}}^* + r_{\mathbf{k}} r_{\mathbf{k}+q} \end{pmatrix}. \end{aligned}$$

We will now assume that the chemical potential $\mu > M \geq 0$, meaning that the Fermi level will lie in the + fermion band, and hence only the positive-helicity fermions will be free to interact. We therefore keep only the upper diagonal term in the above matrices, resulting in

$$j(q) = \frac{J\bar{m}}{\beta V} \sum_k \frac{\psi_{+}^{\dagger}(k+q)\psi_{+}(k)}{\sqrt{n_{\mathbf{k}} n_{\mathbf{k}+q}}} \begin{pmatrix} (s_{\mathbf{k}} r_{\mathbf{k}+q} + s_{\mathbf{k}+q}^* r_{\mathbf{k}}) \cos \theta - (s_{\mathbf{k}} s_{\mathbf{k}+q}^* - r_{\mathbf{k}} r_{\mathbf{k}+q}) \sin \theta \\ i(s_{\mathbf{k}} r_{\mathbf{k}+q} - s_{\mathbf{k}+q}^* r_{\mathbf{k}}) \end{pmatrix}. \quad (\text{A2})$$

We therefore get, dropping the + subscript on the fields,

$$\begin{aligned} \delta S_{\text{TI}} &= -\frac{J^2 \bar{m}}{4(\beta V)^3} \sum_{q, k, k'} D(q) \frac{\psi^{\dagger}(k'+q)\psi^{\dagger}(k-q)\psi(k)\psi(k')}{\sqrt{n_{\mathbf{k}} n_{\mathbf{k}-q} n_{\mathbf{k}'+q}}} \\ &\times [(s_{\mathbf{k}'} s_{\mathbf{k}-q}^* r_{\mathbf{k}'+q} r_{\mathbf{k}} + s_{\mathbf{k}} s_{\mathbf{k}'+q}^* r_{\mathbf{k}'} r_{\mathbf{k}-q}) (\cos^2 \theta + 1) + (s_{\mathbf{k}'} s_{\mathbf{k}} s_{\mathbf{k}'+q}^* s_{\mathbf{k}-q}^* - s_{\mathbf{k}'} s_{\mathbf{k}'+q}^* r_{\mathbf{k}'} r_{\mathbf{k}-q} \\ &- s_{\mathbf{k}} s_{\mathbf{k}-q}^* r_{\mathbf{k}'} r_{\mathbf{k}'+q} + r_{\mathbf{k}} r_{\mathbf{k}-q} r_{\mathbf{k}'} r_{\mathbf{k}'+q} - s_{\mathbf{k}'} s_{\mathbf{k}} r_{\mathbf{k}'+q} r_{\mathbf{k}-q} - s_{\mathbf{k}'+q}^* s_{\mathbf{k}-q}^* r_{\mathbf{k}'} r_{\mathbf{k}}) \sin^2 \theta \\ &- (s_{\mathbf{k}'} s_{\mathbf{k}} s_{\mathbf{k}-q}^* r_{\mathbf{k}'+q} + s_{\mathbf{k}} s_{\mathbf{k}'} s_{\mathbf{k}'+q}^* r_{\mathbf{k}-q} + s_{\mathbf{k}} s_{\mathbf{k}-q}^* s_{\mathbf{k}'+q}^* r_{\mathbf{k}'} + s_{\mathbf{k}'} s_{\mathbf{k}'+q}^* s_{\mathbf{k}-q}^* r_{\mathbf{k}} \\ &- s_{\mathbf{k}'} r_{\mathbf{k}'+q} r_{\mathbf{k}} r_{\mathbf{k}-q} - s_{\mathbf{k}} r_{\mathbf{k}-q} r_{\mathbf{k}'} r_{\mathbf{k}'+q} - s_{\mathbf{k}'+q}^* r_{\mathbf{k}'} r_{\mathbf{k}} r_{\mathbf{k}-q} - s_{\mathbf{k}-q}^* r_{\mathbf{k}} r_{\mathbf{k}'} r_{\mathbf{k}'+q}) \cos \theta \sin \theta] \end{aligned} \quad (\text{A3})$$

$$\equiv -\frac{J^2 \bar{m}}{4(\beta V)^3} \sum_{q, k, k'} D(q) \Lambda_{\mathbf{k}\mathbf{k}'}(q) \psi^{\dagger}(k'+q)\psi^{\dagger}(k-q)\psi(k)\psi(k'), \quad (\text{A4})$$

where $D(q)$ and $\Lambda_{\mathbf{k}\mathbf{k}'}(q)$ are defined in the main text.

APPENDIX B: HUBBARD-STRATONOVICH DECOUPLING

We perform a Hubbard-Stratonovich decoupling [47] by using the identity

$$1 = \int \mathcal{D}\varphi_q^\dagger \mathcal{D}\varphi_q \exp \left[\beta V \sum_{q,k,k'} \varphi_q^\dagger(k') [V_{k'k}(q)]^{-1} \varphi_q(k) \right]. \quad (\text{B1})$$

Rescaling the bosonic fields φ_q ,

$$\varphi_q^\dagger(k') \rightarrow \varphi_q^\dagger(k') + \frac{1}{(\beta V)^2} \sum_p \psi^\dagger \left(p + \frac{q}{2} \right) \psi^\dagger \left(-p + \frac{q}{2} \right) V_{pk'}(q), \quad (\text{B2})$$

$$\varphi_q(k) \rightarrow \varphi_q(k) + \frac{1}{(\beta V)^2} \sum_p V_{kp}(q) \psi \left(-p + \frac{q}{2} \right) \psi \left(p + \frac{q}{2} \right), \quad (\text{B3})$$

we get

$$\begin{aligned} \beta V \sum_{q,k,k'} \varphi_q^\dagger(k') [V_{k'k}(q)]^{-1} \varphi_q(k) &\rightarrow \beta V \sum_{q,k,k'} \varphi_q^\dagger(k') [V_{k'k}(q)]^{-1} \varphi_q(k) \\ &+ \frac{1}{\beta V} \sum_{q,k} \left[\varphi_q^\dagger(k) \psi \left(-k + \frac{q}{2} \right) \psi \left(k + \frac{q}{2} \right) + \varphi_q(k) \psi^\dagger \left(k + \frac{q}{2} \right) \psi^\dagger \left(-k + \frac{q}{2} \right) \right] \\ &+ \frac{1}{(\beta V)^3} \sum_{q,k',k} \psi^\dagger \left(k' + \frac{q}{2} \right) \psi^\dagger \left(-k' + \frac{q}{2} \right) V_{k'k}(q) \psi \left(-k + \frac{q}{2} \right) \psi \left(k + \frac{q}{2} \right). \end{aligned} \quad (\text{B4})$$

Hence, we arrive at the functional integral given in Eq. (32).

APPENDIX C: MATERIAL PARAMETERS

Unless otherwise stated, we have used the parameter values presented in Table I.

-
- [1] D. J. Scalapino, *Rev. Mod. Phys.* **84**, 1383 (2012).
[2] G. R. Stewart, *Adv. Phys.* **66**, 75 (2017).
[3] T. Moriya, Y. Takahashi, K. Ueda, T. Moryia, Y. Takahashi, and K. Ueda, *J. Phys. Soc. Jpn.* **59**, 2905 (1990).
[4] P. Monthoux, A. V. Balatsky, and D. Pines, *Phys. Rev. Lett.* **67**, 3448 (1991).
[5] P. Monthoux and D. Pines, *Phys. Rev. Lett.* **69**, 961 (1992).
[6] P. Monthoux, A. V. Balatsky, and D. Pines, *Phys. Rev. B* **46**, 14803 (1992).
[7] T. Moriya and K. Ueda, *Adv. Phys.* **49**, 555 (2000).
[8] T. Moriya and K. Ueda, *Rep. Prog. Phys.* **66**, 1299 (2003).
[9] T. Moriya, *Proc. Jpn. Acad., Ser. B* **82**, 1 (2006).
[10] T. R. Kirkpatrick, D. Belitz, T. Vojta, and R. Narayanan, *Phys. Rev. Lett.* **87**, 127003 (2001).
[11] H. Suhl, *Phys. Rev. Lett.* **87**, 167007 (2001).
[12] T. R. Kirkpatrick and D. Belitz, *Phys. Rev. B* **67**, 024515 (2003).
[13] N. Karchev, *Phys. Rev. B* **67**, 054416 (2003).
[14] R. Kar, T. Goswami, B. C. Paul, and A. Misra, *AIP Adv.* **4**, 087126 (2014).
[15] H. Funaki and H. Shimahara, *J. Phys. Soc. Jpn.* **83**, 123704 (2014).
[16] M. Kargarian, D. K. Efimkin, and V. Galitski, *Phys. Rev. Lett.* **117**, 076806 (2016).
[17] X. Gong, M. Kargarian, A. Stern, D. Yue, H. Zhou, X. Jin, V. M. Galitski, V. M. Yakovenko, and J. Xia, *Sci. Adv.* **3**, e1602579 (2017).
[18] N. Rohling, E. L. Fjærbu, and A. Brataas, *Phys. Rev. B* **97**, 115401 (2018).
[19] H. G. Hugdal, S. Rex, F. S. Nogueira, and A. Sudbø, *Phys. Rev. B* **97**, 195438 (2018).
[20] E. Erlandsen, A. Kamra, A. Brataas, and A. Sudbø, *Phys. Rev. B* **100**, 100503(R) (2019).
[21] E. L. Fjærbu, N. Rohling, and A. Brataas, *Phys. Rev. B* **100**, 125432 (2019).
[22] E. Erlandsen, A. Brataas, and A. Sudbø, *Phys. Rev. B* **101**, 094503 (2020).
[23] S.-S. Lee, P. A. Lee, and T. Senthil, *Phys. Rev. Lett.* **98**, 067006 (2007).
[24] Ø. Johansen, A. Kamra, C. Ulloa, A. Brataas, and R. A. Duine, *Phys. Rev. Lett.* **123**, 167203 (2019).
[25] M. Z. Hasan and C. L. Kane, *Rev. Mod. Phys.* **82**, 3045 (2010).
[26] X.-L. Qi and S.-C. Zhang, *Rev. Mod. Phys.* **83**, 1057 (2011).
[27] J. Bardeen, L. N. Cooper, and J. R. Schrieffer, *Phys. Rev.* **108**, 1175 (1957).
[28] V. L. Berezinskii, Pis'ma Zh. Eksp. Teor. Fiz. **20**, 628 (1974), [JETP Lett. **20**, 287 (1974)].
[29] A. Balatsky and E. Abrahams, *Phys. Rev. B* **45**, 13125(R) (1992).
[30] P. Coleman, E. Miranda, and A. Tsvelik, *Phys. Rev. Lett.* **70**, 2960 (1993).
[31] P. Coleman, E. Miranda, and A. Tsvelik, *Phys. B (Amsterdam)* **186-188**, 362 (1993).
[32] P. Coleman, E. Miranda, and A. Tsvelik, *Phys. Rev. B* **49**, 8955 (1994); L. Vinet and A. Zhedanov, *J. Phys. A: Math. Theor.* **44**, 085201 (2011).

- [33] E. Abrahams, A. Balatsky, D. J. Scalapino, and J. R. Schrieffer, *Phys. Rev. B* **52**, 1271 (1995).
- [34] F. S. Bergeret, A. F. Volkov, and K. B. Efetov, *Rev. Mod. Phys.* **77**, 1321 (2005).
- [35] Y. Tanaka, M. Sato, and N. Nagaosa, *J. Phys. Soc. Jpn.* **81**, 011013 (2012).
- [36] J. Linder and A. V. Balatsky, *Rev. Mod. Phys.* **91**, 045005 (2019).
- [37] A. Auerbach, *Interacting Electrons and Quantum Magnetism* (Springer, Berlin, 1994).
- [38] S. Rex, F. S. Nogueira, and A. Sudbø, *Phys. Rev. B* **95**, 155430 (2017).
- [39] P. Fulde and R. A. Ferrell, *Phys. Rev.* **135**, A550 (1964).
- [40] A. I. Larkin and Yu. N. Ovchinnikov, *Zh. Eksp. Teor. Fiz.* **47**, 1136 (1964) [*Sov. Phys.-JETP* **20**, 762 (1965)].
- [41] V. Barzykin and L. P. Gor'kov, *Phys. Rev. Lett.* **89**, 227002 (2002).
- [42] O. Dimitrova and M. V. Feigel'man, *Phys. Rev. B* **76**, 014522 (2007).
- [43] D. F. Agterberg and R. P. Kaur, *Phys. Rev. B* **75**, 064511 (2007).
- [44] F. Loder, A. P. Kampf, and T. Kopp, *J. Phys.: Condens. Matter* **25**, 362201 (2013).
- [45] E. Lake, C. Webb, D. A. Pesin, and O. A. Starykh, *Phys. Rev. B* **93**, 214516 (2016).
- [46] H. G. Hugdal and A. Sudbø, *Phys. Rev. B* **97**, 024515 (2018).
- [47] A. Altland and B. Simons, *Condensed Matter Field Theory*, 2nd ed. (Cambridge University Press, Cambridge, 2010).
- [48] G. M. Eliashberg, *Zh. Eksp. Teor. Fiz.* **38**, 966 (1960) [*Sov. Phys.-JETP* **11**, 696 (1960)].
- [49] G. M. Eliashberg, *Zh. Eksp. Teor. Fiz.* **39**, 1437 (1960) [*Sov. Phys.-JETP* **12**, 1000 (1961)].
- [50] G. D. Mahan, *Many-Particle Physics*, 3rd ed. (Kluwer Academic, New York, 2000).
- [51] M. Sigrist, in *Lectures on the Physics of Highly Correlated Electron Systems IX: Ninth Training Course in the Physics of Correlated Electron Systems and High-Tc Superconductors*, AIP Conference Proceedings, Vol. 789 (AIP, Melville, NY, 2005), p. 165.
- [52] B. Nijholt, J. Weston, J. Hoofwijk, and A. Akhmerov, *Python-adaptive/adaptive: version 0.11.2* (Zenodo, 2020), <https://doi.org/10.5281/zenodo.1182437>.
- [53] M. Eschrig, *Phys. Today* **64**(1), 43 (2011).
- [54] J. Linder and J. W. A. Robinson, *Nat. Phys.* **11**, 307 (2015).
- [55] M. Eschrig, *Rep. Prog. Phys.* **78**, 104501 (2015).
- [56] Y. V. Fominov, Y. Tanaka, Y. Asano, and M. Eschrig, *Phys. Rev. B* **91**, 144514 (2015).
- [57] H. Zhang, C.-X. Liu, X.-L. Qi, X. Dai, Z. Fang, and S.-C. Zhang, *Nat. Phys.* **5**, 438 (2009).
- [58] J. G. Analytis, J.-H. Chu, Y. Chen, F. Corredor, R. D. McDonald, Z. X. Shen, and I. R. Fisher, *Phys. Rev. B* **81**, 205407 (2010).
- [59] A. T. Lee, M. J. Han, and K. Park, *Phys. Rev. B* **90**, 155103 (2014).
- [60] S. R. Yang, Y. T. Fanchiang, C. C. Chen, C. C. Tseng, Y. C. Liu, M. X. Guo, M. Hong, S. F. Lee, and J. Kwo, *Phys. Rev. B* **100**, 045138 (2019).
- [61] H. G. Bohn, W. Zinn, B. Dorner, and A. Kollmar, *Phys. Rev. B* **22**, 5447 (1980).

This document was typeset using the typographical look-and-feel `classicthesis` developed by André Miede and Ivo Pletikosić. The style was inspired by Robert Bringhurst’s seminal book on typography “*The Elements of Typographic Style*”. `classicthesis` is available for both \LaTeX and LyX :

<https://bitbucket.org/amiede/classicthesis/>

The figures were created using the Python library `matplotlib`, and the \LaTeX packages `TikZ`, `PGFPLOTS` and `TikZ-Feynman` [248].

ISBN 978-82-326-6945-5 (printed ver.)
ISBN 978-82-326-5597-7 (electronic ver.)
ISSN 1503-8181 (printed ver.)
ISSN 2703-8084 (online ver.)



NTNU

Norwegian University of
Science and Technology